University of Alberta

Design and Construction of a Temperature Cell to Study the Effect of Temperature Rise on Particle-Drop Impact

by

Mina Karimi

A thesis submitted to the Faculty of Graduate Studies and Research
in partial fulfillment of the requirements for the degree of

Master of Science

Department of Mechanical Engineering

Fall 2013
Edmonton, Alberta

Abstract

An experimental device aimed at simulating interactions in a fluidization process was designed, built, and tested to allow future study of drop-particle impact at high temperatures. The design parameters were defined based on theoretical investigations. A feasibility study were developed using QFD method to select appropriate mechanisms for the device. The available experimental data were analyzed and the required calculations were conducted to determine the design values. The technical drawings and procurement documents were prepared and the device was constructed in the Department of Mechanical Engineering machine shop. The device's performance was tested afterwards in different ways. The device is capable of providing a test environment with different temperatures (ambient to 200 ºC). This experimental device can be used to investigate the influence of different variable parameters, such as drop and particle properties and sizes, collision velocity, impact parameter and collision angles (90º to 180º) on drop-particle impact.

Acknowledgements

I would like to express my deepest appreciation to and respect for all the people who have supported me with their honesty, knowledge and love, and encouraged me to step ahead despite all fears and despair.

I would like to thank my supervisor, Dr. Alidad Amirfazli, for his help, support, responsibility and care. I am truly grateful for his thoughtful advice and brilliant ideas, which drive me to accomplish my work. His care and consideration in reviewing my thesis in spite of his being too busy is highly appreciated.

I would also like to thank my other supervisor, Dr Brian Fleck, for giving me a chance to continue my studies at the University of Alberta and for supporting me financially during my studies. Thank you for helping me to realize my dreams.

I cannot find words to express my gratitude to Bernie Faulkner, our shop specialist technician, for all his help, support and care, even beyond his duties. This work would never have been accomplished without his support, expertise and brilliant comments. Thank you, Bernie, for being there whenever I needed help or advice. Thank you for all your caring and kindness and all your encouragement.

I would like to thank our shop technicians, Rick Conrad and Daniel Mooney, for their valuable contribution and help. Thanks, Rick, for your excellent advice and solutions to the problems encountered during the work.

I would also like to thank my professors, Dr. David Nobes, Dr. Morris Flynn, Dr. Warren Finley, Dr. Larry Kostiuk and Dr. Carlos Lange, for offering precious information and sharing their knowledge in their courses, which helped me to better understand and manage my experimental works.

I am grateful to Dr. Jason Carey, my committee member, for the time he has spent reviewing my thesis, and for his useful comments.

I would like to thank my colleagues, Oliver Peise and Stefan Strzebin, for providing me with the results of their experiments on drop-particle collision in ambient temperatures.

I am truly grateful to Deborah Waldman, the writing advisor at the student success centre at the University of Alberta, for her kind consideration in proofreading and editing my thesis.

My special thanks goes to my dear friend Dr. Sara Madani who not only supported me with her kind, caring friendship but also helped me a lot on my thesis by sharing her knowledgeable advice.

I am so grateful to all my colleagues in the surface engineering lab for creating a warm atmosphere and for their unforgettable friendship, especially, Maryam, Manindarjit, Huanchen and Alberto for their support and encouragement.

I would like to thank David Dubyk and Virginia Makofka in our IT group for their instant help and kind consideration whenever I encountered a problem or needed advice.

I would like to extend my appreciation to the office staff of the Department of Mechanical Engineering for their support and commitment, especially, Donna Waring, Richard Groulx, Gail Dowler, Catherine Evens and Linda Paulic.

I am greatly indebted to all my undergraduate professors at the University of Tehran, who played a significant role in my education. Dr. Vahid Esfahanian, Dr. Farshad Kowsary, Dr. Mohammad Hassan Rahimian, thank you all for giving me a chance to follow my wishes by trusting me and recommending me for my graduate studies.

I would like to express my deep appreciation to my uncle Ali Raees' family in Toronto, for their warm reception and caring during my first months of immigration to Canada. I also deeply appreciate Mehrdokht and Farshid, my two dear friends, who accepted me warmly in their home during my fist days of stay in Edmonton.

Although I'm far away from my beloved family, I have a wonderful Canadian family whose motherly care and support heal all suffering and sadness, and give me hope to keep

going on my way. My dear Marjie, Phil and Shima, I am blessed with your presence in my life. Neda, I'm happy to have you around and I'm thankful for trusting me and all sharing. Dear Marjie, now "I think I can!"

It is not easy to express your feelings for your beloved ones. I am indebted in my life to my family, especially my mother, who sacrificed all her wishes and future for our happiness. I am the most luckiest person in the world to have such a sincere father and I'm fortunate to have my two brothers, Behrang and Behnam, and my sister-in-law, Nasrin, who always supported me and encouraged me with their pure love and caring.

And finally but importantly, I would like to thank my dear friend Kamel for his presence in my life and for all the goodness and happiness he has brought to my life. Thanks for every single day that you were there for me and thanks for the small piece of heaven you made for all of us by your sincere effort and pure heart.

Mina Karimi

Table of Contents

List of Tables

List of Figures

Abbreviations

α	Particle initial velocity angle with respect to the horizon/thermal diffusivity
β	Collision angle
γ	Dynamic surface tension
Δ	Drop diameter ratio
ΔT	Temperature rise
θ	Final particle-drop velocity angle
μ	Dynamic viscosity
ν	Kinematic viscosity
ρ	Density
σ	Kinematic surface tension (defined in thesis)
A	Surface area
Bo	Bond number
CCD	Charge-coupled device
CMOS	Complementary metal-oxide semiconductor
CHR	Confocal chromatic sensoring technique
Ca	Capillary number
CS	Carbon steel
CMC	Constant momentum collision
c	Specific heat
d	Drop diameter
d_d	Drop diameter
d_p	Particle diameter
dl	Distance between collision point and launcher tip
DI	Deionized water
D_d	Drop diameter
D_p	Particle diameter
DOF	Degree of freedom
EMV	Experimental measured velocity
f	Coriolis force
Fr	Froude number
g	Acceleration of gravity

GRE	Glass reinforced epoxy
HOQ	House of quality
HVAC	Heating, ventilation, and air conditioning
h	Distance between collision point and generator tip
IAT	Image analysis technique
IR	Infrared
k	Thermal conductivity/spring constant
LED	Light-emitting diode
L	Characteristic length
m_p	Mass of particle
m_d	Mass of drop
m	Mass (general)
N/A	Not applicable
Oh	Ohnesorge number
PVC	Polyvinyl chloride
PVDF	Polyvinylidene fluoride
PDA	Phase doppler anemometry
PID	Proportional-integral-derivative
PIC	Perfectly inelastic collision
QFD	Quality function deployment
$\dot{q}$	Heat flux
Re	Reynolds number
Ro	Rossby number
SR	Surface roughness
S	Non-dimensional surface roughness
SS	Stainless steel
s	Wall thickness
T	Temperature inside the cell
t	Time
T_o	Outside temperature
T_S	Wall temperature
TB	Temperature at bottom heater block
TL	Temperature at launcher heater block

TU	Temperature at top heater block
TI	Temperature inside the cell close to the launcher tip
TP	Temperature inside the particle launcher
U	Characteristic velocity
u	Drop velocity
u_d	Drop velocity
u_p	Particle velocity
V	Relative velocity
V_{p1}	Velocity of particle before collision
V_{d1}	Velocity of drop before collision
V_2	Velocity of attached particle and drop after collision
V_{p2}	Velocity of particle after collision
V_{d2}	Velocity of drop after collision
V_{Rltv}	Required relative velocity at collision
V_{PI}	Particle initial velocity at launcher tip
V_{PC}	Particle velocity at collision point
V_{DI}	Drop initial velocity at drop generator tip
V_{DC}	Drop velocity at collision point
V_F	Final velocity of bonded particle and drop after collision
v	Velocity of plunger
We	Weber number
X	Impact parameter
x	Non-dimensional impact parameter/displacement made by the spring

Chapter 1
Introduction

The drop interaction with another drop, a liquid film or a solid surface has been one of the main topics of interest for many researchers since the 19th century. The emergence and development of high-speed photography during the early part of the 19th century, played a significant role in the advancement of such investigations and opened a new era in understanding numerous industrial and natural phenomena [31, 67]. Describing the atmospheric and meteorological phenomena such as precipitation formation, physics of clouds and the determination of collision efficiency, was one of the early motivations for drop collision studies [3, 4, 10]. Most of the investigations have been dominated by spray technology: spray painting, spray coating, spray cooling and spray combustion [25, 39, 65]. Combustion technology also has benefited, mostly from drop collision studies both in pollutant reduction and combustion efficiency [5, 14, 25]. However, drop collision has found its way into a variety of areas, including the polymer industry [4, 8], chemical reactors [8], inkjet printing [27, 47, 48], metallurgical and steel production industries [31], plasma spraying, the drug industry, aerosol depositions, delivery of agrochemicals [39], insecticide sprays [47], erosion in turbo-machinery [49], the food industry [51], fire protection and fire fighting [25, 55, 69], catalytic cracking [80] and fluidization [83]. The drop collision phenomenon has been investigated experimentally in three main categories: drop-drop collision, drop-surface collision and drop-liquid film collision; however, many other experiments have been conducted on drop-liquid jet collision, drop-heated surface collision, drop-granular medium collision, drop-particle collision, etc.

1.1 Motivation

Drop-particle impact is the main contributing interaction in the fluidization process, especially in liquid fluidizations. A fundamental study of individual drop-particle impact is crucial in understanding the fluidization mechanism and improving the reactions. Although there are many theoretical or numerical investigations in this field, the

experimental studies are limited to drop impacts onto stationary particles and objects. No experiments have been done on the impact of a drop onto a particle in midair.

1.1.1 Fluidization

"Fluidization is a process whereby a bed of solid particles is transformed into something closely resembling a liquid" [1]. As shown in Figure 1-1, a pressurized fluid in either a liquid or gas state is injected into a bed of stationary particles through spray jets inside a vessel. If the flow rate reaches a certain amount, called the fluidization point, the particles start to flow inside the liquid, showing the liquid properties in motion. In the fluidization point, the drag force equals the gravitational force on each particle. Having individual particles moving freely inside the medium, the mass and heat are transferred uniformly as they are in the fluids [1].

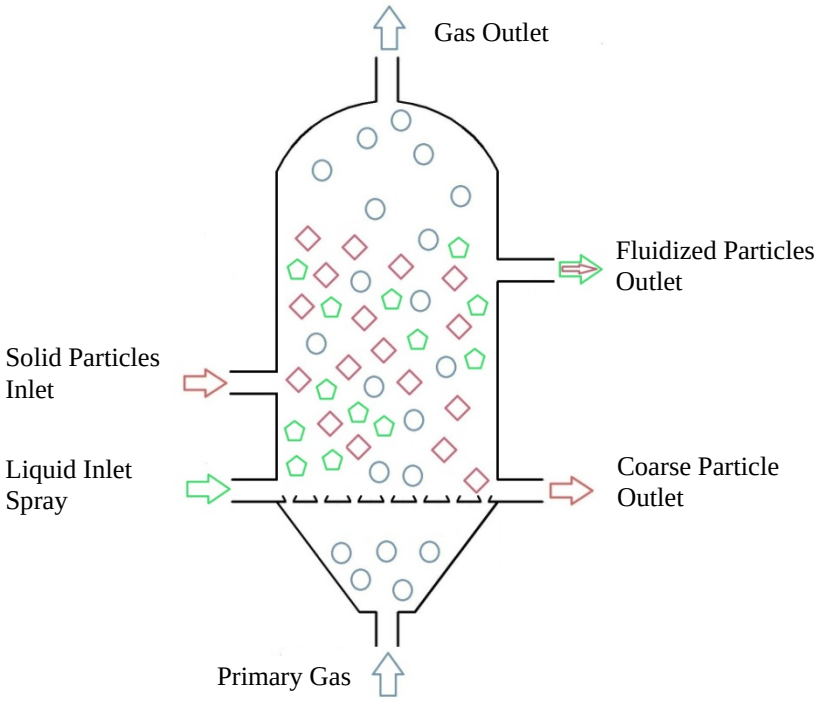

Figure 1-1 Simplified schematic diagram of a conventional fluidized bed reactor

To explain the fluidization phenomena, Gibilaro [1] used a simple traditional demonstration of placing one metal and one plastic toy ducks onto a bed of fine sand. The metal duck, which was heavy, was placed on top of the bed. The light plastic one was buried in the sand. When pressurized air was applied to the system, the plastic duck

floated and the metal duck sank at fluidization point. Also used to illustrate what happens inside the fluidization reactors are the popcorn poppers [1].

The first gaseous fluidized bed was introduced to the power industry in 1921 by Fritz Winkler. He injected gaseous products of combustion into a crucible of coke particles and produced the first bubbling fluidized bed [2].

Usually two different mechanisms are specified to define the fluidization state: bubbling and homogeneous fluidization. Bubbling fluidization usually occurs in a gaseous medium. The process of the particles rising under balancing forces is similar to what happens when a liquid boils. However, homogeneous fluidization is more common in liquid fluidizations when the entire bed moves and expands homogeneously; that is, individual particles move more uniformly relative to each other. These two mechanisms are referred to as extreme fluidization qualities. The intimate interaction between fluid and particle determines the quality of chemical reactions inside the reactors. Therefore, studying the fluidization quality and, specifically, individual particle-drop interactions, is vital to improve the chemical reactions [1].

1.1.2 Application

The main application of a fluidized bed is in the catalytic-cracking reactor of petroleum refineries, where the pressurized vaporized crude oil is injected into the catalyst bed in order to break down the large molecules of crude oil into small molecules such as gasoline, diesel and fuel oil. Gas-fluidized beds are used mostly in chemical reactors and combustors, while liquid-fluidized beds are mostly used in water treatment, mineral processing and fermentation technology [1].

Basu [2] classifies the application of a fluidized bed into five main categories:

- The energy conversion industry, including steam generation, gasification and incineration
- Petrochemical processes, including fluid catalytic cracking units
- The mineral processing industry, including alumina calcination, ore roasting, iron ore pre-reduction and cement pre-calcination

- Chemical and pharmaceutical industries, including transforming phthalic anhydride from naphthalene, decomposing sulfate and chloride, butane oxidation to maleic anhydrite and methanol to olefins conversion
- Physical processing, including drying, coating the particles, heat exchanger and flue gas cleaning and heat treatment

1.2 Objectives and Thesis Outline

As mentioned in previous sections, many industries are using fluidized beds and fluidization process. Therefore, understanding the fluidization mechanism is crucial in enhancing the performance of many industrial units. Since the drop-particle impact is the main contributing interaction in fluidization, studying individual drop and particle impact at high temperatures is the first fundamental step in discovering the main parameters which influence the process. There are different theoretical, numerical and experimental approaches to studying the phenomenon. However, the objective of this thesis was to develop an experimental apparatus to make it possible to investigate the fundamental step in the fluidization process. A simulation was initiated in this thesis. It looked at only the individual drop-particle collision. In this simulation, a liquid was spray-injected into a solid particle bed. To achieve this simulation, an experimental device was designed, built and tested to allow future study of the drop-particle collision in a high temperature environment.

Before going through the main design process, the previous works in drop collision were reviewed. Chapter 2 includes that review, as well as the theory behind the mechanism. In Chapter 3, the design plan is clarified in different steps and the design process begins with justifying the basic design elements. The required analysis and calculations are provided in Chapter 4. Chapter 5 contains the detailed design of each part. Chapter 6 includes the performance test results. The conclusion and future works are discussed in Chapter 7.

Chapter 2
Literature Review

2.1 Previous Works

Drop Collision has been one of the interesting topics in research for decades and hundreds of articles have been published based on the theoretical, numerical and experimental studies of the phenomenon. In this thesis, the focus is on the experimental works only [3 to 84]. The theoretical and numerical methods in previous works are excluded from the review. Of the articles selected for review, the only sections chosen for discussion in this thesis are those that pertain to the experimental setup and application. The results of and discussion about the collision outcomes are not considered. The review focuses on articles published between 1990 and 2012. Older articles are mentioned only to provide historical context. The articles are presented in this review in a semi-chronological order; that is, in general the articles are presented in chronological sequence while in many parts similar or related works or the articles of the same authors are grouped together regardless of the year of publication. The previous works are studied in five categories: Drop-Drop Collisions, Drop-Solid Surface Collisions, Drop-Heated Solid Surface Collisions, Drop-Liquid Surface Collisions and Drop-Particle Collisions.

2.1.1 Drop-Drop Collision

The study of drop-drop collision emerged from atmospheric and meteorological science to study the precipitation formation, physics of clouds and collision efficiency. Telford and Thorndike [3] studied the collision of small drops between 20μm and 60μm to support the theoretical works of Hocking [3]. One of the important works on drop-drop collision was conducted by Magarvey and Geldart [4] to study the effect of drop size on precipitation formation. An experimental apparatus was used to observe drops colliding under free fall conditions. Two drop generators and drop selectors were located at two different levels to generate drops of different sizes and velocities. The drop generators consisted of two water jets. Periodically, the water jets were disturbed, which generated the drops. The drop selectors were used to allow only an individual drop to go through

the test section. Two cameras were located in the test section to record the experimental data [4].

Park provided a complete review of drop collision investigations up to 1970. Park's own investigations are also one the most outstanding works of that era [5]. Park and Crosby [6] designed and constructed a device to control the collision between the two drops. The major problems of the previous experimental investigations were difficulties in controlling and reproducing the phenomenon, and the lack of quantitative measurements. A new device was developed to reduce these deficiencies. The device consisted of a cylindrical collision chamber to maintain a constant collision condition, and a vibration transmitter system to generate drops from the jet [6].

In early works, to generate uniform-sized drops, water was pumped into a capillary to produce a water jet, and a mechanical device was used to introduce a disturbance to the water jet to break the jet into a stream of drops. However, Adam et al. [7] used a new drop generator to conduct a set of experiments to study the effect of drop size, charge, velocity, and impact parameter. In their drop generator, a piezoelectric transducer was used to launch vibrations into the water jet [7].

Scheele and Leng [8] investigated the effect of drop size, impact velocity and collision angle on coalescence or rebound of anisole drops in the water medium. In many processes such as extraction, suspension polymerizations and "conversion of reactants in a chemical reactor," the coalescence rate is important. Two drop generators submerged into the 25mm depth of a 0.04 m^3 tank were used to generate anisole drops under water. The pressurized nitrogen forced the anisole to flow toward the drop generator. An electromagnetic pulse was introduced to the system to generate drops from the continuous fluid flow. The pulse frequency and the flow rate controlled the drop size in the device [8].

McTaggart-Cowan and List [9] investigated how water drops in terminal velocities collide and break up in a vertical motion. Their work was a new approach in studying of drop-drop collisions.

To study the effect of atmospheric electrical force on rain formation, Paul et al. [10] conducted new experiments on how water drops collide in the oil medium in the presence of an electrical field. The experimental setup consisted of a vertical chamber filled with mustard oil or kerosene oil. The electrical field was generated by two copper plates located on the top and bottom of the chamber connected to a variable DC power supply. The drop generator was made of two glass syringes which were adjustable laterally and vertically to control the collision between the two drops [10].

Ashgriz conducted a number of interesting studies of drop-drop collisions. Applying sprays in combustion processes such as in "jet propulsion engines, diesel engines, industrial boilers and furnaces" drove Ashgriz and Givi [11] to start their studies in fuel drop collisions. They introduced three regions in industrial sprays: dilute spray, dense spray and churning flow regions. Then, they focused their investigations on the dense spray region. In order to simulate the high temperature of the combustion engines, they used both burning and non-burning n-hexane fuel drops in their experiments. They designed a piezoelectric drop generator to generate uniform-sized streams of drops. The device consisted of an ejector, a piezoelectric bimorph and a glass nozzle. This arrangement was connected to a fuel reservoir and a function generator. The fuel was pumped toward the ejector using a pressurized nitrogen tank, and the function generator agitated the piezoelectric bimorph, resulting in controlled impulses. Two special stands provided required targeting movements of the drop generators [11].

Finding the coalescence efficiencies of two fuel drops was an important target in studying the spray combustion process. At the time of Ashgriz and Givi [12], the coalescence efficiency had been studied and determined in precipitation phenomena. However, the coalescence efficiency of fuel drops had been not yet investigated. Ashgriz and Givi [12] conducted a series of experiments to study the coalescence efficiencies of n-hexane fuel drops. In these experiments the burning and non-burning fuel drops were tested to estimate the effect of the combustion processes' high temperature environment [12].

Finally, Ashgriz and Poo [5] conducted a complete set of experiments on water drop collisions to verify different types of collision regimes, as well as to determine the boundaries between the specified regimes. Using the experimental results, they also provided the theoretical model for predicting numbers of collision outcomes. The results

of their investigations had an important influence on studies of atmospheric raindrop formation, liquid-liquid extraction, emulsion polymerization, waste treatment and hydrocarbon fermentation, as well as dense spray systems [5].

Studying spray combustion led Jiang et al. [13] to investigate the effect of the Weber number and impact parameter on the collision behavior of equal-sized water and normal-alkane drops. This was one of the fundamental studies in the 90's, which introduced different regimes of collision. In their experiments, Jiang et al. [13] connected two piezoelectric drop generators to a glass nozzle to generate a uniform and stable stream of drops. The size and velocity of the drops were controlled by voltage generator pulses and the diameter of the drop nozzles. Two positioning mechanisms were used for targeting and controlling the trajectory of the drops: a three-dimensional positioning mechanism used to mount one drop generator and a rotational mechanism to provide rotation in the vertical plane. The shadowgraph photography was applied using a strobe light operating both independently from and synchronized with the pulse generator [13].

Following the studies of Jiang et al.'s [13], Qian and Law's [14] investigations on the binary drop collision of water and hydrocarbon drops introduced the B-We graphs (impact parameter versus Weber number). Qian and Law [14] used different gases (air, nitrogen, helium and ethylene) under different pressures as the experimental environments. They focused on the effect of environmental and liquid properties to determine the transition regimes in collision outcomes. Their investigations resulted in the B-We graphs showing five different collision regimes which were used as one of the most important references in drop collision studies. These studies focused on raindrop formation, nuclear fusion, spraying processes and combustion engines [14].

Stating that the most experimental studies of drop collision had been performed on water drop impacts in meteorological studies, Orme [15] presented a review of the experimental study of drop collision. That study focused on both fuel drops and water drops, and demonstrated the importance of recent studies on fuel drop collision in combustion and showed the significant difference in collision outcomes [15].

Orme continued her investigations on fuel drop collisions by conducting experiments on fuel drop collision in a vacuum environment (Willis and Orme [16, 17]). An aluminum

chamber with Plexiglas windows for photography access was used as the vacuum chamber in Willis and Orme's [16, 17] experimental setup. Using a diffusion and vacuum pump, the pressure inside the cell reached 10^{-4} Torr. Two piezoelectric-orifice drop generators were connected to a compressed gas vessel and a fluid accumulator to generate stable drop streams. Due to the low pressure (near vacuum), low vapor pressure oil should be used in the setup [16, 17].

Spray technology led Brenn to introduce a monodisperse spray generator (Brenn et al. [18]) and to conduct several experiments on randomly generated drops (Brenn et al. [19]). The process of the satellite formation in unstable binary drop collisions was one of the topics which had been investigated by Brenn and his colleagues both experimentally and theoretically (Brenn et al. [20]) [18, 19, 20].

Brenn and Kolobaric [21] studied the effect of drop size and liquid viscosity on the formation of satellite drops in unstable binary collisions. Two drop generators connected to pressurized liquid vessels and signal generators formed part of the setup used in their experiments. The laminar liquid jet releasing from the drop generator nozzle plates was converted to monodisperse drops by piezoceramic vibrators agitated by an electric DC square-wave signal. The relative velocities were controlled by either the pressure of liquid reservoirs or by changing the collision angle. The phenomenon was recorded by camera and a high-intensity LED synchronized with the drop generators excitation signal. The images were processed by a Matlab code [21].

Rong-Horng Chen conducted several experiments on drop collisions to study the process of spray combustion in diesel engines. Chen [22] investigated the collision between diesel drops with diesel and ethanol drops. He used piezoelectric drop generators to generate drops streams of about 700-800μm with the velocity of 1-2m/s. The drop generators were connected to two pressurized containers filled with the working liquids. A stroboscope synchronized with the frequency of the drop generators provided the background light for the photography. To distinguish the drops from each other, he used dyed ethanol drops in his experiments [22].

The same experimental setup was used previously by Chen and his colleagues to study the near head-on collision regimes of immiscible drops with large deference in surface

tension; Chen R.H. and Chen C.T. [23] investigated the collision between water drops and diesel oil drops. Gao et al. [24] studied the collision between water drops and ethanol drops [23, 24].

Spray combustion, spray painting and coating and fire fighting via liquid injection drove Pan et al. [25] to conduct one of the more interesting drop collision experiments in recent years. They investigated different liquid drops to identify head-on drop collision regimes in high Weber numbers. They were able to discover various regimes beyond the common, previously determined regimes at moderate Weber numbers. They generated high speed drops of 23 m/s to reach the Weber number of about 5100. The drop generator used to generate the high speed drops comprised a gas cylinder fed by an air compressor and two liquid cylinders connected to the gas cylinder via movable pistons. A continuous high speed liquid jet was produced by pneumatic compression and released from a 0.45mm nozzle of the drop generator. To generate drops out of these high speed jets, a rotating disc with a knife edge was used to cut the jet into stable drops. To generate a head-on collision the second drop generator was located upward, and aligned with the first one. The second generator used the piezoelectric diaphragm vibration technique to generate more accurate targeted drops. The entire experiment was performed inside a Plexiglas chamber to reduce the surrounding air influences [25].

Despite other investigations into binary drop collisions in midair, Fujimoto et al. [26] investigated the drop impact on a hemispherical stationary drop on a solid surface. This study was followed by one conducted by Nikolopoulos et al. [27], who investigated the drop impact on a stationary drop on different surfaces. Their motivation was to study surface cooling or coating, spray injection in internal combustion, and inkjet printing. Different impact regimes were identified versus different Weber numbers and surface wetting properties. The drop generator used in the Nikolopoulos et al. study setup consisted of a needle connected to a tank. A solenoid valve was used to impose a pressure pulse on the tank to detach the drops. The experiment was recorded by a CCD camera. A triggering system of a laser beam and a photodiode was used to control the flash duration of the flash lamp [27].

One of the recent works in drop-drop collision was done by C. Planchette in the study of the collision between immiscible liquids focusing on spray application. Planchette et al.

[28] identified different collision regimes by changing water and oil properties, drop size, relative velocity and impact parameter. The experimental setup consisted of two drop generators which applied the Rayleigh–Plateau instability to generate monodisperse drop streams. These generators were adapted from Brenn et al.'s [18] monodisperse spray mechanism. The drop generators were connected to different pressurized tanks of different immiscible liquids. Different drop sizes between 150μm and 350μm were produced by changing the nozzle sizes. The collision was recorded by a high-speed camera [28, 18].

The same setup was used by Planchette and his colleagues to study the immiscible liquids collision: Roisman et al. [29] studied the head-on collisions of immiscible liquids, and Planchette et al. [30] investigated the phenomenon of immiscible liquid drops encapsulating each other.

2.1.2 Drop-Solid Surface Collision

The study of drop-surface collision has become the focus of many studies since the 1970's, due to its industrial applications such as thin film coating, spray painting and coating, injection systems and spraying molten metal in the metallurgical industry. Schmidt and Knauss (1976) studied the impact of mercury drops on a rotary atomizer. Levin and Hobbs (1971) studied the impact of water drops on a copper hemispherical surface. Their works were continued by Stow and Hadfield (1981) to determine the size of splashed drops with more accuracy. Walzel (1980) studied the impact of water-glycerin mixture drops on dry and wet surfaces [31].

To find an experimental model to describe the impact of spray drops on a flat surface, Mundo et al. [31] conducted a series of experiments using monodisperse water-ethanol sucrose drops with different viscosities and surface tension, and a cold stainless steel surface. The experimental setup consisted of a vibrating orifice drop generator and a rotating disc with a rubber rim. The liquid was forced through an orifice to form the drop, and a piezo-quartz was used to perturb the outflow jet. The drops were directed toward the rotating disc. The collision angle was determined by the disc's angular velocity. The constant normal component of the velocity was determined by the drop generator operating frequency. The rubber rim was used to remove the remaining liquid film from

the previous experiments. A synchronized lighting with drop impact was used for high speed photography in these experiments [31].

Studying the mechanism of spray cooling and painting, ink-jet printing and fuel injection motivated Rioboo et al. [32] to start a set of experiments about drop-surface impact. They studied the effect of different parameters on collision outcomes. These parameters included drop diameter and velocity, and fluid properties such as surface tension and viscosity. They used acetone, isopropanol, ethanol, water, silicone oils, and mixtures of glycerin and water as liquid drops; and glass, PVC, wax, and polymer coatings as tested surfaces [32].

They used a precision syringe to generate drops in the setup. The velocity of the drop was determined by the height of the needle from the test section. The shadowgraph photography technique was used to record the impact. The stroboscope and the CCD camera were synchronized and triggered by the drop passing through a light barrier [32].

Sikalo et al. [33] studied the effect of impact parameter on drop-surface impact. Water, isopropanol and glycerin liquid drops were tested on different surfaces: smooth glass, PVC, wax and rough glass. One of the most important parameters considered in these experiments was the effect of wettability on drop-surface impact. The setup used in the experiments was quite similar to the one used by Rioboo et al. [32], consisting of a drop generator, an impact plate and a photography system. The drop generator comprised an elevated liquid tank connected to a syringe through a feeding tube and a valve. The test section was located inside a Plexiglas tube to protect it from any external disturbances. The same photography technique was also used in this setup [33].

Sikalo et al. [34] continued their studies on drop-surface by investigating the drop impact on dry surfaces and surfaces with liquid films. The low impact angles and normal Weber numbers were considered. The setup in Sikalo et al. [33] was employed to conduct these experiments [34].

One of the recent works on drop-surface impact was conducted by Mangili et al. [35] on investigating the dynamic of the collision between water drops and a soft, dry PDMS surface. They analyzed the drop evolution as well as the deformation of the surface. A

sensor implemented in the substance was used to measure the deformation caused by the impact. Three-dimensional photography was used to monitor the impact. The images were analyzed using Matlab code [35].

Fujimoto et al. [36] studied the liquid-surface contact area of a drop after the drop landed on a solid surface. The setup consisted of a distilled water reservoir connected to a needle unit as a drop generator, and a prism out of an optical glass as the solid surface. The optical system was synchronized with the impact: it was triggered when the drop passed the detection laser beam. The camera and the strobe light were located below the prism. They recorded the experiments by reflecting the light from the prism surface [36].

Fujimoto et al. [37] repeated the same experiments to investigate the impact outcomes on a 45º oblique surface.

Following their previous studies, Fujimoto et al. [38] investigated the impact of two successive drops on a solid surface. A stream of drops was generated by a piezoelectric vibrator. Two successive drops were isolated from the stream by means of a slit hole on a rotating disc. The disc was located below the drop generator, preventing unwanted drops from impinging on the test surface. The same triggering system was used for the flash photography of the impact [38].

Crooks et al. [39] investigated the way that surface tension and elasticity in Newtonian and non-Newtonian liquid drops affected the drop-surface impact. The results of their investigation were important in many industrial applications such as plasma spraying, aerosol deposition in the deep lung, and delivery of agrochemicals. The experimental setup comprised a drop generator, a test surface and a pulse strobe photography system, the latter of which was triggered by a laser beam disconnected by the drop [39].

To investigate the variety of impact velocity, Rouxa and Cooper-White [40] studied the water drop and glass surface collision. They used a single syringe pump as the drop generator. A glass syringe was connected to the needle via a silicon tube. A special optic technique was used to record the collision simultaneously from the top and the side. White background lighting was provided using optical fibers, and a cube beam-splitter was employed to provide two views at the same time [40].

The quality of impact between fuel drops and surfaces in an internal combustion engine influences combustion efficiency. Moita and Moreira [41] investigated this topic. Specifically, they studied the effect of surface topography, roughness and temperatures on drop-surface collision outcomes, looking at fuel drops of different viscosities [41].

Surface topography, which is one of the parameters used to determine the hydrophobicity of surfaces, was the subject of much research. Kannan and Sivakuma [42] studied the effect of topography on drop-surface collision outcomes using a grooved stainless steel surface and water drops. They used the same setup as previous studies: a drop generator, test surface, synchronized strobe lamp, and high-speed camera triggered by the drop passing through a photo transducer sensor [42].

The next step was taken by Merlen and Brunet [43] by investigating the impact of liquid drops on a superhydrophobic surface. A water and glycerol mixture was used to generate liquid drops by means of a dripping faucet connected to a needle. The non-wetting surface was covered by a layer of chemical-coated nano-wires [43].

Li et al. [44] carried out a series of experiments to study the impact of a falling drop on a stationary drop sessile on a solid surface. A syringe pump was used as a drop generator and the drop was released from a pipette nozzle connected to the syringe with a glass tube. A "vertical motion stage" was used to change the height of the nozzle to regulate the drop velocity. A polished stainless steel surface was located on a "horizontal motion stage" to relocate the surface and adjust the point of impact of the second drop. Distilled water and ethylene glycol were used as the tested liquid in Li et al.'s experiments [44].

Fathi et al. [45] employed a setup to investigate the collision outcome of a drop and a moving surface in order to explain the mechanism of such impacts quantitatively. The drop generator in their experimental setup consisted of a beaker to provide the fluid supply, a prismatic pump, a dosing pump, a damper and a "jetting head." The prismatic pump pumped the liquid from the beaker to the dosing pump. The damper smoothed the flow rate and the pressure of the liquid to the "jetting head." A bio-degradable resin mixed with isopropanol was used as the test liquid to generate the drops. A single drop was generated by a piezoelement which was vibrated by an amplifier. The "jetting head"

was located on a 3D motion stage to adjust the location of impact as well as the speed of the drops. The test surface was located on a linear motion stage which provided the linear motion of the test section [45].

Dupuya et al. [46] studied the impact of a drop on a surface in a high pressure environment. Two different conditions were tested: decane in the liquid phase with CO2 or N2 in the gas phase, and two-phase pure CO2 in saturation. A polished stainless steel plate was used as the test surface. A stainless chamber with two large optical glass and access holes was used as the pressure cell. A nozzle injected the drop stream into the cell. A "pipe deflector" was used to separate the test section from the injection section. The central part of the drop stream entered the test section via a bended piece of pipe. The final drop was generated inside the pipe and impinged on the test surface. A combined photography technique was used to monitor the experiment. Shadowgraph, high-speed photography was used with particle tracking velocimetry [46].

Pan et al. [47] investigated the high energy impact of different liquid drops onto surfaces with different surface roughness. The impingement of rain drops on earth, meteorite collision onto the earth, spray combustion, insecticide sprays, inkjet printing, and spray coating, cooling and painting were introduced as the main applications of these experiments. To investigate the effect of liquid properties and surface roughness, different liquids such as water, glycerol–water, heptane, nonane, and alcohol were used on rough and polished aluminum plates and a glass surface. To accelerate the drops generated by a piezoelectric-diaphragm generator, a high-speed flow of air was used. The flow was generated by a compressor and passed through a porous plate to become uniform. The uniform flow then entered a contraction nozzle and reached a required speed. The drop was carried by the flow toward the test section. Velocities up to 42 m/s were tested on this setup [47].

Sahaya Grinspan and Gnanamoorthy [48] arranged a setup to measure the impact force of different drops on a solid surface. The impact forces of hydraulic oil and lubrication oil drops on an aluminum plate were compared with a water drop. The drops were generated manually using a syringe and speeded up by gravity to 3m/s. A PVDF piezoelectric film attached to the test surface was used to determine the impact force. The voltage generated by the piezoelectric film impacted by the drop was measured and converted to the force

using a linear conversion factor. This investigation led to enhancements of the jet peening, cutting and drilling technologies as well as in spray coating and inkjet printing [48].

Li et al. [49] simulated the effect of the impact of water drops on rotary parts of turbo-machines such as impellers and blades of turbines, fans and compressors by setting up an experiment in which a water drop collided onto a rotating disc. The falling velocity of the drop, the rotational speed of the disc and the impact radii were selected as variable parameters. This experiment introduced the Rossby number (the ratio of inertial force to Coriolis force; $Ro = U/Lf$) to the drop-surface investigations. The setup consisted of a syringe pump as the drop generator and an aluminum disc as the test surface, which was attached to a direct current motor [49].

An and Lee [50] studied the impact of shear-thinning and Newtonian liquid drops on dry hydrophilic, moderate and hydrophobic surfaces. Water, glycerin and xanthan were selected as working liquids. Glass, stainless steel and parafilm-M were used as test surfaces. The effect of impact velocity, viscosity, shear-thinning characteristics and wettability were investigated. In the setup used for this experiment, a syringe pump was used to generate liquid drops. Common shadowgraph photography was used in high speed imaging [50].

The study of drop-surface collision has been so developed these days that it is possible to track its footprint even in the food industry and, specifically, in food engineering. Andrade et al. [51] conducted experiments on the impact of water, glycerol–water and tween 20–water drops on banana and purple cabbage epicarps. A syringe pump drop generator was used to produce drops with different velocities [51].

2.1.3 Drop-Heated Solid Surface Collision

Combustion engines and spray cooling systems are the main industrial areas involved in interactions between fluid drops and heated surfaces. One of the early works in this area was done by Wachters and Westerling (1963), who studied the impact of a single drop onto a heated surface to resolve the heat transfer and evaporation rate. This study was developed by Bolle and Moureau (1982) to investigate the collision of polydisperse spray

and a solid surface. Photographic measurements were introduced by Chandra and Avedisian (1991) to determine the deformation phases [31].

One of the early works on drop-heated surface collision was performed by Labeish [52], who investigated the heat-transfer and the hydrodynamics of a drop colliding on a heated surface. An "electromechanical resonance generator" was used in their experimental setup to generate drops of different liquids such as water, methanol, ethanol and butanol. The drop generator comprised a liquid reservoir connected to a regulating valve and a needle. An "acoustic frequency generator" was used to vibrate an elastic plate using the resonance frequency to release the drops from the needle tip. To measure and control the temperature of the heated target plate, an internal thermocouple was built using the plate as one of the thermo-electrodes in the thermocouple. An oxide film was used to separate the thermo-electrodes from each other. Different combinations of target plate-electrodes were used in the experiments: "nickel-nichrome, stainless steel-nichrome, copper-constanstan, and silver-nichrome." The experiments were performed in the dark. "Spark photography," using a strobe lamp, was used along with a "stereo-photocamera" to record the experimental data. The photography system was triggered and synchronized with the collision using a photo sensor. As the drop crossed a light beam focused toward a photodiode, a signal would transfer to a control box to run the strobe lamp and the camera [52].

Bernardin et al. [53] investigated the effect of drop velocity and surface temperature on the drop-heated surface collision using both still and high-speed photography. The experimental setup comprised a drop-generating unit, target "impact module," photography system and triggering system. The working liquid (de-ionized water) was provided by a reservoir and pumped to the drop generator by a magnetic pump. The pumping unit is connected to a hypodermic needle and a needle valve with a stainless steel tube. Two target surface "modules" were prepared for each single and drop stream impact. The first "module" was made of aluminum and located on an insulating casing made of fiberglass plastic. The second "module" was made of thin, "gold-plated copper," located on the same insulating casing. The entire block was mounted on a micrometer-driven structure to provide precise positioning. An aluminum block with embedded cartridge heaters and equipped with thermocouples was used as a heat source attached to the target surface module. The high speed video photography was used in qualitative

investigations while the stroboscopic photography was employed to produce more high quality photos used in quantitative studies. The stroboscopic photography was performed in a dark room. The triggering system for the stroboscopic photography consisted of a He-Ne laser and a photoresistor sensor connected to a control box. The triggering signal was transferred to the stroboscope when the drop crossed the laser beam, disturbing the laser-detector connection [53].

Manzello and Yang [54] used methoxy-nonafluorobutane and n-heptane as working liquids to study the collision of drops onto a heated polished stainless steel surface. The drop velocity was held constant in their experiments while the surface temperature and drop properties were variable parameters. A programmable syringe pump was employed to generate drops. A digital high-speed camera observed and recorded the experiment. A copper block with embedded miniature cartridge heaters was used as the heater unit. A thermocouple measured the surface temperature [54].

S-L.Chiu and T-H.Lin [55] employed a special device to generate compound drops consisting of water in the core and diesel in the shell. They investigated the dynamic of the collision of these drops with a heated surface. This phenomenon can be found in pray cooling, fire protection and diesel combustion engines. To generate the compound drops, a "compound drop generator" was designed, including a piezoelectric plate attached to a simplifier and a pulse generator and a nozzle connected to two liquid reservoirs. The nozzle was built of a dental needle inserted concentrically inside a hypodermic needle. The water reservoir was connected through a valve and a tube to the dental needle and the diesel reservoir was connected the same way to the hypodermic needle. Colored water was used to enhance the visualization. By controlling the flow rate and the pulse exerted to the piezoelectric plate, drops with different "core-to-shell mass ratio" were produced. Stroboscopic digital photography was used for the imaging system. The stroboscope was synchronized with a delay with the pulse generator. The target was a polished stainless steel surface connected to a temperature controller and a thermocouple. The surface temperature was maintained above the Leidenfrost temperature at about 450ºC. The target plate could be rotated up to 60º to provide different collision angles [55].

Following the investigations of S-L.Chiu and T-H.Lin [55], Chen et al. [56] studied the impact of various-sized diesel oil drops onto a heated, inclined stainless steel surface. The

same experimental setup was used, except that the water reservoir connection was removed [56].

Chen and Huang [57] investigated the collision of liquid drops on the edge part of a heated plate. The ethanol drops were generated using a syringe pump and impacted on the edge of a plate which was heated above the Leidenfrost temperature. The plate was seated on a support with three positioners driven by micrometer. Two linear and one angular motion were provided by these positioners. Due to the change in the drop trajectory during each try, the experiment was repeated several times to achieve the same results [57].

Cossali et al. [58] employed two optical measurement techniques: PDA (phase Doppler anemometry) and IAT (image analysis technique) to study the secondary atomization in a drop-heated surface impact and to determine the size and the velocity of the produced drop. Surface temperature, surface roughness and viscosity were selected as variable parameters to determine the boiling and atomization regimes. The drop generator in the setup consisted of a needle connected to a pressurized tank with a tube. The frequency of drop generating was regulated by a throttling device and the size of drops was determined by the inside diameter of the needle. The drop generator was mounted on a variable height mechanism to provide different velocities. Distilled water and a water–glycerin mixture were selected as test liquids. An aluminum alloy disc heated by electrical heaters was used as the target surface. The temperature was maintained above 330ºC using a PID controller. A thermocouple connected to the bottom of the disc provided the feedback thermal signal to the controller. A He–Ne laser coupled with a photodiode was used to trigger the camera: the camera was triggered when the drop disrupted the laser beam. The same triggering signal was used for the PDA measuring unit [58].

Cossali et al. [60] continued their previous studies using an experimental method to investigate how the heat-transfer mechanism, impact velocity and surface characteristics affect secondary atomization. The secondary atomization occurred when a water drop made contact with a heated aluminum surface. In their new experiments they used stroboscopic illumination and an infrared triggering system instead of the previous techniques. The main applications for Cossali et al.'s [60] studies are combustion engines, spray cooling and HVAC systems [60].

The effect of fuel atomization on efficiency and "pollutant emissions" of the internal combustion engines led Moita and Moreira [59] to study the impact of water and fuel drops on a heated surface to characterize the impact outcomes. Drop size and velocity were chosen as variable parameters in these experiments. The experimental setup employed a syringe pump to generate the drops. The imaging system was triggered by the drop passing through a laser beam aimed at a photodiode. A copper block heated by a cartridge heater was used to heat the target surface to 310ºC. The surface temperature was controlled and measured by a temperature controller and a thermocouple respectively. An IR camera was also used to measure the surface temperature distribution [59].

Bertola [61] studied the Leidenfrost phenomenon in the presence of polymer additives. He used a dilute solution of Polyethylene oxide and pure water to produce different sizes of drops. A mirror polished aluminum was used as working material and the velocity was used as variable parameter. A screw-driven syringe with a hypodermic needle mounted on a Vernier guiding support was used to generate drops. The aluminum block was equipped with two embedded cartridge heaters as heat sources. A thermocouple and a PID controller were used to maintain the temperature to the desired value. The images were taken by back-illuminating imaging and analyzed using LabView software[61].

The impact of monodisperse water drops on a heated, polished nickel surface was studied by Castanet et al. [62]. Drop velocity and size, collision angle and surface temperature were selected as variable parameters. A two-mode monodisperse drop generator was employed in this experiment. The generator consisted of a piezoelectric ceramic tube, a glass capillary embedded inside the ceramic tube and a pulse generator. The inner diameter of the tube was variable and adjusted by exerted voltage on the piezoelectric. This drop generator functioned in two "drop-on demand" and "monodisperse drop stream" modes. In the "drop-on demand" mode, a large contraction was applied so that only one drop could be released from the nozzle. To have a "monodisperse drop stream," high pressure was applied to the system. To provide different collision angles, the generator was mounted on a rotating support [62].

The target surface was a block fabricated of nickel alloy. An electrical resistance embedded inside the block and thermocouples connected to the power regulator were

used as the heating system in the setup. Three different optical systems were applied for monitoring and measurement: A "high speed shadowgraph photography" for monitoring and recording the phenomena, "two-color laser-induced fluorescence thermometry" for measuring the temperature of the drops and infrared photography for measuring the temperature of the target surface [62].

Gambaryan-Roisman et al. [63] proposed an investigation on hydrodynamics and heat transfer in drop-heated surface collision. The temperature gradient in the target plate was measured using seven thermocouples attached to the plate. The impact dynamic and evolution of the temperature in the drop-surface interface was recorded using "high-speed infrared thermography." The "chromatic confocal imaging technique" was also used to measure the change in the film's thickness. Two experimental setups were designed to perform the experiments [63].

The device designed for measuring the film thickness during the collision, consisted of a drop generator, a film generator and a confocal chromatic sensoring technique with a high speed imaging system. The de-ionized water drops were generated by a syringe mounted on a variable height supporting structure. Another syringe was used to generate the initial liquid film on the targeted glass plate. The glass plate was turned to a hydrophilic surface using chemical treatment. The water was injected into the glass plate surface through 22 laser-drilled holes in the plate. A CHR ("confocal chromatic sensoring technique") sensor was located below the glass plate aligned with the drop generator. A light source and a high-speed camera were also targeted to the collision point. The imaging and CHR systems were synchronized and triggered by the computer. The thermography setup comprised the same drop generator mechanism, a heated target surface, heating control system, high-speed IR camera and high-speed CMOS camera. The IR camera was used to record the temperature evolution and the high-speed camera was used for dynamic measurements. Both cameras were trigged by "crossing a photoelectric barrier." Smooth and structured copper plates were used as target surfaces. The plates were heated by a resistance heating foil [63].

Okawa et al. [64] used titanium-dioxide nano-particles dispersed in distilled water as the working liquid to investigate the boiling heat transfer in drop-heated surface collision. A polished stainless steel plate located on a ceramic block was used as the target surface.

Seven thermocouples spot-welded underneath the plate were used to measure the temperature in different sections of the plate. A heat gun was used as the heat source in the setup. A variable height syringe pump was used as the drop generator. To prevent the secondary drops generated by the impact from falling back to the surface, the target surface was positioned with a 40º-inclination with respect to the horizon. The common shadowgraph photography technique was used for observation and recording in the experiments [64].

Negeed et al. [65] studied the effect of the oxide layer over surfaces on drop-heated surface collision. This phenomenon can be found in spray cooling systems in many industries such as nuclear power and steel production plants. The effect of different drop size, impact velocity and the thickness of the oxide layers were investigated in the experiments. A micro jet dispenser was used to generate the working drops. The diameter and velocity of the drops were controlled by a magnetic valve, the liquid pressure and the inside diameter of the nozzle. To prepare the test surface, Negeed et al. [65] first polished cylindrical stainless steel blocks with chrome oxide and then heated them up to 1000ºC. As the temperature was augmented, the thickness of the oxide layer varied. To measure the oxide layer's thickness, Negeed et al. [65] masked a part of the surface during heating and unmasked it after cooling. They used a microscope to measure the height of the two levels to determine the thickness of the oxide film. The entire experiment was recorded by back illumination photography using a collimated light [65].

2.1.4 Drop-Liquid Surface Collision

The drop-liquid film impact came to the attention of researchers at the end of the 19th century, when Lord Rayleigh began to study the physical mechanism of the impact of rain drops on the surface of ponds [66]. Worthington (1897) started to study the impact of liquid drops on a liquid surface using instantaneous photography [67]. One of the early studies was done by Jayaratne and Mason (1964), who studied the effect of low impact momentum on collision outcomes [31].

Pumphrey and Elmore [68] carried out a series of experiments on drop-liquid surface impact in order to investigate different types of bubble entrainment during the impact. The drop generator used in these experiments consisted of a liquid reservoir, a glass tube, a valve, a hypodermic needle and a loudspeaker cone. The liquid flowed to the needle

through the valve and the drop was released from the needle by vibrations from a large-amplitude square wave emitted from the loudspeaker. The size of the drop was determined by changes in the wave frequency. The amplitude of the wave was adjusted to the value by which the drop was detached [68].

Rein [67] conducted a series of experiments to determine the transition condition between coalescence and splashing on the drop-deep liquid surface collision. The drop-generating mechanism was quite similar to that used by Pumphrey and Elmore [68]. A pendant drop was formed on the needle tip by releasing the liquid from the reservoir. When the desired size was achieved, the drop was detached using an impulse caused by an iron cylinder which was accelerated by an electromagnetic field. The shadowgraph imaging was used with a light pulse generator which was triggered by the camera [67].

Inspired by the knowledge that cooking fires are the main cause of household fires in most countries, Manzello et al. [69] conducted an experiment on water drop impact on heated cooking oil to learn how to reduce the hazard. They used a syringe pump to produce distilled water drops and a small diameter cylindrical pool of peanut oil to provide the liquid surface. A copper block and miniature cartridge heaters were used as the heating unit. The entire setup was placed inside a Plexiglas box [69].

Vander Wal et al. [70] studied the effect of the fluid film depth on drop-liquid film collision. Other parameters involved in the experiment were the influence of viscosity, surface tension and velocity. The setup comprised two units: the drop generator and the liquid film section. The drop generator consisted of a needle and a drop releasing mechanism driven by a rubber band. The drop was placed manually on the needle and detached from the needle by releasing the pre-tensioned rubber band. This mechanism pulled back the needle, releasing the drop toward the test section. The test section comprised a liquid container with a movable aluminum disc inserted inside. The depth of the liquid film was determined by the insertion depth of the aluminum disc [70].

Motivated by a study that looked at the level of noise generated by rain drops falling on water pools and forming gelled beads, Pregent et al. [71] carried out experiments on the impact of viscoelastic drops on a viscoelastic liquid bath. To determine the parameters that affect the phenomena, they used different polyethylene oxides with different

viscosities and molecular weights. They used a syringe pump to generate drops and a square beaker as the liquid pool to run their experiments [71].

To find a theoretical model to predict a collision outcome, Bisighini et al. [72] studied how a crater forms in a drop-liquid surface collision. They used the same liquid for both drops and the target liquid surface, and chose a semi-finite liquid pool for their investigations. Distilled water and acetic acid were used as the tested liquids. In their experimental setup, they used a level pool connected to the test pool to maintain the desired level of the test section. A dripper connected to a container was used to generate drops, and the drop velocity was changed by changing the dripper height. All the images were processed using different image-processing techniques [72].

The same setup arrangement was used by Bisighini and Cossali [73] to investigate the early stage of impact of single and double drops on a deep fluid film.

Alghoul et al. [74] studied the effect of movement of the target liquid film on drop impact outcomes. The experimental setup comprised a syringe pump to generate the drops, an open channel in which the moving liquid film flowed (driven by gravity), and a back illuminating imaging system [74].

Continuing his studies on diesel drop impacts, Chen started investigations on fuel and water interactions in fires. Chen and Lai [66] carried out experiments on the impact of water drops onto a diesel fuel pool. As is common in most drop-liquid surface collision setups, their device consisted of a drop generator, a target liquid pool and an imaging system. The drop generator comprised a water reservoir, and a drop nozzle made of a syringe needle. The reservoir was connected to the drop nozzle with a needle valve and tubing. The needle valve was selected to control the water flow accurately and ensure the free fall of the drops. The back-illuminating technique was also used for the photography, with both digital and high-speed video cameras. When high resolution images were required, Chen and Lai used a synchronized stroboscope for imaging [66].

Zhao et al. [75] investigated the transition phenomenon between bouncing and coalescence collision outcomes in drop-liquid surface impact. The same liquid was selected for both the drops and the targeted pool. The principle of Plateau-Rayleigh

instability was used to design the setup's drop generator. A liquid tank was connected to a "pinhole nozzle" through a valve and tubing. A "mono-dispersed stream of liquid drops" was generated from the nozzle. A rotating "slotted disc" located below the drop stream was used to produce the single drops from the stream. The velocity of the drops was controlled by regulating the pressure of the liquid tank and the diameter of the pinhole nozzle. The target liquid pool was a cuvette filled by liquid, in which the free surface level of the liquid was maintained to the overflow level [75].

One of the latest works on drop-surface collision was performed by Thoroddsen et al. [76] on low velocity impacts. In this study, a special ultra-high-speed video camera was used to observe micro-bubbles forming during the interaction [76].

2.1.5 Drop-Particle Collision

Among the fundamental studies in drop collision, drop-particle collision is rarely addressed, especially when it comes to the individual drop and particle collision in midair. Most of the investigations in this field are carried out theoretically or numerically.

One of the early works in this area was conducted by Smith and Van De Ven [77]. They introduced a new experimental model to simulate the flotation process, especially in oil sand refineries to increase the systems' efficiency. Their experimental model consisted of the interaction between liquid drops and solid particles in a shear flow of an immiscible fluid medium. They used silicone oil as the medium and pale-4-oil, ucon oil and distilled water as the drop. Polystyrene spheres were used as the test particles. They designed a couette device comprising two concentric Plexiglas cylinders which were connected to a motor drive. The two cylinders rotated in opposite directions and the speed and acceleration were controlled accurately by the motor. The annular gap was filled with the liquid medium and the particles were located in a stationary plane. The drops were injected to the medium by means of a micropipette. The interaction was recorded using two cameras from two perpendicular plans [77].

Hardalupas et al. [78] arranged an experimental setup to investigate the drop impact onto a stationary spherical particle. The drop sizes varied between 160μm and 230μm and the particle diameter varied between 800μm and 1300μm. Water, ethanol and glycerol solutions were selected as the drop liquid. Stainless steel was selected as the particle

material. Drop and particle size, impact velocity, liquid viscosity and surface tension were the variable parameters in the experiments. The experimental setup consisted of a drop generator unit, a particle platform and an imaging system. A pressurized liquid reservoir was connected to an orifice through which a laminar jet of test liquid was produced. Two piezoelectric transducers were used to generate monodisperse drops from the liquid jet based on the principle of Rayleigh instability. To adjust the distance between impacted drops, an electrostatic deflector was employed. This deflector was synchronized by the drop generator so that in every 19th drop the electric charge deflected the stream of drops into a drain pit and prevented the impacted drop from being influenced by other drops. The test platform consisted of a particle support which was relocated by a micrometer. A He-Ne laser and a phase Doppler anemometer (PDA) were used to trigger the camera and the back-illuminating LED to provide stroboscopic images. This system was also employed to determine the drop size and velocity of the impacted drops [78].

Hung and Yao [79] investigated the impact of distilled water drops onto a stainless steel cylindrical wire. The size of the wire and drops and the impact velocity were the variable parameters. The experiments were run on waxed and un-waxed wires. This study was a fundamental experimental simulation of numbers of industrial phenomena such as spray cooling, spray painting and spray forming [79].

The setup employed an impulse liquid spray to generate a stream of drops. The distilled water was pumped from a container through a glass nozzle plate, producing a water jet. A piezoelectric plate agitated by a pulse generator broke the jet into the stream of drops. The flow rate was controlled by a rotameter and a control valve. Two air jets were added to the system to convert the drop stream to scattered drops when heating the target. Similar to previous experiments, back-illuminating stroboscopic imaging was used to record the data [79].

In order to understand and explain industrial processes such as fluid catalytic cracking, polyethylene synthesis and electronic materials, coating Ge and Fan [80] developed a numerical simulation of drop impact onto a high temperature stationary particle followed by an experimental validation. A syringe mounted on a variable height support was used to generate liquid drops. The target brass particle was located on a heating block below

the syringe needle. A thermocouple inserted inside the spherical particle was used to measure the particle's temperature and adjust the heating block temperature. A thermal insulation was used to protect the syringe from heated sections. Two back and front light sources were used in high speed photography in this study [80].

Rozhkov et al. [81] conducted experimental and theoretical investigations on the impact of surfactant drops onto the polished top surface of a small stainless steel cylinder. The drops were generated by a capillary tip connected to a syringe pump. For imaging, two qualitative and quantitative methods were used: single top-view high-speed photography with an inclined mirror to provide a top view, and synchronized photography by two cameras located at the top and the side to provide top and side views [81].

A very interesting result was revealed from one of the recent works done by Juarez et al. [82]. They investigated the collision of liquid drops onto the small solid targets of different geometrical cross-sections. The experimental setup was similar to what Rozhkov et al. [81] used in their experiments. A syringe pump connected to a capillary generated drops of deionized water and glycerol. For ease of photography, food coloring was added to the liquid. The target particles were made of polyoxymethylene [82].

Amirfazli et al. [83] investigated the drop-particle collision outcomes in order to establish collision regimes corresponding to different Weber numbers. Deionized water and acrylic, nylon and Teflon were selected as drop liquid and tested particles respectively. The experimental setup consisted of a syringe, a spring-driven particle-launching gun and an imaging system. One single drop was released by the syringe passing through a photo sensor, and a signal was sent to a solenoid connected to the gun to release the spring. The particle was launched and the collision was recorded by two high-speed cameras providing top and side views. A mirror was used to provide a top view while the two cameras were located in one plane [83].

As concluded from previous studies, numerous investigations have been done in drop-drop collision, drop-surface collision and drop-liquid film collision. However, investigations on drop-particle collision are rare or limited to the impact of a drop onto a stationary particle target. The collision of a drop onto a flying particle needs more investigation. As mentioned before, Amirfazli et al. [83] started such an investigation in

ambient temperatures. In this thesis, the goal is to continue their work by designing, building and testing an experimental device to allow the future study of the impact of a falling drop onto a flying particle in a high temperature environment.

2.2 Theory

According to Ashgriz and Poo [5], drop-drop impact is governed by different parameters such as drop density, viscosity, surface tension, velocity, diameter, relative velocity of the two drops and impact parameter [5]. Also, Mundo et al. [31] stated that the impact of a drop onto a surface is affected by above-mentioned fluid physical properties as well as surface conditions [31].

Table 2-1 shows all relevant parameters in drop collision (drop-drop, drop-surface, drop-liquid and drop-particle) in three categories: physical properties, kinematic parameters and geometrical parameters.

Table 2-1 Relevant parameters which affect the impact of a drop onto another drop or a solid surface

Fluid Physical Properties	Kinematic Parameters	Geometrical Parameters
ρ: Density	u: Drop Velocity	d: Drop Diameter
μ: Viscosity	β: Collision Angle	SR: Surface Roughness
γ: Surface Tension	V: Relative Velocity	
	X: Impact Parameter	
	g: Acceleration of Gravity	

The subscripts l and s in the following equations in this section denote large and small liquid drops, respectively. The relative velocity is defined as [5]:

$$V = \sqrt{u_l^2 + u_s^2 - 2u_l u_s \cos\beta} \qquad 2\text{-}1$$

It is useful to introduce two other physical properties derived from the basic physical properties: kinematic viscosity and surface tension:

$$Kinematic\ Viscosity: \nu \left[\frac{m^2}{s}\right] = \mu \left[\frac{N.s}{m^2}\right] \Big/ \rho \left[\frac{N.s^2}{m^4}\right] \qquad 2\text{-}2$$

$$"Kinematic\ Surface\ Tension": \sigma\ \left[\frac{m^3}{s^2}\right] = \gamma\ \left[\frac{N}{m}\right] \Big/ \rho\ \left[\frac{N.s^2}{m^4}\right] \qquad 2\text{-}3$$

The unit of density is rewritten in terms of force (N). The similar deriving approach, eliminating the force factor (N) and introducing the factor of $(m^2/s)^2$ in both units, suggests the term "kinematic surface tension" for the surface tension/density ratio, similar to kinematic viscosity. In this thesis, the terminology is used to refer to the surface tension/density ratio.

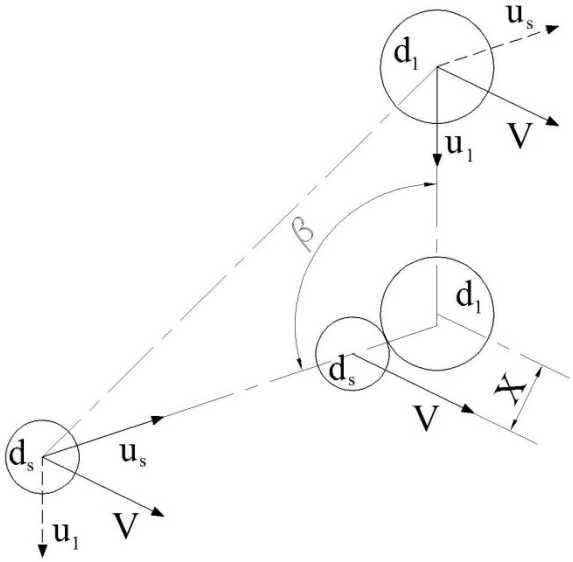

Figure 2-1 Relative velocity and impact parameter diagram in drop-drop collision

To reduce the number of independent parameters, all above-mentioned parameters can be defined using the following dimensionless parameters [5, 31]:

$$Reynolds\ Number \overset{\text{def}}{=} \frac{Inertia}{Viscous\ Force}: \quad Re = \frac{\rho d_l V}{\mu} = \left[\frac{1}{\nu}\right].[\ \ _lV] \qquad 2\text{-}4$$

$$Weber\ Number \overset{\text{def}}{=} \frac{Inertia}{Surface\ Tension}: \quad We = \frac{\rho d_l V^2}{\gamma} = \left[\frac{1}{\sigma}\right].[d_l V^2] \qquad 2\text{-}5$$

By dividing the square root of the Weber number by the Reynolds number, a new non-dimensional number is introduced:

$$Ohnesorge\ Number \overset{\text{def}}{=} \frac{\sqrt{We}}{Re} \tag{2-6}$$

$$Ohnesorge\ Number \overset{\text{def}}{=} \frac{Viscous\ Force}{\sqrt{Inertia\ .Surface\ Tension}} : Oh = \frac{\mu}{\sqrt{\rho\gamma d_l}} = \left[\frac{\nu}{\sqrt{\sigma}}\right].\left[\frac{1}{\sqrt{d_l}}\right] \tag{2-7}$$

$$Bond\ Number \overset{\text{def}}{=} \frac{Body\ Force}{Surface\ Tension} : Bo = \frac{{d_l}^2 \rho g}{\gamma} = \left[\frac{1}{\sigma}\right].\left[{d_l}^2 g\right] \tag{2-8}$$

$$Drop\ Diameter\ Ratio:\ \ \Delta = \frac{d_l}{d_s} \tag{2-9}$$

$$non-dimensional\ Impact\ Parameter\ x = \frac{2\ \mathrm{X}}{d_l + d_s} \tag{2-10}$$

$$non-dimensional\ Surface\ Roughness\ S = \frac{\mathrm{SR}}{d_l} \tag{2-11}$$

Ashgriz and Poo [5] introduced the Weber number, Reynolds number, drop diameter ratio and non-dimensional impact parameter to define the drop-drop collision outcomes. The Reynolds number, Ohnesorge number, surface rouphness, Weber number and Bond number were introduced by Mundo et al. [31] to explain the drop-surface impact.

The Froude number is another non-dimensional parameter introduced by Prosperetti and Oguz [84] to specify the cavity size in drop-liquid film impact.

$$Froude\ Number \overset{\text{def}}{=} \frac{Impact\ Velocity}{Gravitational\ Wave\ Velocity} : Fr = \frac{V^2}{gd} \tag{2-12}$$

To determine the effect of surface forces and viscous forces on drop collision, the capillary number has been introduced as follows [82]:

$$Capillary\ Number \overset{\text{def}}{=} \frac{Viscous\ Force}{Surface\ Tension} : Ca = \frac{\mu V}{\gamma} = \left[\frac{\nu}{\sigma}\right].[V] \tag{2-13}$$

The non-dimensional numbers in Equations 2-4 to 2-13 are rearranged so that the effects of fluid physical properties and the kinematic/geometrical parameters are represented separately.

In this thesis it is assumed that the same parameters also affect the drop-particle collision phenomenon. However, since the drop-particle collision inside a fluidized bed is simulated, a setup is designed so that the impact of these parameters can be studied in an environment with different temperatures from ambient to 200ºC.

Chapter 3
Basic Design

Prior to any design, the scope of the work and the design steps should be clearly defined in a design plan. A concrete design criterion and definite steps assure one of having a process targeted to the appropriated objectives. Hence, before proceeding to basic design, it is necessary to discuss the design plan.

3.1 Design Plan

3.1.1 Scope of Work

Based on the parameters discussed in Section 2.2, it is assumed that the particle-drop collision outcomes are governed by fluid physical properties (ν and σ), solid surface roughness (SR), drop and particle diameters (d_d and d_p), impact parameter (X) and relative velocity (V). The latter is a function of individual drop and particle velocities (u_d and u_p) and collision angle (β). This hypothesis should be validated through either an analytical, numerical or experimental study. In this thesis, a facility is designed to allow study of such parameters in particle-drop collision. To study all the parameters through an experimental process, the value of each variable should be adjustable and controllable in the setup.

The scope of work in this thesis is to design and build a temperature cell to allow future study of the effect of collision parameters on drop-particle impact in different temperatures to simulate the interactions in a fluidized bed.
The design variable parameters in the setup are as follows:

- Fluid physical properties (can be changed by temperature and by using different fluids)
- Particle/drop diameter (500μm – 2000 μm)
- Solid surface roughness (can be changed by using different particle materials)

- Particle and drop velocity (will be discussed in Section 4.2.4)
- Collision angle (from 90º to 180º)
- Impact parameter
- Temperature (ambient to 200ºC)

Since the setup is a first prototype for the experiment, the particle/drop size range (between 500μm and 2000μm) and the maximum temperature (200ºC) were defined to gain an understanding of the experimental setup's capability and limitations. Since the interactions occur at high speeds and on a small scale, an appropriate imaging technique is required.

3.1.2 Design Process

Once the working criteria are in place, the design process should be pre-planned and the required steps in design and construction should be defined. Figure 3-1 demonstrates the main steps of the work in six categories. The work starts with the basic design, in which the functional feasibility of the experimental setup is studied based on the criteria defined in Section 3.1.1. A general outline of the setup is suggested in Section 3.2 to cover all the experimental requirements. When the outline is finalized, the next step is to select appropriate mechanisms and materials to fulfill the experiments' requirements. The House of Quality in design is used as a rational choice method to pick the optimum system for the setup based on the design criteria. The analysis and calculation provide a bridge from the basic design to the detailed design. When all quantitative parameters are determined, it is time to turn the idea into reality. After the detailed design is completed and all shop drawings and bill of materials are finalized, the procurement phase will start. Inquiries are sent to vendors for specific parts and the offers from different manufacturers are analyzed and checked for compatibility with the experimental requirements. The most compatible offer will be selected and the required equipment and materials will then be ordered from the selected vendor. The fabrication will take place in the Department of Mechanical Engineering machine shop and electrical shop; parts are assembled in the lab. The final stage in the development process is the performance test in which different parts of the setup are tested separately within the design criteria. When the functionality of individual parts is assured, the setup will undergo a collision test in different collision conditions.

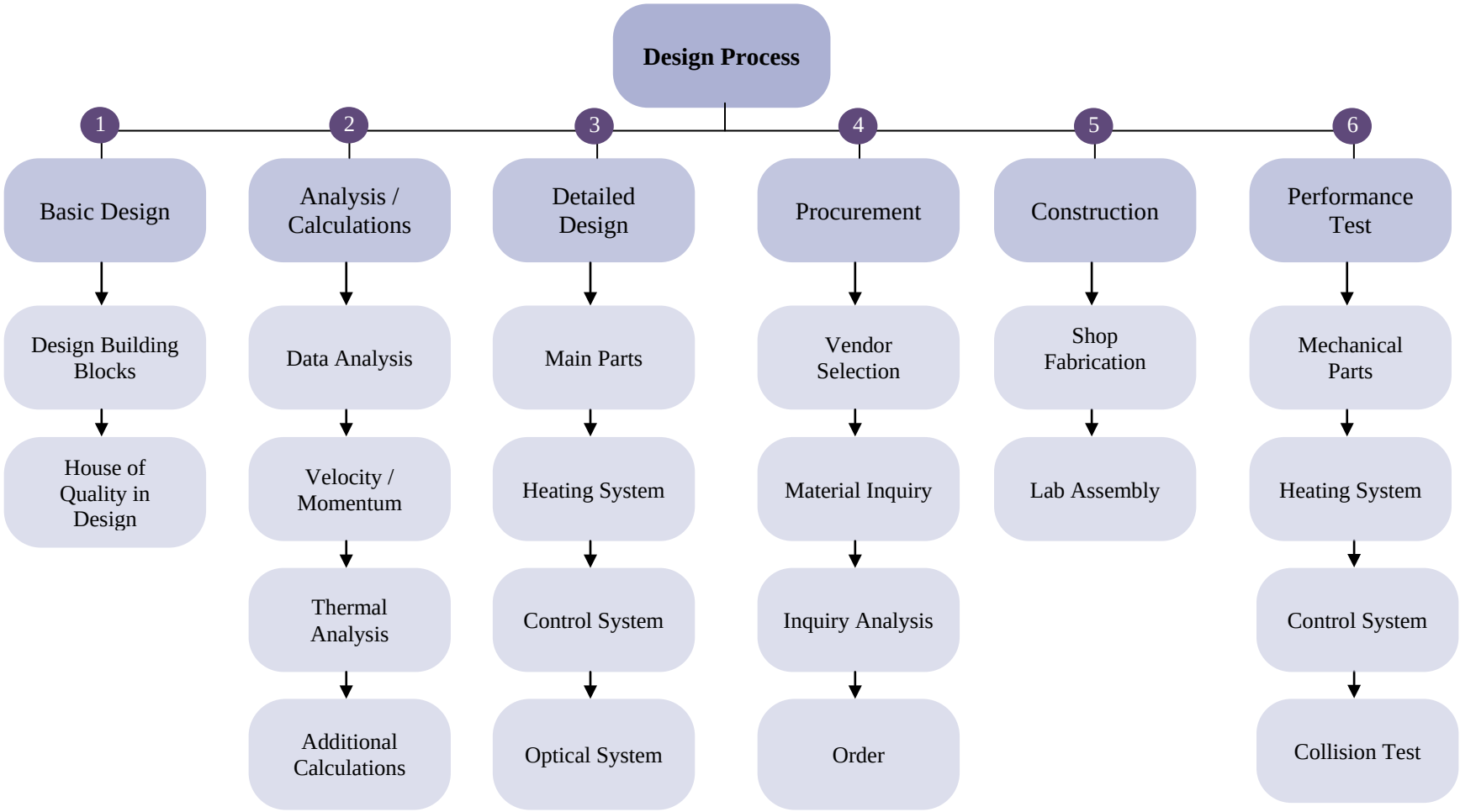

Figure 3-1 Design process diagram (representing six design steps)

3.2 Design Building Blocks

To start the design, it is necessary to have an outline of the required parts based on the setup's functional goal. The setup functions can be defined by classifying the design parameters discussed in Section 3.1.1.

- Parameters related to the particle and drop characteristics, which are fluid physical properties, particle surface roughness and particle/drop sizes
- Parameters related to kinematic properties, which are particle/drop velocity, collision angle and impact parameter
- Temperature

The first category is related to the setup's feeding material. All the parameters in this category can be changed using different types or sizes of the drop and particle. However, to study the effect of other parameters, a specific mechanism must be designed. There are two main functional mechanisms which should be fulfilled by the setup: one is to have one particle collide with one drop at different velocities, angles and impact parameters. The other is to provide an environmental temperature that can be changed for the experiments. All these functions need to be controlled to the desired conditions and all the phenomena should be recorded by cameras to be studied both quantitatively and qualitatively.

Previous discussions in this section suggested defining four main systems for the setup: mechanical, heating, control and optical. The mechanical system comprises a particle launcher, a drop generator and a chamber called the temperature cell.

Table 3-1 Main systems of the setup

Mechanical System	**Heating System**	**Control System**	**Optical System**
Temperature Cell	Heaters	Heater Controllers	High-speed Cameras
Particle Launcher	Insulations and Gaskets	Triggering and Timing Controllers	Background Lights
Drop Generator			Sight Glass

The particles and drops are released by a particle launcher and a drop generator, respectively, to the collision point. To have the particle and the drop collide at a proper point, appropriate timing is required; hence, a triggering and timing control system should be added to the mechanism. The entire experiment should take place in a chamber with a controlled temperature. To maintain the temperature to the design value, a heater and a heating control system are required. An appropriate optical system will be added to the setup to monitor the experiment and record the required data. Table 3-1 summarizes the setup components and Figure 3-2 shows the main required components of the setup schematically.

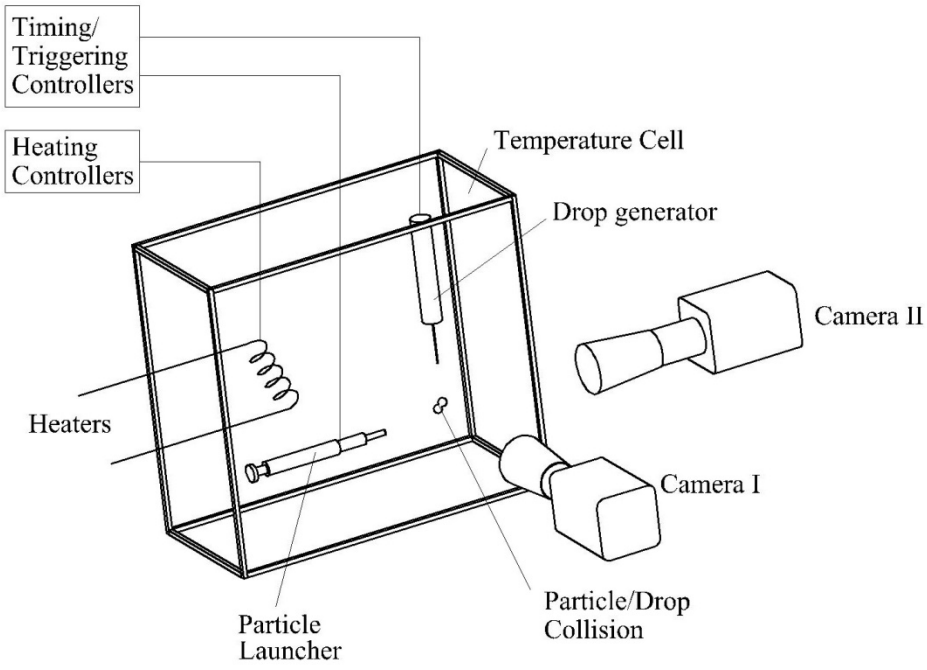

Figure 3-2 Preliminary design schematic

3.3 House of Quality in Design

To select the most suitable component for each system, it is necessary to define the design criteria and assess each design option based on the design requirements. This process, which uses a management approach to determine the optimum solution based on the compatibility assessment, is called House of Quality (HOQ) or quality function deployment (QFD). The House of Quality was introduced to the industry for the first time

in 1972 by Mitsubishi's Kobe shipyard site. The method was developed later on by Toyota. The method is based on the fulfillment of customers' demanding quality and functions as a "conceptual map which provides the means for inter-functional planning and communications"[85]. Manufacturers of a variety of products (i.e., electronics, home appliances, clothing, construction equipment, cars, etc.) have used this method to design and manufacture their products [85].

Different industries have different configurations for a House of Quality (or a QFD) chart (shown in Appendix A, Figure A-1). The type of the chart depends on the type of industry and application. A traditional House of Quality consists of the following assessment matrices [86, 87]:

- Customer attributes or requirements
- Engineering characteristics or parameters
- Planning matrix (determining importance weight)
- Roof of the house; inter-relationship between the engineering parameters
- Direction of improvement
- Relationship values
- Competitive analysis or customers feedback on other products
- Technical priorities (calculated from the planning matrix and relationship values)
- Assessment results or targets (overall assessment considering all HOQ matrices)

To implement this method in the design of the experimental apparatus in this thesis, the traditional QFD chart was modified to a more applicable and simpler configuration. In this thesis, the House of Quality is used as a compatibility assessment to select the best out of a number of different design options. Therefore, the roof of the house ("correlation between the engineering parameters" [86, 87]) and direction of improvement are not applicable. This apparatus is the first prototype; hence, there is no competitive analysis available. Also, some of the titles in the traditional House of Quality chart were modified: the "customer requirements" is represented as the "design criteria" and the "engineering parameters" is replaced by the "design option." All design criteria should be fulfilled by the setup; hence, the importance weight factors of 3 to 5 (importance weight value is between 1 and 5) are considered for each design criterion in the planning matrix. The relationship values of 0, 1, 3 and 9 are considered to determine inter-relationship between

the design criteria and the design options. Finally, technical priorities are represented by compatibility weight and calculated based on the planning matrix and relationship values. The assessment results are finalized based on the technical priorities [86, 87].

The House of Quality is represented in this thesis only to select the main mechanisms of the apparatus (i.e., temperature cell configuration, particle launcher, drop generator and materials). The selection and design of the auxiliary parts and details are only discussed.

3.3.1 Mechanical System

3.3.1.1 Cell Configuration

The goal is to provide an environment, called the temperature cell, with different temperatures (ambient to 200°C). The temperature cell must be able to maintain the experimental condition in a specific temperature for each set of experiments. Different options are considered for the temperature cell. A simple idea is to have a box or a cylinder which will be heated to the design temperature. The particles and the drops can be generated either inside or outside the cell and be directed into the cell by means of a special mechanism.

To provide the 90° collision angle, a rotating mechanism is required either for the particle launcher or drop generator in a fixed chamber, or for the entire setup with a fixed launcher and drop generator relative to the chamber. A sample drawing is provided in Appendix C, drawing number MS-001-01, for a rotating setup with fixed particle launcher. As will be discussed in Section 3.3.1.7, since a syringe will be used to generate the drops, only a free fall motion for the drops will be considered. Hence, to provide different collision angles, either the particle launcher or the entire cell should rotate. In both options, the drop generator is fixed in rotation relative to the chamber. To decide which configuration is more applicable for the experimental setup, a simplified House of Quality is used as a compatibility assessment. Table 3-2 shows the design criteria and the cell configuration compatibility assessment for the suggested options.

The compatibility percentage in Table 3-2 was calculated within each design option separately; for instance, the compatibility percentage of the rotating cell mechanism was calculated by dividing the compatibility value of the rotating cell mechanism, divided by the sum of compatibility values of the rotating and fixed cell mechanisms only.

Table 3-2 Cell configuration compatibility assessment (HOQ)

Relationship Values: 9: Maximum compatibility / 3: Medium compatibility / 1: Minimum compatibility / 0 : Not Applicable
Importance Weight: 1 (less important) to 5(most important)
A: Accepted, R: Rejected, C: to be Considered as an alternative
(In this table the compatibility percentage is calculated within each design option separately)

Design Criteria	Importance Weight	% Importance Weight	Particle Launcher/ Drop Generator Position		Cell Shape		Cell Mechanism	
			Design Option		Design Option		Design Option	
			Inside	Outside	Cubic	Cylindrical	Rotating	Fixed
Simplicity (Operation)	4	8.2	1	9	0	0	3	9
Simplicity (Construction)	3	6.1	1	3	9	3	3	9
Simplicity (Maintenance)	4	8.2	1	9	9	9	3	9
Simplicity (Mechanism)	5	10.2	1	3	0	0	1	9
Connection to particle launcher and drop generator	5	10.2	0	0	9	3	9	3
Providing 90º collision angle range	5	10.2	9	3	0	0	9	9
Providing enough height for different drop velocities	5	10.2	3	3	9	3	0	0
Installing windows for cameras and lighting	5	10.2	0	0	9	3	0	0
Heater Installation	5	10.2	0	0	9	3	3	9
Inherent heating system for drop liquid and particles	4	8.2	9	1	0	0	0	0
Easy to be heated	4	8.2	9	3	9	9	0	0
Compatibility Weight			302.0	289.8	569.4	287.8	291.8	508.2
Compatibility Weight %			51.0	49.0	66.4	33.6	36.5	63.5
Assessment Result			C	C	A	R	R	A

To clarify the assessment values, the next section includes a brief discussion for each design criterion. For each design criterion the drawbacks of each design option with respect to the others are discussed to justify the "demerit points."

3.3.1.2 Assessment Discussion

Simplicity (Operation)

Due to the cell's high operating temperature, it is almost not possible to work inside the chamber and the internal launcher/drop generator option is not acceptable. The shape of the chamber does not necessarily affect its function; however, since the setup is connected to the cameras for photography, a rotating cell requires the entire optical system to move and rotate to adjust to the observation area.

Simplicity (Construction)

When designing an experimental setup, one should look for the simplest construction which fulfills all the design criteria and can be easily built in a local shop. This enables one to modify or rebuild the setup parts when necessary. Having an internal launcher/drop generator in high temperature conditions makes the mechanisms more complicated; thermal stresses, material compatibility, thermal expansions and other issues will be added to the design, unnecessarily. Although an external launcher/drop generator mechanism eliminates all these complexities, designing appropriate connections will be added to the system to direct the particles launched in different directions into the cell.

Using a standard pipe and flanges to build the chamber body may seem to make it easier to construct; however, installing sight glass and connections to other parts will become more complicated. Working with a cubic chamber is more straightforward and it is easy to make different shapes and configurations with less restrictions. Finally, a rotating chamber requires a complicated supporting structure compared to a fixed mechanism.

Simplicity (Maintenance)

It is obvious that maintenance and modification will be easier when working parts (particle launcher and drop generator) are outside the chamber. The shape of the chamber does not affect the maintenance process, and having rotating supports for the chamber will increase the chance of damage and maintenance difficulties.

Simplicity (Mechanism)

Simplicity in the mechanism is one of the major factors in designing an experimental setup. In an experimental study, one is seeking the effect of an individual parameter on a specific phenomenon; therefore, reducing the intruding parameters is necessary for a

concrete result. In a simple setup it is easier to track all the parameters involved in the experiment and eliminate the effect of unwanted noises; however, a complicated setup introduces new and sometimes unknown parameters to the study. In this setup, the goal was to make as simple a device as possible, one which would fulfill design targets without being concerned about the unwanted noises. Eliminating the internal launcher and drop generator reduced the effect of thermal stresses on the parts, and using a fixed chamber reduced the chances of additional unwanted momentum or vibration relative to a rotating mechanism.

Connection to Particle Launcher and Drop Generator

Connecting to external parts in a cylindrical shape is more complicated than in a cubic shape, due to the curves and restrictions in a cylinder. In a rotating chamber, the connections to the external parts are fixed and therefore easier to build while the launcher in a fixed chamber requires rotating connections.

Provide 90 º collision angle ranges

Both rotating and fixed chambers are able to provide 90º of rotation. However, having a rotating launcher outside the chamber requires elaborate connections to the cell.

Provide enough height for different drop velocities

In a free-fall motion, velocity is a function of the height (in this setup the distance between the drop generator tip and the collision point). To reach the high velocities in drop motion, the distance between the generator tip and the collision point must be increased; therefore, choosing an internal drop generator augments the size of the chamber. On the other hand, having the generator completely outside the cell makes it impossible to reach very low velocities. Section 4.2.4 will include a discussion about how, in some low relative velocities, a collision point is required close to the drop generator tip. The rotating or fixed chamber does not affect these criteria.

Installing windows for cameras and lighting

As was previously discussed, it is easier to install windows on the flat wall of a cubic chamber than on the curve of a cylinder. Although there is standard sight glass for pipes, the shape, size, material and configuration of the prefabricated sight glass put restrictions on the design.

Heater Installation

A cubic shape provides more accessibility, making it easier to install different types of heaters and, due to electrical connections, a fixed chamber is preferable.

Inherent heating system for drop liquid and particles

If the drop generator and the particle launcher are installed outside the chamber, an extra heating system is required to heat them, but if they are inside the chamber, the chamber heating system will heat them.

Easy to be heated

Although the shape of the chamber results in different heat distribution and temperature gradients inside the cell, the steady state conditions in both cases fulfill the design experimental conditions. However, as discussed before, having the particle launcher and drop generator inside the cell eliminates extra heaters and results in a uniform heating of the drops and particles inside the chamber.

Conclusion

The quantitative assessment in Table 3-2 shows that a fixed cubic chamber is the best option for the temperature cell. However, the assessment values are almost equal for a launcher installed inside or outside the temperature cell. Therefore, an alternative mechanism is needed, one that has the advantages of both options. One solution is a launcher and a drop generator with feeders and working parts outside the chamber and the drop/particle container and releasing tips inside the chamber.

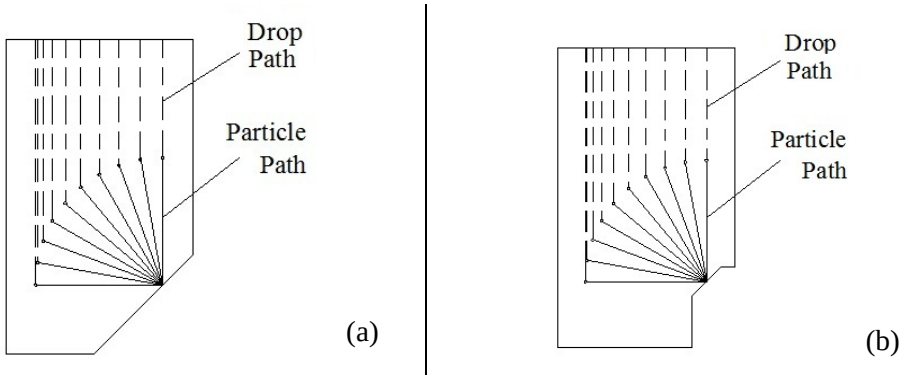

Figure 3-3 Cell configuration schematics (front view)
(a) Cubic cell with beveled edge to install the rotating launcher / (b) Modified beveled edge to track the particle and drop motion in right-angled collisions close to the launcher tip

The general configuration of the temperature cell was determined; however, the cell had to be modified to make it more compatible with other parts. Since a fixed chamber was chosen, a rotating launcher is needed to provide the desired collision angles. Figure 3-3 shows the particle and drop path inside the chamber at different collision angles. The figures are exaggerated so that the different collision paths can be distinguished.

It can be concluded from Figure 3-3 that in order to have both right-angled and head-on collisions, a chamfer is required at one edge; otherwise, by placing the rotating launcher on an edge without a chamfer, one or both of the right-angled and head-on collisions will be missing. To track the motion of the particle/drop in a right-angled collision, the chamfer wall was modified as shown in Figure 3-3 (b).

3.3.1.3 Cell Material

Similar to the previous section, a simplified House of Quality is used to select the appropriate material for the cell body. According to material compatibility assessment in Table 3-3, aluminum alloy was selected to build the chamber. The main properties of aluminum are listed in Table 3-4 and physical properties of other materials are listed in Table B-2 of Appendix B for comparison.

Table 3-3 Cell material compatibility assessment (HOQ)

Relationship Values: 9: Maximum compatibility / 3: Medium compatibility / 1: Minimum compatibility / 0 : Not Applicable
Importance Weight: 1 (less important) to 5(most important)
A: Accepted, R: Rejected, C: to be Considered as an alternative

Design Criteria	Importance Weight	% Importance Weight	Material Options				
			Aluminum Alloy	CS	SS	Fiberglass	Thermoplastics
Low Density	5	17.9	3	1	1	9	9
High Thermal Conductivity	5	17.9	9	3	3	1	1
Low Thermal Expansion	5	17.9	3	9	9	9	1
High Operating Temperature	5	17.9	9	9	9	1	1
Availability	4	14.3	9	9	9	3	9
Ease of Fabrication	4	14.3	9	9	9	1	3
Compatibility Weight			685.7	650	650	414.3	385.7
Compatibility Weight %			24.62	23.33	23.33	14.87	13.85
Assessment Result			A	C	C	R	R

Table 3-4 Main properties of aluminum

Density	Thermal Conductivity	Thermal Expansion	Melting Point
2700 kg/m^3	~250 W/ (m.K)	23 × 10^{-6} /ºC	660 ºC

3.3.1.4 Launcher Mechanism

Regarding Section 3.1.1, to study the effect of particle size, material and velocity, the launcher should be capable of launching different types of particle material in different sizes and velocities. Since a fixed cell is chosen, to provide a 90° to 180° collision angle, a rotating particle launcher is necessary. The different impact parameters can be controlled by an off-axis movement of the launcher relative to the drop generator.

As was stated in the previous section, the launcher is mounted on a chamfered wall, and it is essential to have the feeders and triggering parts outside the chamber and the launching tip and the particle container inside. Figure 3-4 shows a preliminary sketch of the launcher mounted on the cell's chamfered wall. The other parameter which should be taken into account when selecting a particle launcher is compatibility with high temperature working conditions. Several types of launching propellant can be used in the particle launcher, including electromagnetic, electro-thermal, pneumatic and mechanical launching mechanisms.

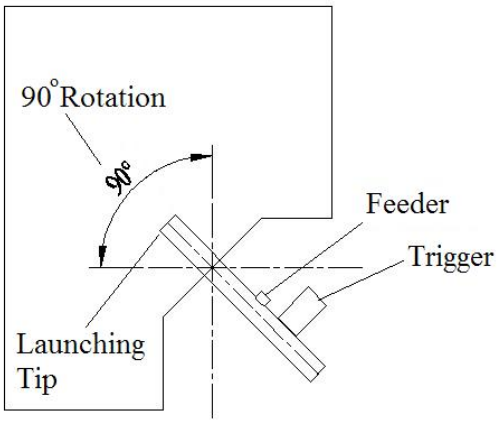

Figure 3-4 Schematic diagram of mounted launcher

Electromagnetic Launcher

The electromagnetic launcher or rail gun converts electromagnetic energy to kinetic energy and accelerates the projectiles. As illustrated in Figure 3-5, this launcher consists

of an inducing coil, ferric core (in this case, the plunger) and an electrical circuit. The plunger, which is a solid conductor, is placed in the core. The electrical current induces the magnetic field on the core and accelerates the plunger. The particle barrel can be made separately and connected by a coupling to the induction part. Or as shown in Figure 3-5 the barrel and the induction part can be constructed together as one unit. Since the particles are not ferric in general using a ferric plunger is necessary for launching [88].

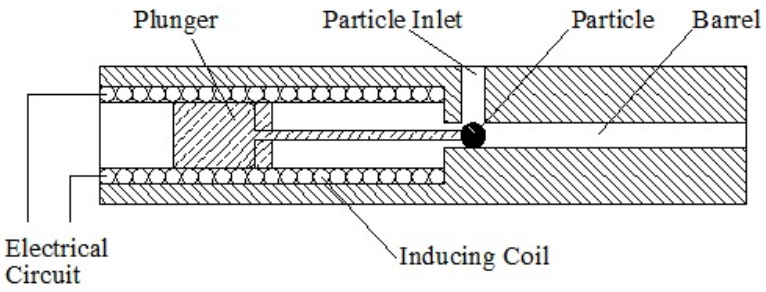

Figure 3-5 Simple diagram of electromagnetic launcher (sketched by the author)

Electro-thermal Launcher

Electro-thermal launchers are the modified versions of ordinary ignition guns. Instead of chemical ignition, they use electrical energy to heat and pressurize the gas inside the chamber to accelerate the projectiles. An electro-thermal launcher propellant, as shown in Figure 3-6, consists of a cathode and an anode which produce the electrical energy to heat the chamber. The ablation liner is vaporized by the heat and produces ionized high temperature gas which forms pressurized plasma. The high pressure plasma expands into the plunger case and quickly accelerates the plunger. In this launcher the particle barrel and the plunger case are connected to the electro-thermal chamber by a coupling [90].

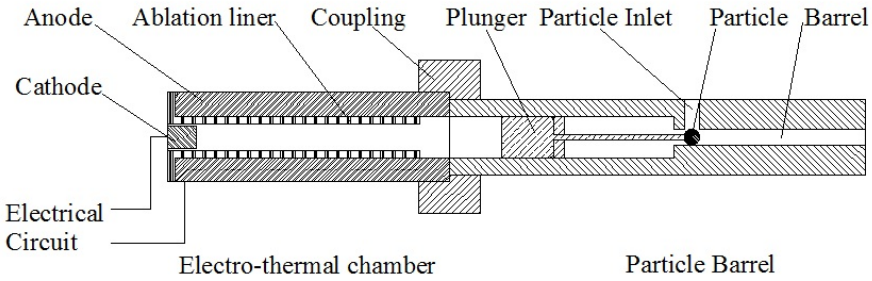

Figure 3-6 Schematic diagram of an electro-thermal launcher mechanism (sketched by the author)

Pneumatic launcher

Figure 3-7 shows the pneumatic launcher and a simple pneumatic control circuit. The pneumatic system can be used either by a pre-fabricated pneumatic jack or a special manifold barrel (shown in Figure 3-8). The pre-fabricated jack is connected to a plunger and the particle is accelerated by the plunger inside a barrel.

Since it is difficult to find an appropriately sized jack to match the other parts of the cell, an alternative manifold barrel can also be used instead of the prefabricated pneumatic jack and plunger system. The air supply can be connected to the particle barrel through a small air chamber. The pressurized air will cause the particle to accelerate.

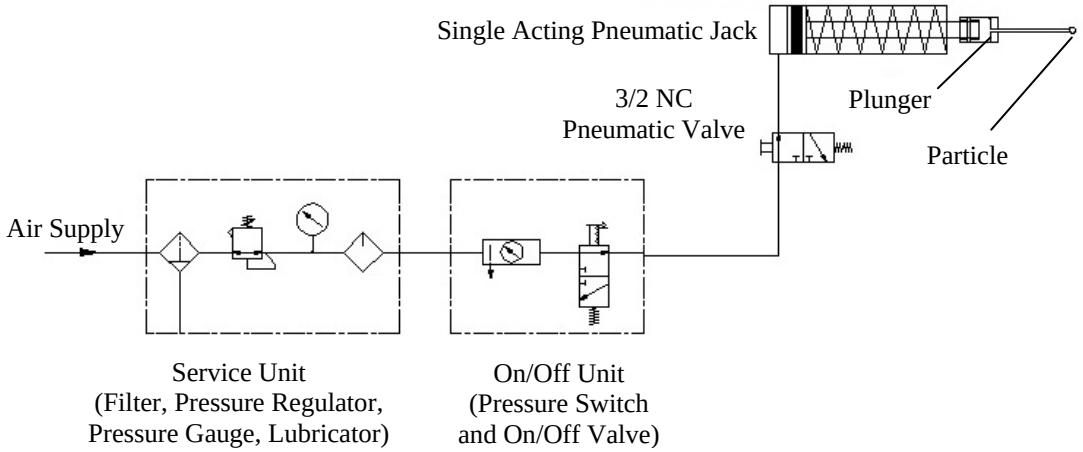

Figure 3-7 Simple diagram of pneumatic launcher mechanism (sketched by the author) [91]

To prevent the high pressure air from entering the temperature cell, an air-block piston should be designed inside the barrel. Figure 3-8 shows the alternative mechanism for the pneumatic jack.

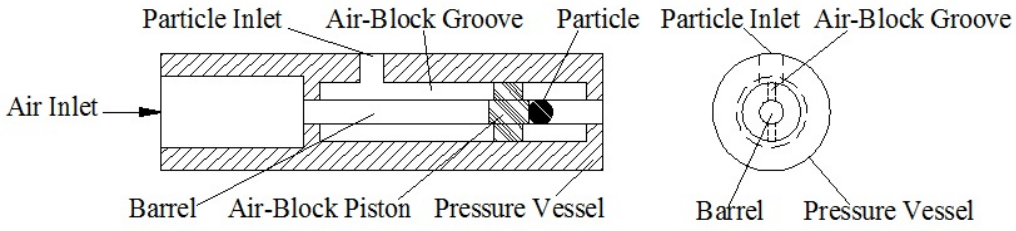

Figure 3-8 Manifold barrel for pneumatic launcher (sketched by the author)

Mechanical Launcher

The mechanical launcher shown in Figure 3-9 consists of a plunger, spring and pre-tension screw. In this launcher, the potential energy of the spring turns into the kinetic energy in the plunger and accelerates the particle.

Another compatibility assessment is applied here using a simplified House of Quality to select the most appropriate launcher for the setup. Table 3-5 shows the assessment values for each design criteria.

Table 3-5 Particle launcher mechanism compatibility assessment (HOQ)
Relationship Values: 9: Maximum compatibility / 3: Medium compatibility / 1: Minimum compatibility / 0 : Not Applicable
Importance Weight: 1 (less important) to 5(most important)
A: Accepted, R: Rejected, C: to be Considered as an alternative

Design Criteria	Importance Weight	% Importance Weight	Design Options			
			Electro-magnetic Launcher	Electro-thermal Launcher	Pneumatic Launcher	Mechanical Launcher
Simplicity (Operation)	4	8	9	9	3	9
Simplicity (Construction)	3	6	3	1	1	9
Simplicity (Maintenance)	4	8	3	1	1	9
Simplicity (Mechanism)	5	10	1	1	3	9
Providing required particle velocity range	5	10	9	1	3	9
Velocity adjustment precision	5	10	3	1	3	3
Capability to launch different particle sizes and shapes	5	10	9	9	9	9
Providing 90º collision angle range	5	10	9	9	9	9
Connections to the cell and the barrel	5	10	9	1	1	9
Compatibility with high temperature operating conditions	5	10	9	9	9	9
Easy to heat the particles inside the launcher	4	8	9	9	9	9
Compatibility Weight			676.0	468.0	480.0	840.0
Compatibility Weight %			27.4	19.0	19.5	34.1
Assessment Result			R	R	R	A

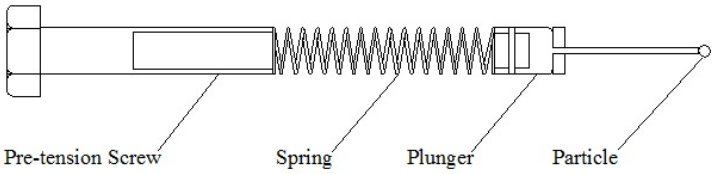

Figure 3-9 Simple diagram of mechanical launcher mechanism (sketched by the author)
The main idea of the spring mechanism is adopted from previous particle-drop collision setup built by S.T. Mehmood and D. Chevrollier (2010)

3.3.1.5 Assessment Discussion

Simplicity of (Operation)

To have a reliable result, it is necessary to repeat the experiments several times without difficulty; therefore, it is important that the setup work simply and the experiment be repeated in conditions as close to the original as possible. In each experiment there are usually two steps: the start-up process and the operation. There is no start-up process for the electromagnetic and mechanical launcher. Since an aberration liner is used in the electro-thermal launcher, there is no need to refill the external gas for each experiment, although a long-term replacement of the liner is needed. However, for a pneumatic system it is always necessary to control the service unit in order to protect the system. Regarding the operation itself, all the launchers are triggered using a switch. Most of the launchers use similar switches.

Simplicity (Construction)

The goal here is to design a mechanism which is simple enough to be made in the machine shop of the Department of Mechanical Engineering and meanwhile fulfills all the required functions of the experimental setup. As mentioned earlier, the mechanical launcher has the simplest structure, consisting of a screw, spring and plunger, while an electro-thermal launcher requires a specific chamber with an appropriate liner and supplemental electrical circuit. Although the electromagnetic launcher mechanism is simple compared to the electro-thermal launcher, it still has additional electrical circuits attached to it. The pneumatic launcher also consists of several pneumatic components, shown in Figure 3-7.

When using a pneumatic or electro-thermal launcher, it is important to prevent the air from entering the temperature cell so that the air motion will not affect the experiment.

Figures 3-6 and 3-8 show two sample mechanisms which can be used for both launchers. In the mechanical launcher, a piece of cord can be used to return the plunger to its initial position for the next launch. A more complicated system should be considered for the other launchers, due to their structure.

Due to maintenance issues in the pneumatic and electro-thermal launchers, it is important to make the propellant and particle barrel parts separately and use a special coupling to connect the them. These connections add another level of complexity to the setup when connecting the launcher to the cell.

Simplicity (Maintenance)

The more complicated the mechanism, the more complicated the maintenance. That is, troubleshooting in a complicated mechanism is more difficult due to the number of parameters involved. The maintenance issue in the mechanical launcher is the most straightforward compared to the others because it has a small number of elements. Apart from unpredictable failures which may occur in experimental setups, regular services and maintenance are required in certain mechanisms; as a case in point, the aberration liner should be replaced frequently in the electro-thermal launcher, and the service unit in the pneumatic launcher needs occasional full inspections.

Simplicity (Mechanism)

As discussed earlier, in a simple setup it is easier to track all the parameters which influence the experiment, and eliminate the effect of unwanted parameters. In the mechanical launcher, the potential energy of the spring is converted to the kinetic energy of the particle. No other force or energy field is imposed by the mechanism. In the electromagnetic launcher, an electromagnetic field is imposed on the particle. In the electro-thermal mechanism, the ignition may make the launcher function unpredictable. The sealing mechanism in electro-thermal and pneumatic launchers is another issue which can affect the experiments in case of failure.

Providing Required Particle Velocities

Pneumatic jacks and valves usually work within a certain definite pressure; therefore, regulating the pressure to control the plunger velocity may not cover all required velocities. By adjusting the electromagnetic field energy it is possible to reach different

values for velocity in electromagnetic launchers. Although the electromagnetic launchers are usually used in high speed launching [88], it is assumed here that they can cover low velocities as well. Since the electro-thermal launcher utilizes the ignition phenomenon in accelerating the projectile, achieving low velocities is not simple [89]. In the mechanical launcher; however, by replacing different springs with different spring stiffness, it is possible to cover both low and high velocities.

Velocity Adjustment Precision

The velocity adjustment is not possible in the electro-thermal launcher. That is, the propellant in this launcher is the gas ignition which is not controllable. In the other mechanisms, it is possible to adjust the velocities to some extent but not precisely.

Capability of Launching Different Particle Sizes and Shapes

Barrels have been designed in different sizes to fit each particle. Each barrel is used to direct its specific particle into the chamber. The barrels can be replaced and can also be connected to any kind of particle launcher. Therefore, all launchers are similarly compatible with this criterion.

Provide 90º Collision Angle Range

To make the launcher rotate 90°, it is essential to use a special connection. The same mechanism can be used for all the launchers; hence, there is no difference between these launchers in this criterion. However, finding an applicable rotating mechanism for each launcher depends on the structure of the launchers. Finding such a mechanism may be complicated in some cases.

Connections to the Cell and the Barrel

Mounting the mechanisms on the temperature cell is another concern when deciding which launcher to use in the setup. The accessories attached to the pneumatic, electro-thermal and electromagnetic launchers require special connections and more space than the accessories attached to the mechanical launcher. On the other hand, since the particle barrel had to be completely isolated from the air chamber in the electro-thermal and pneumatic launchers a dedicated sealing mechanism should be designed for the plunger in these launchers.

Compatibility with High Temperature Operating Conditions

The launchers will be fabricated in two parts: the propellant section and the particle barrel. As discussed previously, the particle barrel and feeder are mounted inside the temperature cell to be heated, while the propellant is installed outside the cell. Although these two parts are connected to each other by means of a coupling, and there is definitely a heat transfer to the propellant side, the distance from the heat source is sufficient to prevent these parts from overheating. However, the launchers are unlikely to fail to work at high temperature environments due to their structure.

Conclusion

It can be concluded from Table 3-5 and the discussion above that the mechanical launcher is the most suitable launcher option for the setup. The experimental results for the mechanical launcher presented in Figures 4-5 to 4-7 also showed promise, which is evidence that the same mechanism should be used in the setup.

Table 3-6 Particle launcher material compatibility assessment (HOQ)

Relationship Values: 9: Maximum compatibility / 3: Medium compatibility / 1: Minimum compatibility / 0 : Not Applicable

Importance Weight: 1 (less important) to 5(most important)

A: Accepted, R: Rejected, C: to be Considered as an alternative

Design Criteria	Importance Weight	% Importance Weight	Material Options				
			Aluminum Alloy	CS	SS	Fiberglass	Thermoplastics
Low Density	5	15.2	9	1	1	9	9
High Thermal Conductivity	5	15.2	9	3	3	1	1
Low Thermal Expansion	5	15.2	3	9	9	1	1
High Operating Temperature	5	15.2	9	9	9	1	1
Resistant to erosion	5	15.2	3	9	9	3	3
Availability	4	12.1	9	9	9	3	9
Ease of Fabrication	4	12.1	9	9	9	3	3
Compatibility Weight			718.2	687.9	687.9	300	372.7
Compatibility Weight %			25.96	24.86	24.86	10.84	13.47
Assessment Result			A	C	C	R	R

3.3.1.6 Launcher Material

Table 3-6 shows that aluminum is the most compatible of all the materials listed. The main properties of aluminum are listed in Table 3-4 and the physical properties of other materials are shown in Table B-2, Appendix B.

However, since any deviation in the particle path line will affect the collision results, to reduce the effect of erosion on the particle barrel, this part will be made out of carbon steel, which is more resistant to particle erosion. Another advantage is that the steel launcher has lower thermal conductivity; this prevents particles from overheating when the heater set point is higher than the required particle temperature. Meanwhile, unlike aluminum, it reduces the heat loss when working without insulation.

3.3.1.7 Drop Generator Mechanism

A simple syringe or an automatic drop-jet dispensers can be used to generate the drops. To justify the selection, it is necessary to conduct another compatibility assessment using a House of Quality, as shown in Table 3-7. The assessment makes it possible to use a simple syringe in this stage and avoid the complexity of automatic drop-jet dispensers.

The syringe relies on a mechanism, construction, and maintenance that are far more simple than those used in an automatic drop-jet dispenser. However, there is not much difference in terms of ease of operation between the syringe and the dispenser. Since loading the particles is a manual process, using a manual syringe provides the operator with enough time to launch the particles.

In both drop generators (the syringe and the dispenser), the drops reach the collision point through a free fall, and the velocity is a function of height. Therefore, the velocity range and adjustment are the same in both systems. Both generators are capable of generating different-sized drops. Case in point: by changing the syringe needle, different-sized drops can be released.

Both generators require a special clamp to be connected to the cell. The drop-generating tip in the automatic drop-jet dispensers is separated from the device by a hose. Therefore, the high temperature in the cell will not affect the device's operation. It is possible to heat

the drop fluid inside the syringe. However, due to the limited operating temperature of the automatic drop-jet dispenser device, it is not possible to heat the fluid inside the device.

Table 3-7 Drop generator mechanism compatibility assessment (HOQ)
Relationship Values: 9: Maximum compatibility / 3: Medium compatibility / 1: Minimum compatibility / 0 : Not Applicable
Importance Weight: 1 (less important) to 5(most important)
A: Accepted, R: Rejected, C: to be Considered as an alternative

Design Criteria	Importance Weight	% Importance Weight	Design Options	
			Automatic drop-jet dispensers	Syringe
Simplicity (Operation)	4	8	9	9
Simplicity (Construction)	3	6	1	9
Simplicity (Maintenance)	4	8	1	9
Simplicity (Mechanism)	5	10	1	9
Providing Required Drop Velocity Range	5	10	9	9
Velocity Adjustment Precision	5	10	3	3
Capability to Launch Different Drop Sizes	5	10	9	9
Single Drop Control	5	10	3	9
Connections to the Cell	5	10	9	9
Compatible with High Temperature Operating Conditions	5	10	9	9
Easy to Heat the Drop Inside the Drop Generator	4	8	1	9
Compatibility Weight			524	840
Compatibility Weight %			38.42	61.58
Assessment Result			R	A

3.3.1.8 Syringe Material

The material selected for the syringe should resist the high temperature operating conditions. Table 3-8 suggests a stainless steel syringe for the setup so that the drop liquid inside the syringe can be heated and drops can be generated while the syringe is attached to the temperature cell. The material physical properties are tabulated in Appendix B, Table B-2.

The mechanism and material of the main parts of the setup have now been chosen, but there are still accessories and equipment which are required to operate the setup. In

following sections, these auxiliary parts are discussed in brief. Chapter 5 will include detailed specifications.

Table 3-8 Syringe material compatibility assessment (HOQ)
Relationship Values: 9: Maximum compatibility / 3: Medium compatibility / 1: Minimum compatibility / 0 : Not Applicable
Importance Weight: 1 (less important) to 5(most important)
A: Accepted, R: Rejected, C: to be Considered as an alternative

Design Criteria	Weight	% Weight	Material Options		
			SS	Plastics	Glass
Low Density	5	17.2	1	9	3
High Thermal Conductivity	5	17.2	9	1	3
Low Thermal Expansion	5	17.2	3	1	1
High Operating Temperature	5	17.2	9	1	1
Resistant to Corrosion	5	17.2	9	9	9
Availability	4	13.8	3	9	9
Compatibility			575.9	486.2	417.2
Compatibility %			38.9	32.9	28.2
Assessment Result			A	R	R

3.3.2 Heating System

Electrical heaters are the most convenient heating systems for the setup due to their simplicity in installation, energy consumption, ease of operation and temperature control, and capability of high temperature set point compared with other heating systems such as steam heating, hot water and induction heating. Steam and hot water heating systems require auxiliary equipment which makes the systems more complex. The heating set points in these heaters (steam and hot water) are not high enough to fulfill the design requirements. Since a high temperature environment is sought to run experiments, it is necessary to heat the enclosed space of the cell; therefore, induction heaters are not applicable either. Induction heaters are usually used to heat a ferrous object located in the core of an inducing coil.

A variety of electrical heaters have been designed for different applications. These heaters include strip heaters, cartridge heaters, heat trace cables, flexible heaters, band

heaters, tubular and coil heaters, nozzle heaters and infrared heaters. Selecting the appropriate electrical heaters depends on the required temperature set point and installation restrictions. Due to the configuration of the cell and the temperature, cartridge heaters are selected as the most applicable heaters. The detail specification is provided in Chapter 5.

3.3.3 Control System

Two control systems are required for the setup: one for heating control and one for timing and triggering. The former maintains the cell temperature to the design set point and the latter adjusts the launcher triggering time with the drop generator so that the collision occurs between the drop and the particle in the appropriate position and time.

Since the setup is used as an experimental device only, a manual operating system was selected for the other tasks; that is, feeding the particles in to the launcher, releasing the drops and starting the cameras. A detailed discussion about control systems is provided in Chapter 5.

3.3.4 Optical System

3.3.4.1 Photography Technique

In the study of particle-drop collision it is necessary to record the videos of the experiment and analyze the video frames to collect the experimental data. However, since the collision occurs in high speeds and the particles and the drop sizes are relatively small (order of sub-millimeters to a few millimeters), ordinary photography techniques are not applicable. To analyze the size and the velocity of the particle and drop as well as the details of the collision structure, video frame images are needed. According to some of the studies discussed in Section 2.1, the most applicable imaging technique is shadowgraph imaging. This technique uses an intense background light and a high-speed camera with high magnifying lens. The object is placed between the light source and the camera. Figure 3-10 shows the shadowgraph photography technique employed in the setup. This technique is usually used to record videos of small, high-speed objects.

3.3.4.2 Sight Glass

Since the experiment occurs inside a chamber, sight glass is required for the cameras and background lights. The location and configuration of the sight glass will be discussed in Chapter 5. This section will discuss only the material of the sight glass.

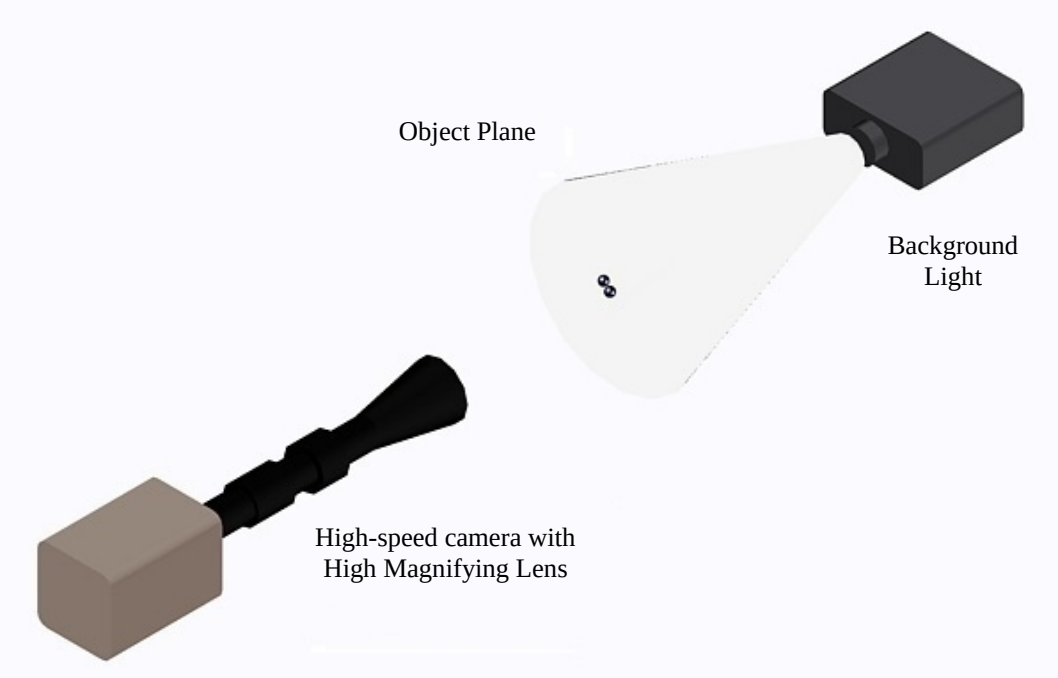

Figure 3-10 Schematic of shadowgraph technique [98]

Since sight glass is used for the photography, an optical glass should be selected so that the effect of the glass's texture can be reduced on the photos. Because of the high temperature operating condition of the cell, it is also important to take into account the material's operating temperature. Schott and Ohara are the main optical glass manufactures producing a wide variety of optical glass. Fused Silica/Quartz and BK7 are the most common suitable optical glass due to their high operating temperature. Fused Silica/Quartz and BK7 have maximum temperatures of 950°C, 1000°C and 350°C and annealing points of 1120°C, 1280°C and 550°C. Fused Silica/Quartz glass is applicable for deep UV transmission elements and minimum scattering systems. It is resistant to thermal shocks. BK7 is designed for optical imaging in the visible spectrum and laser optics, and can be used in stable temperature environments [92]. Although the thermal performance of Fused Silica/Quartz glass is higher, BK7 optical glass was chosen due to the availability of the products and the optical performance, which is more suitable for the visual spectrum and minimum scattering effects on laser beams. The working

temperature of the cell is 200°C and the maximum temperature of the electrical heaters is calculated as 300°C (see Section 4.3). The heating and cooling procedure will be gradual; therefore, the thermal condition of the setup matches the thermal condition of the glass. The thermal and optical properties of BK7 optical glass are listed in Table 3-9.

Table 3-9 Thermal and optical properties of the BK7 [92]

Max Temperature Continuous (Optical Performance)	Annealing Point	Thermal Conductivity	Optimum Transmission Range
350 ºC	550 ºC	1.1 W/(m.K)	350nm-2.0µm

Chapter 4
Analysis and Calculations

With the overall design elements decided, it is necessary to conduct a number of calculations and data analyses before stating the detailed design process. The result of these calculations will be used to determine the chamber dimensions, and select required spring and heaters, etc., as described below:

- Analysis and calculations required to determine chamber dimensions:
    - Collision pattern analysis: This analysis results in predicting collision outcomes, observation area and collision model (defined in Section 4.2.2)
    - Required velocity calculations: These calculations result in the range of velocities needed to cover all collision outcome patterns (collision regimes)
    - Collision model (defined in Section 4.2.2): This model is used to predict the velocities and direction of motion after the collision
    - Thermal analysis: This numerical analysis provides an approximate idea about the temperature gradient inside the chamber and verifies the suitability of the heating system

- Calculations required to select an appropriate spring:
    - Required velocity calculations: These calculations provide the velocity range by which the spring stiffness should be calculated
    - Spring stiffness calculation(calculated based on the required velocities): This calculation is used to select the needed springs

- Calculations required to select the heaters:
    - Thermal analysis: This numerical analysis provides an approximate idea about the set point of the heaters and temperature gradient inside the chamber

- Start-up and operating heat requirement calculations: These calculations help to determine the power of the selected heaters

These analyses and calculations will be described in detail in the following sections. The final calculated values will be highlighted at the end of each section for use in the detailed design process.

4.1 Data Analysis

The data analysis in this section is carried out based on the experiments conducted by Amirfazli et al. [83]. The drop impact onto a spherical flying particle was studied using an experimental setup designed and built by S.T. Mehmood and D. Chevrollier in the Surface Engineering Lab at the University of Alberta in 2010. (The experimental setup is shown in Figure A-2 in Appendix A). The experiments were performed at room temperature using deionized water (DI water) drops that were 2mm in diameter, and Teflon/nylon/acrylic particles that were 1.6mm in diameter. The collision angle was selected as 90º [83]. This analysis results in an estimate of the motion, deformation and outcome velocities of the particles and drops after collision. It also estimates how fast the phenomenon is and the size of the required space for monitoring the collision.

4.1.1 Collision Patterns

The observation area must be defined to observe the drop-particle motion using a fixed camera. This study focuses on the collision phenomenon itself. The observation area is defined as a region where the entire collision phenomenon takes place. The subsequent motions will be ignored. Collision phenomenon starts when a drop and a particle first come into contact. It continues until the interactions reach a stable point.

To obtain a concrete view of the impact outcomes, more than 300 videos were analyzed and different collision outcomes were observed. To represent the results clearly, the outcomes are grouped in four dominant collision patterns (collision regimes) and two velocity categories as shown in Figures 4-1 to 4-4.

Figures 4-1 to 4-4 were generated using two video frames: one before the drop and particle came into contact and the other after the collision interactions stabilized. The first

frame is overlaid with the second one to demonstrate the distances travelled by both the particle and the drop. In each photo, the cross lines show the initial velocity direction of the particle and drop, and the rectangle delimits the needed observation area.

❖ Low Velocity Patterns

In relative velocities between about 1.5 m/s and 2.5 m/s, dominant collision patterns are called bonding and semi-bonding. In bonding collisions, which occur mostly in lower velocities, the drop attaches to the particle after the collision. The observation area in this category starts at the first point of contact and follows the attached particle-drop body until all the vibrations and pulses of both the drop and particle vanish and the parts continue to move in a relative equilibrium. Figure 4-1 shows the observation area in the bonding collision.

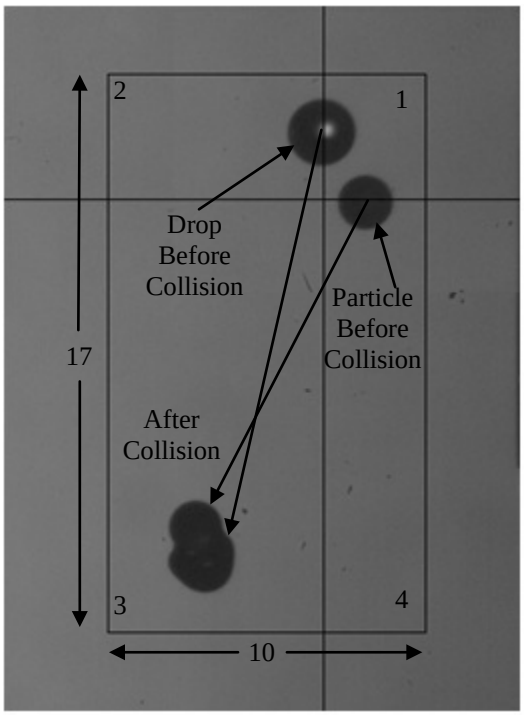

Figure 4-1 Sample shot of the bonding collision pattern (DI water drop/Teflon particle)
The solid crossed lines show the initial velocity direction of the particle and drop. The rectangle shows the limits of the observation area. Dimensions are in mm.
(Relative impact velocity: 1.5 m/s-2.5m/s)

The second category, called semi-bonding, occurs predominantly in off-axis hits. A small part of the drop attaches to the particle and the larger part continues its trajectory separately. In this category, the observation area shown in Figure 4-2 includes the area in

which the two bodies reach the collision point and the larger part of the drop separates completely from the group and forms its relatively stable shape.

❖ High Velocity Patterns

Dominant collision patterns in high velocity collisions are linear shattering and shattering. These patterns occur in relative velocities between about 3m/s and 6.5m/s. In linear shattering which occurs at average and high velocities (3m/s - 6.5m/s), the drop forms one or more attached drops, one or more small separate drops and one separate relatively large drop all in a line (Figure 4-3). The observation area is defined as an area in which the drop hits the particle and all mentioned drops form their relatively stable shapes and motion.

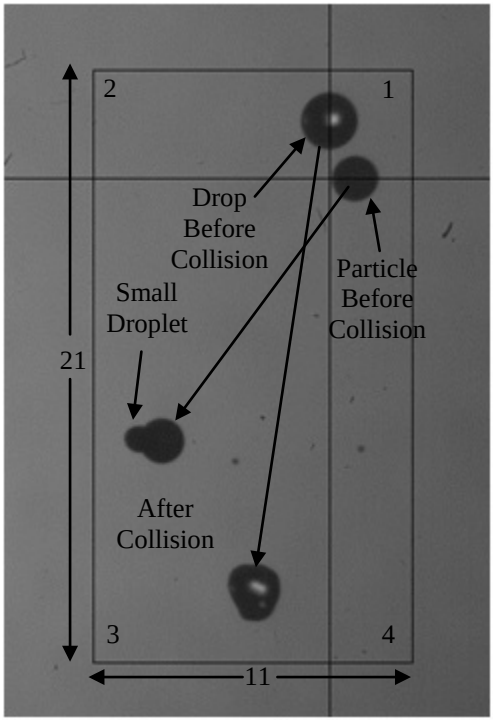

Figure 4-2 Sample shot of the semi-bonding collision pattern (DI water drop / Teflon particle)
The solid crossed lines show the initial velocity direction of the particle and drop. The rectangle shows the limits of the observation area. Dimensions are in mm.
(Relative impact velocity: 1.5 m/s-2.5m/s)

In last category, called shattering, the collision forms a jellyfish shape. This pattern occurs in high velocities and results in a random scattering of drops. In this category the observation area begins with the first point of collision and ends when the lamela separates from the core and small satellite drops form (see Figure 4-4).

These video analyses resulted in three main design requirements: predicting the collision outcomes, identifying the observation area in different types of collisions and choosing an appropriate collision model (defined in Section 4.2.2). In this thesis, only these aspects of the analysis have been considered. Explaining the collision phenomenon is beyond the scope of this thesis.

The two crossed lines in Figures 4-1 to 4-4 are guides to verify the area where the collision outcomes take place. The horizontal line represents the direction of the particle's initial velocity, and the vertical line shows the direction of the drop's initial velocity. These two lines also represent the direction of the momentum that each particle and drop exert on each other. As shown in Figures 4-1 to 4-4, these crossed lines divide the observation area into four areas (quadrants) marked by numbers from 1 to 4. The observations show that almost all collision outcomes take place in the third quadrant.

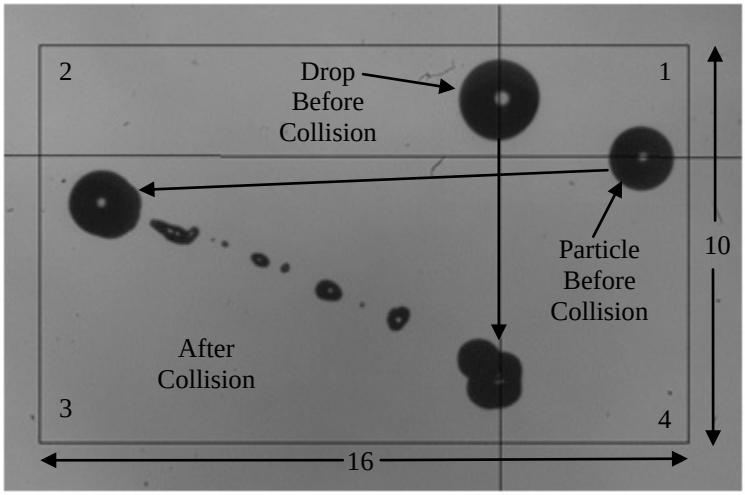

Figure 4-3 Sample shot of the linear shattering collision pattern (DI water drop / Teflon particle)
The solid crossed lines show the initial velocity direction of the particle and drop. The rectangle shows the limits of the observation area. Dimensions are in mm.
(Relative impact velocity: 3m/s - 5m/s)

If one defines the aspect ratio of an image frame as the ratio of the width of the frame to its height, one can conclude from the image frames of the experiments that the aspect ratio in images from low velocity collisions is less than one while in high velocity collisions the aspect ratio of the images is more than one.

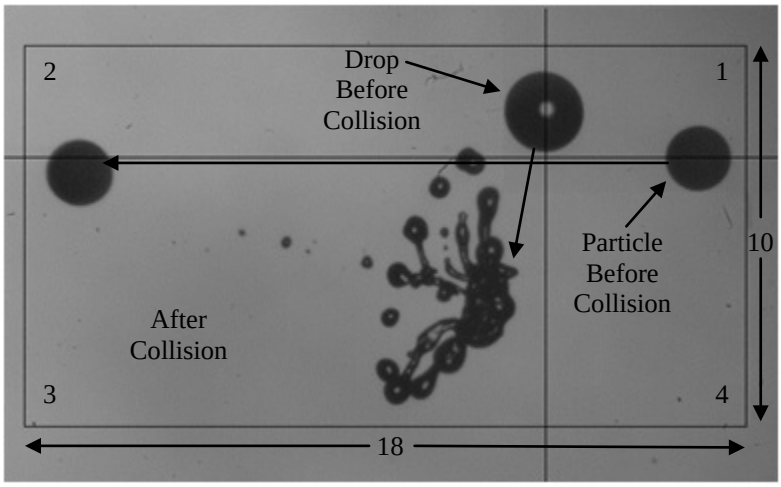

Figure 4-4 Sample shot of the shattering collision pattern (DI water drop / Teflon particle)
The solid crossed lines show the initial velocity direction of the particle and drop. The rectangle shows the limits of the observation area. Dimensions are in mm.
(Relative impact velocity: 4.8m/s - 6.5m/s)

The observation area has been measured for all experiments and the maximum area has been found to be 50mm×25mm, taking into consideration a safety factor of 1.2 in the horizontal direction. Although the results belong to the water drop and Teflon/nylon/acrylic particles, they give an overall estimation about the size of the observation area with respect to the particle/drop size. These dimensions will be used in the following sections to determine the overall cell dimensions and sight glass required for imaging.

4.1.2 Required Velocities

To estimate velocity ranges required to cover all different collision outcome patterns (i.e. collision regimes), the results of Amirfazli et al.'s [83] experiments under the following conditions were analyzed:

- Particle: acrylic/nylon/Teflon
- Drop: DI water
- Drop diameter: 2mm
- Diameter ratio: 1.3 (drop to particle)
- Right angled collision
- Temperature: 20ºC

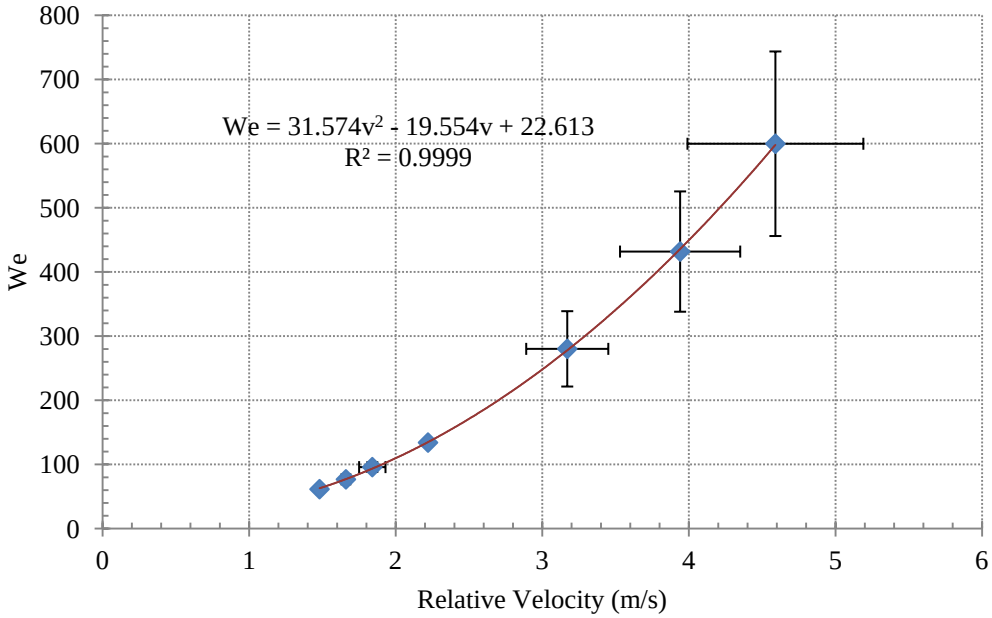

Figure 4-5 We number versus relative velocity in drop-particle collision
DI water-acrylic at 20ºC

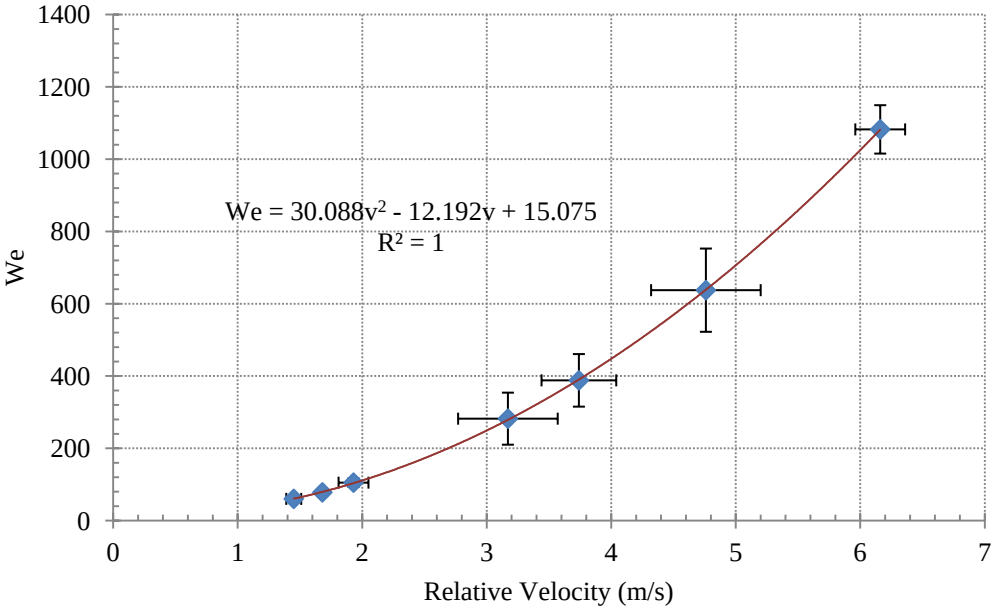

Figure 4-6 We number versus relative velocity in drop-particle collision
DI water- nylon at 20ºC

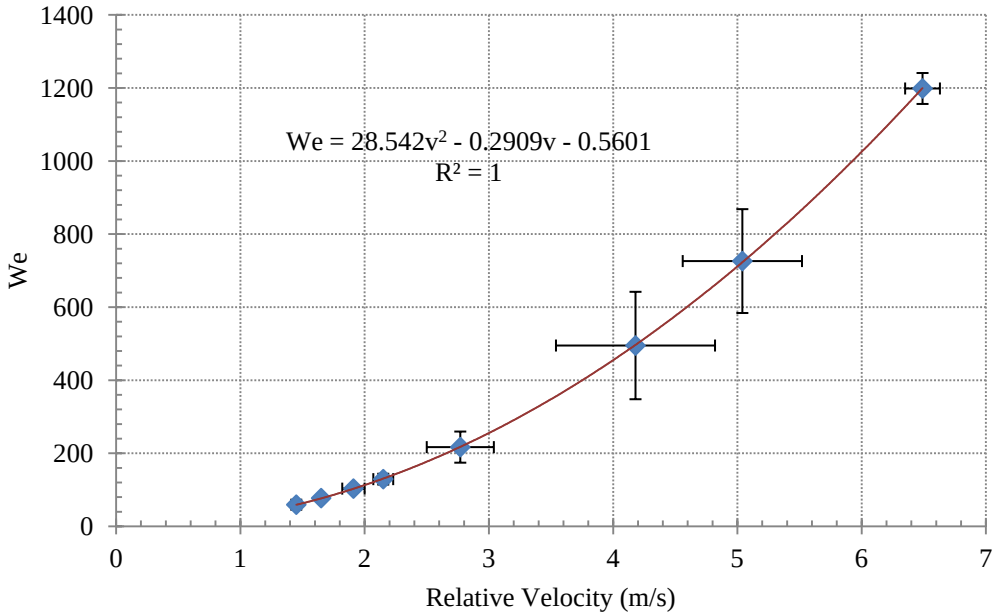

Figure 4-7 We number versus relative velocity in drop-particle collision
DI water- Teflon at 20ºC

It is obvious that velocities obtained from these data are only estimated design values and may vary in other experimental conditions. Figures 4-5 to 4-7 show the Weber number variation with respect to relative velocity in Amirfazli et al.'s [83] experiments.

Each graph in Figures 4-5 to 4-7 corresponds to a different particle material that has collided with a DI water drop. The curves used to fit the data points in these graphs are polynomials of power two, which is the best fit according to physical definition of the Weber number. As regards to Equation 2-5, the Weber number is proportional to the relative velocity of power two. Each point represents the average value of one experimental test set corresponding to one spring pre-tension, which results in almost the same particle velocity (the number of runs in each experimental test set is provided in Appendix A, Tables A-1 to A-3).

The error bars in Figures 4-5 to 4-7 show an increasing standard deviation in high velocities, especially for acrylic-water experiments. The deviation is reduced in later experiments by modifying the experimental setup. In the drop-particle collision setup used by Amirfazli et al. [83], a metal rod was used to move the plunger backwards. This exerted extra momentum on the plunger and resulted in inconsistencies in particle

velocities. The rod was replaced by a cord similar to the plunger positioning cord designed by the author and shown in Figures 5-8 and 5-9. The enhancement is tangible in Figures 4-6 and 4-7 in velocities higher than 5 m/s. These velocities correspond to the experiments conducted after the setup modification.

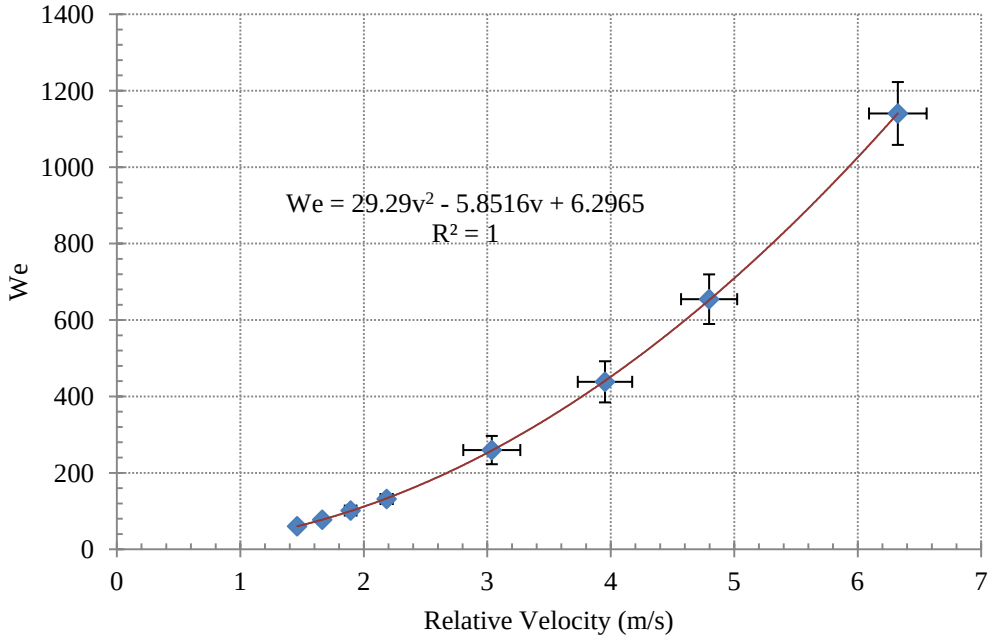

Figure 4-8 Weber number versus velocity using water drop at 20ºC
Average values from Figures 4-5 to 4-7

Regarding the existing experimental data by Amirfazli et al. [83], the average drop velocity and size were 1.24m/s and 2.03mm, respectively. These values were measured at ~80mm below the drop generation point. The particle velocities vary between 0.7m/s and 6.3m/s, resulting in relative velocities between 1.44 m/s and 6.56 m/s, Weber numbers (Equation 2-5) between 60 and 1,200 and Reynolds numbers (Equation 2-4) between 2,900 and 13,000. As mentioned in Section 2.2, liquid drop properties, drop diameter and relative velocity were used to determine Weber and Reynolds numbers. This range of Weber numbers covers all different observed collision outcome patterns, which are called collision regimes. Detailed data tables are provided in Appendix A, Tables A-1 to A-3.

To avoid unnecessary calculations, all the data from Figures 4-5 to 4-7 are combined in a new graph shown in Figure 4-8. Each data point in Figure 4-8 represents the average value of corresponding data points from Figures 4-5 to 4-7. Since an estimated method is

used in design basics, an overall Weber number/relative velocity range is sufficient for the calculations.

4.1.2.1 Data Adjustment

The setup is designed to work at 200ºC. It is not possible to use the same particles and drops as in previous experiments. The appropriate drop fluid and particle material should be selected. Considering the flash point of the fluids and that they are nonhazardous at high temperatures (i.e., not being flammable), heat transfer fluids, bath fluids, motor oil and some silicon oils were found suitable to generate drops. Appendix B, Table B-1, provides the physical properties of a number of appropriate fluids. Ceramic, Glass or some stone beads are also appropriate to operate in high temperature conditions. For instance, glass beads have a high melting point of above 1400°C.

To adjust the findings from previous experimental data (Amirfazli et al. [83]) to the materials and experimental conditions mentioned above, it is necessary to recalculate the Weber number/relative velocity for selected sample drops and sample particles. In this case, silicone and motor oil drops and glass beads were the selected materials in the velocity calculations. It is obvious that using a fluid with the different density and surface tension requires different velocity to achieve the same Weber number; however, the question is how dramatically these changes affect the velocity range. Since estimation is needed, it is acceptable to run the calculations based on one sample material to gain insight into the values and adjust the results to cover other materials.

4.2 Velocity/Momentum Calculations

4.2.1 Velocity Range Based on Adjusted Weber Numbers

As mentioned in Section 2.2, the Weber number and Reynolds number are proportional to relative velocity by power two and one, respectively. Hence, by selecting the velocity as the variable parameter, it is possible to calculate the Weber number and Reynolds number based on the existing velocity data. Inversely, the relative velocity can be calculated based on either the given Weber or Reynolds numbers. This mathematical argument leads to the introduction of three approaches to estimate the required velocity range for the conditions discussed in Section 4.1.2.1, based on the previous experimental data (Amirfazli et al. [83]) which covers all collision regimes:

- Assuming that the collision regimes are governed directly by relative velocity:

In other words, the same collision regimes in experimental conditions discussed in Section 4.1.2.1 will occur in the same relative velocities as in previous experiments (Amirfazli et al. [83]). In this case, to define the velocity ranges, it is appropriate to use the same velocity ranges obtained from previous experiments (Amirfazli et al. [83]).

- Assuming that the collision regimes are governed by the Weber number:

In this approach, the same collision regimes in new experimental conditions discussed in Section 4.1.2.1 will occur in the same Weber numbers as in previous experiments (Amirfazli et al. [83]). The velocity ranges corresponding to the Weber numbers acquired from the previous experiments are calculated based on the new experimental conditions. These velocity ranges are assumed to be the required velocity ranges.

- Assuming that the collision regimes are governed by the Reynolds number:

This means that the same collision regimes in new experimental conditions (discussed in Section 4.1.2.1) will occur in the same Reynolds number as in previous experiments (Amirfazli et al. [83]). In this approach, the velocity ranges corresponding to the Reynolds numbers are calculated based on the new experimental conditions. (The Reynolds numbers are acquired from Amirfazli et al.'s [83] experiments.) These velocity ranges are assumed to be the required velocity ranges.

Relative velocity does not appear in the Ohnesorge number, since it is the ratio of the square root of the Weber number to the Reynolds number; hence, it is not considered in design calculations. Froude and Capillary numbers are not applicable in the calculations either, since they are employed in drop impact onto a liquid film [82, 84].

According to Ashgriz and Poo [5], collision outcomes are governed mostly by the Weber number rather than the Reynolds number. The following analysis is performed based on the Weber number and relative velocities. The effect of the Reynolds number on velocity ranges will be discussed briefly at the end of this section.

As mentioned in Section 2.2, any change in fluid properties directly changes the kinematic surface tension (defined in Section 2.2) and, consequently, the Weber number, and affects the collision outcomes.

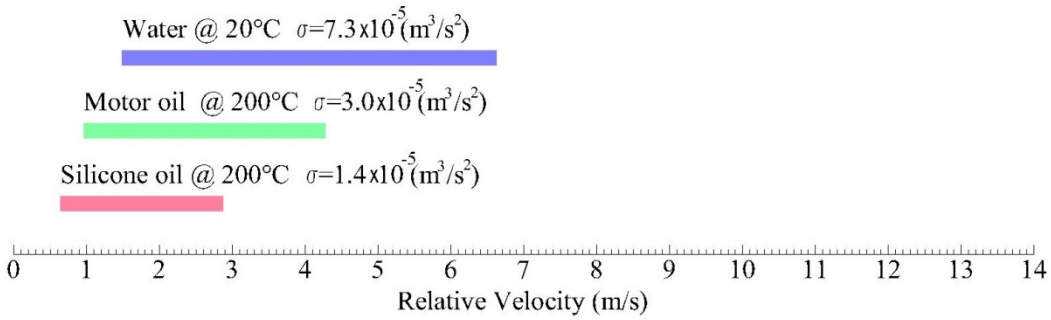

Figure 4-9 Velocity ranges corresponding to We = 60 to 1200 for a 2 mm drop

Relative velocities corresponding to Weber numbers between 60 and 1200 have been calculated for two sample liquids with relatively low and medium kinematic surface tension compared to water. Figures 4-9 and 4-10 show the velocity band, which covers the Weber numbers between 60 and 1200 for each fluid (compared to water), for two extreme drop sizes.

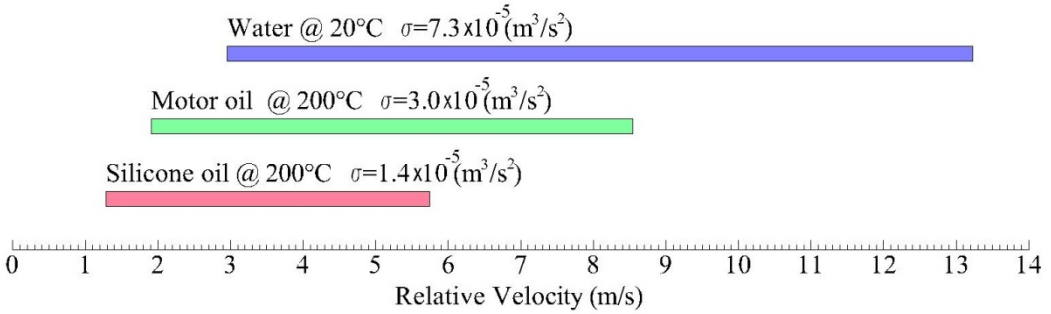

Figure 4-10 Velocity ranges corresponding to We = 60 to 1200 for a 0.5 mm drop

It can be deduced from the Figures 4-9 and 4-10 that when kinematic surface tension decreases, the same Weber number occurs in lower velocities. This results in a narrower velocity band (colored bars in Figures 4-9 and 4-10) in lower kinematic surface tension values compared to higher kinematic surface tension values.

Detailed calculations are provided in Appendix A, Tables A-4 and A-5. The velocity ranges between 0.6 m/s and 5 m/s have been selected for drop size of 2 mm, and the velocity ranges between 1.2 m/s and 9 m/s for drop size of 0.5 mm. This range of velocities covers both low and intermediate kinematic surface tension fluids.

As mentioned earlier, the Weber number approach was chosen in the design calculations; however, to have an idea of the velocity ranges achieved by the relative velocity and Reynolds number approaches, a brief comparison discussion is provided here. The relative velocities obtained from previous experiments (Amirfazli et al. [83]) are between 1.44 m/s and 6.56 m/s, which is already covered by the velocity range obtained in the Weber number approach (see Tables A-4 and A-5 in Appendix A). Tables A-6 and A-7, in Appendix A, show the velocity range calculated based on the Reynolds number approach. The lower velocities obtained from the Reynolds number approach are covered in the Weber number approach (see Tables A-4 and A-5 in Appendix A). However, the higher velocities rise up to 2,700m/s which is far too high to be captured by available cameras and is not applicable in this thesis.

4.2.2 Collision Model

To calculate the velocity of the individual particle/drop after impact, it is necessary to study the dynamics of the collision. The collision model is defined as a mathematical model which describes the dynamics of the collision and is able to predict the particle and drop motion after the collision. Predicting the motion (i.e., the value and direction of the velocity vector) of the drop and particle after the collision makes it possible to estimate the dimension of the observation area.

The different collision patterns acquired from the video frames in Section 4.1.1, reveal important information to verify the collision model for each collision regime. Since in these collisions, one body is rigid and the other is a fluid, the elastic collision model will not apply. In high velocities (i.e., Figure 4-4) the particle passes through the drop and basically keeps its original momentum; however, the momentum transferred by the particle to the drop is not sufficient to drag the scattered drops, and the drops continue their previous vertical motion after the collision. Hence, it is reasonable to consider that the particle and drop motion directions and velocities have changed very little. That is, the particle and drop move close to the right angle lines of original trajectories (Figures 4-3 and 4-4). On the other hand, in low velocities (i.e. Figures 4-1), a perfectly inelastic behavior is seen; the drop attaches to the particle and the greatest momentum exchange between the two bodies takes place. In this case, the conservation of momentum equation can be used as a model to predict the velocity and the direction of

particle-drop. This model can be applied with approximation to semi-binding collisions as well.

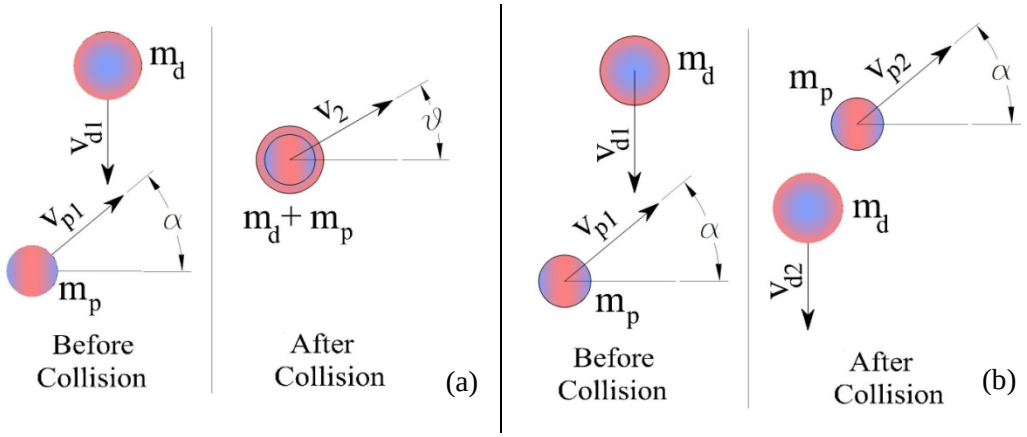

Figure 4-11 Collision model diagram
(a) perfectly inelastic collision (low velocity collisions) / (b) constant momentum collision (high velocity collisions)

Figure 4-11 shows the two collision model diagrams for low and high velocities; in high velocities the constant momentum collision applies, which assumes that the velocities of collision bodies remain constant before and after collision. In low velocity collisions, the perfectly inelastic collision model is employed, which uses the conservation of momentum equation to predict the velocities after collision. The equations of motions in both models are as follows:

Low Velocities

It is assumed that in low velocities, the perfectly inelastic collision (PIC) model governs the motion after the collision. It is represented by Equations 4-1 and 4-2

$$X:\ m_p\, V_{p1}\, \cos\alpha = \left(m_d + m_p\right) V_2\, \cos\theta \qquad 4\text{-}1$$

$$Y:\ m_d\, V_{d1} + m_p\, V_{p1}\, \sin\alpha = \left(m_d + m_p\right) V_2\, \sin\theta \qquad 4\text{-}2$$

where m_p and m_d are masses of the particle and drop; V_{p1} and $V_{d1}$are initial velocities of the particle and drop; V_{p2} and V_{d2} are velocities of the particle and drop after collision; V_2 is the velocity of the attached particle and drop after collision; α corresponds to the

particle's initial velocity angle with respect to the horizon, and θ is the final particle-drop velocity angle.

High Velocities

In high velocities the constant momentum collision (CMC) model is the closest model to define the motion of the individual components after collision and is represented mathematically in Equation 4-3:

$$\vec{V}_{d1} \approx \vec{V}_{d2} \ and \ \vec{V}_{p1} \approx \vec{V}_{p2} \qquad 4\text{-}3$$

To verify how close these models are to the actual experimental conditions, the data from previous experiments (Amirfazli et al. [83]) are considered.

4.2.3 Verification of the Collision Model

To verify the collision models, a sample group (see Appendix A, Table A-8) of in-axis shots (with low standard deviation in velocity) has been selected in both high and low velocity collisions. Table 4-1 uses the collision models discussed earlier to show the average measured velocities after collision, in both high and low velocity groups, compared to the calculated values.

Table 4-1 Verification of the collision model
V_p and V_d are particle and drop velocities; EMV stands for experimental measured velocity; PIC stands for perfectly inelastic collision and CMC represents the constant momentum collision model. More details can be found in Appendix A, Table A-8

Velocity Range	Before Collision		After Collision			Error	
	EMV	EMV	EMV	PIC Model	CMC Model	EMV vs. PIC	EMV vs. CMC
	V_p [m/s]	V_d [m/s]	V_p [m/s]	V_p [m/s]	V_p [m/s]	V_p (%)	V_p (%)
Low	0.74	1.26	0.30	0.28	0.74	5.68	59.14
High	4.51	1.22	3.68	1.79	4.51	51.45	18.40

It can be seen from the errors in Table 4-1 that the collision model is closer to assumption of the perfectly inelastic collision in low velocities, representing the average error of 5.7% versus 51.5% in high velocities. On the other hand, comparing the measured

experimental velocities after collision and constant momentum collision model shows that velocity changes about 18% in higher velocities while in low velocities there is about a 59% variation between the constant momentum collision model and the measured values. Therefore, the assumption of perfectly inelastic collision in low velocities and constant momentum collision in high velocities can be a reasonable approximation to calculate the particle and drop velocities.

4.2.4 Velocity Calculations Based on Dynamic Models

To estimate the velocities of each individual particle and drop, two limiting values of relative velocities calculated in Section 4.2.1 have been considered for two limiting drop sizes; that is, relative velocities 0.6 m/s and 5 m/s for the drop size of 2mm diameter; and relative velocities 1.2 m/s and 9 m/s for the drop size of 0.5mm diameter. Equations 4-1 and 4-2 were used to estimate the velocities after collision in the low velocity collision regimes. Equation 4-3 estimates the final velocities in high velocity collision regimes. These calculations have been categorized for the two limiting particle sizes (0.5mm and 2mm) and three collision angles illustrated in Figure 4-12.

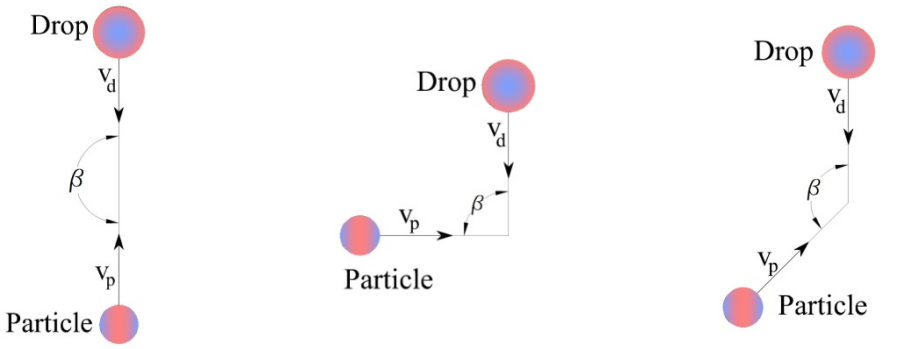

Head-on collision
β = 180º

Right-angled collision
β = 90º

Oblique collision
β = 135º (sample)

Figure 4-12 Collision angles in drop-particle collision

The following calculations reveals two major results: (1) predicting the motion after collision and (2) estimating the distance between the collision point and the particle launcher/drop generator tip.

4.2.4.1 Low velocities

Using the PIC model, the velocities after collision were calculated for each drop size (i.e., 0.5mm and 2mm) in three collision angles for the two limiting particle sizes (0.5mm and 2mm). Different drop-particle velocity combinations were considered in the calculations to achieve the desired relative velocity. The detailed calculations are provided in Appendix A, Tables A-9 to A-11. The velocities in these tables were selected arbitrarily to cover the velocity range and may vary in the experiments. In each pair of velocities, the trajectory diagram was used to understand how consistent the projectile direction and speed were, and how the velocity changed with respect to the distance from the generating/launching point. A sample diagram and calculation table has been provided in Appendix A, Tables A-13 to A-15 for the minimum velocities.

Table 4-2 Velocity calculation based on PIC model in low velocities
(Minimum possible velocity combination considering the distance from the launcher and drop generator tips)
V_{Rltv} : Required relative velocity at collision, V_{PI} : Particle initial velocity at launcher tip, V_{PC} : Particle velocity at collision point, dl : distance between collision point and launcher tip, V_{DI} : Drop initial velocity at drop generator tip, V_{DC} : Drop velocity at collision point, h : distance between collision point and generator tip, V_F : Velocity of bonded particle and drop after collision, θ : Direction of motion of bonded particle and drop after collision with respect to horizon, D_d (mm) : Drop diameter, D_p (mm) : Particle diameter, β: Collision angle

Collision Type	D_d (mm)	D_p (mm)	V_{Rltv} (m/s)	Particle			Drop			Final Velocity Vector	
				V_{PI} (m/s)	V_{PC} (m/s)	dl (mm)	V_{DI} (m/s)	V_{DC} (m/s)	h (mm)	$\|V_F\|$ (m/s)	θ (D)
Head-on (β=180°)	2	2	0.6	1	0	51	0	0.6	19	0	-90
		0.5	0.6	1	0	51	0	0.6	19	0	-90
	0.5	2	1.2	1	0.6	32	0	0.6	19	0.6	90
		0.5	1.2	1	0.6	32	0	0.6	19	0.45	90
Oblique (β=135°)	2	2	0.6	0.2	0.2	5	0	0.45	10	0.11	-3
		0.5	0.6	0.2	0.2	5	0	0.45	10	0.42	-89
	0.5	2	1.2	0.8	0.7	11	0	0.6	19	0.69	45
		0.5	1.2	0.8	0.7	11	0	0.6	19	0.43	31
Right-angled (β=90°)	2	2	0.6	0.4	0.4	5	0	0.45	10	0.32	-20
		0.5	0.6	0.4	0.4	5	0	0.45	10	0.43	-88
	0.5	2	1.2	0.9	0.9	9	0	0.8	33	0.9	0
		0.5	1.2	0.9	0.9	9	0	0.8	33	0.71	-16

For each velocity combination, the minimum distance to the syringe and particle launcher tip was verified. The appropriate combination of velocities would be the one in which the minimum cell dimension is achieved and a collision close to the launcher or drop generator tip is avoided. Having the bonding collision in minimum velocities provides the opportunity to have the closest distance to both tips of the particle launcher and drop generator since there is no fluid splashing and shattering in these collisions. Velocity calculations for low velocity collisions based on the perfectly inelastic collision are summarized in Table 4-2 and all the values are rounded off.

Achieving low velocities for particles is not simple. In low velocities the particle's trajectory will quickly turn to a parabolic path (see Table A-13). To have a specific velocity at a specific angle, it is necessary to move the collision point close to the launcher tip. On the other hand, low velocity drops result in the collision point being close to the drop-generator tip. This does not allow the drops to form a stable spherical shape. The triggering/timing is another issue which prevents having the collision so close to the tips. Considering all these issues, the minimum possible velocity combination is tabulated in Table 4-2. The results show the required distance from the drop generator and particle launcher tips. Head-on collisions occur about 30 mm to 50mm above the launcher tip and continue to move upward or downward depending on the drop size. In oblique and right-angled collisions, the maximum distance between the collision point and launcher tip was calculated as about 10mm. The distance from the collision point and the drop generator tip varies between 10mm and 30mm in different collision angles. The calculated velocities after collision confirm that the attached particle-drop moves within the initial velocity vectors as shown in Section 4.1.1.

4.2.4.2 High velocities

As mentioned earlier, in high velocities both the particle and the drop follow nearly their original trajectory. That is, the particle continues its motion with almost the same velocity as the launching velocity. Drops continue their free fall, although they are being scattered. The goal here is to select a drop-particle velocity combination so that the cell dimensions can be minimized. Table A-12 in Appendix A shows different possible velocity combinations to achieve the relative velocities within the range calculated in Section 4.2.1. At high velocities, particles maintain their initial velocity and directions in the first 10mm from the launcher point; therefore, it is possible to consider the collision

point at this distance. The problem arises; however, when considering the drop. Since the drop velocity is an indirect function of height (i.e., the distance from the drop-generator tip), a higher velocity requires longer distance. In order to keep the cell dimensions as small as possible, drop velocities of more than 1.2m/s (corresponding to generation point height of ~70mm) were avoided (the final dimensions of the cell are discussed in Chapter 5). The corresponding height for each drop velocity was calculated in Table A-12 to verify the inapplicable velocity combinations. In this case, for instance, the particle launcher spring should be able to launch the particle up to 9 m/s in the right-angled collision for the drop size of 0.5mm.

Calculations provided in this section make it possible to find three main design parameters: final velocity vectors, the proper drop/particle velocity combination, and the appropriate collision point.

The after-collision calculated velocity vectors confirm that the particle/drop continues its motions either on initial velocity vectors or between the initial drop/particle velocity vector (quadrant 3) as shown in Figures 4-1 to 4-4.

Tables 4-2 and A-12 show that the maximum required observation height that occurs in head-on collisions is approximately 50mm and the maximum distance between the launcher tip and the collision point is 10mm. Therefore, the maximum height of the observation area becomes 60mm. The maximum required observation width occurs in right-angled collisions: by adding the maximum distance between the collision point and the launcher tip (10mm) to the width of the observation area measured in Section 4.1.1 (50mm), the required width for the observation area becomes 60mm. To follow the symmetry in the design, a 60mm×60mm rectangle is considered as the observation area or the field of view of imaging for all collision types.

4.3 Thermal Analysis

To determine the power required to heat the cell and estimate the temperature gradient inside the cell, a simplified heat transfer analysis was done by solving the 3D steady state thermal diffusion equation for a semi-cubic geometry. A simplified computational domain used in numerical analysis is illustrated in Figure 4-13.

Equation 4-4 shows the general unsteady thermal diffusion equation.

$$\frac{\partial T}{\partial t} - \alpha \nabla^2 T = 0 \qquad 4\text{-}4$$

The 3D steady state governing equation in Cartesian coordinates is shown in Equation 4-5.

$$\frac{\partial^2 T}{\partial x^2} + \frac{\partial^2 T}{\partial y^2} + \frac{\partial^2 T}{\partial z^2} = 0 \qquad 4\text{-}5$$

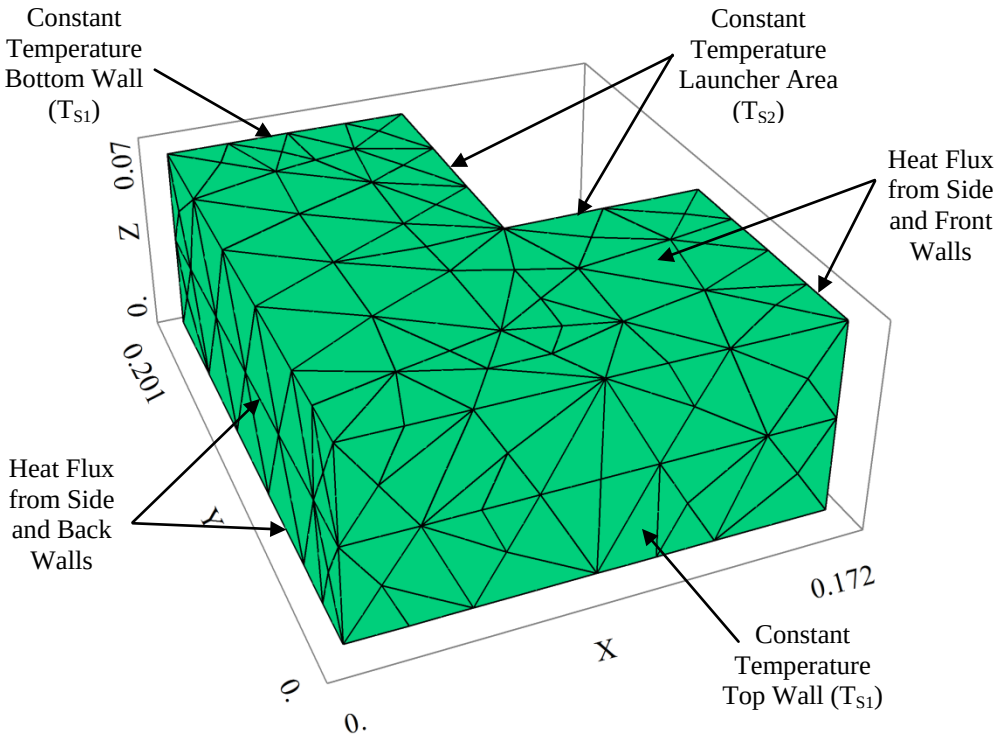

Figure 4-13 Computational domain and 3D mesh generated by the Flex PDE software

The following boundary conditions have been applied to the cell for the maximum cell temperature (200°C):

Constant temperature at top and bottom walls: T_{S1}= 575 K (heaters are installed at top and bottom walls)

Constant temperature at launcher area walls: T_{S2}= 525 K (heaters are installed at launcher area)

Heat flux at side walls: T=(kA/s)×(T-Tout)

in which:

T (K): temperature inside the cell

k (W/mK) : thermal conductivity of the glass walls

A (m^2) : wall area

s (m): wall thickness

T_o(K): outside temperature

T_{S1}(K) and T_{S2}(K): wall temperatures

Since the goal is to find an estimate, convection is neglected inside the cell and conduction is considered as the only source of heat distribution inside the cell. This is the worst case scenario because convection helps heat distribution inside the cell and make the cell reach the steady state conditions faster. The thermal model has been solved applying the finite element method using FlexPDE software (PDE Solution Inc./ version 5.1.0s). Based on the results shown in Appendix A, Figures A-3 to A-9, if the temperature of the bottom and top walls is kept at 300°C and the temperature of the launcher area at 250°C, the temperature of the collision area will reach the desired 200°C. Since the collision occurs in a small area and not in the entire cell, it is not necessary to have a uniform temperature throughout the cell.

4.4 Additional Calculations

4.4.1 Spring stiffness

Equation 4-6 shows the energy balance used to select the appropriate spring for the launcher system.

$$\frac{1}{2}kx^2 = \frac{1}{2}mv^2 \qquad 4\text{-}6$$

where k is the spring stiffness, x is the displacement made by the spring, m is the total mass of the plunger and v is the velocity of the plunger. In this equation the kinetic energy of the plunger is balanced by the potential energy of the spring and the friction is neglected in the first step. Table A-16 in Appendix A shows the spring stiffness calculated for a range of velocities between 0.2m/s and 9m/s obtained in Section 4.2.4. It can be concluded from this table that the friction force can be ignored with respect to the spring force.

4.4.2 Heat Requirement

The energy requirement to size the heaters for the temperature cell is determined using two approaches: "start-up heat requirement" and "operating heat requirement" [97]. The start-up heat which is the amount of energy required to heat the system to the operating temperature, is calculated using Equation 4-7:

$$\dot{q} = m\, C\, dT/t \tag{4-7}$$

where m is the mass of the heated material, C is the specific heat, dT is the temperature rise, t is the heat-up time and $\dot{q}$ is the energy required to heat the cell environment.

The operating heat, the heat needed during steady-state operation, is calculated based on the heat losses through the walls at the set point of the operating temperature. The heat loss through insulated and un-insulated walls is calculated by Equation 4-8:

$$\dot{q} = A\frac{k}{s}\, dT \tag{4-8}$$

where A is the total surface area, k is the thermal conductivity of the walls, s is the thickness of the wall, and dT is the temperature difference between the heated wall and the ambient temperature. The start-up heat and the operating heat energy are calculated in Table A-18 in Appendix A. The larger value (~2900W) is obtained from the operating heat equation and is the heat required for the temperature cell. By applying a safety factor of 10% [97], the total energy required to heat the temperature cell will be ~3,200W.

Chapter 5
Detailed Design

In this chapter the design of all main parts and auxiliary equipment is discussed in detail, using the information and calculations provided in previous chapters. For reference, all technical drawings and equipment models and data sheets are provided in the appendices.

5.1 Main Parts

5.1.1 Cell Chamber

Figure 3-4 in Chapter 3 represents the final configuration of the temperature cell chamber. In this section, dimensions and construction details will be added to this sketch so that it can be fabricated in the Department of Mechanical Engineering machine shop at the University of Alberta. As calculated from the estimations provided in Section 4.2, an observation area of 60mm×60mm is required close to the launcher tip. Regarding the rotation of the launcher, this area forms a 90° sector of a circle as shown in Figure 5-1.

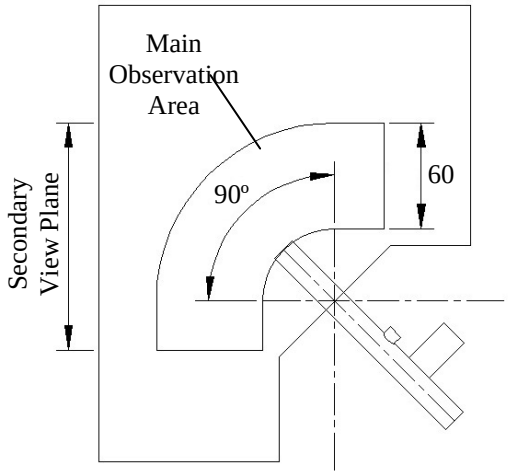

Figure 5-1 Observation area of the cell

The width of the secondary view plane, which is perpendicular to the main view plane, is considered the same (60mm); however, since the collision point occurs in different heights due to the rotation of the launcher, the height of the observation area at this plane will be almost equal to the height of the cell.

Given the size of the launcher, launcher rotation, observation area, connections, etc., the overall dimensions of the temperature cell structure were determined as 185mm×214mm×80mm. Figures 5-2 and 5-3 show the detail drawing of the cell. According to the compatibility assessment in Chapter 3, the body of the temperature cell is made of 6061-T6 aluminum alloy, which is supplied locally from the machine shop in the Department of Mechanical Engineering at the University of Alberta. However, as will be discussed in Section 5.2.3, four windows should be installed on all side walls for imaging and observation purposes.

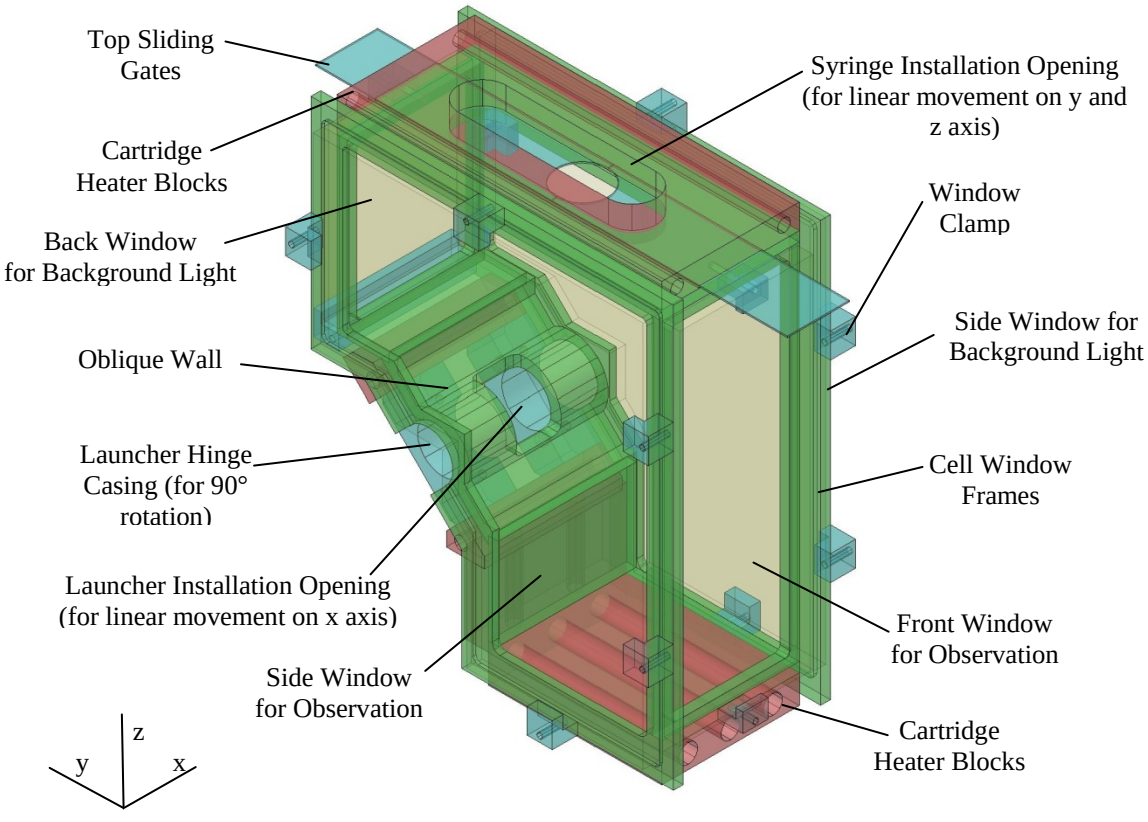

Figure 5-2 Cell configuration - View I

Although a 90° sector of a circle is enough as the observation area, due to the difficulties in making curved surfaces, especially in the glass, a decision was made to construct the entire side wall out of glass. The low conductivity coefficient of the glass compared to aluminum helps protect the cell from unwanted heat loss. The same condition was considered in thermal analysis and heat requirement calculations; that is, complete glass side walls were considered in the numerical analysis and calculations. The BK7-ESCO-USA optical glass was selected as window material (see Chapter 3). A water jet was used to cut the glass to the required shape. The window frames were provided in four sides of the cell and the glass was fixed to the frame using bolted clamps as shown in Figures 5-2 and 5-3. These bolted clamps in the windows provide required access to the inside of the cell. All the side windows can be used as access doors. The windows should be cleaned before running the experiments, and the consumed particles and oil drops should be removed from the cell after each set of experiments. The detail drawings of the window frames and glass are provided in Appendix C, drawing No. TC-001-01 and TC-002-01.

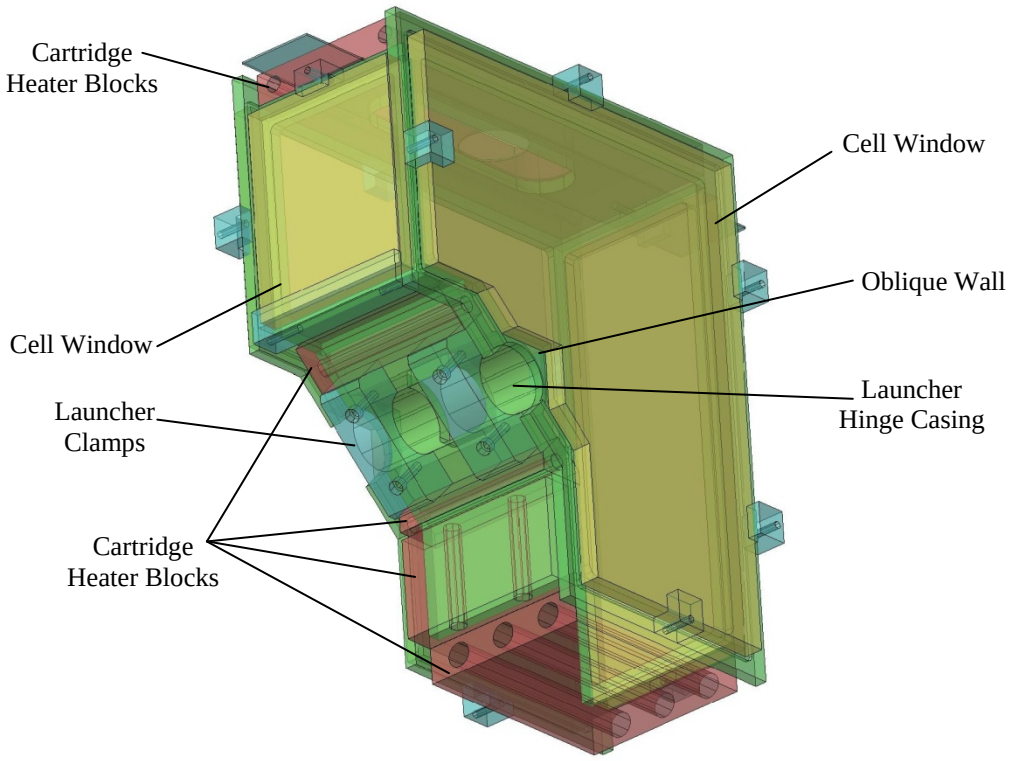

Figure 5-3 Cell configuration - View II

One of the most important parts in the cell is the oblique wall where the particle launcher is attached. This wall is designed as a special hinge casing to provide 90º rotation in the

particle launcher and to isolate completely the inside space of the cell from the surroundings. The launcher hinge core (Figure 5-6) is connected to this hinge casing by means of the launcher clamps (Figure 5-3). For maintenance and parts replacement, the launcher can be dismantled from the cell by unscrewing the clamps. Figure 5-2 shows, an opening on the oblique wall which provides an off-axis movement of the particle launcher to align the launcher tip with the drop generator tip or to facilitate off-axis collisions.

The top wall consists of a slot (Figure 5-2) to direct the drop generator into the cell. This 100mm-long slot provides the required movement of the drop generator on the y-axis for different collision point locations. Two sliding gates are located on the top wall to close the rest of the opening. These slides move while attached to the drop generator.

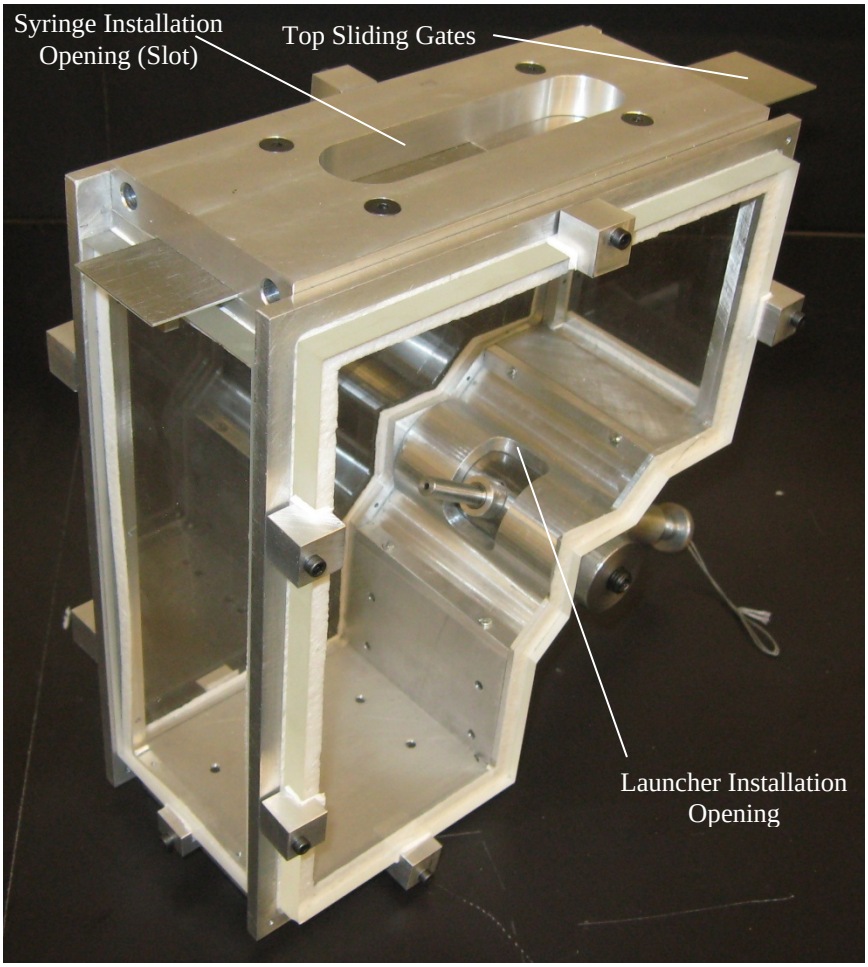

Figure 5-4 Constructed cell body- View I

Other walls are reserved to install the heaters; however, the dimensions of these walls and particle launcher diameter were carefully selected to prevent any overlap between the launcher and heater blocks in any directions. Drawing No. TC-003-01 in Appendix C provides the detail drawings of the cell aluminum walls. Section 5.2.1 contains an explanation of how the cartridge heaters were selected to heat the cell. To install the cartridge heaters, special heater blocks (Figure 5-5) were designed and attached to the allocated walls. Drawing No. TC-004-01 shows the details of the heater blocks and cartridge holes.

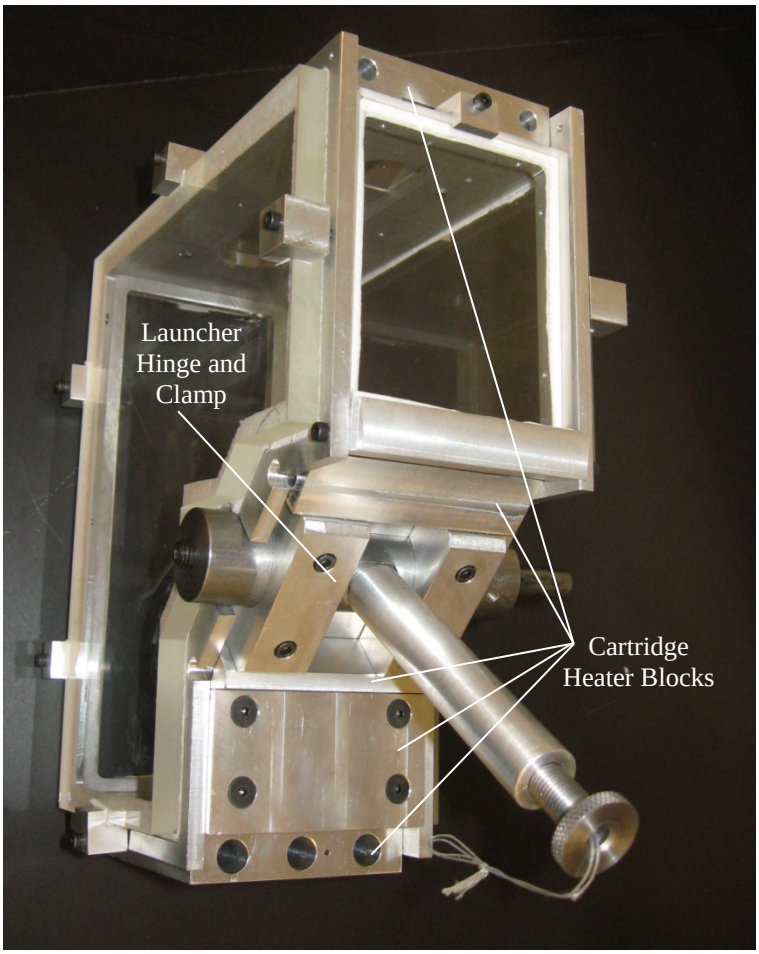

Figure 5-5 Constructed cell body- View II

To facilitate maintenance and repairs, all walls, heater blocks and clamps are fixed in position using joint screws. These bolted joints also compensate for the thermal expansion of jointed parts and prevent the cell from deformation. Drawing No. AD-003-

01 shows the steps of assembling the cell body. Figures 5-4 and 5-5 are photographs of the constructed cell.

5.1.2 Particle Launcher

Chapter 3 showed that the mechanical launcher is the most appropriate system for the setup. The launcher consists of a propellant and a feeding section as shown in Figure 5-6. The propellant comprises a plunger, spring, adjustment screw, cord and casing. The feeding part is made up of a particle feeding tube and particle barrel. The feeding parts are variable due to the size of the particles. All the parts are connected into a hinge core to be installed in the hinge casing shown in Figure 5-2. As an initial step, two particle launchers were built for 1mm and 2mm particles.

The velocity of the plunger and consequently the particle can be adjusted by pre-tensioning of the spring and/or by using the different springs (with different rates of stiffness). The plunger positioning cord holds the plunger in place behind the solenoid pin. The spring is adjusted to a definite pre-tension position by the adjustment screw.

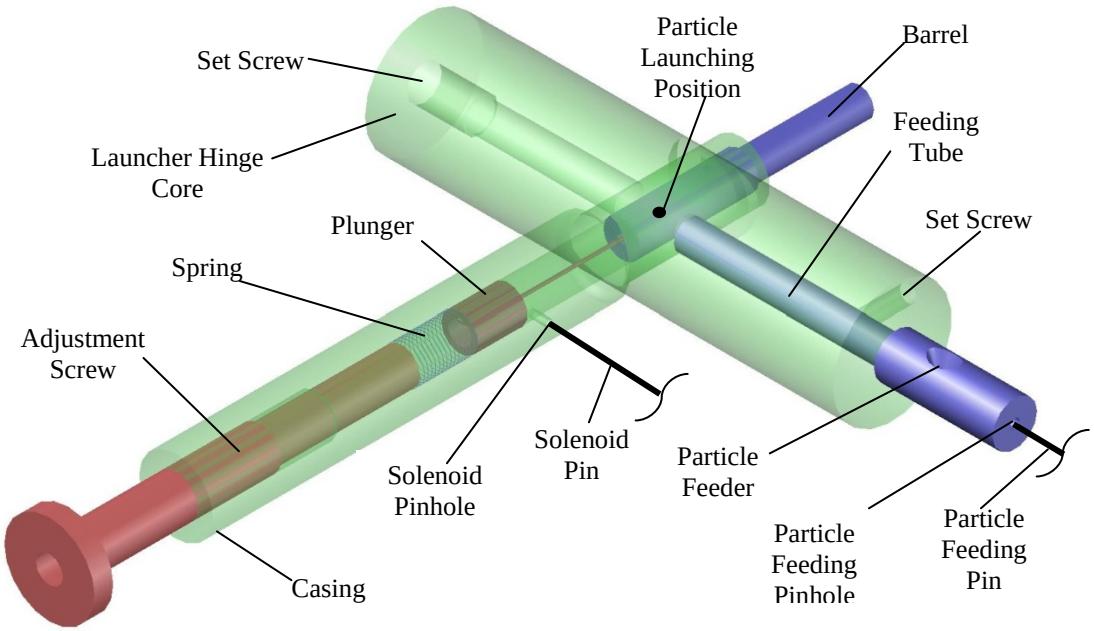

Figure 5-6 Particle launcher overall view

The particle is fed through the particle feeder hole at the launching position using the particle feeding pin (Figure 5-7). Once the solenoid pin is released, the particle is launched into the cell through the particle barrel tip.

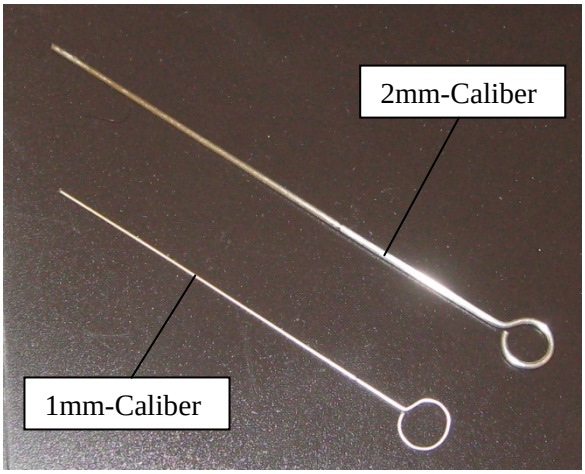

Figure 5-7 Particle feeding pins

Figures 5-8 and 5-9 show photographs of the constructed launcher parts. All launcher parts are made of 6061-T6 aluminum alloy; however, to prevent the moving parts from erosion, the hinge core, barrel, plunger and feeding tube were made of Steel-1018. Based on calculations in Section 4.4, different springs (with different rates of stiffness) are required for different velocities. Table A-17 in Appendix A tabulated a list of springs selected from Gardner Spring, Inc.-USA. The detail mechanical drawings of the particle launcher are provided in Appendix C, drawing No. AD-001-01 and PL-001-01.

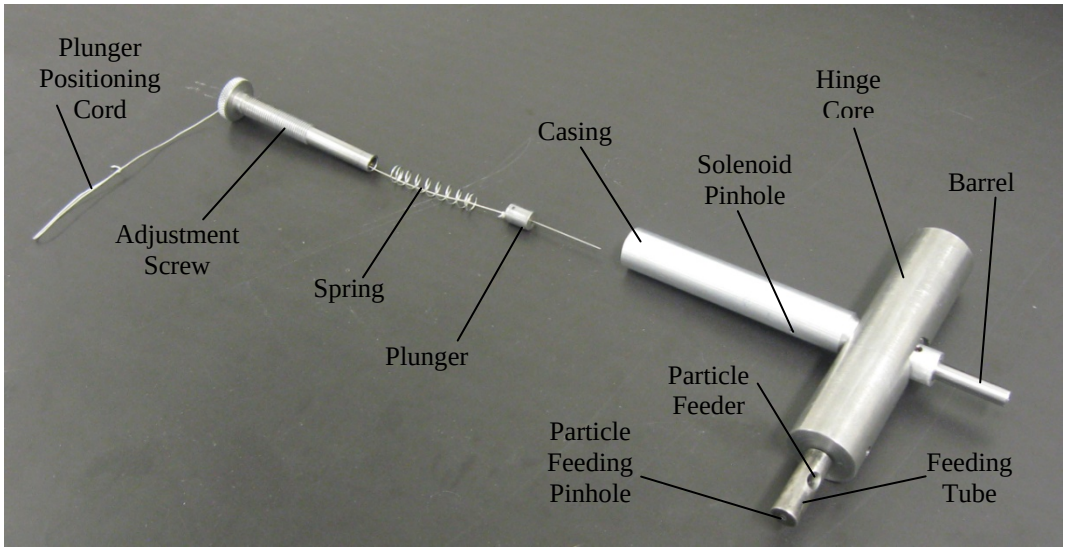

Figure 5-8 Constructed particle launcher-internals

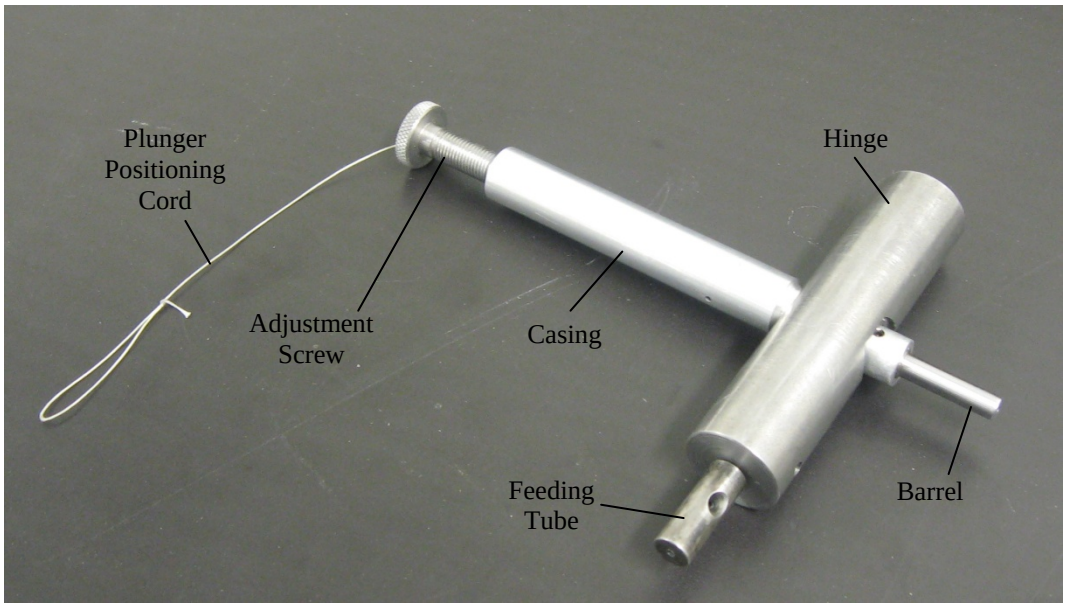

Figure 5-9 Constructed particle launcher

5.1.3 Drop Generator

In Chapter 3, a suitable stainless steel syringe was selected to work as the drop generator. The syringe was selected from among the syringe pump manufacturer's auxiliary products: 750 psi 20 ml. Stainless Steel Syringe with Luer-Lock and Chemraz O-ring - New Era - USA. This syringe comes with a luer-lock-type needle connection compatible with standard hub needles. The Chemraz o-rings replace the common Viton o-rings. The maximum operating temperature of the Chemraz o-rings is 260ºC which is higher than the cell operating temperature. The original plastic needle fixture nut was also replaced by a fabricated metal one to resist the high temperature. The syringe has the capacity to hold a large amount of fluid (20 ml) at high temperatures, which means that the operator does not have to keep filling it during the experiment.

Two metal hub needles were used and connected to the syringe to generate drops of 1.5mm and 1.2mm (NDL (27/2"/3) and NDL (33/2"/3) - Hamilton 91027-USA.) To generate different sizes of drops, different needle sizes can be used. According to Jiang et al. [13], the drop diameter is usually about twice the needle diameter. However, this scale will change for different drop fluids in different temperatures. Figure 5-10 shows the syringe and needle used in the setup.

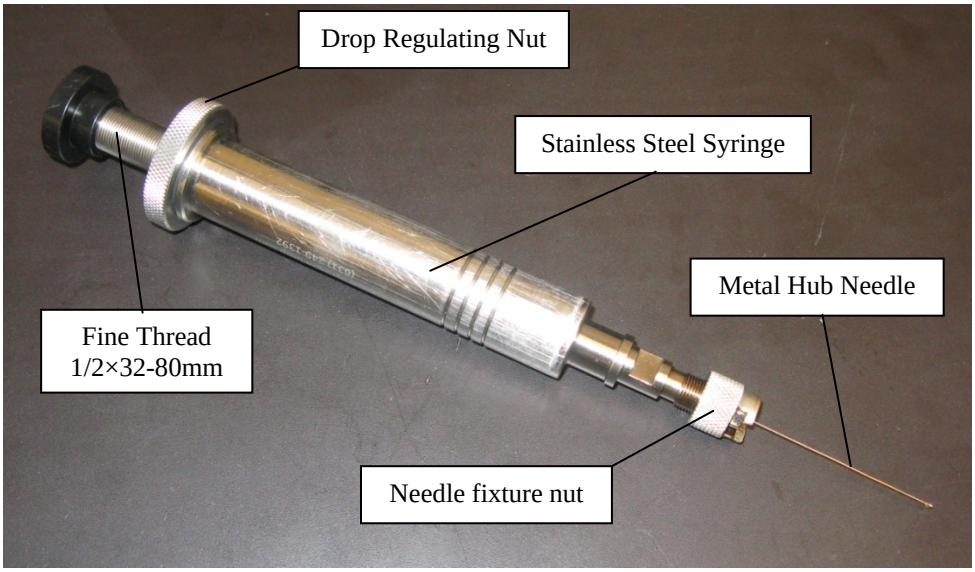

Figure 5-10 Drop generator
(Stainless steel syringe, metal hub needle, drop regulating nut)

To control the drop generation sequence, a regulating mechanism was added to the syringe. A fine thread of 1/2×32 was applied to the piston stem and a regulating nut with the same thread was fabricated and used as the motion controller. As shown in Figure 5-10, the nut is positioned at the top edge of the syringe cylinder and fixes the piston stem at its initial position, preventing the drops from dripping. To release the drop the nut is loosened, which allows the piston stem to move down. As the temperature rises, the fluid inside the syringe expands and the needle starts to drip. In this case, this regulating mechanism is crucial to control the sequence of the drop generation. The other advantage of using this regulating nut is to control the initial velocity of the drops.

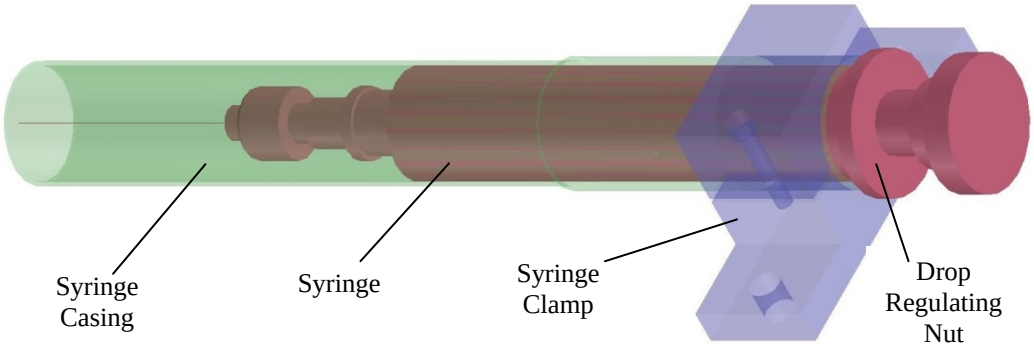

Figure 5-11 Drop generator overall view

The syringe is hung by a special clamp and support over the upper opening of the cell. A syringe casing is placed over the syringe body to connect the syringe into the interior space of the cell. This casing helps transfer the heat from the cell into the syringe through both convection and conduction. Figure 5-11 shows the assembled drop generator.

To generate drops with different velocities, the height of the syringe is adjusted with respect to the collision point by loosening the clamp around the syringe casing neck. The detail drawings of the casing and the clamp are shown in Appendix C drawing No. AD-002-01 and DG-001-01. As shown in these drawings, 6061-T6 aluminum alloy was selected for the syringe casing and clamp.

5.1.4 Temperature Cell Assembly

Figure 5-12 shows the temperature cell assembly including the temperature cell chamber, particle launcher and drop generator. The detail drawings of the assembled setup are provided in Appendix C, drawing No. AD-004-01.

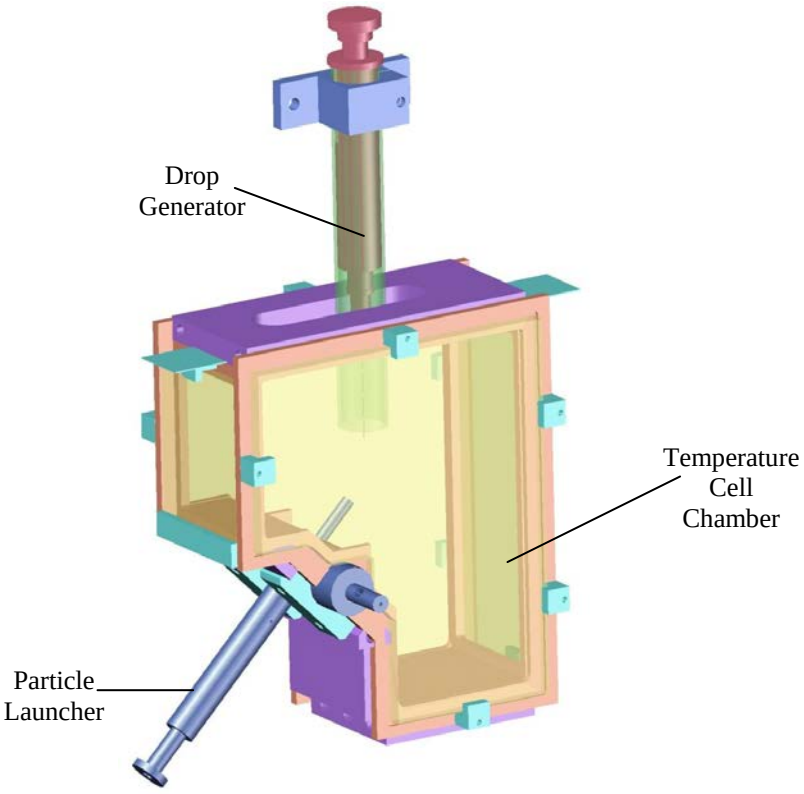

Figure 5-12 Temperature cell assembly

5.2 Auxiliary Parts

5.2.1 Heating System

To have a uniform heating system, the idea was to wrap the entire cell chamber with heat tracing; however, the operating temperature, energy requirement, cell configuration and glass walls put restrictions on using the electrical tracing heating system in this setup. According to the thermal analysis in Chapter 4, the walls of temperature cell must be heated to approximately 300°C. Although most of the electrical tracing cables work in lower temperatures, it is possible to find high temperature heating tapes with sufficiently high working temperatures. However, the installation procedures for these heating tapes prevent them from being used in this cell configuration. These heaters are designed to be installed completely attached to the surface without any gaps and overlaps, which makes them almost impossible to install on the temperature cell with sharp edges and corners. On the other hand, the amount of energy generated by these heaters is far less than what is required for the temperature cell. As an example, Omega Engineering Inc. supplies high temperature heating tapes which work up to 760°C; however, a tape of 25mm×2.5m generates only about 1250 Watts of energy which is about one-third of what is required.

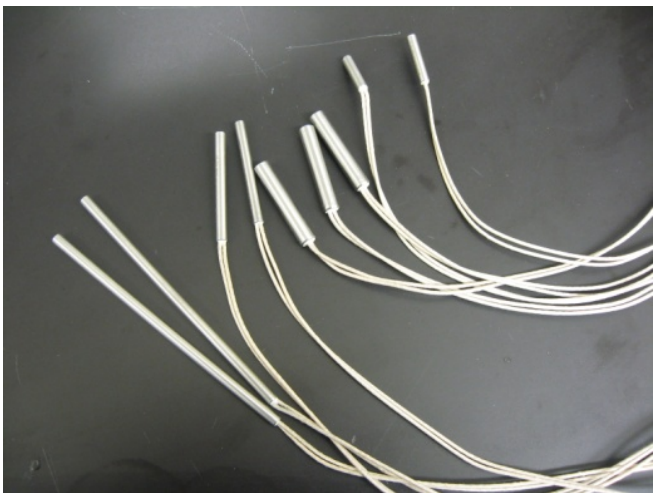

Figure 5-13 Cartridge heaters required to heat the chamber

The alternative approach is to use cartridge heaters. These heaters generate high energy and provide the high sheath temperature. By inserting the cartridges into heating blocks attached to the temperature cell walls, the heat will transfer through all aluminum walls into the cell. Figure 5-13 shows the cartridge heaters used in the setup. The wattage

capacity of the cartridges is determined based on the calculations in Section 4.4 and is listed in Table B-3. The cartridge heaters were selected from the CIR high watt density cartridge heater series from Chromalox-USA. The Incoloy Sheath provides a high operating temperature of 800ºC, which makes it possible to raise the temperature without damaging the heaters.

To ensure a more uniform temperature distribution, the heating blocks are installed on all aluminum walls as shown in Figure 5-14. A heat transfer compound (Anti-Seize Cartridge Heater Coating -850°C / Part No. CML00020 TEMPCO-USA) was applied to cartridge heater surfaces to increase thermal conductivity between the surfaces.

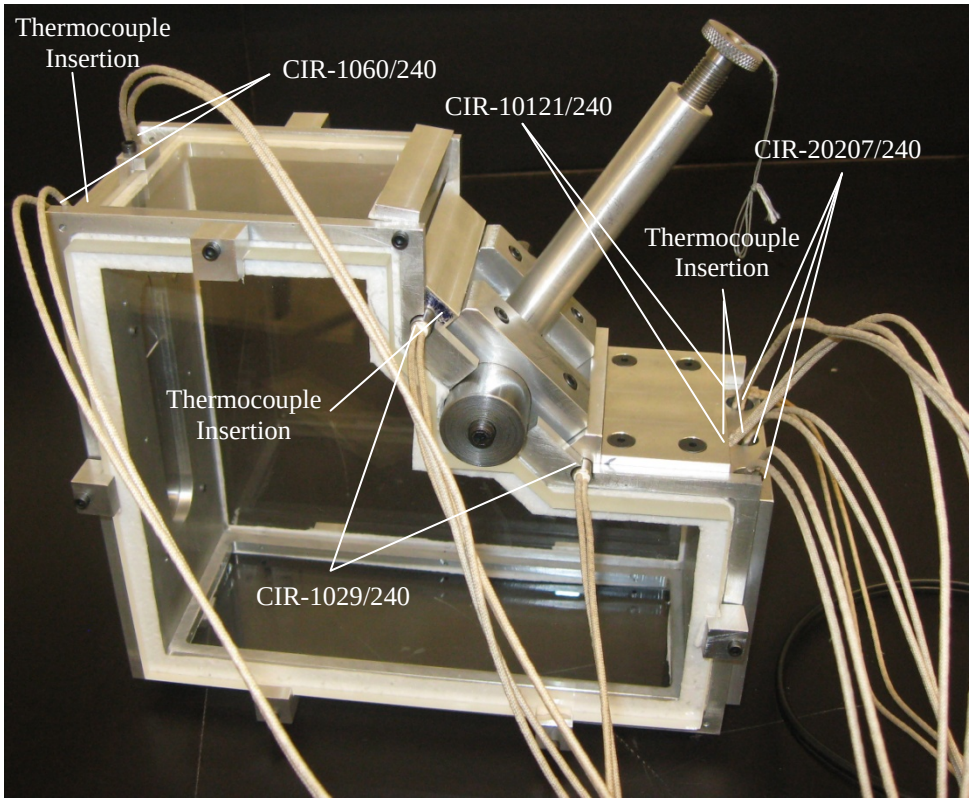

Figure 5-14 Cartridges heaters installed in heater blocks

The particles are heated inside the launcher core before launching and the drop temperature rises inside the syringe casing. Due to the small size of the drops and the particles they quickly reach equilibrium with the environment. Four thermocouple insertion holes are allocated on each heater block to be used for feedback temperature measurements to PID controllers or monitoring purposes.

The system is designed to reach the desired set point without insulation; however, to reduce the amount of heat loss, the top and bottom walls are covered with flexible ceramic insulation (Ultra High Temperature Rolls-8ibs/cu ft.- 1" - K=0.65 @ 800°F-McMaster-Carr-USA). Further flexible ceramic insulation (Extreme Temperature Rolls-1/16” - K= 0.71 @800°F-McMaster-Carr-USA) is located between the glass and aluminum window frames to protect the glass from the wall's extreme heat and to reduce the risk of breaking when attached directly to metal surfaces. For safety purposes, other parts should also be covered with insulation to provide the maximum temperature of 60ºC. Although all regulations and adjustments are done before heating the cell, safety gloves should be used during the experiments.

5.2.2 Control System

5.2.2.1 Heating Control System

Two Autotune PID temperature controllers are used to control the cell's temperature. The lower heaters are controlled by one controller and the upper heaters are controlled by the other. This provides the opportunity to control the temperature of different parts of the cell separately. Since the particles are heated inside the launcher hinge core, controlling the side heaters separately makes it possible to keep the temperature at the desired set point. The settings of the two controllers are shown in Table A-19. These settings were used for the performance tests and may vary in different experiments.

Two K-type thermocouple probes connected to a handheld thermometer are used to monitor the temperature of different surfaces to prevent the blocks from being excessively hot. Two other thermocouples are used to provide the controllers' feedback signals. However, by changing the feedback thermocouples' location, it is possible to manage the thermal energy generated by the heaters to reach the design temperature at each point. The arrangement of the thermocouples used in performance tests is shown in Figure 6-6 and the handheld thermometer can be seen in Figure 5-31. Figure 5-15 shows the heating control box. The diagram of the control circuit is provided in Appendix C, drawing No. EL-001-01, and the part list is tabulated in Table B-4 in Appendix B.

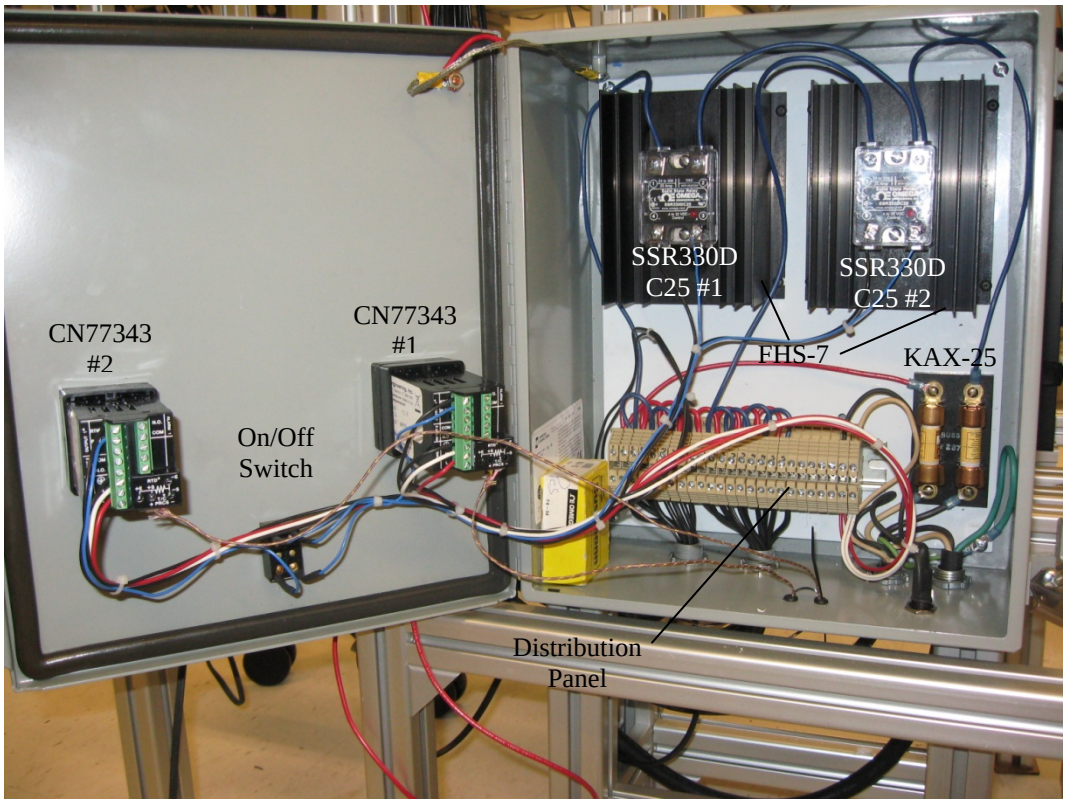

Figure 5-15 Heating control box

5.2.2.2 Triggering and Timing System

Since the collision occurs in a fraction of a second, a timing-triggering mechanism is required to synchronize the particle launcher with the drop generator. Figure 5-16 shows a simple diagram of the triggering/timing system which consists of a laser module (LTG-Apinex-USA), photo transducer, triggering/timing control box and solenoid (527-1009-ND-Pontiac Coil Inc-USA). Figure 5-17 shows an overall view of the elements of the triggering system for the setup. The photo transducer and triggering dot laser are located aligned with respect to each other in two opposite sides of the cell (Figure 5-19). A fabricated solenoid pin (Figure 5-18) is attached to the solenoid core to be positioned in the solenoid pinhole of the particle launcher (Figure 5-6). The solenoid pin is used as the launcher trigger.

The laser is aimed at the transducer through the temperature cell. Once the drop is released from the drop generator, the laser beam is disrupted and a signal is transferred via the timing control box to the solenoid. Depending on the delay set point, the solenoid releases the plunger by removing the solenoid pin from the solenoid pinhole as shown

schematically in Figure 5-6. The electrical circuit of the triggering/timing control system is shown in Appendix C, drawing No. EL-002-01.

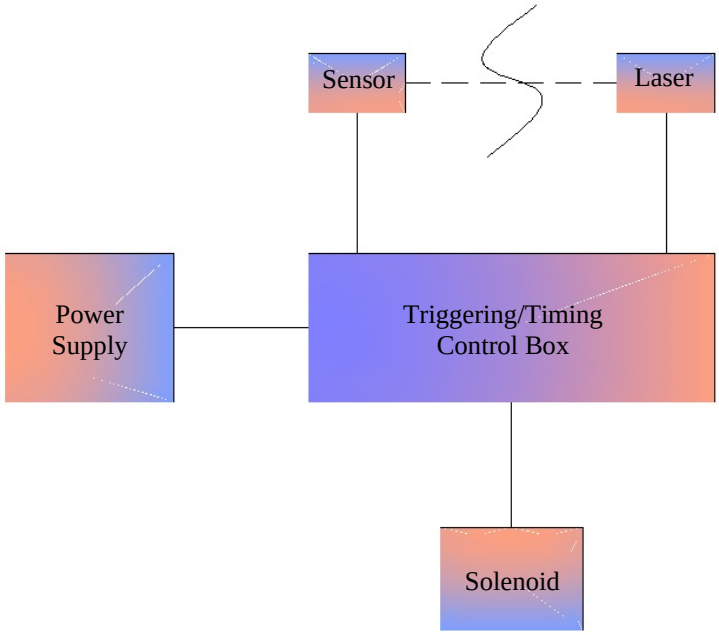

Figure 5-16 Schematic diagram of the triggering/timing control system

The connections of the triggering-timing control box are shown in Figure 5-20. There are two 3V and one 5V input connections for lasers at the back: one for the triggering laser, one for the alignment laser and one for reserve. Two other ports are allocated for testing purposes. One (delay time port) can be connected to an oscilloscope to monitor the delay signals and the other is used to connect to a triggering signal (trig in port). The solenoid and power supply connection ports are located in the front. The control box was connected to a power supply of Max 25V shown in Figure 5-21.

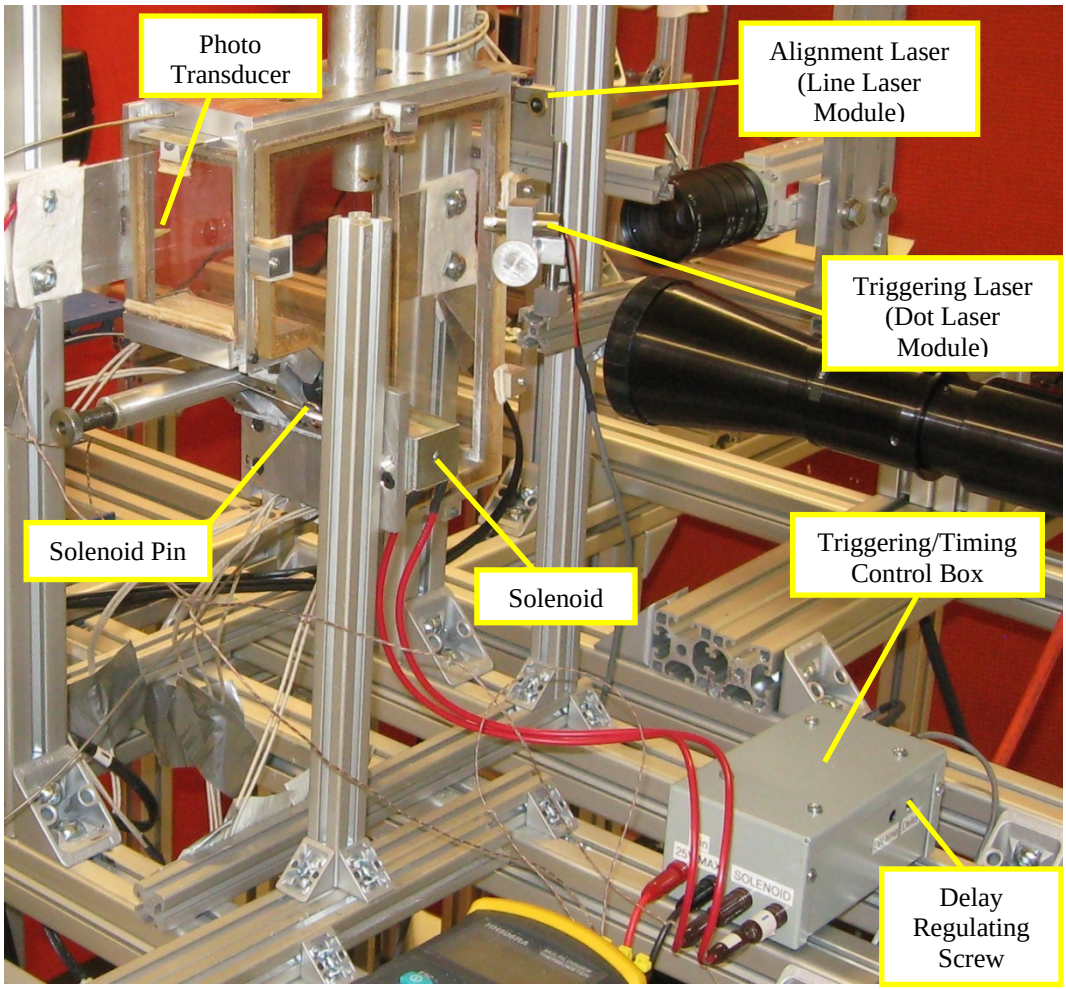

Figure 5-17 Triggering system
(lasers, solenoid, photo transducer, triggering/timing control box)

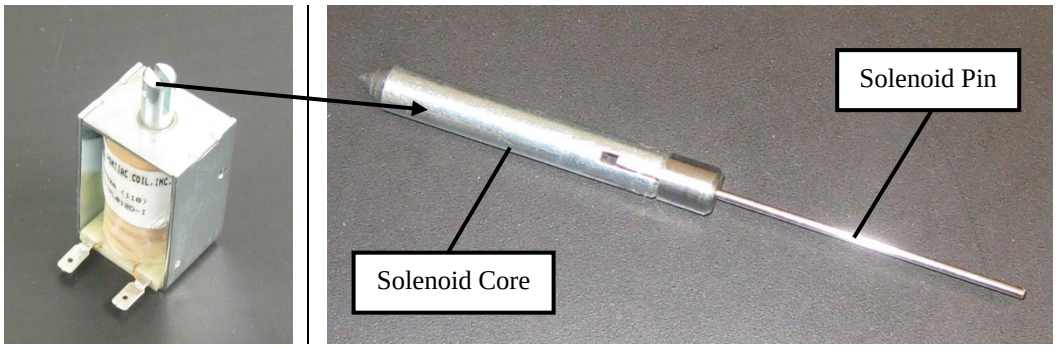

Figure 5-18 Left: solenoid / Right: solenoid core and solenoid pin

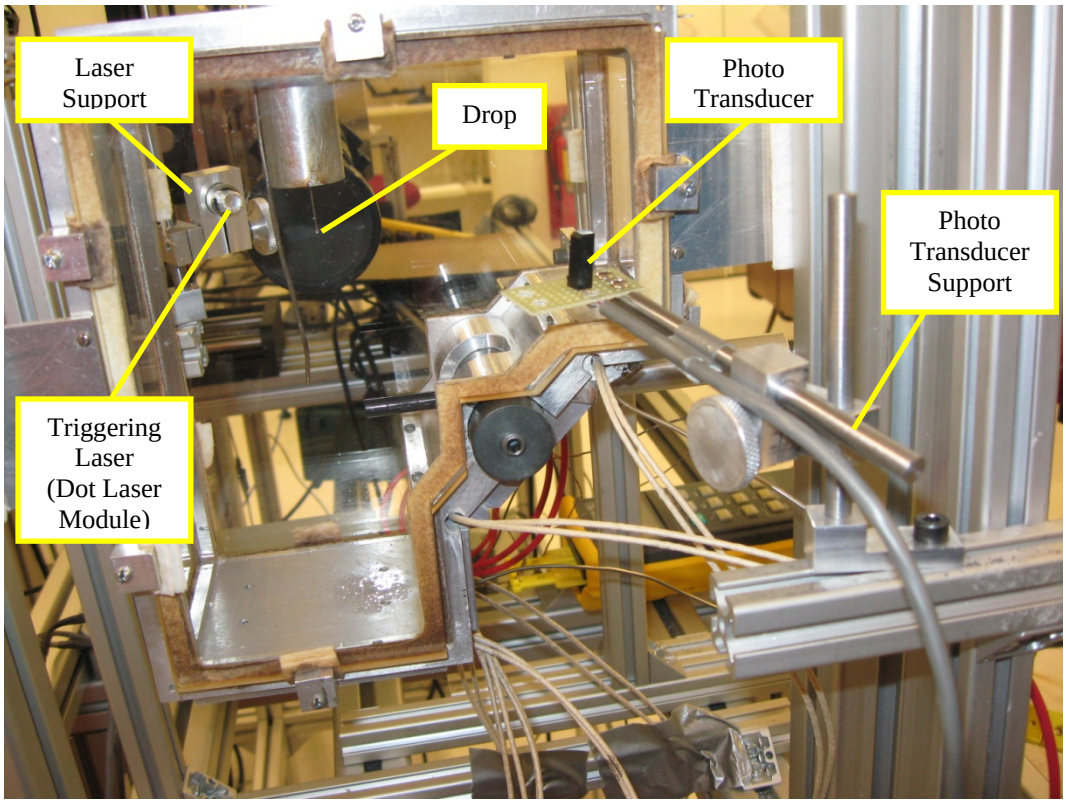

Figure 5-19 Triggering system arrangement (dot laser diode and photo transducer)

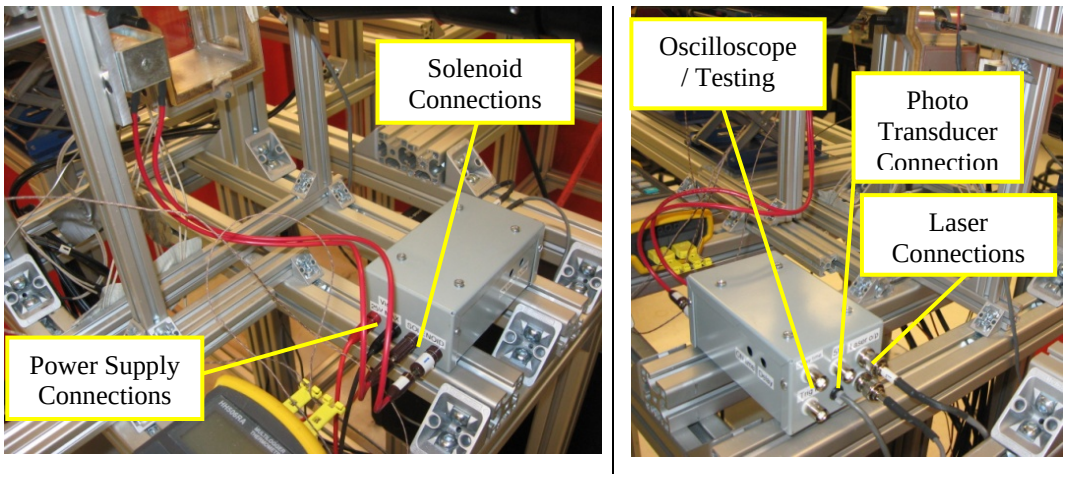

Figure 5-20 Triggering/timing control box connections

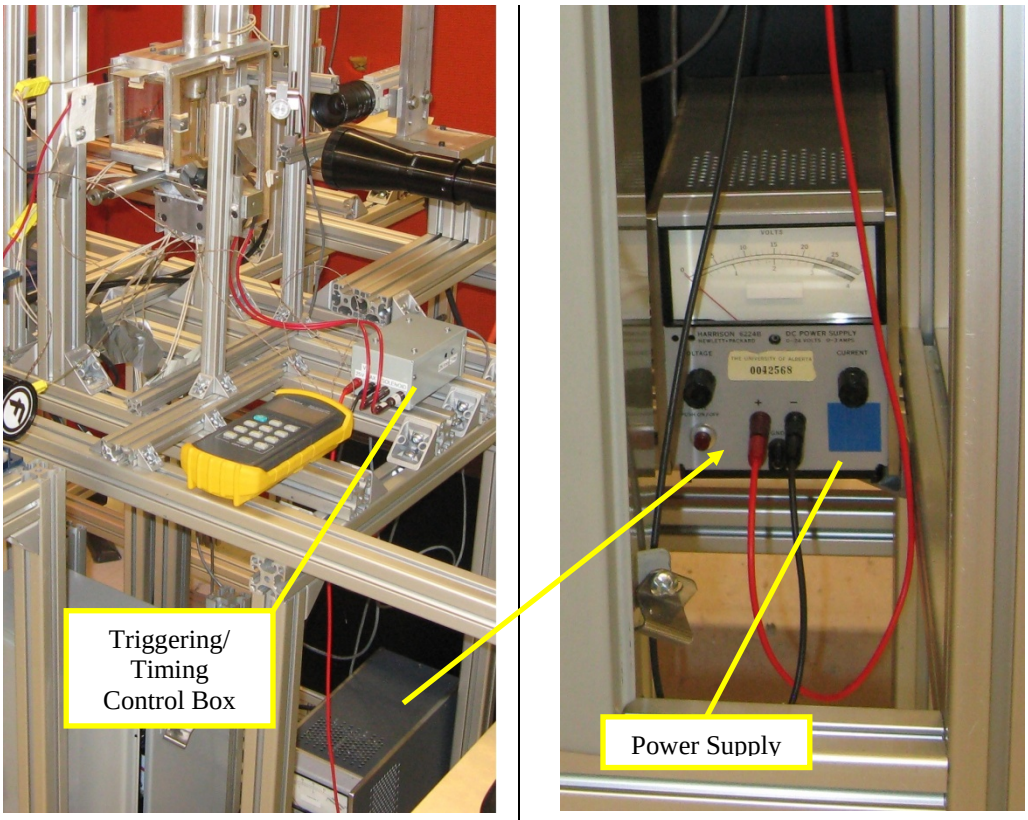

Figure 5-21 Triggering/timing control System
Left: upper deck (lasers, photo transducer, solenoid, control box) Right: lower deck (power supply)

5.2.3 Optical System

5.2.3.1 Photography

As mentioned in Section 3.3.4, due to the size and velocity of the particles and drops, the shadowgraph technique with the high-speed camera is suitable in the imaging system. Two windows are required for each view plane. The light source is located at one window providing the background light. The high-speed camera is located at the opposite window to capture the videos. Since the collision phenomenon is observed from two view planes, it is necessary to have four windows in two perpendicular planes. The main camera is located towards the side windows and the auxiliary camera will cover the phenomenon form the front/back view. The main camera is equipped with high magnifying lens and all the measurements will be conducted using the video frames captured by this camera. The auxiliary camera is used to view the off-axis deformations and interaction of the drop and particle after collision. Figure 5-22 represents the photography system used in the setup.

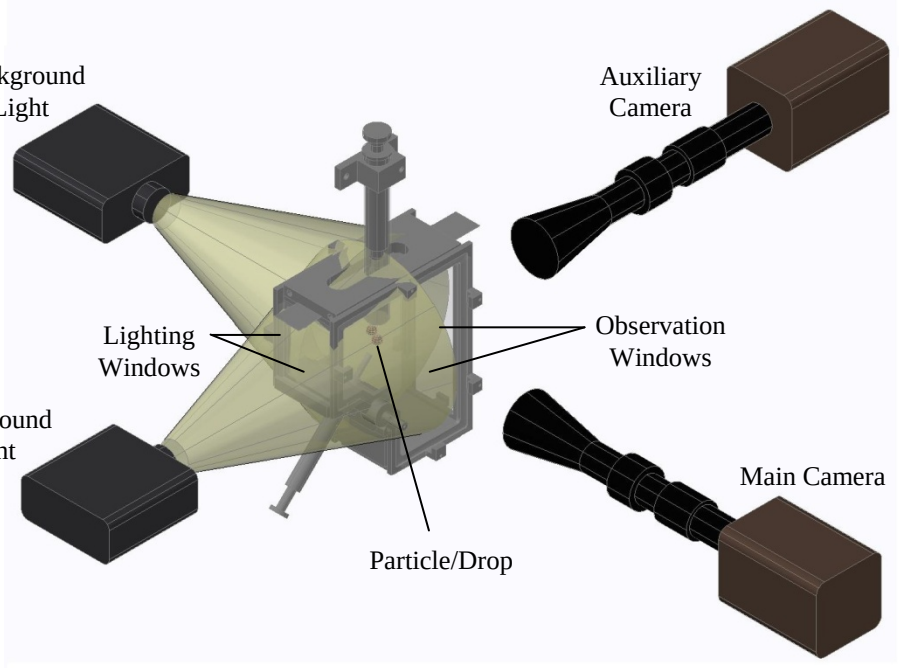

Figure 5-22 Double-plane shadowgraph technique

The cameras are manually triggered by the imaging software (Phantom Camera Control / Vision Research Inc. Version: 9.0.649.0-C PhCon:649) right before the drop is released from the syringe. Due to the rotation of the launcher, collisions occur in different parts of the cell; therefore, a mechanical mechanism was employed to relocate the cameras to the desired position. The required parameters are measured using the imaging software based on the video frames.

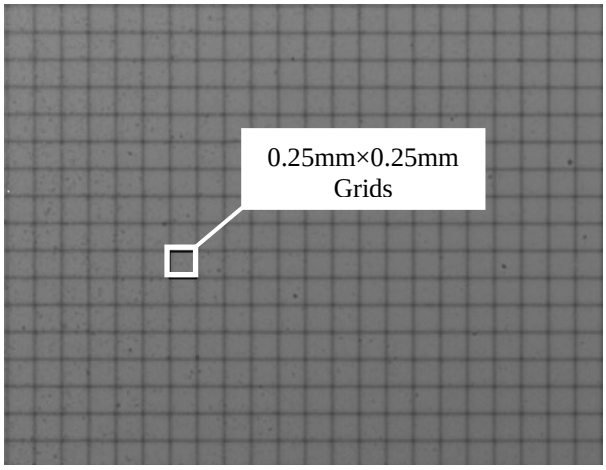

Figure 5-23 Calibration grid

5.2.3.2 Calibration

The size and velocity of the particles and drops and angle of collision are the parameters which should be measured using the video frames. The pattern of collision outcomes also needs to be analyzed qualitatively. The camera was calibrated in two ways: linear measurement and image sharpness. For the linear measurement calibration, a calibration grid was used for each set of experiments.

The calibration grid (Figure 5-23) was aligned with the launcher tip and the syringe needle. The photograph taken from this grid was used to find the conversion factor of pixels to mm, since all the measurements done in the imaging software were in pixel units. The aberration and barrel/pincushion distortions can also be checked by this calibration grid. The sharpness of the images was checked visually using a needle the same size as the particle and the drop.

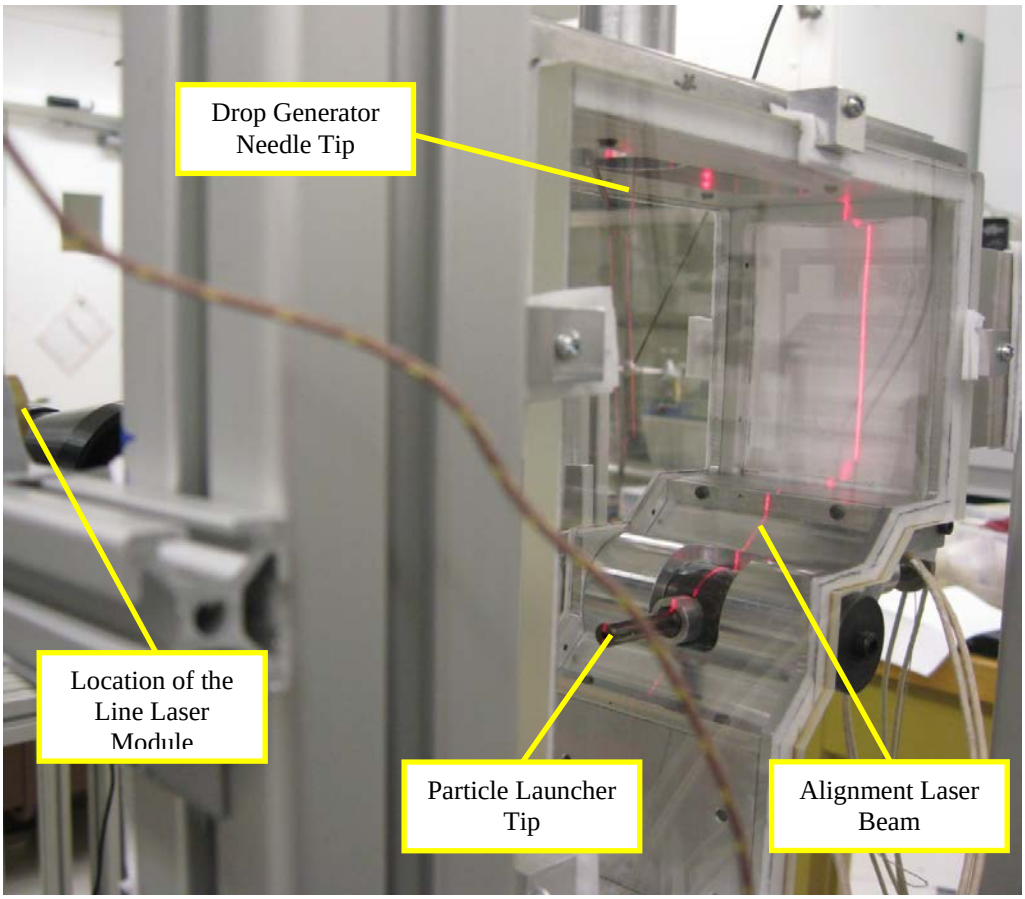

Figure 5-24 Alignment laser beam

5.2.3.3 Alignment

To align the launcher tip with the syringe needle tip, a line laser module was aimed at the cell from the back lighting window. A sliding support was used to clear the laser module out of the lighting window during the experiment. This alignment laser was also used to locate the calibration grid in the right position before starting the experiments. Figure 5-24 shows the laser beam emitted from the alignment line laser which passed through the needle tip and the launcher tip.

5.3 Setup Assembly

The temperature cell assembly introduced in Section 5.1.4, was mounted on a table structure as shown in Figure 5-25. As seen in this picture, the cell was bolted on two columns by two brackets. The tracks on the columns allowed the entire cell assembly to move in the vertical direction to adjust the cell height relative to the structure table. The syringe was mounted by a clamp onto a separate support structure. As shown by the arrows in Figure 5-25, the syringe's supporting structure provides three degrees of freedom to the syringe relative to the cell.

Figures 5-26 and 5-28 show the solenoid mounted on another vertical column. This column was bolted by brackets onto a horizontal track. The latter was also fastened to another horizontal track which was perpendicular to it. The arrows in Figure 5-26 show the three degrees of freedom in motion provided by the solenoid's supporting system with respect to the cell. This makes it possible to adjust the solenoid pin with the solenoid pinhole on the launcher. The same supporting mechanism was used to trigger the laser (Figure 5-26) and the photo transducer (Figure 5-27). Special fabricated clamps [99] were used to mount the triggering laser and the photo transducer on their support structures. These clamps provided the triggering laser and the photo transducer with six degrees of freedom in motion; three linear and three rotational as shown in Figures 5-28 and 5-29. These six degrees of freedom are essential for aligning the laser simultaneously with the needle tip and photo transducer. Three linear and one rotational degrees of freedom were provided by the support system for the alignment laser (Figure 5-29). The two high-speed cameras were also mounted on three-DOF supporting mechanisms. Figures 5-30 to 5-32 show the entire setup mounted on the table structure, including cameras, background lights, control boxes, computer, etc.

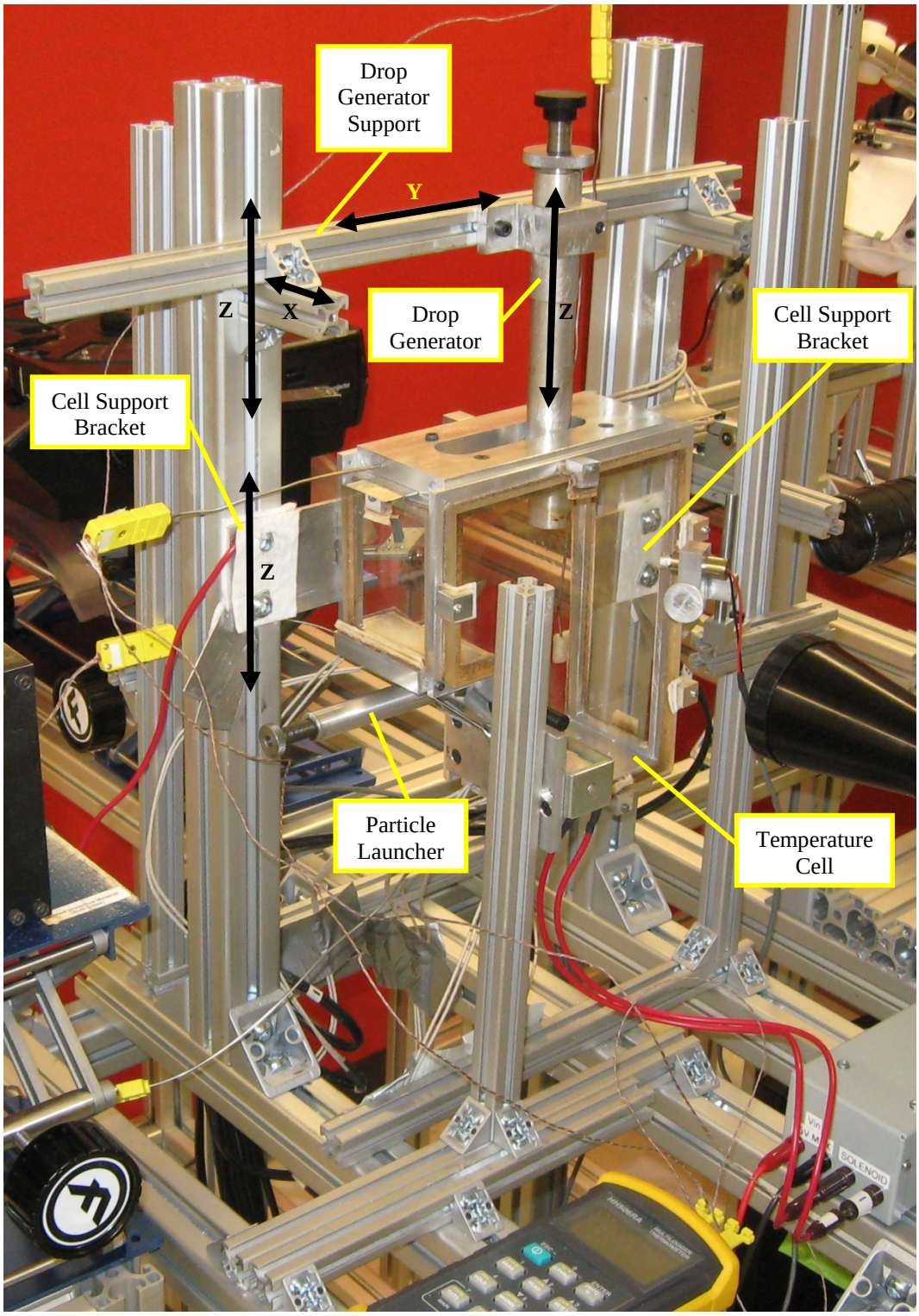

Figure 5-25 The temperature cell assembly mount
Arrows show the 3 DOF for the drop generator with respect to the cell and also a 1 DOF for the temperature cell with respect to the main table structure.

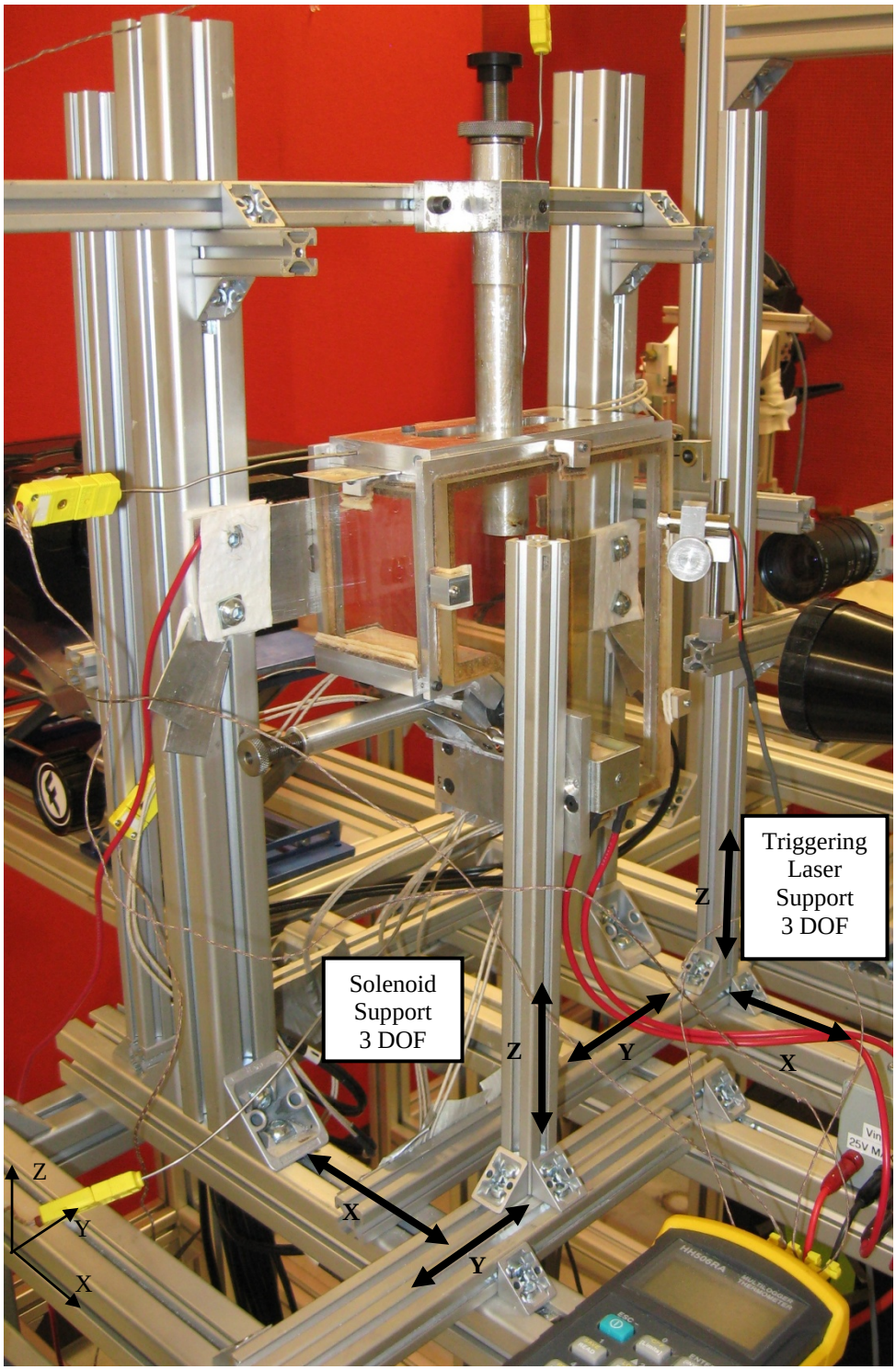

Figure 5-26 Solenoid and triggering laser supporting
Supports allow 3D linear positioning of the laser and the solenoid as indicated by the arrows

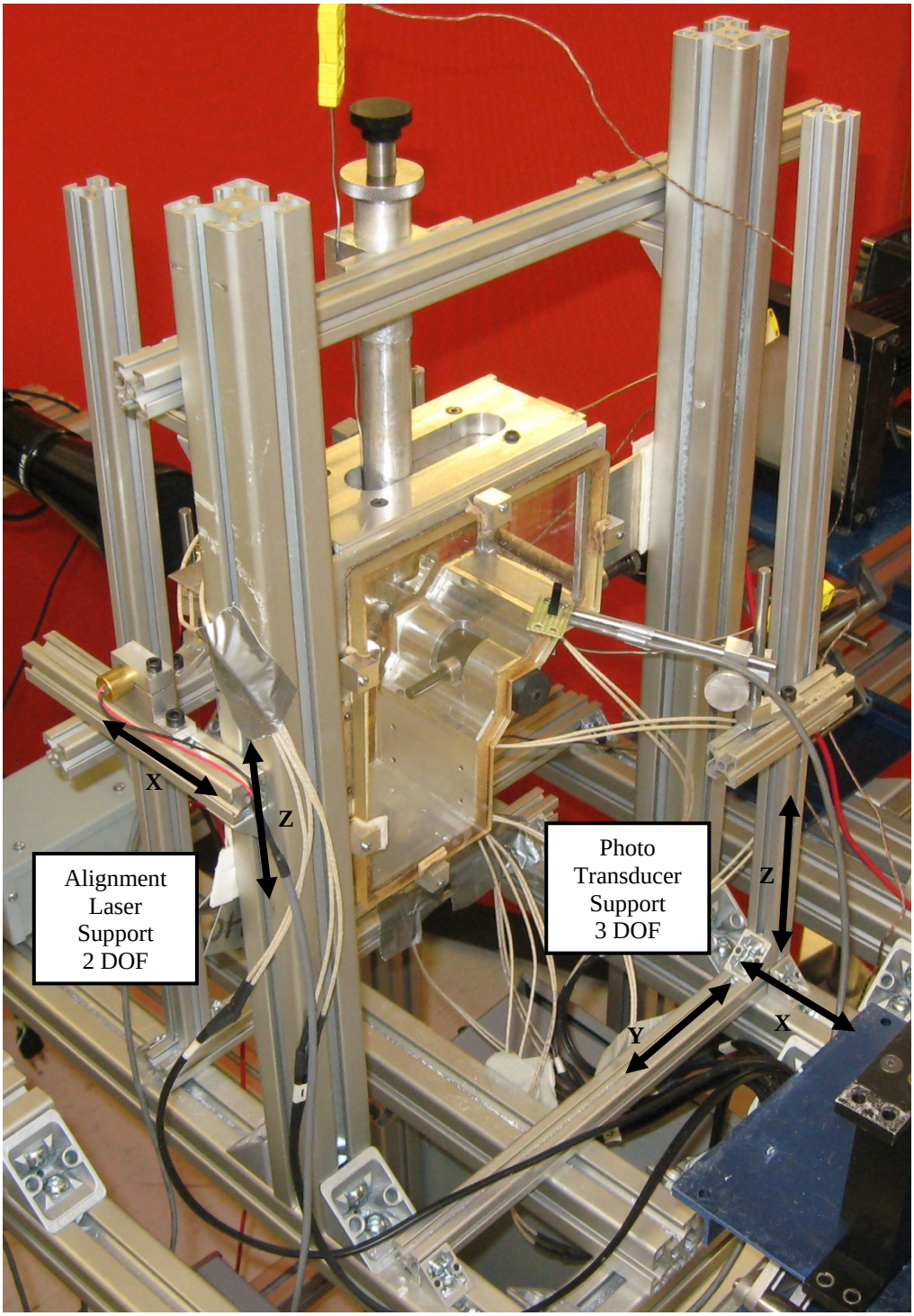

Figure 5-27 Alignment laser and photo transducer supporting
Supports allow linear positioning for the laser and photo transducer as indicated by the arrows

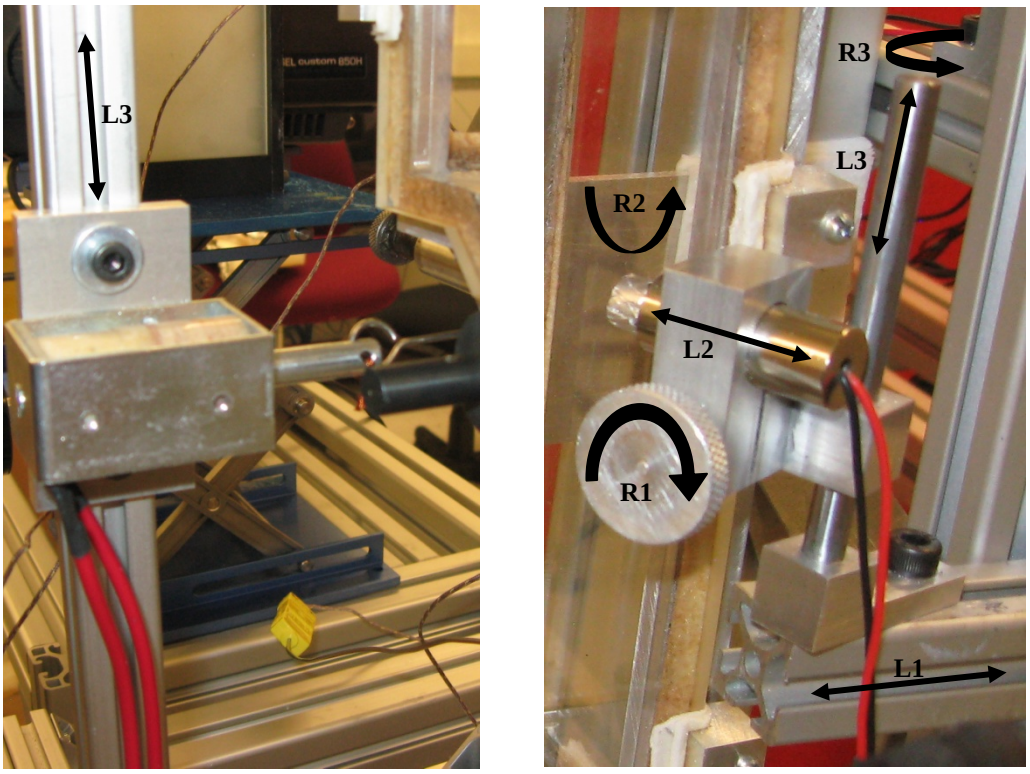

Figure 5-28 Alignment and support mechanism of the triggering/timing instruments
Left: solenoid clamp (1 degree of freedom)/ Right: triggering laser clamp (6 degrees of freedom)

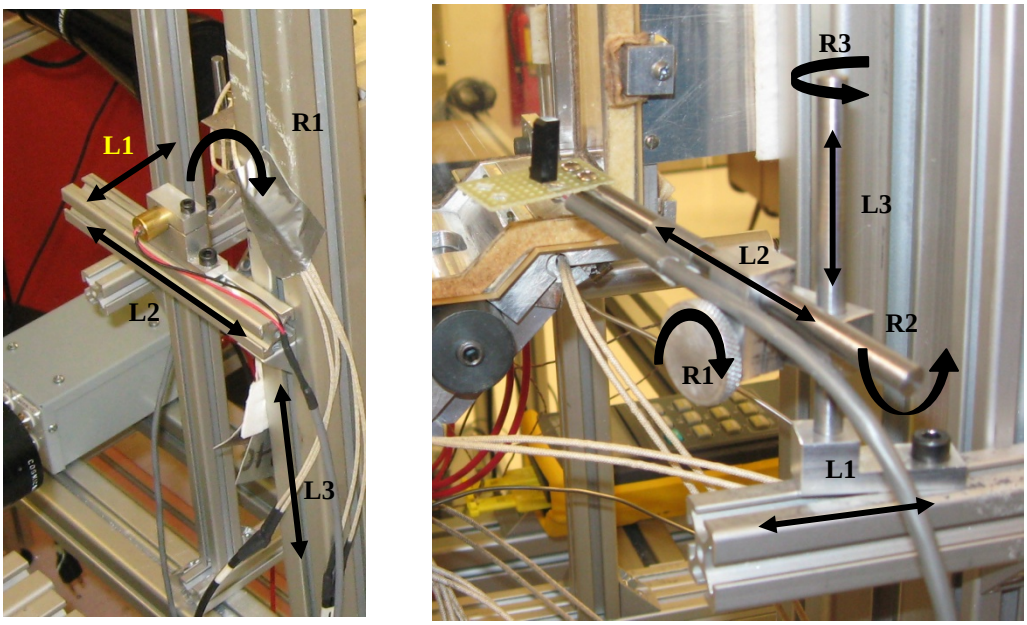

Figure 5-29 Alignment and support mechanism of the triggering/timing instruments
Left: alignment laser clamp (3 degree of freedom)/ Right: photo transducer clamp (6 degrees of freedom)

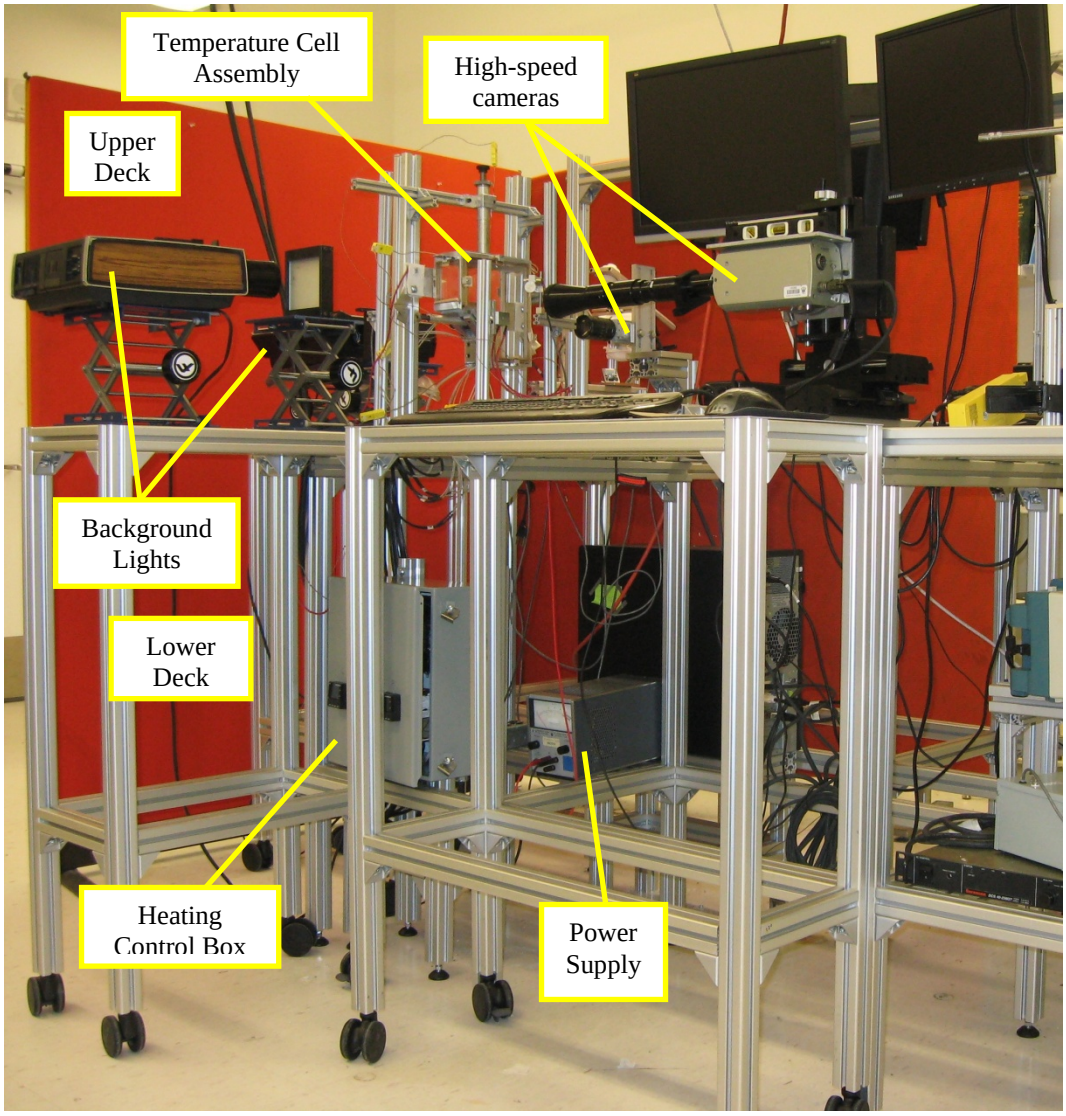

Figure 5-30 Setup assembly general view

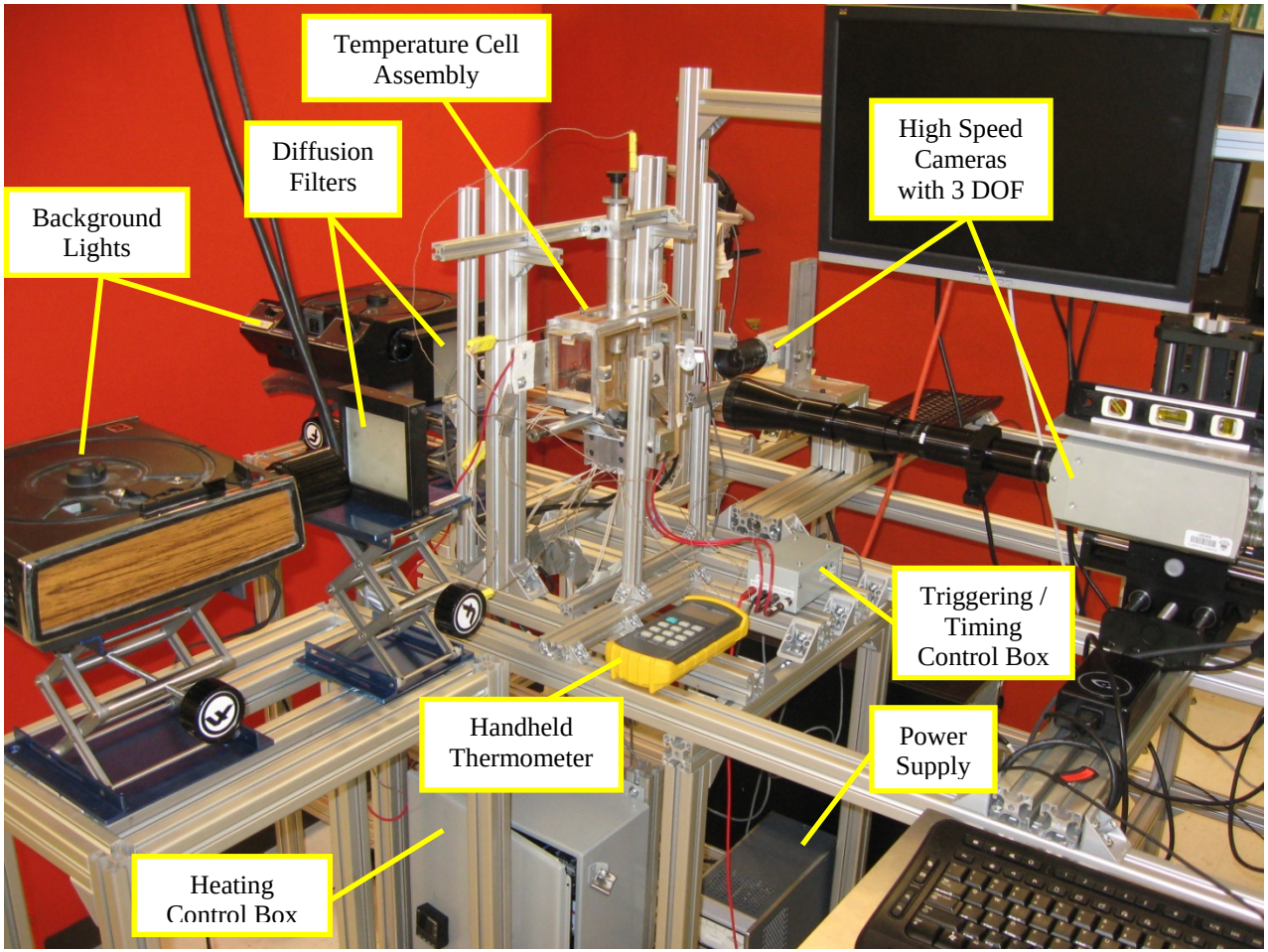

Figure 5-31 Setup assembly upper deck- view-I

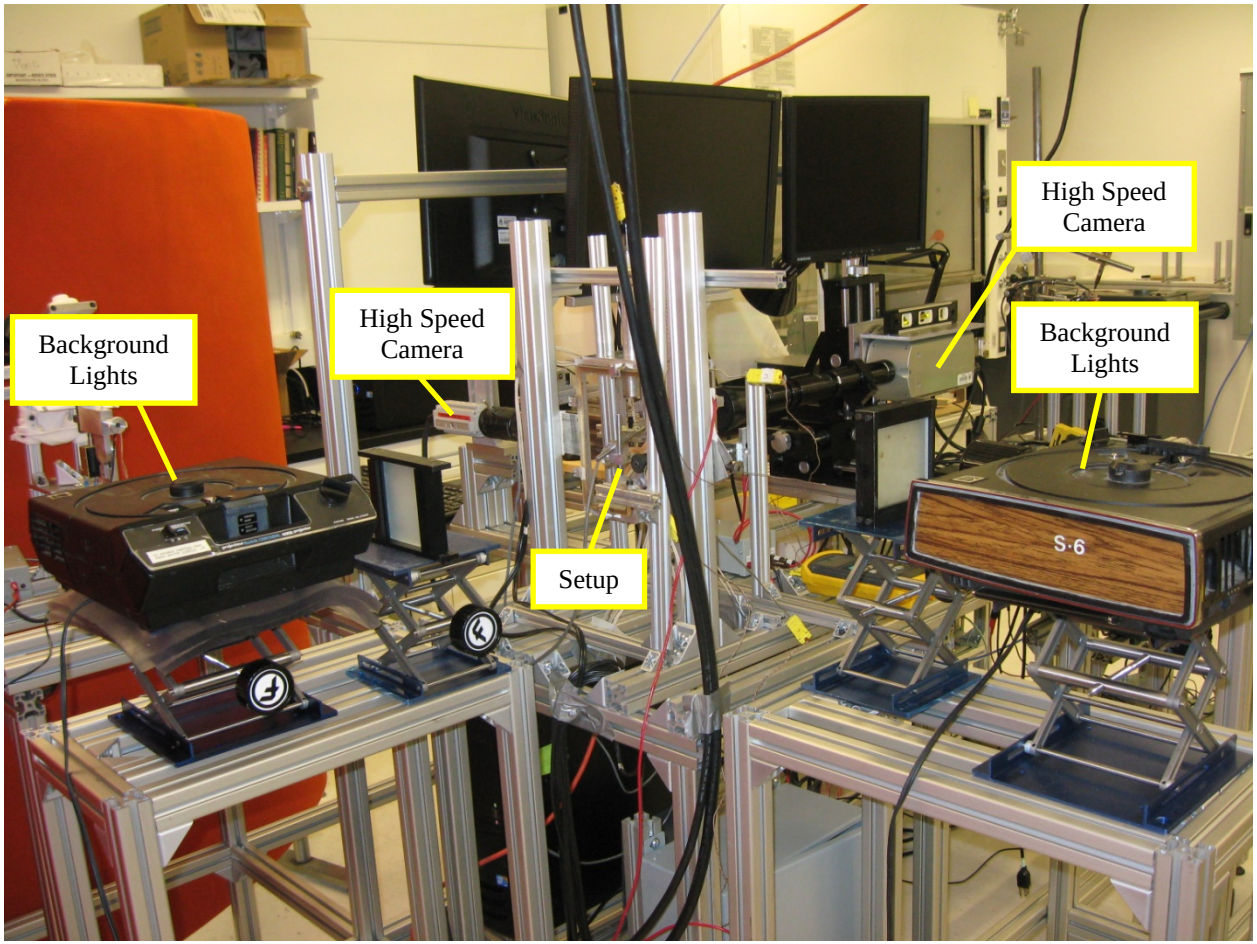

Figure 5-32 Setup assembly upper deck- view-II

5.4 Operation

The following operation procedure is provided as a guideline for the experiments; however, researchers can devise their own procedures to work with the device.

- Open the access door (one of the side windows)
- Collect and remove all consumed particles.
- Clean the chamber, windows, launcher, tools, etc. The cleaning agent selected should be appropriate to clean the test liquid used. The ideal choice would be a solvent that works on the test liquid but will not corrode the aluminum surface. For instance, ethanol and acetone showed promising results for the test liquid (Duratherm S) in performance tests and are not erosive to aluminum surfaces.
- Fill the syringe and fasten the regulating nut to prevent the needle from dripping
- Position the syringe into the syringe clamp
- Position the alignment laser (make sure that the background lights are off)
- Align the launcher tip with syringe needle and adjust the angle of the launcher
- Position the cameras and lights, focus the lenses and turn the cameras on
- Calibrate the imaging system: locate the calibration grid in the same plane of the launcher tip, perpendicular to the main camera, and take the calibration photograph (align the grid with the alignment laser)
- Check the sharpness of the image by taking the image of a needle (the needle should be the same size as the particle and the drop)
- Remove the alignment laser and calibration grid
- Mount the drop-collecting funnel to the position
- Close the access door (the previous steps required the access door to be opened)
- Align the triggering laser with the photo transducer and needle tip
- Cover the photo transducer by the light shield and test the triggering system
- Insert the stroke reducing spacers on launcher plunger if required
- Apply anti-seizing grease to the launcher adjustment screw (a copper-based anti-seizing grease was used in the performance tests)
- Adjust the pre-tension of the launcher's spring using the adjustment screw
- Set the triggering/ timing controller (set the delay)

- Relocate the solenoid to align the solenoid pin with the solenoid pinhole on the launcher
- Locate the thermocouples to the assigned positions
- Check the cartridge heaters for location and the heat transfer compound (it is necessary to apply heat transfer compound to all cartridge heaters before installation)
- Cover the upper and bottom walls of the cell with insulation
- Program the PID controller. The settings and programming of the controllers are provided in the manufacturer's manual; however, the settings used in performance tests are represented in Table A-19.
- Turn the heating system on
- Start the experiment only when the cell reaches the steady-state condition
- Position the plunger in place behind the solenoid pin using the plunger positioning cord and the solenoid pin
- Load the particle: insert a particle into the particle feeder hole, push it to the launching position using the particle feeding pin
- Use the imaging software to start the cameras
- Release the drop using the drop-regulating nut (When the drop is released, the laser beam is cut and the photo transducer sends a signal to the triggering/timing control box, which triggers the solenoid. By releasing the solenoid pin, the particle is released from the launcher tip and collides with the drop at the collision point)
- Stop the cameras

The following hints should be taken into account while working with the experimental device:

- The bolted joints need to be checked frequently and treated with anti-seizing grease; it is important to apply the anti-seizing grease to the spring adjustment screw before heating the device.
- To prevent the syringe from dripping during the heating phase, it is important to check it and fasten its regulating nut while the temperature is rising.

- When connecting the heaters to the controllers, it is important to connect the side and bottom heaters to one controller; otherwise, the high conductivity of the aluminum raises the temperature of the neighbor block over its set point and prevents the adjacent heaters from turning on.
- Since the spring stiffness varies at high temperatures, it is recommended to calibrate the velocities at high temperatures before starting the experiment.

Chapter 6
Performance Test

When the construction phase was completed, a performance test was conducted on the experimental device. First, the individual mechanisms (i.e., mechanical parts, heating system and triggering/timing) were tested for functionality, and then several collision tests were conducted on the entire device. A silicon base heat transfer liquid (Duratherm S- Duratherm- USA) and glass beads (Soda Lime Duke Stds 91000 and 92000 Series-Fisher Scientific-USA) were used as the test liquid and particles, respectively. The results provided in this chapter are based on more than 200 experiments run by the temperature cell designed and built as part of this thesis.

6.1 Mechanical Parts

The calculations in Section 4.2.4 made it possible to estimate the required velocities which would be covered by the setup. The drop generator and the 2mm-caliber and 1mm-caliber launchers were tested in the high temperature (200 ºC) environment to meet these required velocities. Table 6-1 lists one set of possible velocity combinations in extreme conditions.

Table 6-1 Velocity limits for performance test in head-on and right-angled collisions

Collision Condition	Drop Size (mm)	V (Drop) (m/s)	V (Particle) (m/s)	$V_{Rltv.}$ (m/s)
Head-On	1	0.60	0.30	0.90
	1	0.60	5.50	6.10
	2	0.40	0.25	0.65
	2	0.60	3.70	4.30
Right-Angled	1	0.50	0.80	0.94
	1	0.60	6.00	6.03
	2	0.45	0.45	0.64
	2	0.70	4.20	4.26

The horizontal position was selected to find the velocity limits in both launchers due to the constant horizontal velocity after the particle was launched. The velocity was controlled in three ways: by changing the spring stiffness, changing the spring pre-tension, and/or changing the plunger stroke. Since the temperature affects the spring stiffness, it is important to calibrate the velocities at the high temperatures before starting the collision tests to avoid excessive trial and error.

The spring stiffness was changed using three different springs: R1 (a shop-wound spring using stainless steel wire [type-304] spring back, .014" dia, 1/4-lb coil, 475' coil [9495K57-McMaster-CARR-USA]- Free length=26mm, OD=7mm, Pitch=4mm), R2 (36353G from Table A-17) and R3 (36371G from Table A-17). Different spacers were designed to reduce the stroke of the plunger and consequently the speed of the particles in lower velocities. These spacers reduce the stroke of plunger attached to the particle; that is, by inserting the appropriate spacer in front of the plunger the plunger moves a shorter distance along with the particle. Hence, the particle starts to move without propellant force. The spacers used in the performance tests are shown in Figure 6-1. Finally, the adjustment screw was used to change the pre-tension of the springs to achieve the desired velocity. An important step in working with the particle launcher at the high temperature is to apply copper anti-seizing grease to the bolted joints, especially the spring adjustment screw.

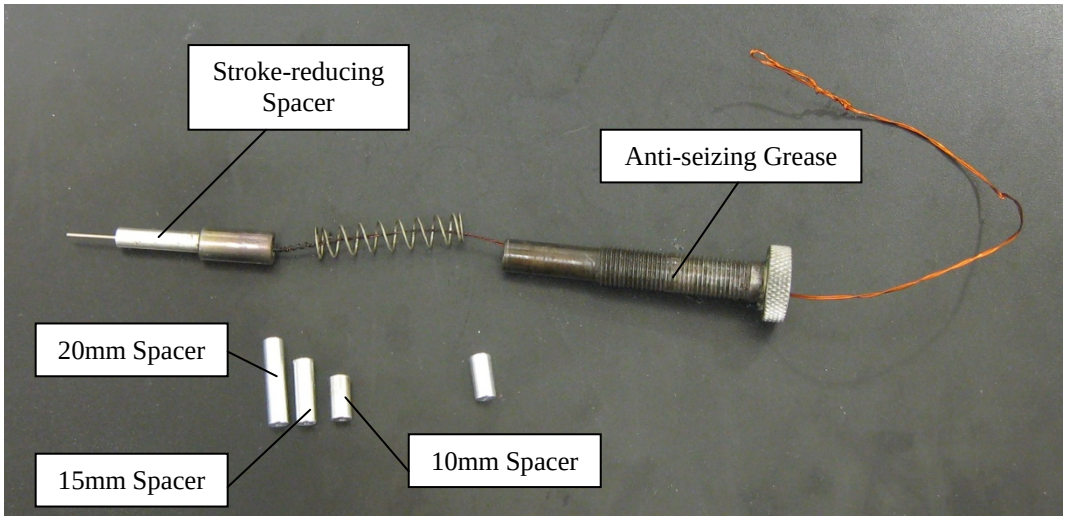

Figure 6-1 Stroke-reducing spacers and anti-seize grease applied on threaded area

The lowest and the highest velocities achieved in the performance tests for each launcher are listed in Table 6-2. It is necessary to mention here that this is only a limited velocity calibration to determine the velocity limits. A full velocity calibration can be performed the same way concerning the experimental requirements. The velocities can be increased by using a stronger spring; however, the performance tests were limited to the calculated velocities.

Table 6-2 Velocity limits in 2mm-caliber and 1mm-caliber particle launchers in 200 ºC in horizontal position
(The sample standard deviation is used in this table)

Launcher	Number of Tests	Spring	Spacer	Pre-tension (mm)	Mean Velocity (m/s)	Standard Deviation
1mm-Caliber	3	R1	20mm	40	0.55	0.05
1mm-Caliber	3	R2	No	30	11.35	0.12
2mm-Caliber	3	R2	15mm	38	0.54	0.11
2mm-Caliber	3	R3	No	38	6.28	0.2

The drop generator was tested in two ways: first, regulating the drop generator to release single drops at the high temperature, and then testing the minimum distance to produce stable drops. Because the fluid expands at high temperatures, it is necessary to design a mechanism to compensate for that expansion and prevent the syringe from dripping. A regulating nut and a fine thread were added to the syringe piston handle to apply an upward force to the syringe piston and stop the fluid from dripping (Figure 5-10). This nut should be fastened gradually as the temperature increases. When the cell reaches the steady-state condition, stable drops will be generated by gently unscrewing this nut.

Considering the minimum distance required for drops to become stable and sufficient space clearance from top walls for triggering system, the velocity of drops varies between 0.5m/s and 1.4 m/s for right-angled collisions and between 0.5m/s and 1m/s for head-on collisions.

6.2 Heating System

The cartridge heaters mentioned in Section 5.2.1 are connected to two PID temperature controllers. Different combinations of heater connections to the controllers and the feedback thermocouple locations were tested. The idea was to find the most efficient

combination which leads to required heat distribution while keeping the heater temperatures at the lowest temperature possible.

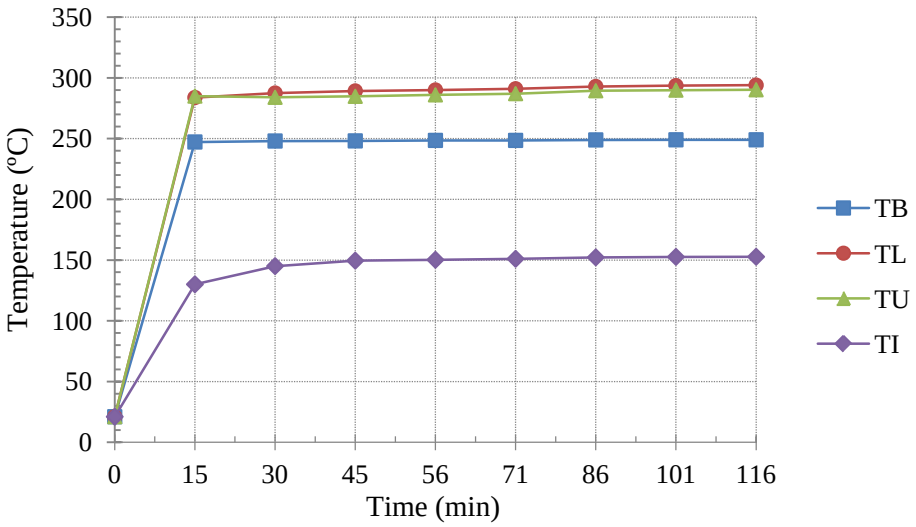

Figure 6-2 Temperature versus time at different locations by 250 ºC and 300 ºC set point
TB: Temp. at bottom heater block, TL: Temp. at launcher heater block, TU: Temp. at top heater block, TI: Temp. inside the cell close to the launcher tip in horizontal position,
Bottom and side heaters set point: 250 ºC
Top and launcher heaters set point: 300 ºC
Temp. inside the particle launcher after two hours: 208 ºC
Temp. at side heater blocks after two hours: 223 ºC

By changing the wires in the distribution panel in the heating control box (Figure 5-15), it is possible to connect different groups of heaters to one controller. It is important to connect side and bottom heaters to one controller; otherwise, due to the high conductivity of aluminum blocks, the heat transferred from one block to the other raises the temperature of the neighbor over the set point and prevents the heaters from turning on. The suitable configuration is connecting the side and bottom heaters to one controller, and the top and launcher heaters to the other one. In this case the feedback thermocouples are connected to the bottom and launcher heater blocks for each controller. The temperatures of other parts were measured by a handheld thermometer with two thermocouple connections. The handheld and controller feedback thermometers were calibrated using the ice and water mixture. The controller settings and heater configurations are presented in Appendix A, Tables A-19 and A-20. Figures 6-2 and 6-3 show the temperature variation in different locations of the temperature cell in two

sample tests. Figure 6-2 shows the temperature variation within two hours with relatively lower set points, while Figure 6-3 shows the temperature variation corresponding to higher set points, which results in the required design temperature. If one defines the steady-state condition as the time when the temperature variation of a particular location is less than 2 ºC. It can be deduced from Figures 6-2 and 6-3 that the steady state condition is achieved after almost one hour.

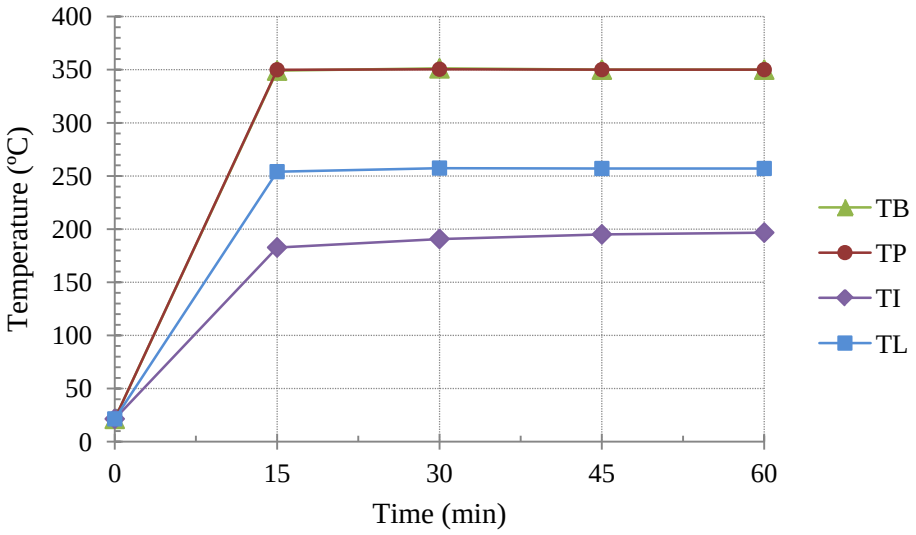

Figure 6-3 Temperature versus time at different locations by 350 ºC set point
TB: Temp. at bottom heater block, TP: Temp. at launcher heater block, TI: Temp. inside the cell close to the launcher tip in horizontal position, TL: Temp. inside the particle launcher
Bottom and side heaters set point: 350 ºC
Top and launcher heaters set point: 350 ºC
Top heater block temperature after one hour: 315 ºC

As mentioned earlier, different configurations are possible for the heaters, thermocouples and controller connections. One of the possibilities is to locate the feedback thermocouples inside the temperature cell to measure the temperature of the experimental area. In this configuration the temperature of the area reaches the required value within minutes and the initial temperature of the heater blocks exceeds the calculated values; however, it is essential to monitor the temperature of all blocks so that the heaters do not become excessively hot. Figure 6-4 shows the temperature measured in three points, in three positions close to the launcher tip.

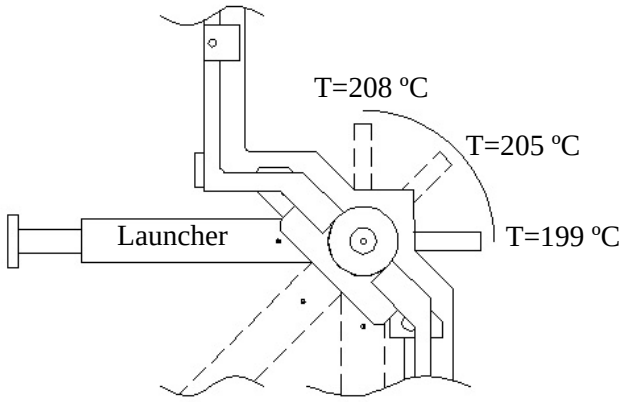

Figure 6-4 Steady state temperature close to launcher tip in three positions

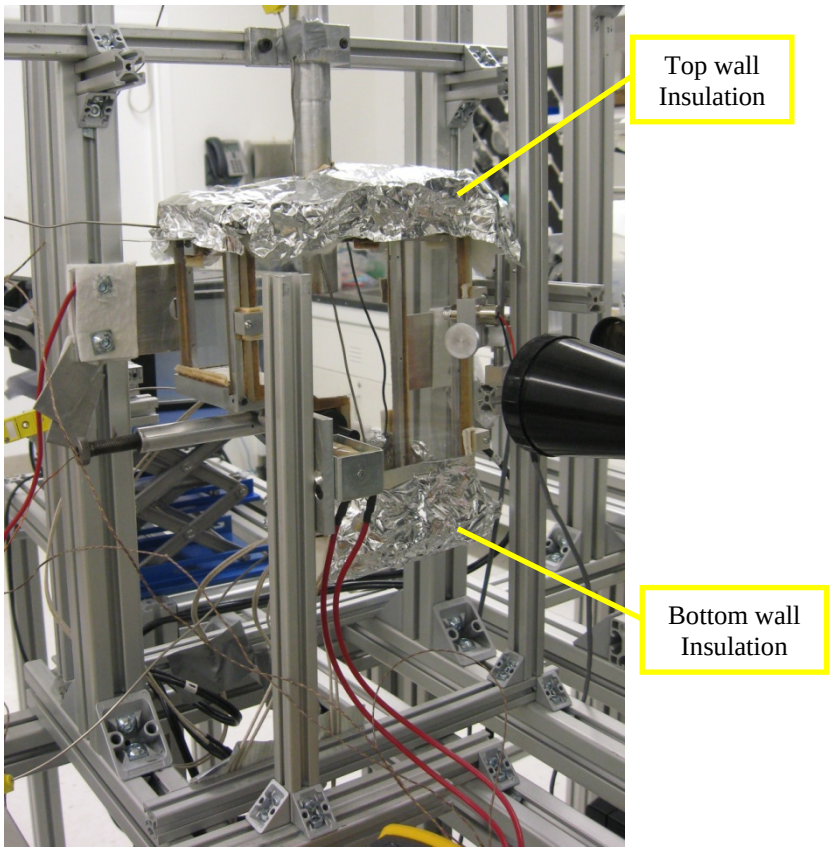

Figure 6-5 Insulations applied on top and bottom heater blocks

To avoid monitoring the temperature in the heater blocks, the configuration described in Table A-20 and Figure 6-3 was selected to conduct the performance tests. The top and the

bottom walls were covered by insulation (Ultra High Temperature Rolls-8ibs/cu ft.- 1" - K=0.65 @ 800°F- McMaster-Carr-USA) (Figure 6-5). During the performance tests, the side wall and the launcher area were uncovered. However, for the operator's safety it is recommended to cover all metal parts with insulation (Extreme Temperature Rolls- 1/16” - K= 0.71 @800°F-McMaster-Carr-USA).

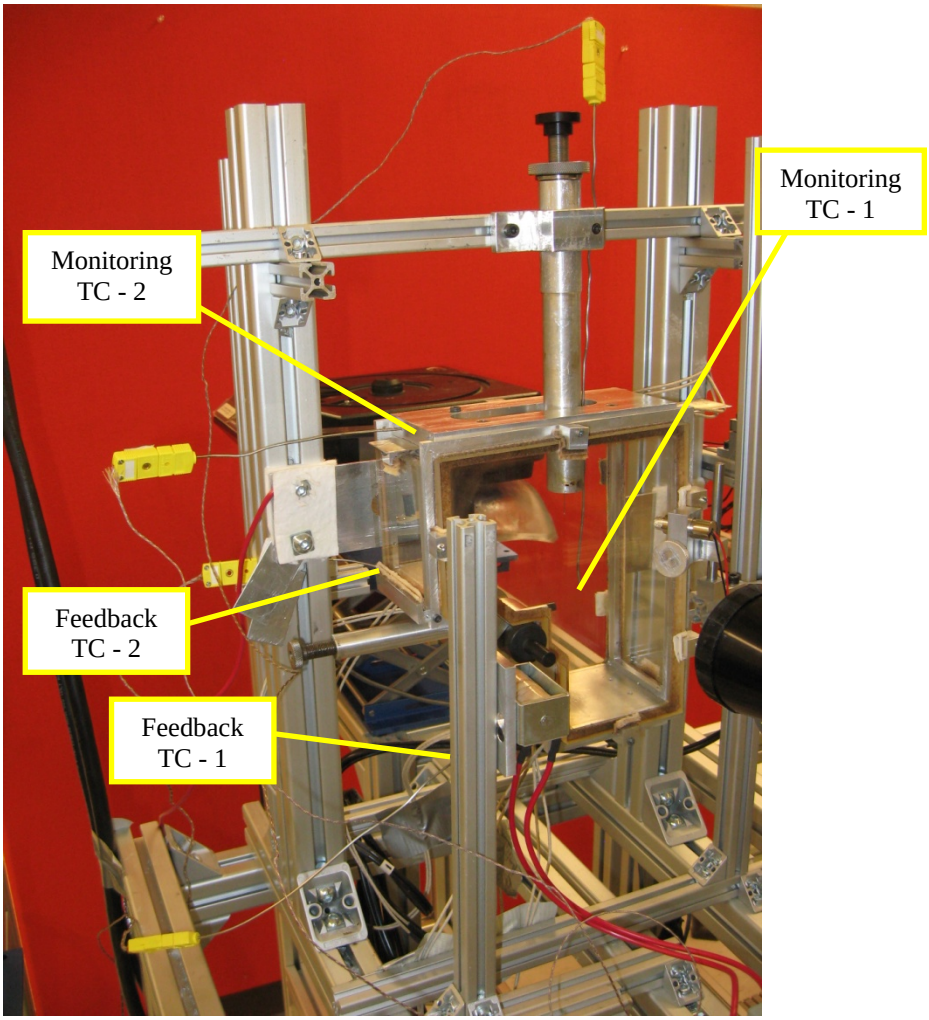

Figure 6-6 Location of thermocouples in performance test

In the performance test, four thermocouples were used to monitor and measure the temperature of different locations of the temperature cell. Two feedback thermocouples were connected to the controllers to measure the temperature of the bottom and launcher heaters, and two monitoring thermocouples were connected to the hand-held thermometer. One of the monitoring thermocouples was fixed inside the cell close to the

collision point and the other was free to be located in different parts of the cell. Figure 6-6 shows the location of the thermocouples used in the performance tests.

6.3 Triggering and Timing System

The triggering system was tested four ways: performance in intense background light, performance with smudged windows, performance in the presence of fog and smoke, and timing (during the collision tests).

The laser beam used in the triggering control system should be a long-focused dot beam; that is, the laser should be focused both on the drop position and the photo transducer in order to trigger the solenoid. Since the smallest drop size used in the setup is 0.5mm, the laser beam diameter should be the same size. The emitting lens of the laser diode was covered by aluminum foil. A very small hole (less than 0.5mm) was located in an appropriate position in front of the lens. This small hole reduced the beam diameter while focusing the laser beam at a desired distance. The aluminum cover with the small emitting hole can be seen on the triggering laser module in Figure 5-19.

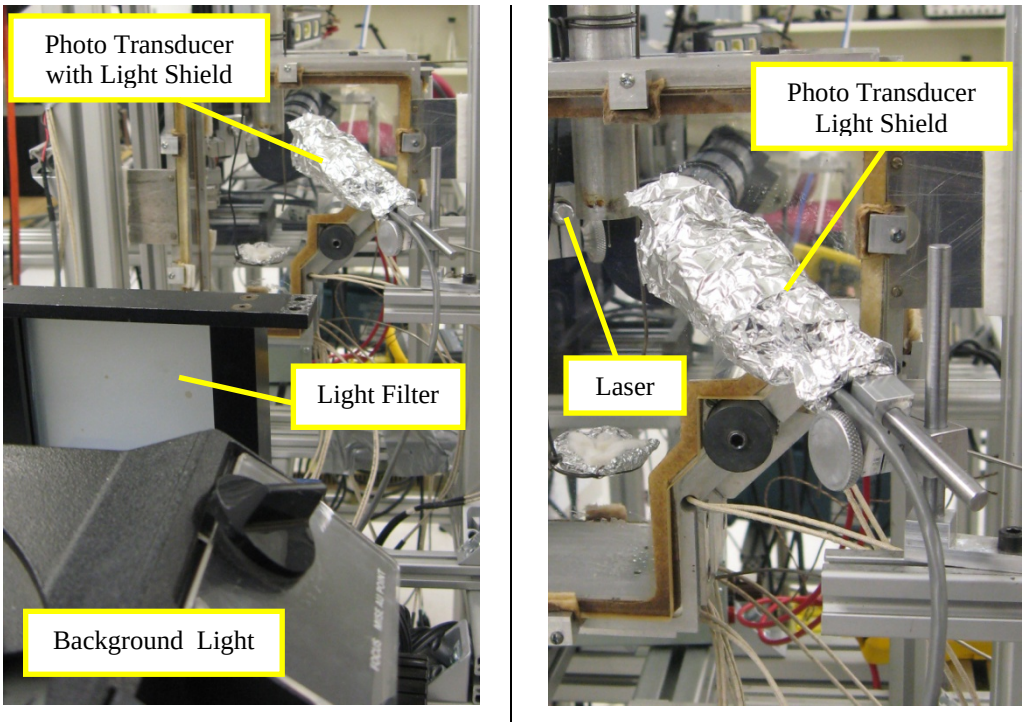

Figure 6-7 Photo transducer light shield

The photo transducer is very sensitive to background light; that is, it does not detect the laser beam in the presence of the intense background light and consequently it does not trigger the solenoid. The solution to this issue is a long narrow slot around the photo transducer facing the laser beam. Since the location and distance of the photo transducer relative to the temperature cell might vary in different experiments, aluminum foil was used as a shield around the photo transducer because it can be formed into different shapes and sizes. Figure 6-7 shows the aluminum foil shield used in the performance tests.

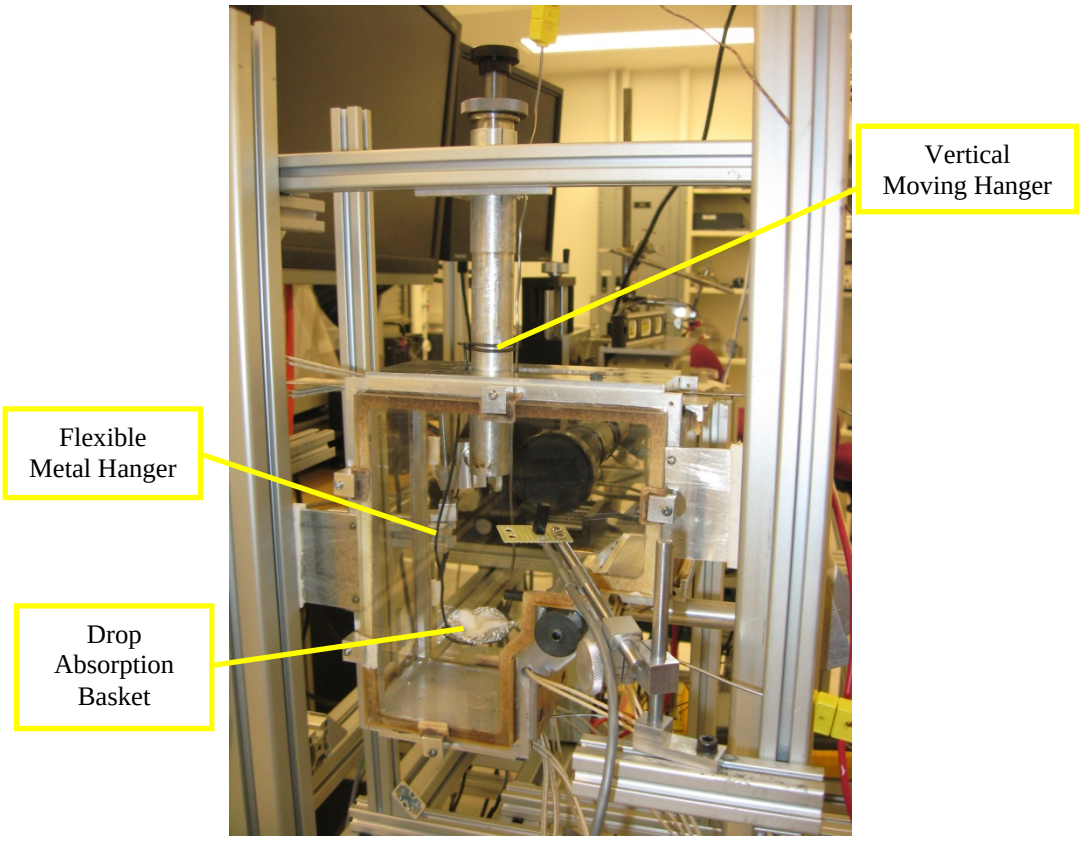

Figure 6-8 Drop collection funnel

Due to the smoke point of the test fluid, during the experiments, when fluid drops hit the hot wall surfaces they emitted smoke and liquid vapor which condensed on window surfaces. (The window surfaces are usually cooler than the rest of the cell.) A funnel was located below the drop generator to collect the used drops and prevent them from hitting the hot wall surfaces. This funnel consists of a flexible metal rod hanger and a basket made of ceramic insulation material located inside a piece of aluminum foil shaped like a

bowl (Figure 6-8). The insulation material resists the high temperature inside the cell and also absorbs the drops. The hanger is fixed around the drop generator and can move, along with the drop generator, in vertical and horizontal directions. This funnel reduces the amount of fog relatively effectively; however, in head-on collisions, it is not possible to prevent drops from hitting the hot surface and the windows covered by condensed liquid. The triggering system was tested in the worst conditions with smudged windows when smoke was emitting from the drops hitting the surface. However, This condition is found infrequently, if at all, in the experiment, since the windows should be clean before each experiment, and it takes time for the drop vapor condensation to cover the windows. The timing ability of the triggering system was tested through collision tests which will be described in next section.

6.4 Collision Test

After completing the performance test for individual parts of the device, collision tests were conducted to determine the entire system's functionality. The goal here was to verify the collision occurrence at high temperatures. The collision occurred at high velocities, most frequently after three to five trials; however, a maximum of 20 trials was needed in some of the low velocities.

In these tests, two different sizes of the drop and particle collided in two limiting velocities; the particle velocities used were shown in Table 6-1. The experiments were carried out at 200ºC in two collision angles; right-angled and head-on. Sample test results are provided in this section using video frames taken by the Phantom v4.3 high-speed camera with background lighting. Since the focus was to test the functionality of the device, one camera was used for imaging and measurement, and on-axis collisions were not considered.

Since having collisions of smaller sized particles is more difficult and needed more precision in the device, the main set of experiments were run using 1mm particles with 1.2mm drops. Figures 6-9 to 6-17 show the video frames of the right-angled collision between a 1mm particle and a 1.2mm drop at 200ºC, which covers the particle velocities between 0.96 m/s and 11.3 m/s and the relative velocities from 1.2 m/s to 11.3 m/s. The head-on collisions were recorded by images shown in Figures 6-18 to 6-24 covering the particle velocities between 0.63 m/s and 20.4 m/s and relative velocities from 1.4 m/s to

21.3 m/s. Since the upper limit of the velocities achieved in the experiments was higher than the limits determined in Chapter 4, the experiments were not continued beyond these values.

The other set of experiments was run using a 2mm particle and 1.5mm drop. Figures 6-25 to 6-30 show the right-angled collisions covering particle velocities between 0.53 m/s and 3.2 m/s and relative velocities between 0.9 m/s and 3.3 m/s. The head-on velocities are shown in Figures 6-31 to 6-33 for particle velocities from 0.77 to 3.59 and relative velocities from 1.6 m/s to 4.2 m/s.

Another phenomenon which can be studied using this device is the impact of the high speed air jet onto a drop. Figures 6-14 to 6-17, and 6-21, 6-22, and 6-24 show sample tests which demonstrate the functionality of the device in drop-air jet impact. However, this is beyond the scope of this thesis, but can be developed in the future using the results achieved in this thesis.

The launcher tip is shown in each video frame to provide an estimation of the dimensions of the field of view and collision interactions. The results provided in this section will not be analyzed for collision outcomes and are only provided here to show how consistently the device performed. Case in point: Figures 6-14 and 6-15 show two collision tests occurred in almost the same relative velocities (8.5m/s and 8.8m/s). The collision outcomes in corresponding time frames are quite similar for both collisions.

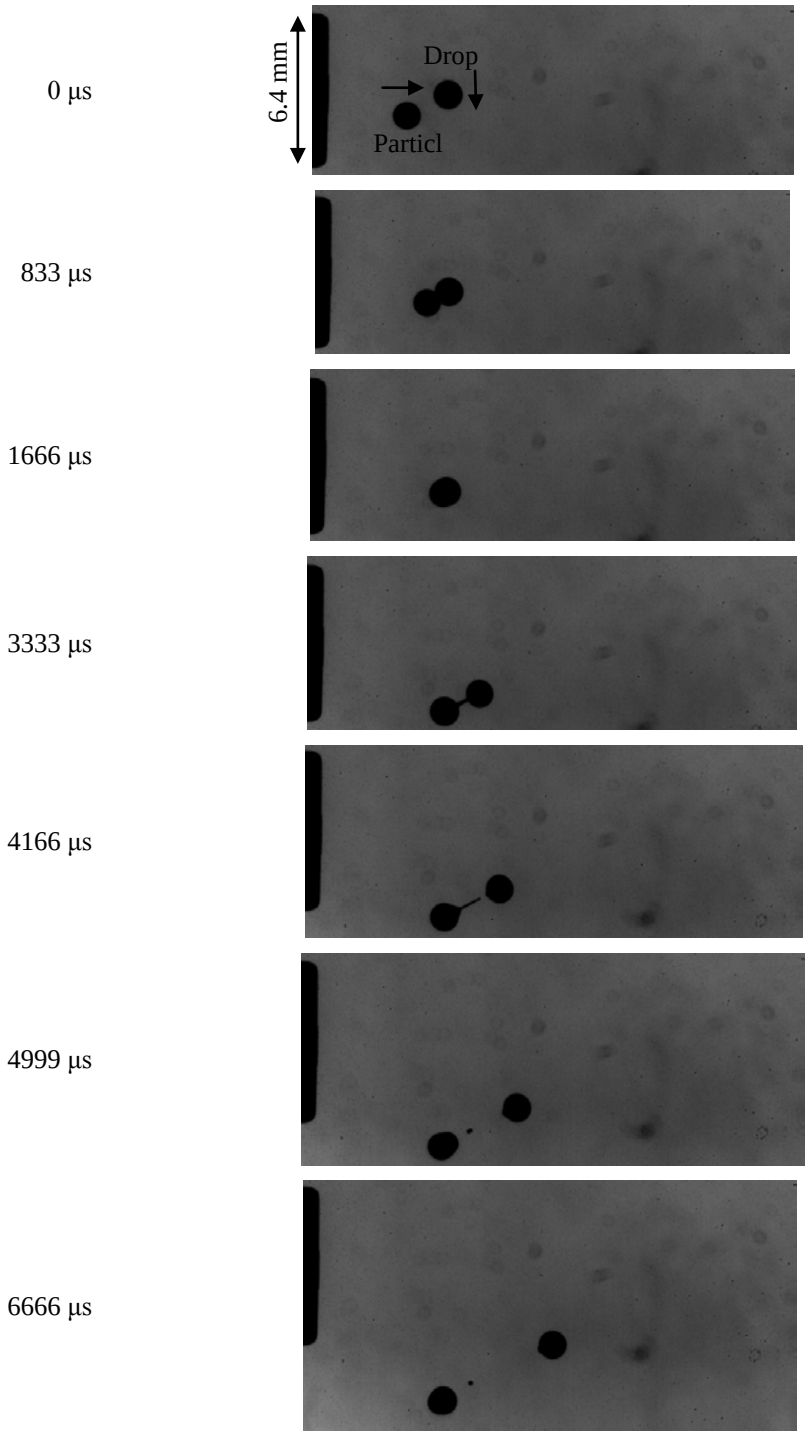

Figure 6-9 Drop-particle right-angled collision at 200ºC - off-axis
Drop: Silicon base heat transfer liquid (Duratherm S) / Particle: Glass bead
Drop: d= 1.2 mm, V=0.75 m/s / Particle: d=1 mm, V=0.96 m/s / V_{rltv} = 1.2 m/s

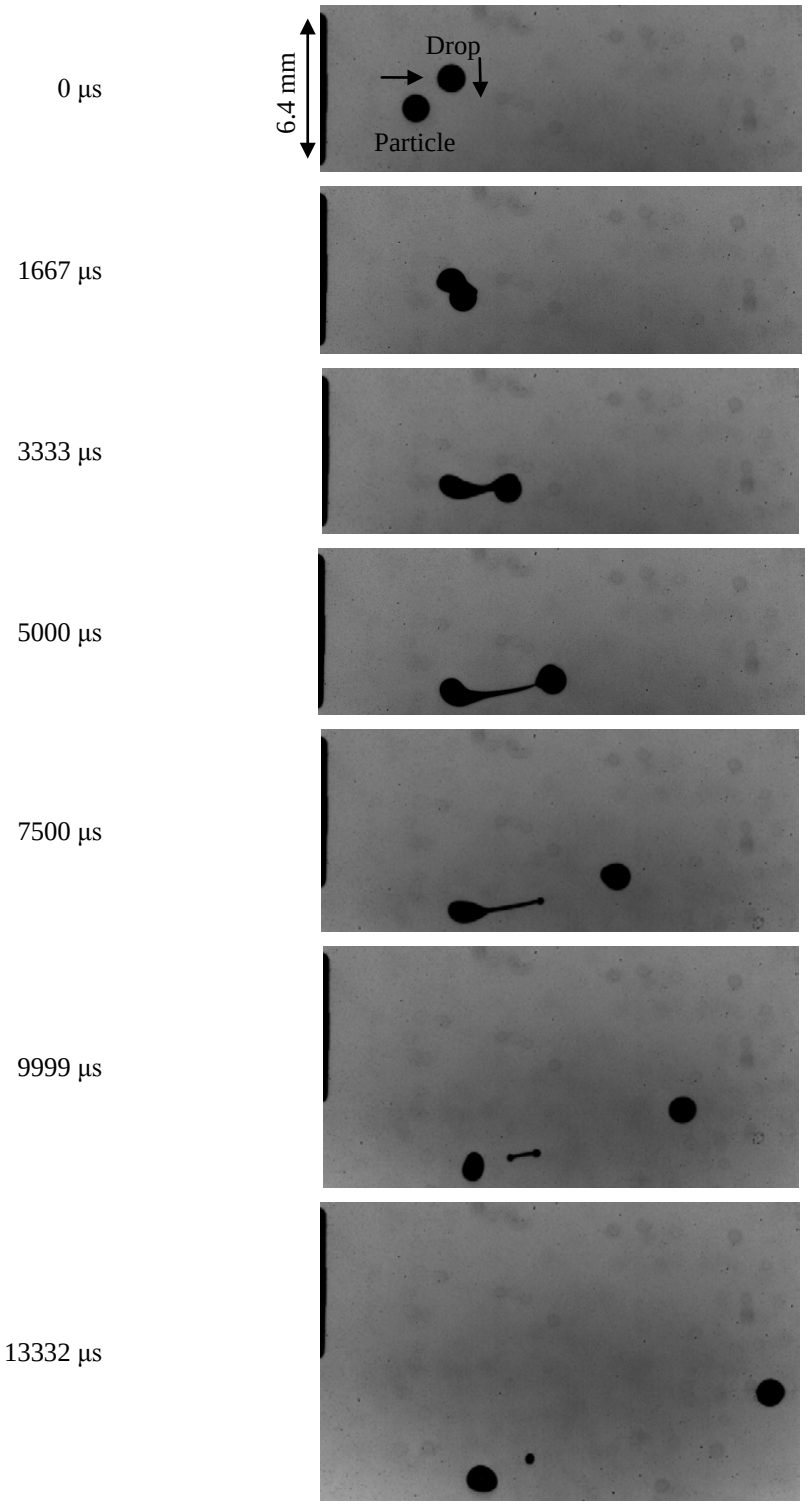

Figure 6-10 Drop-particle right-angled collision at 200ºC - off-axis
Drop: Silicon base heat transfer liquid (Duratherm S) / Particle: Glass bead
Drop: d=1.2 mm, V=0.57 m/s / Particle: d=1 mm, V=1.19 m/s / V_{rltv} = 1.3 m/s

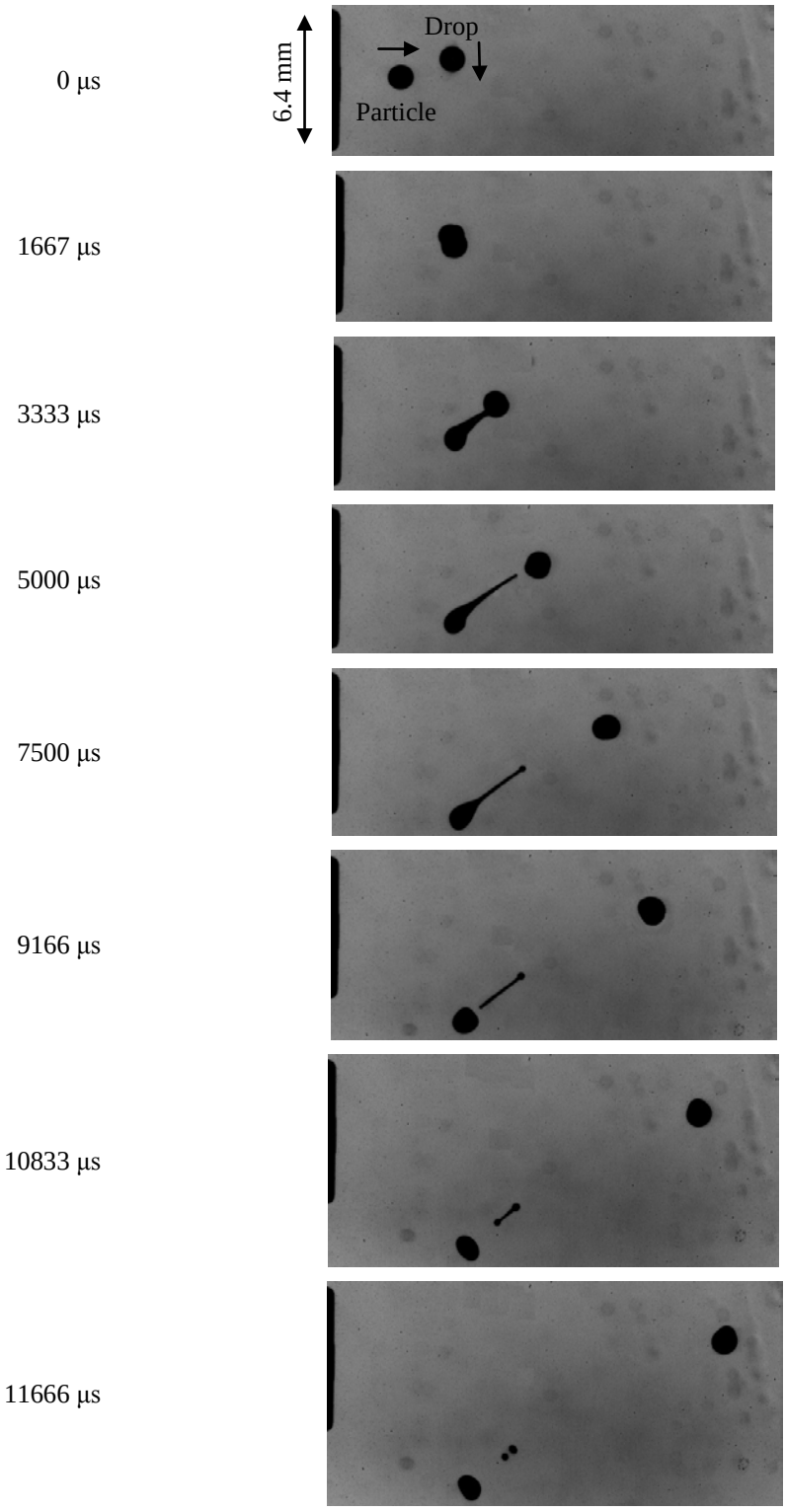

Figure 6-11 Drop-particle right-angled collision at 200ºC - off-axis
Drop: Silicon base heat transfer liquid (Duratherm S) / Particle: Glass bead
Drop: d=1.2 mm, V=0.58 m/s / Particle: d=1 mm, V=1.35 m/s / V_{rltv} = 1.5 m/s

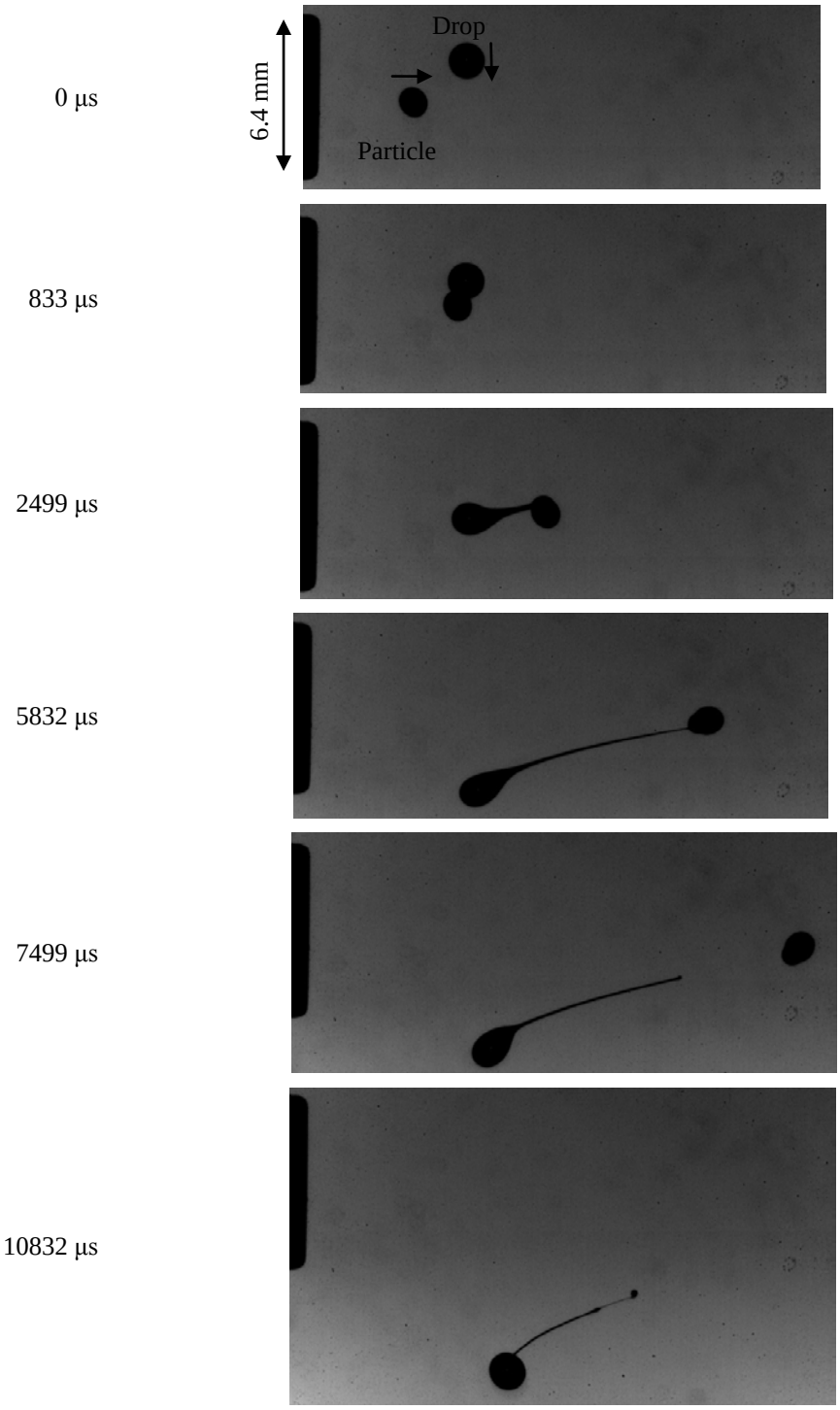

Figure 6-12 Drop-particle right-angled collision at 200ºC - off-axis
Drop: Silicon base heat transfer liquid (Duratherm S) / Particle: Glass bead
Drop: d=1.4 mm, V=0.76 m/s / Particle: d=1 mm, V=2.06 m/s / V_{rltv} = 2.2 m/s

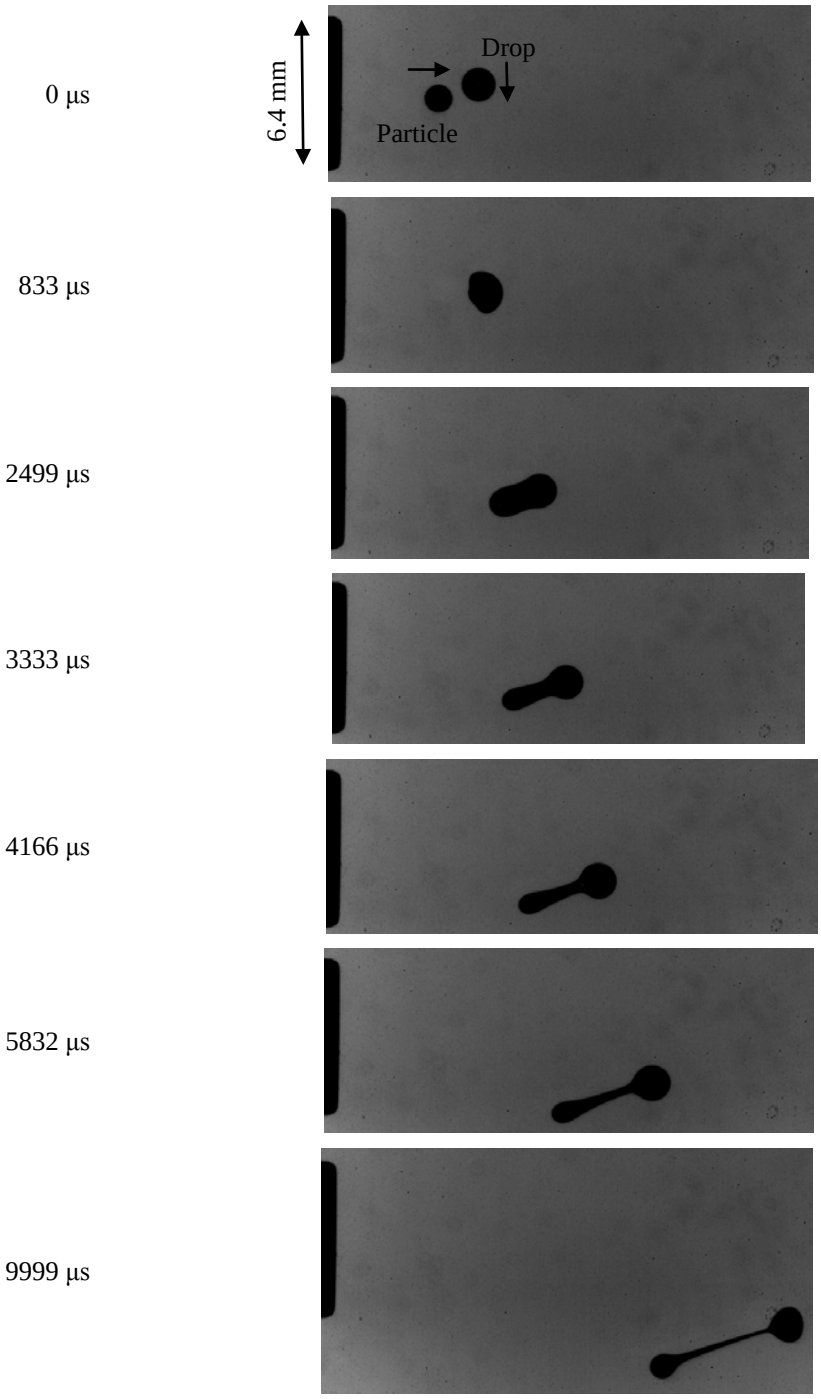

Figure 6-13 Drop-particle right-angled collision at 200ºC - off-axis

Drop: Silicon base heat transfer liquid (Duratherm S) / Particle: Glass bead
Drop: d=1.5 mm, V=0.75 m/s / Particle: d=1 mm, V=2.22 m/s / V_{rltv} = 2.3 m/s

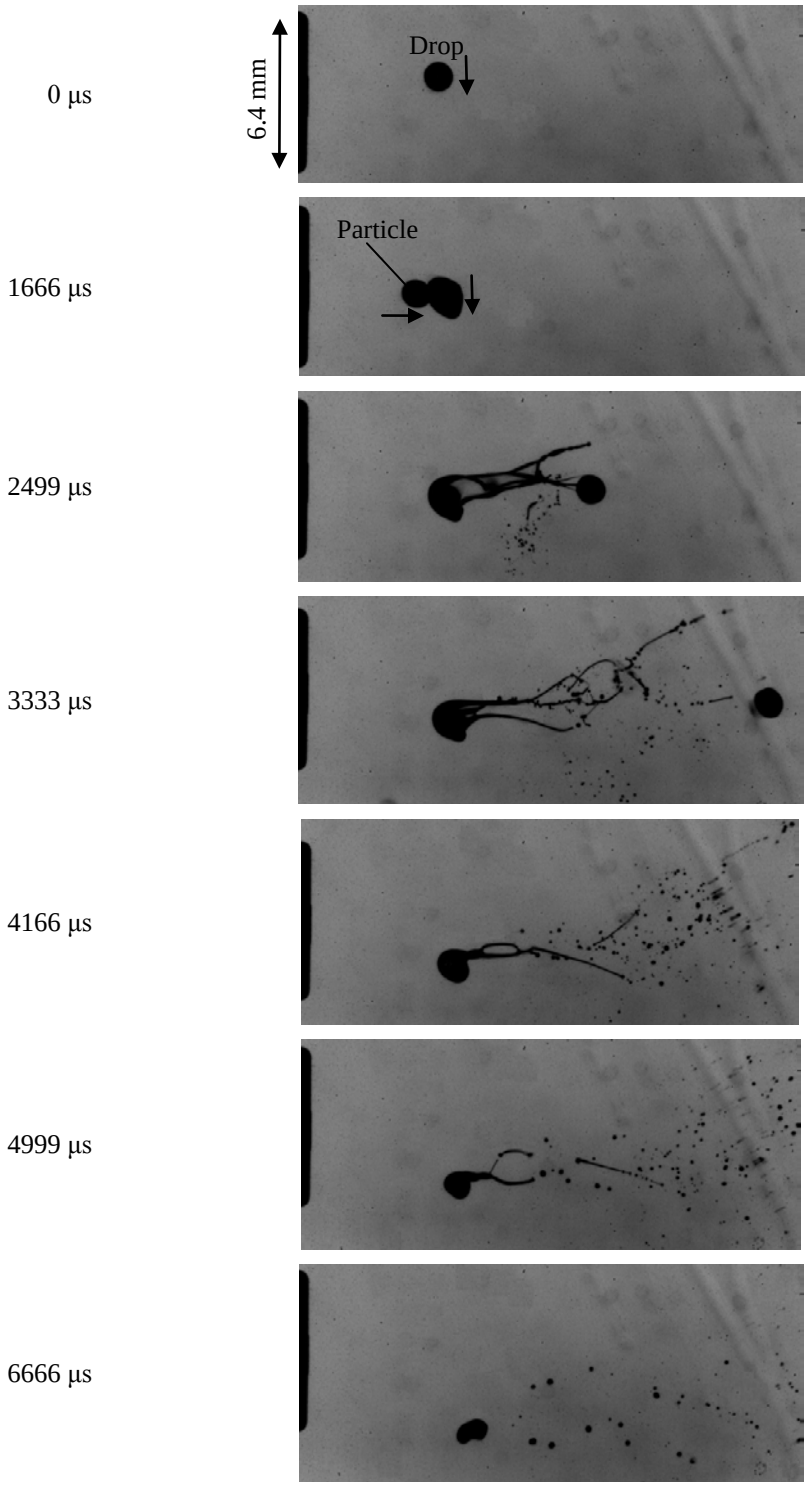

Figure 6-14 Drop-particle right-angled collision at 200ºC - off-axis
Drop: Silicon base heat transfer liquid (Duratherm S) / Particle: Glass bead
Drop: d=1.2 mm, V=0.56 m/s / Particle: d=1 mm, V=8.52 m/s / V_{rltv} = 8.5 m/s

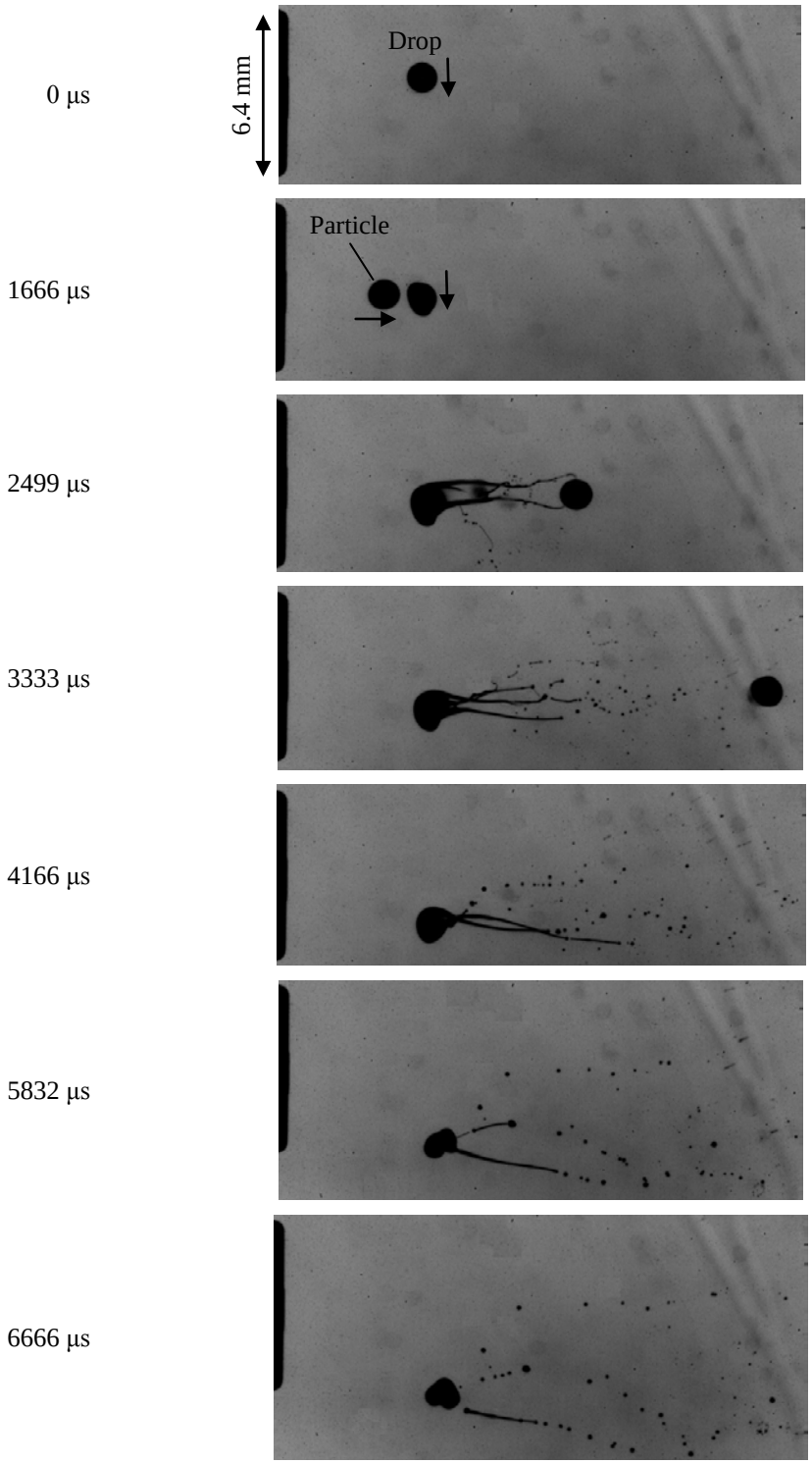

Figure 6-15 Drop-particle right-angled collision at 200ºC - off-axis

Drop: Silicon base heat transfer liquid (Duratherm S) / Particle: Glass bead
Drop: d=1.2 mm, V=0.56 m/s / Particle: d=1 mm, V=8.79 m/s / V_{rltv} = 8.8 m/s

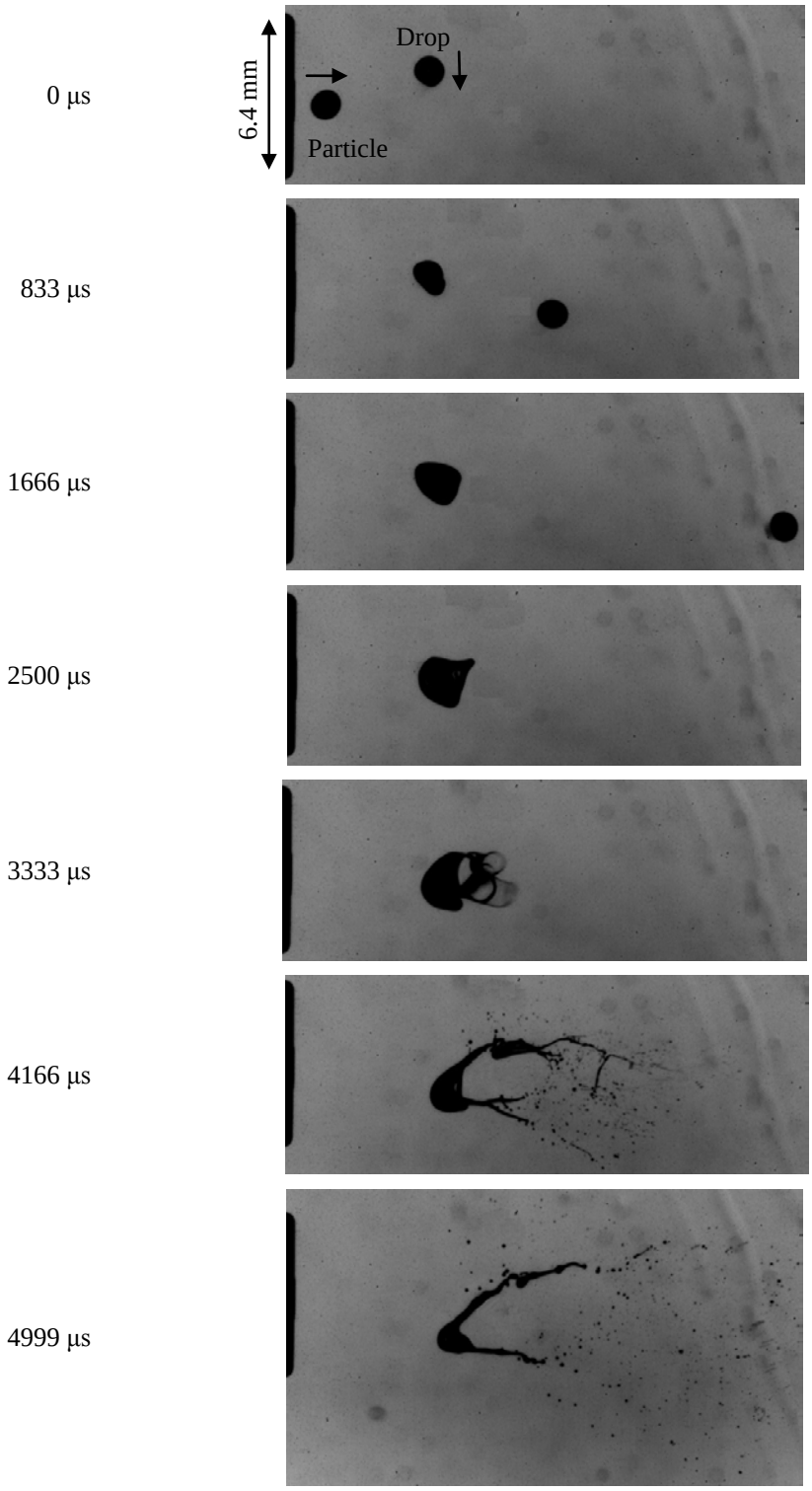

Figure 6-16 Drop-particle right-angled collision at 200ºC - off-axis
Drop: Silicon base heat transfer liquid (Duratherm S) / Particle: Glass bead
Drop: d=1.2 mm, V=0.55 m/s / Particle: d=1 mm, V=10.59 m/s / V_{rltv} = 10.6 m/s

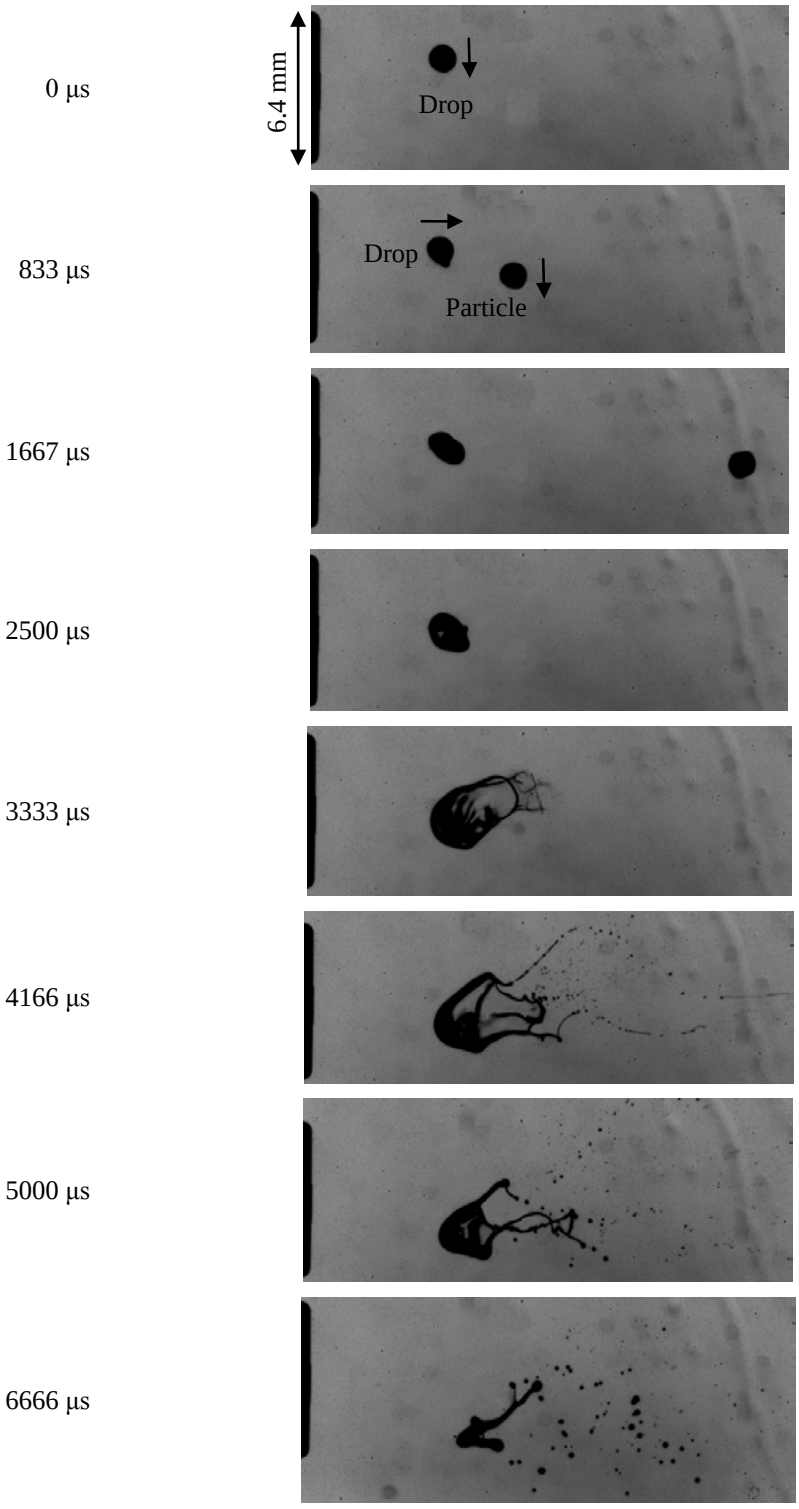

Figure 6-17 Drop-particle right-angled collision at 200ºC - off-axis
Drop: Silicon base heat transfer liquid (Duratherm S) / Particle: Glass bead
Drop: d=1.2 mm, V=0.56 m/s / Particle: d=1 mm, V=11.3 m/s / V_{rltv} = 11.3 m/s

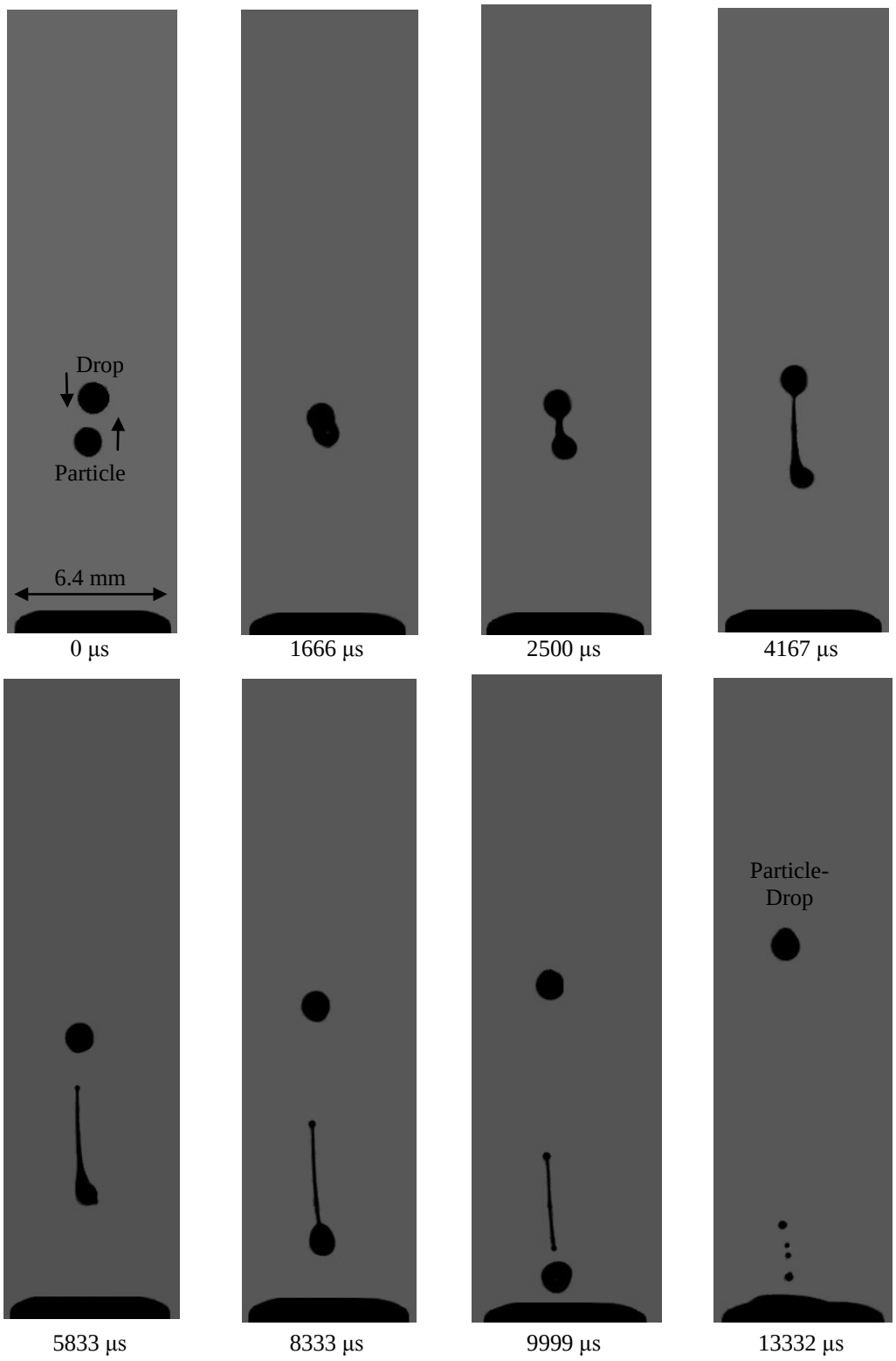

Figure 6-18 Drop-particle head-on collision at 200ºC - off-axis - Enhanced background
Drop: Silicon base heat transfer liquid (Duratherm S) / Particle: Glass bead
Drop: d=1.2 mm, V=0.79 m/s / Particle: d=1 mm, V=0.63 m/s / V_{rltv} = 1.4 m/s

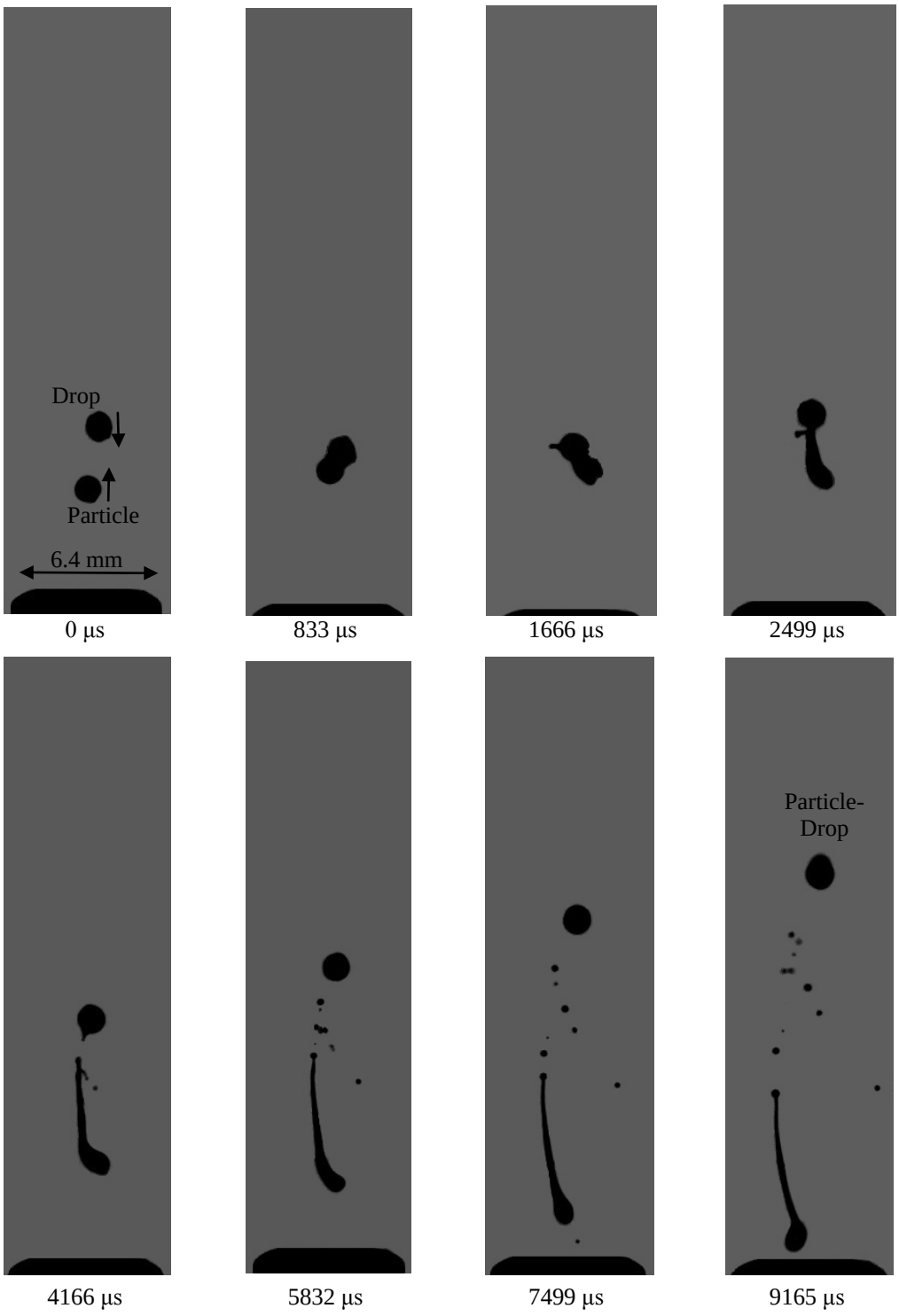

Figure 6-19 Drop-particle head-on collision at 200ºC - off-axis - Enhanced background
Drop: Silicon base heat transfer liquid (Duratherm S) / Particle: Glass bead
Drop: d=1.2 mm, V=0.75 m/s / Particle: d=1 mm, V=1.6 m/s / V_{rltv} = 2.3 m/s

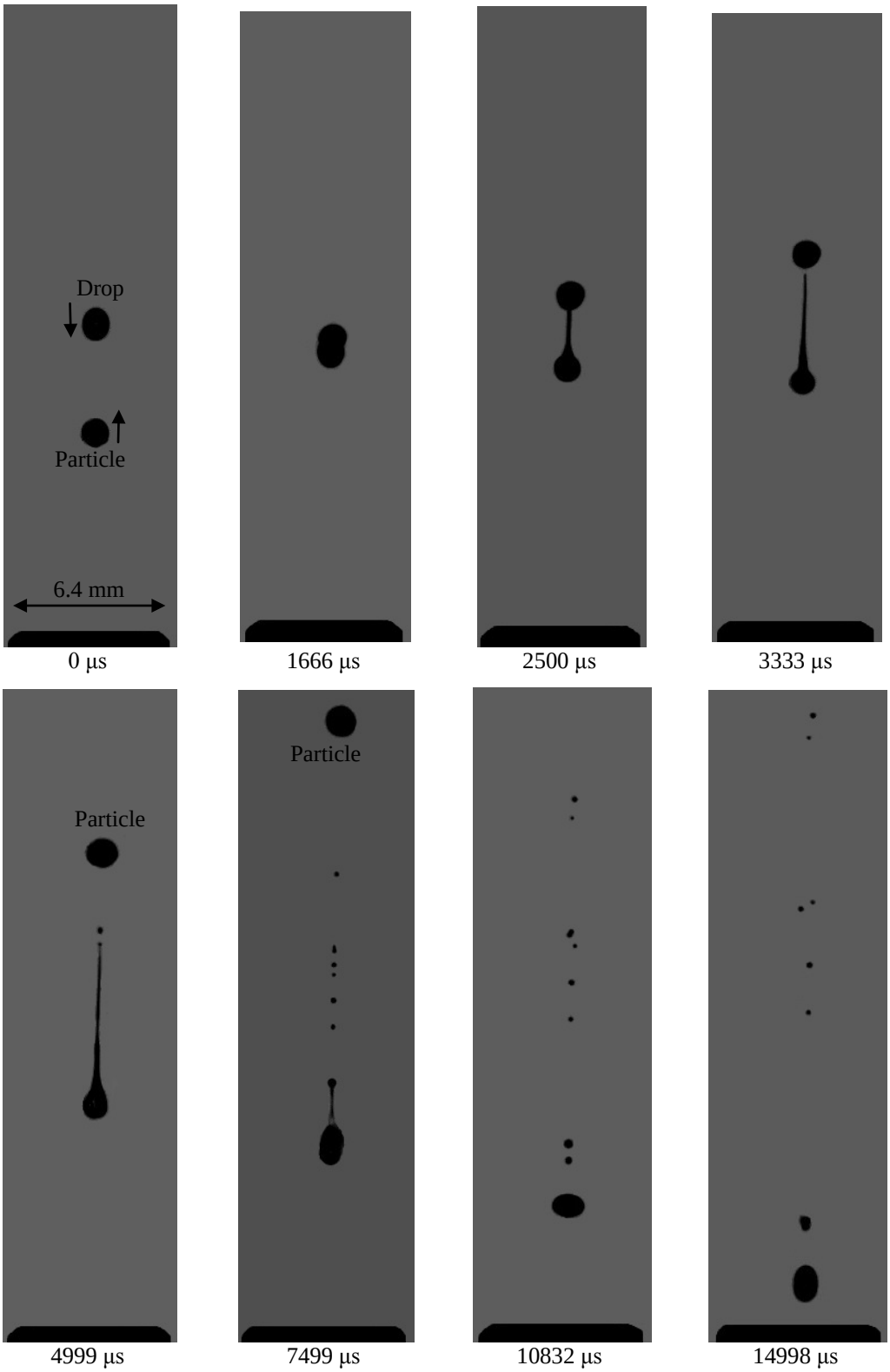

Figure 6-20 Drop-particle head-on collision at 200ºC - off-axis - Enhanced background
Drop: Silicon base heat transfer liquid (Duratherm S) / Particle: Glass bead
Drop: d=1.2 mm, V=0.73 m/s / Particle: d=1 mm, V=1.85 m/s / V_{rltv} = 2.6 m/s

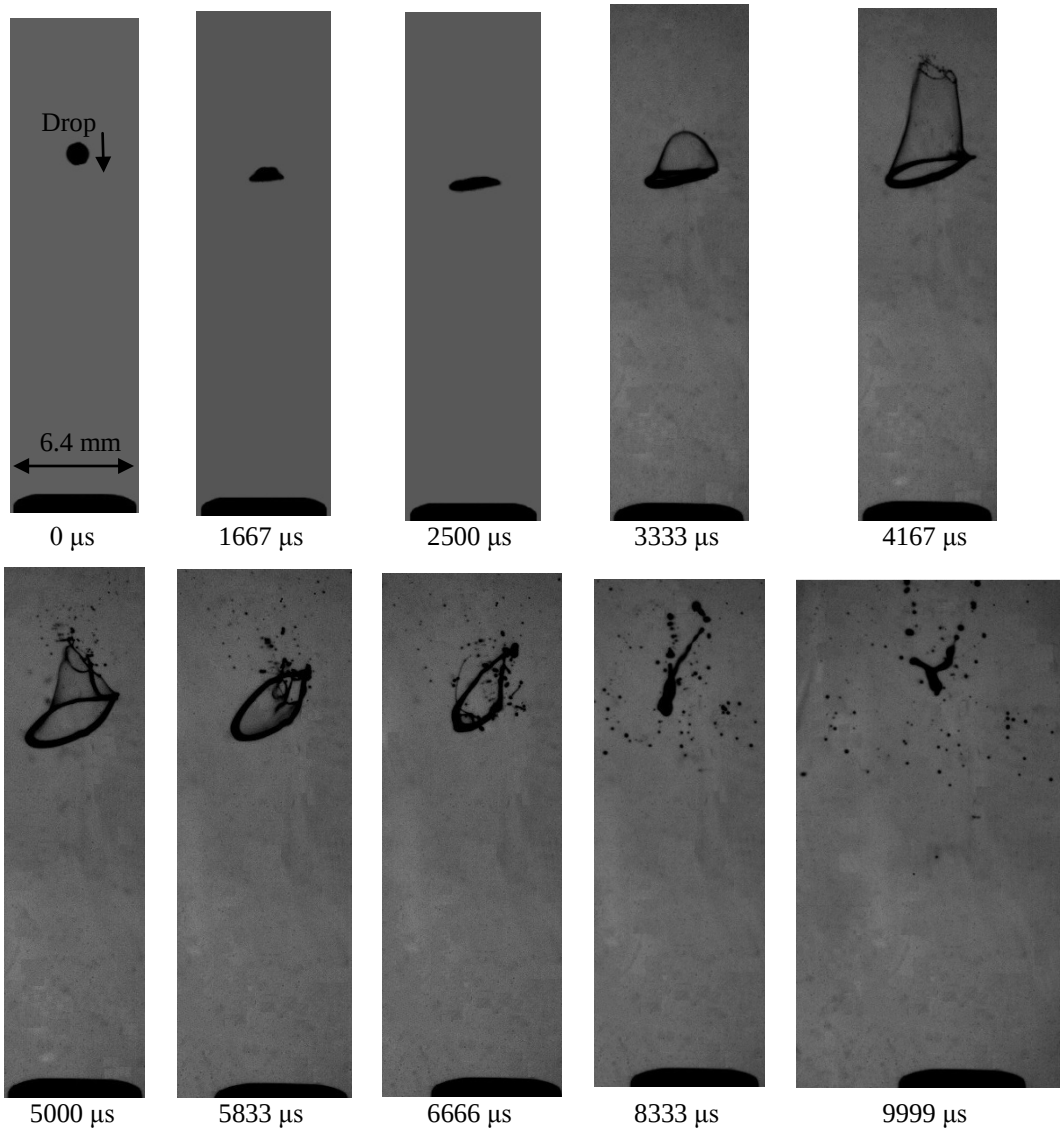

Figure 6-21 Drop-air jet head-on collision at 200ºC - off-axis - Enhanced background
Drop: Silicon base heat transfer liquid (Duratherm S) / Particle: Glass bead
Drop: d=1.2 mm, V=0.83 m/s / (Particle: d=1 mm, V=2.07 m/s / V_{rltv} = 2.9 m/s)

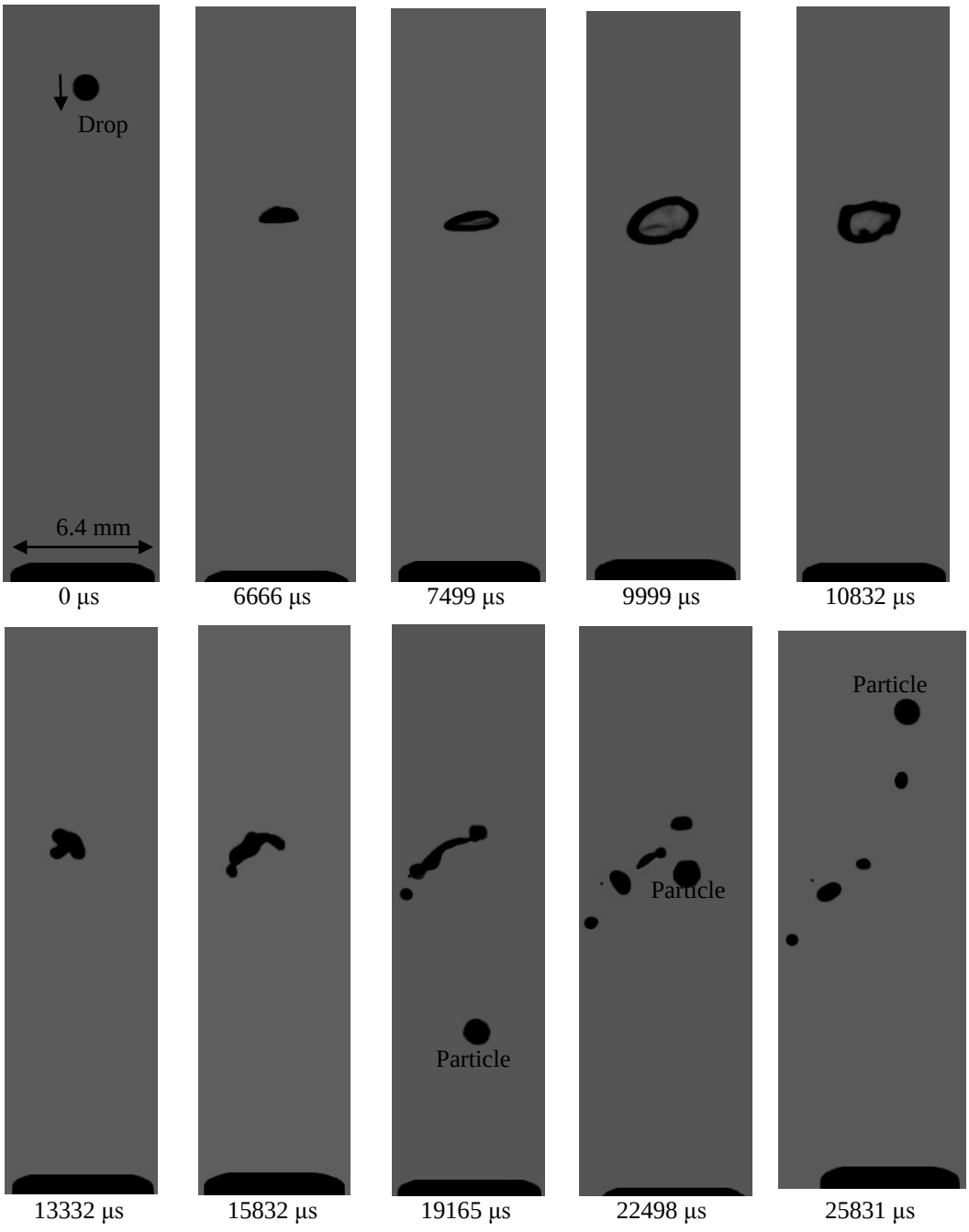

Figure 6-22 Drop-particle/air jet head-on collision at 200ºC - off-axis - Enhanced background
Drop: Silicon base heat transfer liquid (Duratherm S) / Particle: Glass bead
Drop: d=1.2 mm, V=0.84 m/s / Particle: d=1 mm, V=2.23 m/s / V_{rltv} = 3.1 m/s

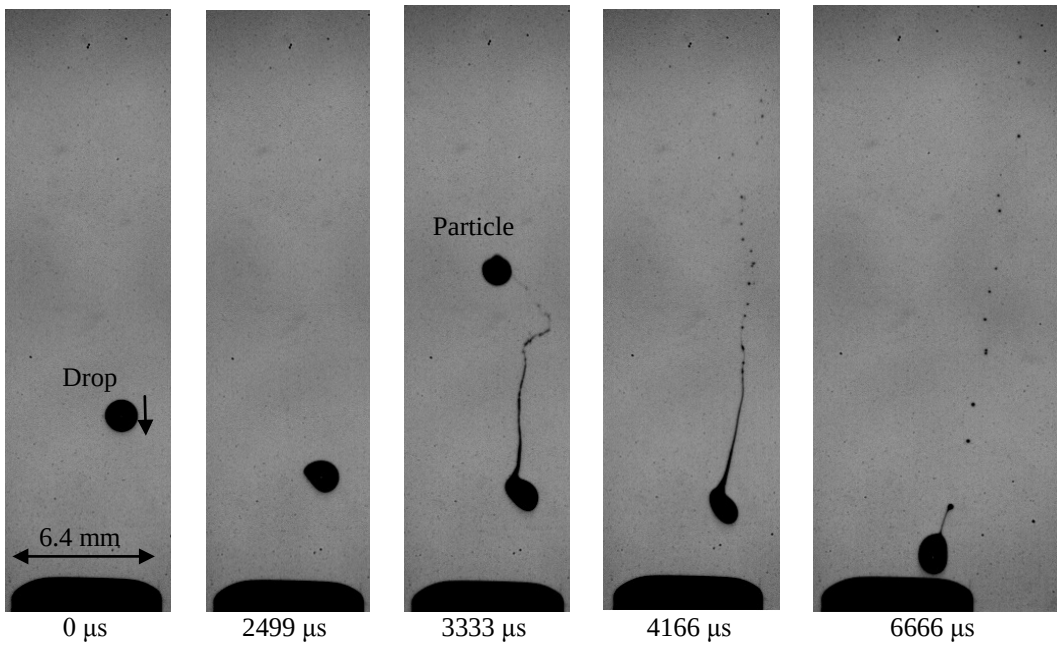

Figure 6-23 Drop-particle head-on collision at 200ºC - off-axis
Drop: Silicon base heat transfer liquid (Duratherm S) / Particle: Glass bead
Drop: d=1.4 mm, V=1.06 m/s / Particle: d=1 mm, V=16.78 m/s / V_{rltv} = 17.8 m/s

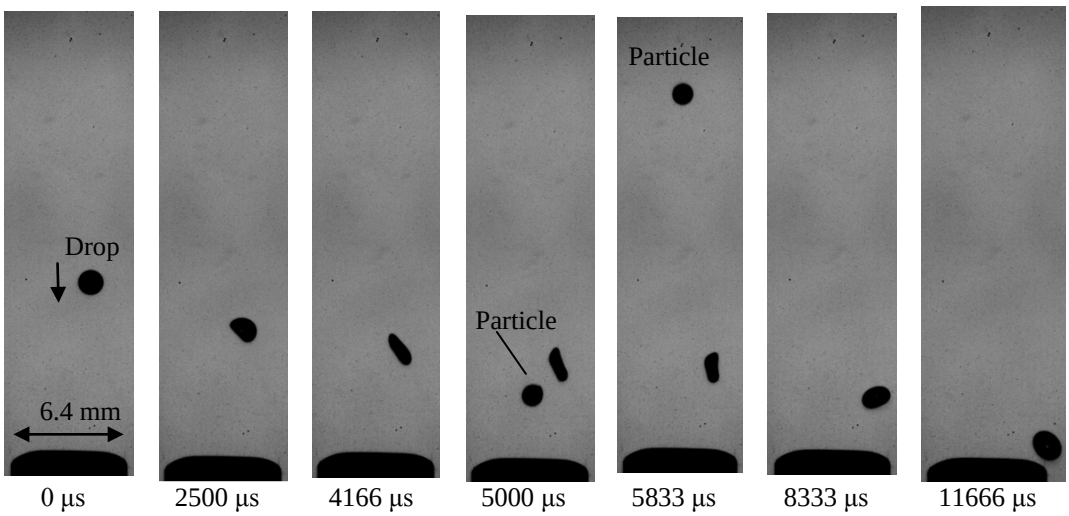

Figure 6-24 Drop-air jet head-on collision at 200ºC - off-axis
Drop: Silicon base heat transfer liquid (Duratherm S) / Particle: Glass bead
Drop: d=1.5 mm, V=0.93 m/s / Particle: d=1 mm, V=20.39 m/s / V_{rltv} = 21.3 m/s

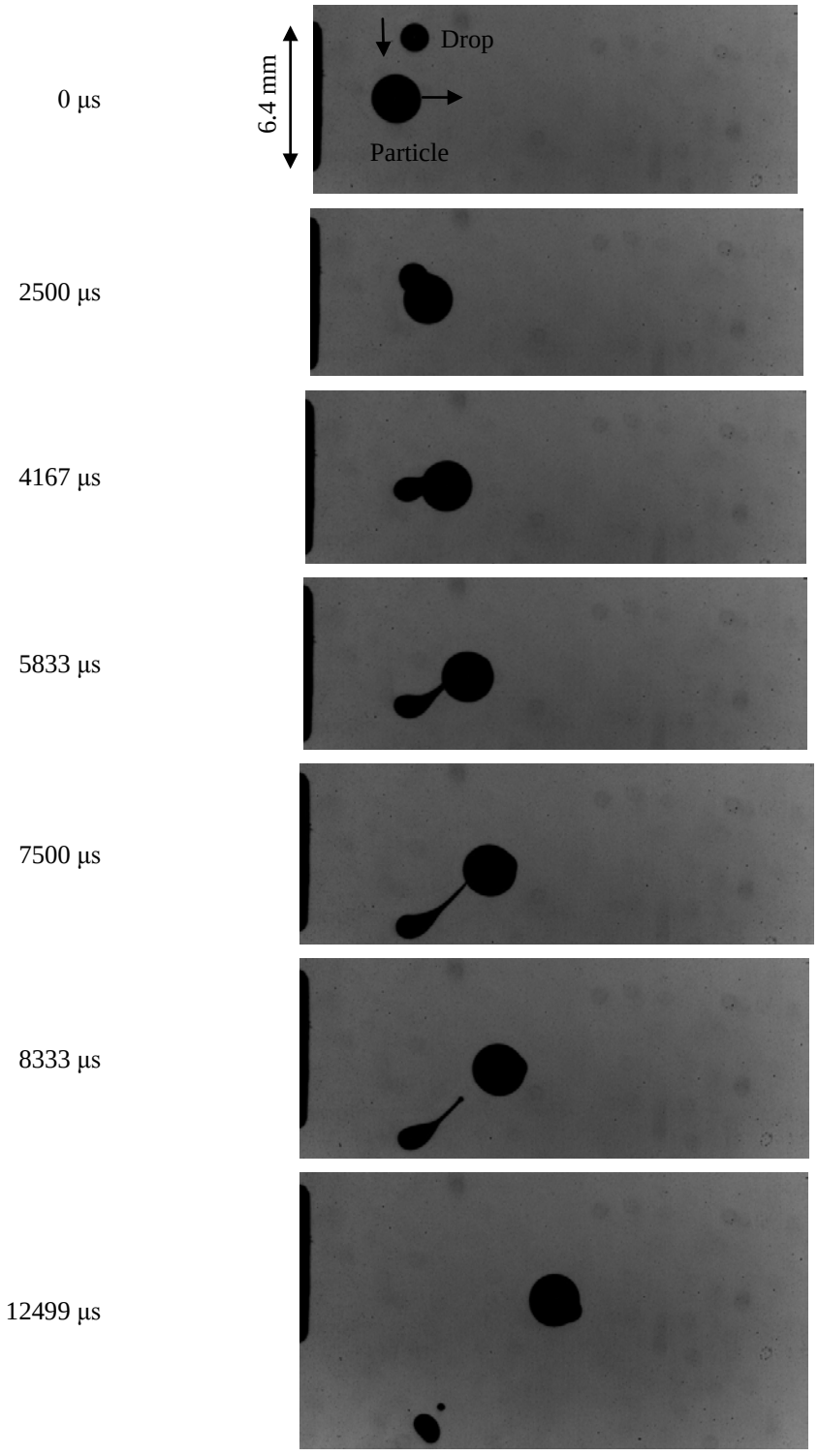

Figure 6-25 Drop-particle right-angled collision at 200ºC - off-axis
Drop: Silicon base heat transfer liquid (Duratherm S) / Particle: Glass bead
Drop: d=1.2 mm, V=0.67 m/s / Particle: d=2 mm, V=0.53 m/s / V_{rltv} = 0.9 m/s

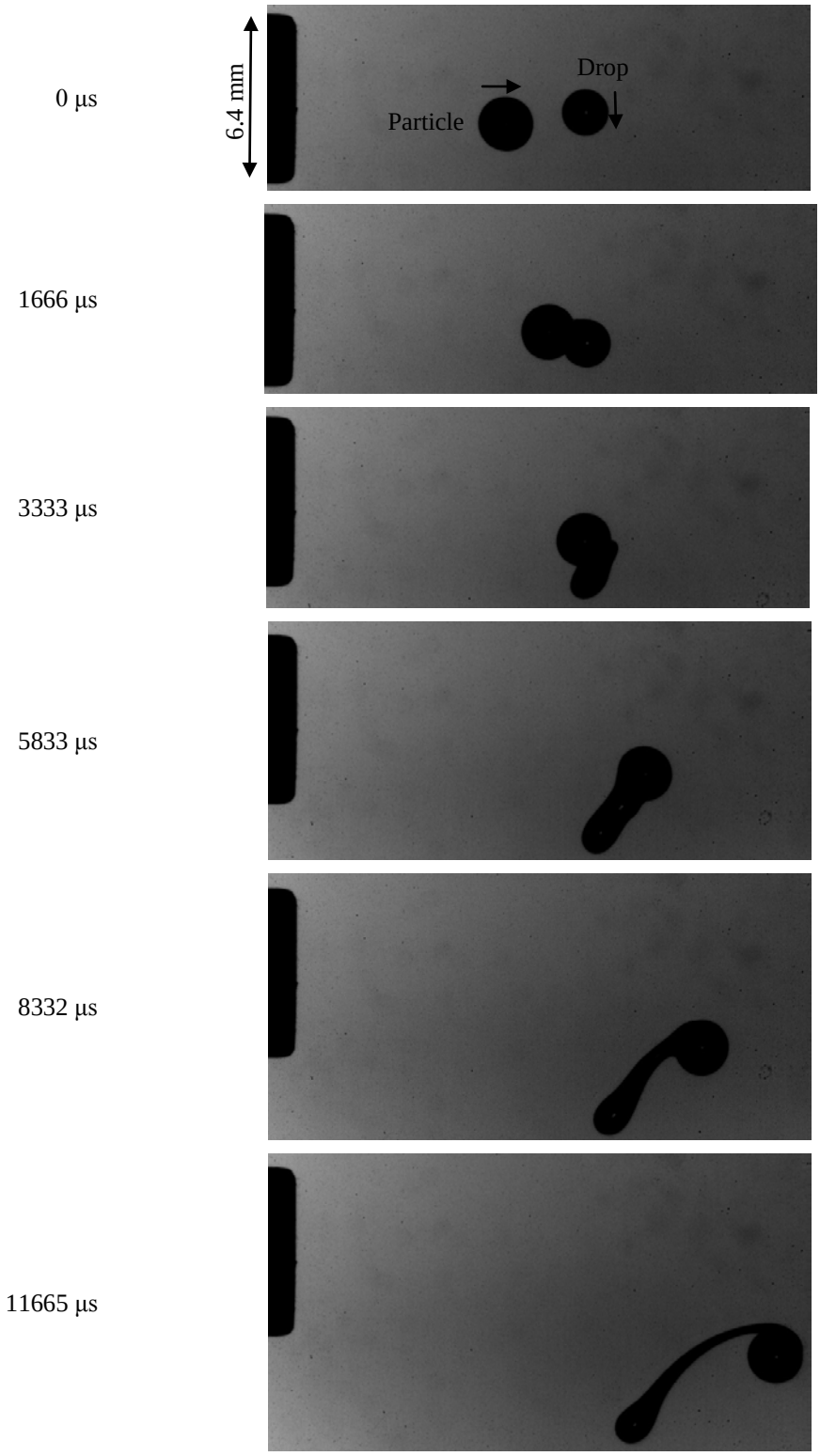

Figure 6-26 Drop-particle right-angled collision at 20ºC - off-axis
Drop: Silicon base heat transfer liquid (Duratherm S) / Particle: Glass bead
Drop: d=1.7 mm, V=0.61 m/s / Particle: d=2 mm, V=0.92 m/s / V_{rltv} = 1.1 m/s

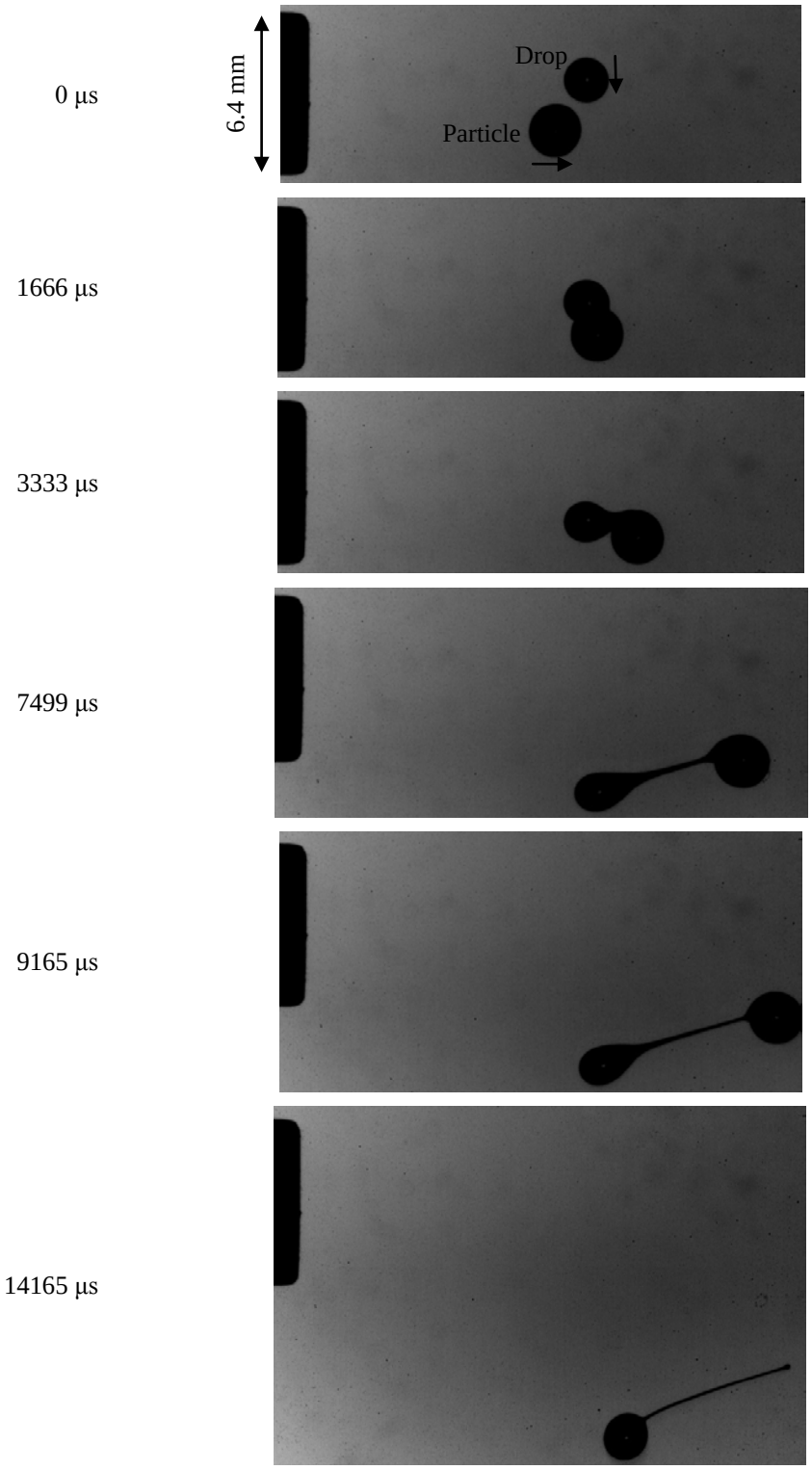

Figure 6-27 Drop-particle right-angled collision at 20ºC - off-axis
Drop: Silicon base heat transfer liquid (Duratherm S) / Particle: Glass bead
Drop: d=1.7 mm, V=0.60 m/s / Particle: d=2 mm, V=0.97 m/s / V_{rltv} = 1.1 m/s

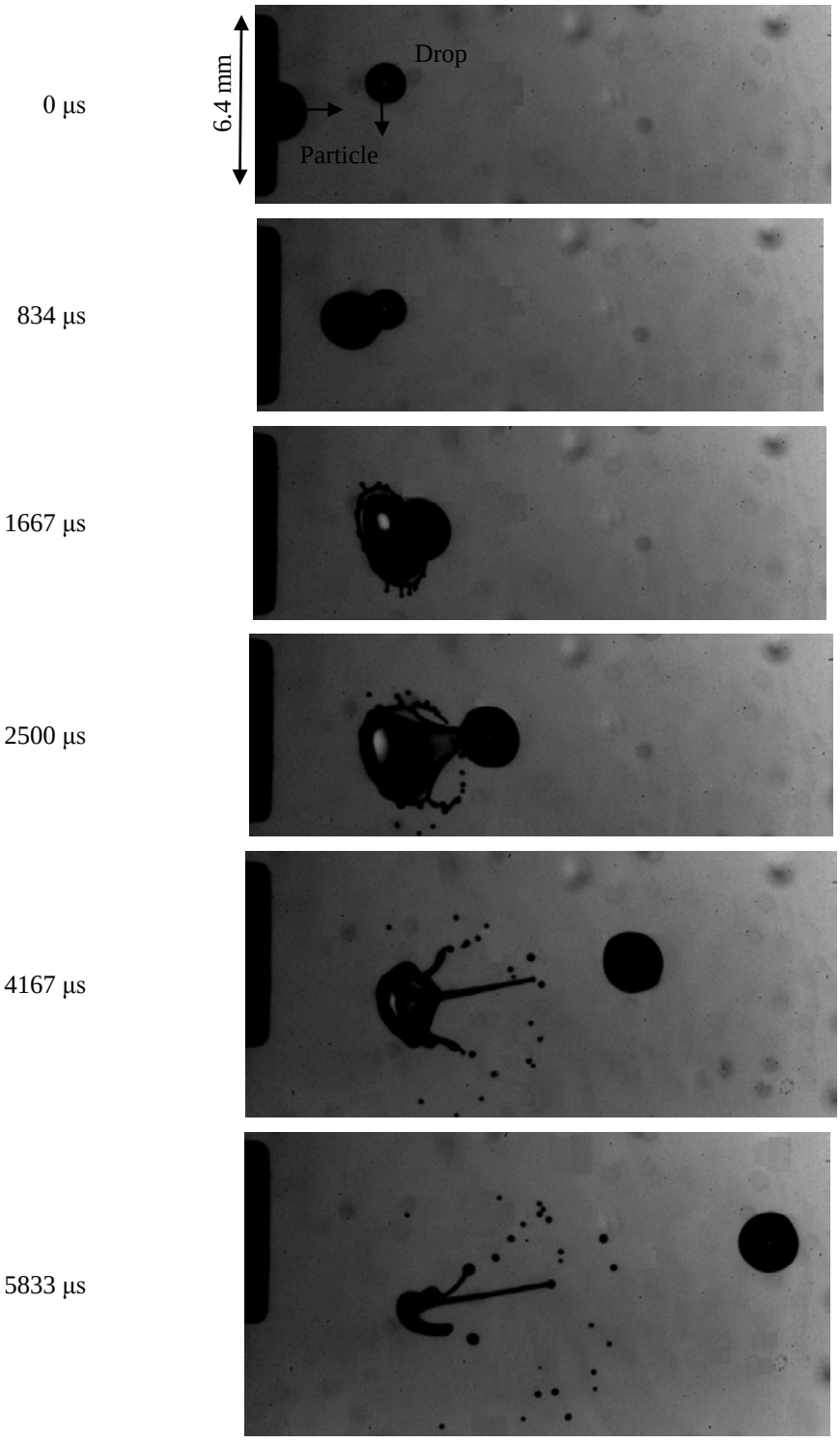

Figure 6-28 Drop-particle right-angled collision at 200ºC - off-axis
Drop: Silicon base heat transfer liquid (Duratherm S) / Particle: Glass bead
Drop: d=1.5 mm, V=0.65 m/s / Particle: d=2 mm, V=2.95 m/s / V_{rltv} = 3 m/s

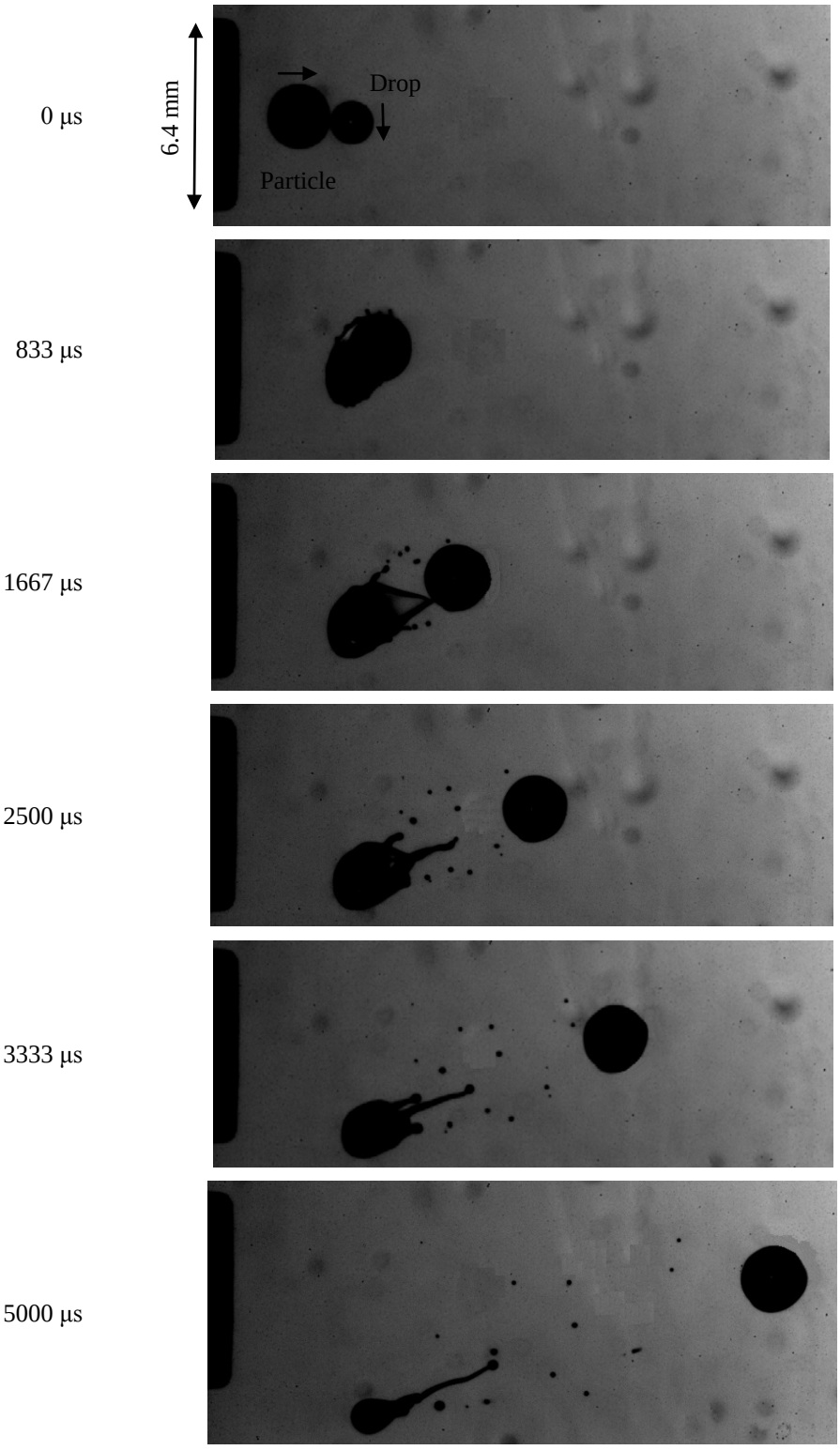

Figure 6-29 Drop-particle right-angled collision at 200ºC - off-axis
Drop: Silicon base heat transfer liquid (Duratherm S) / Particle: Glass bead
Drop: d=1.5 mm, V=0.67 m/s / d=Particle: 2 mm, V=3.07 m/s / V_{rltv} = 3.1 m/s

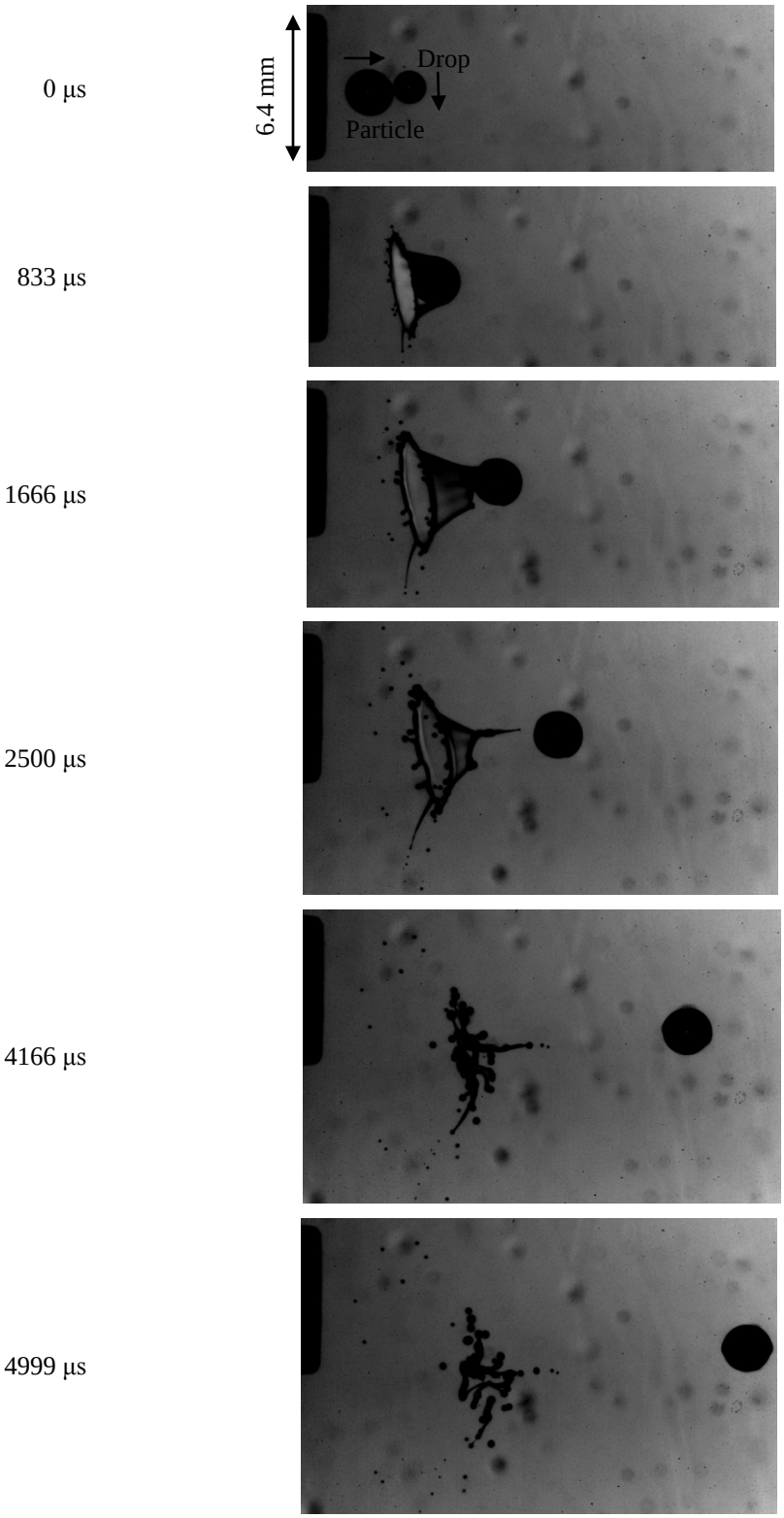

Figure 6-30 Drop-particle right-angled collision at 200ºC - off-axis
Drop: Silicon base heat transfer liquid (Duratherm S) / Particle: Glass bead
Drop: d=1.4mm, V=0.63 m/s / Particle: d=2 mm, V=3.20 m/s / V_{rltv} = 3.3 m/s

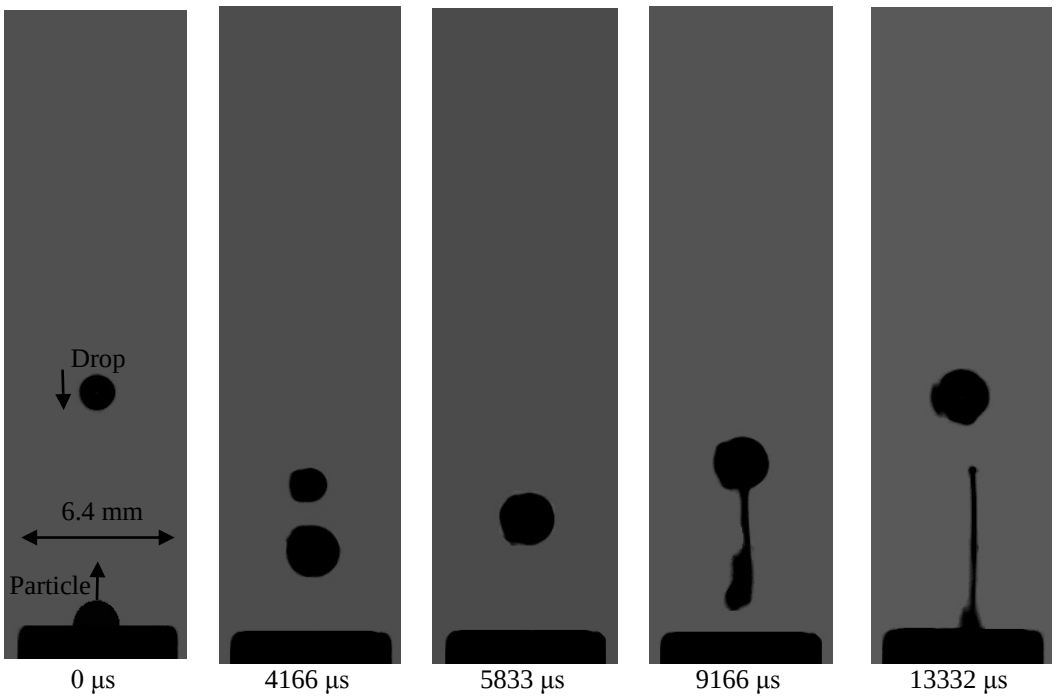

Figure 6-31 Drop-particle head-on collision at 200ºC - off-axis - Enhanced background
Drop: Silicon base heat transfer liquid (Duratherm S) / Particle: Glass bead
Drop: d=1.4 mm, V=0.87 m/s / Particle: d=2 mm, V=0.77 m/s / V_{rltv} = 1.6 m/s

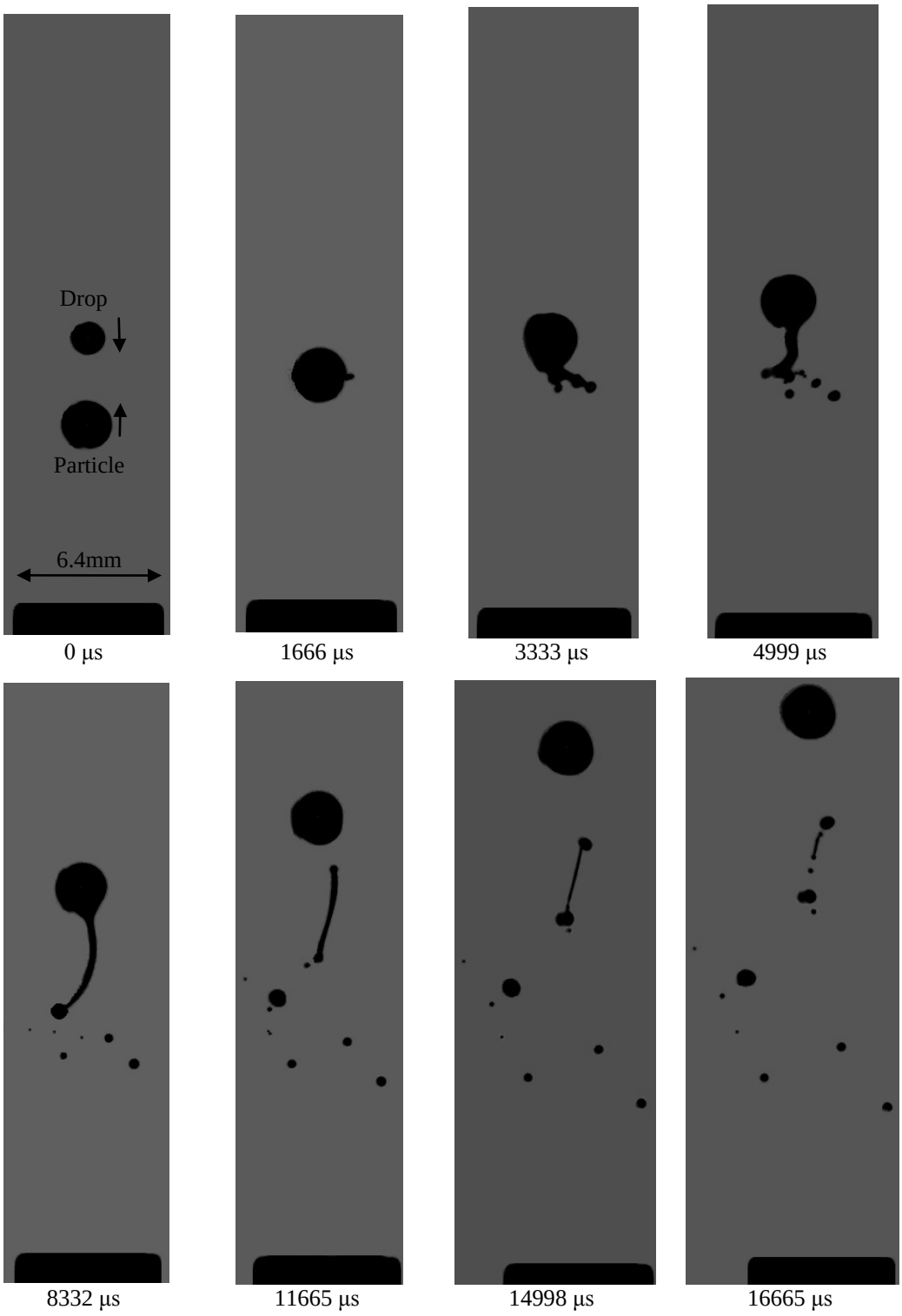

Figure 6-32 Drop-particle head-on collision at 200ºC - off-axis - Enhanced background
Drop: Silicon base heat transfer liquid (Duratherm S) / Particle: Glass bead
Drop: d=1.5 mm, V=0.77 m/s / Particle: d=2 mm, V=1.18 m/s / V_{rltv} = 1.9 m/s

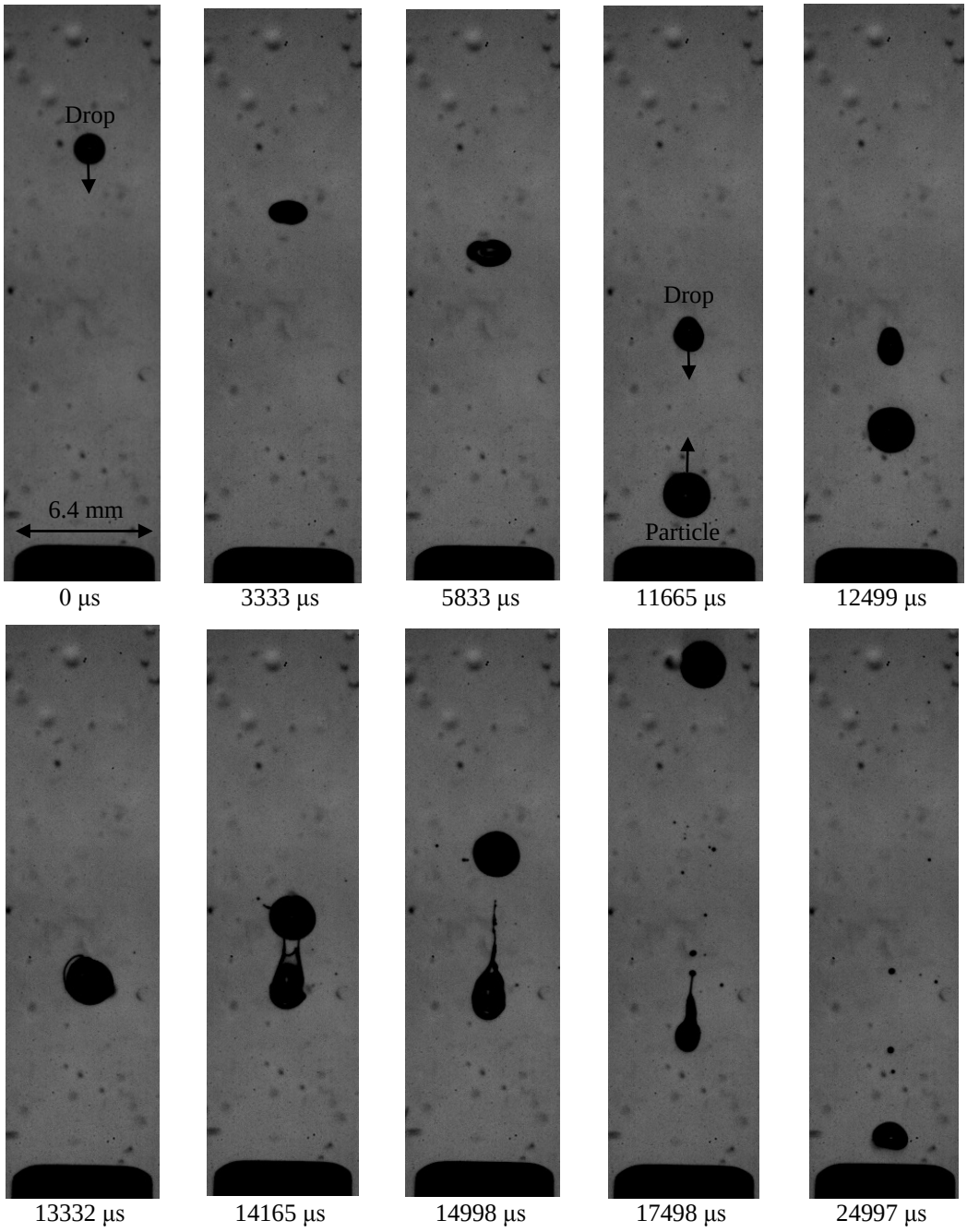

Figure 6-33 Drop-particle head-on collision at 200ºC - off-axis
Drop: Silicon base heat transfer liquid (Duratherm S) / Particle: Glass bead
Drop: d=1.5 mm, V=0.64 m/s / Particle: d=2 mm, V=3.59 m/s / V_{rltv} = 4.2 m/s

6.5 Image Enhancement

As mentioned earlier, it is important to clean the windows to ensure that the images are clear; however, during the experiments, mainly in head-on and high velocity collisions, it is almost impossible to prevent the windows from being smudged (Figure 6-34). As seen in this figure, there are several unwanted visual noises which interfere with further analysis of the images. A simple Matlab command provided in Appendix A was used to remove these noises. The enhanced images shown in Figure 6-35 seem promising.

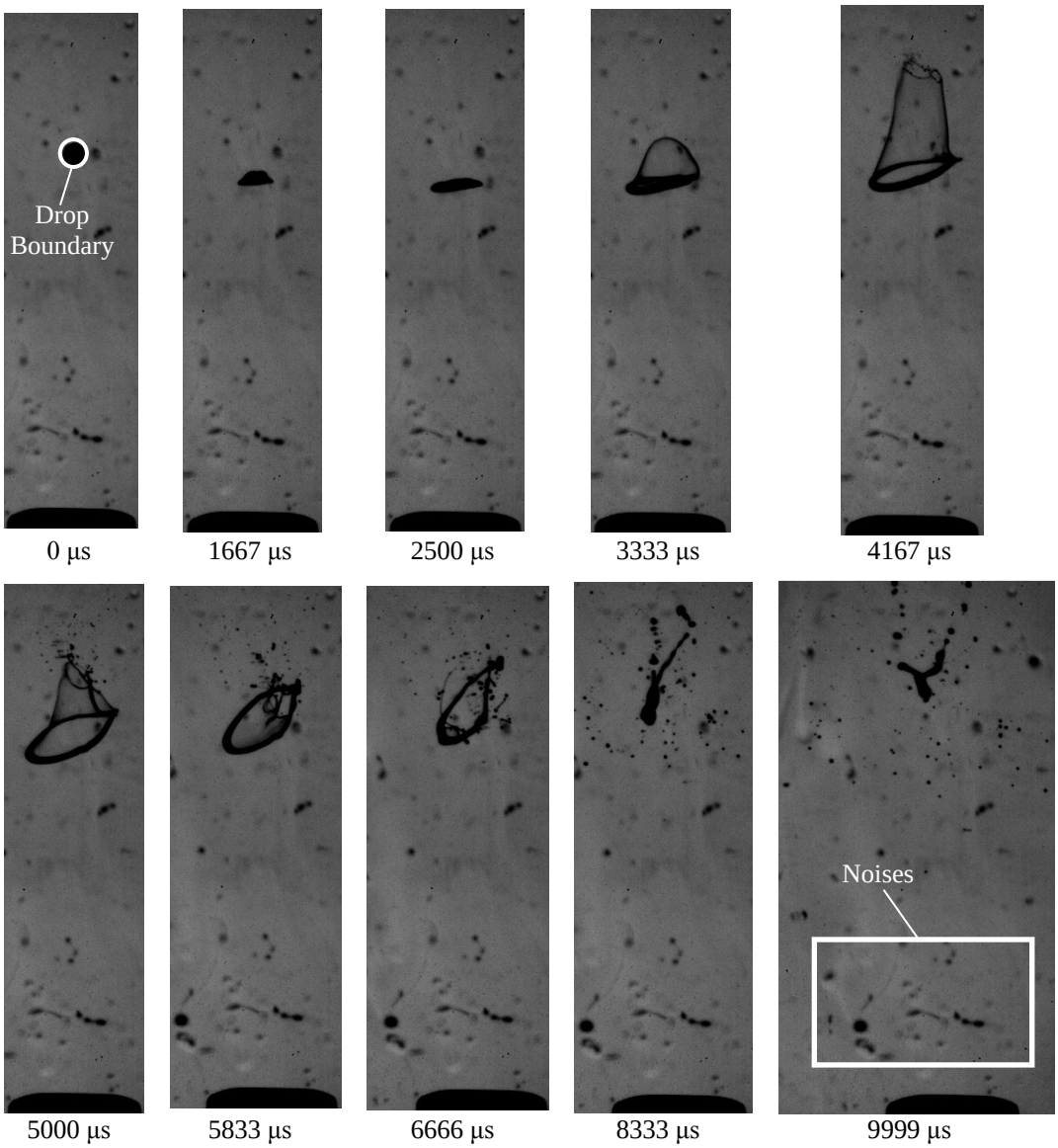

Figure 6-34 Original image frames

There are also several graphical methods to edit the images. A number of the images provided in Figures 6-9 to 6-33 were edited using manual graphical methods. A manual graphical method was used to remove the noises (as seen in on Figure 6-34) and provide a uniform gray background in each image. The approach was to verify the boundary pixels of the drop (see Figure 6-34) and particle in the image and select the color of neighbor pixels outside these boundaries. Converting the color of the entire image (except the drop and particle) to the color of neighbor pixels results in a smooth, clear background in the images. The enhanced image is shown in Figure 6-21.

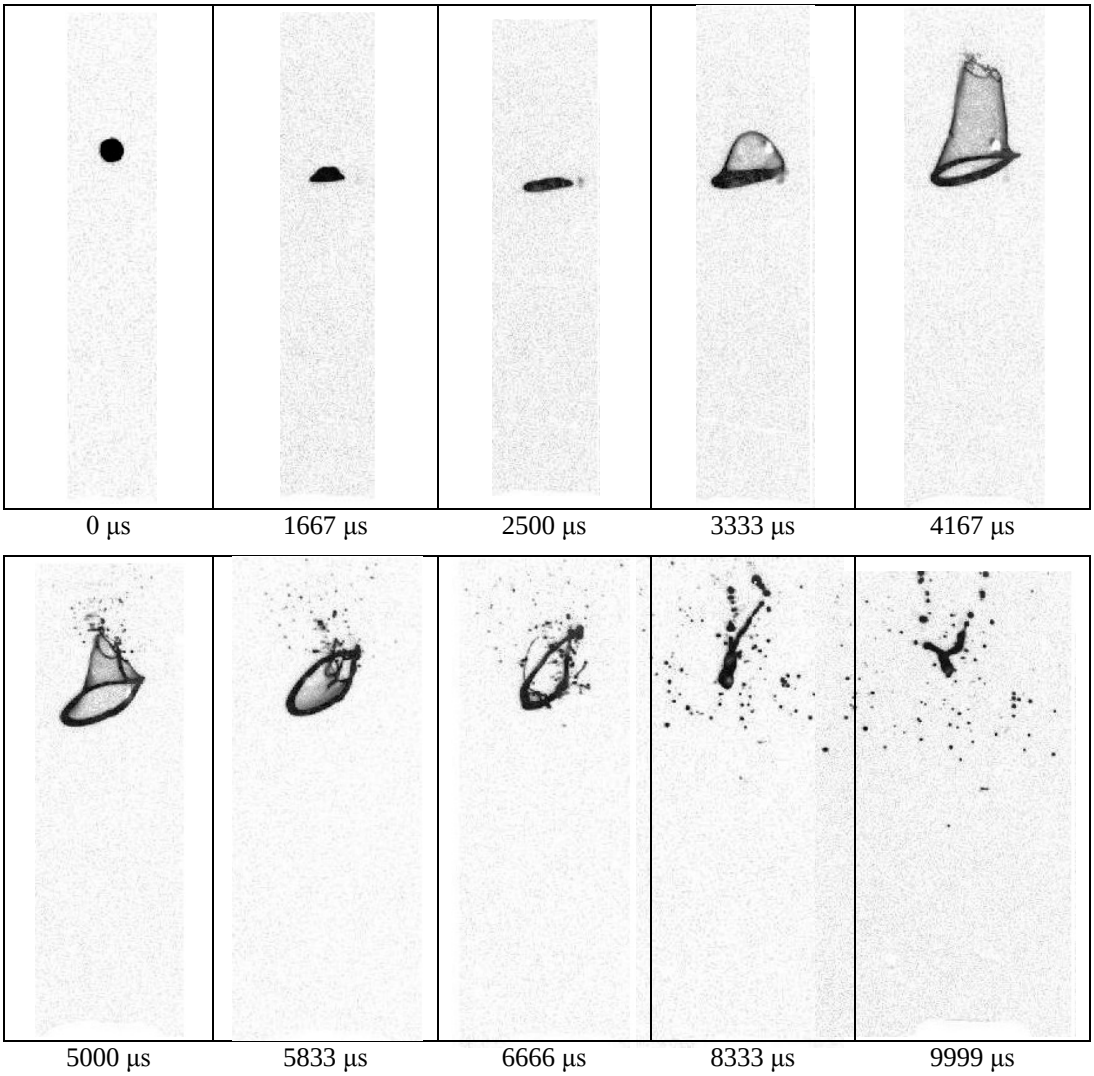

Figure 6-35 Image frames reproduced by Matlab image processing commands
The noises are eliminated from the images (original image frames in Figure 6-34).

Chapter 7
Summary

The fundamental study of the fluidization process was the motivation in this thesis that led to develop an experimental device to simulate the interaction between the individual drop and particle inside a fluidized bed reactor.

7.1 Conclusion

An experimental device was designed, built and tested through a preplanned design process. The House of Quality was used to decide the design options based on the design requirements defined according to the theoretical parameters of the drop-particle impact. The available experimental data on drop-particle impact in ambient temperatures were analyzed and the design values were calculated. The device was designed in detail using the data acquired in basic design and calculations was tested within the design criteria.

The experimental setup consists of the main test device (including a particle launcher, drop generator and temperature cell), heating accessories and controlling system, a triggering-timing system and an imaging system. The device is capable of testing different fluid and particle materials with different sizes; in the first step, two launchers of 1mm and 2mm caliber were built and tested. Two needles with gauges of 27 and 33 were used in the performance test to generate drops of Duratherm S in two 1.5mm and 1.2mm sizes respectively, at 200ºC. The drop sizes generated through one needle varied with fluid properties: either by fluid properties or temperature. The particle velocities between 0.5m/s and 11.3 m/s for the 1mm-caliber launcher were tested at 200 ºC, as were velocities between 0.5 m/s and 6.3 m/s for the 2mm-caliber launcher. In lower temperatures, the velocities achieved by the same spring pre-tension were higher; for instance, velocities of ~15m/s for 2mm- and ~20m/s for 1mm-caliber launchers were tested at 20 ºC. The strongest spring used in those tests was 36371G (with k=0.99 N/mm). The higher limit velocities achieved by the tested springs are already far above the maximum calculated velocities (6 m/s for the 2mm-caliber launcher). The device

provided collision angles between 90º and 180º using a rotating mechanism of the particle launcher. The head-on and right-angled collisions were tested. Different impact parameters can also be reached by a slot implemented in the launcher installation opening.

The maximum temperature of 200ºC at the collision point was also achieved in the performance tests. Since the maximum area covered by the collision outcomes is a few square millimeters around the collision point, it is reasonable to assume that the collision occurs at a constant temperature, although there is a temperature gradient inside the cell.

The device can be employed for two purposes;

- To study the drop-particle impact in an environment with different temperatures
- To study the drop-air jet impact in an environment with different temperatures

7.2 Future Works

Particle launchers were built of two 1mm and 2mm caliber. The next step is to build launchers with lower calibers. A capillary tube with the outside diameter of 1/6" and the inside diameter of 0.02" can be used to make the particle barrel and feeder of a 0.5mm caliber launcher, for instance. The plunger, which has a 0.5mm pin, is very delicate and needs to be used with special care.

The minimum needle gauge found among suppliers was the 33, which produced drops of 1.2mm using Duratherm S at 200ºC. One solution for generating drops below 1mm is to apply Teflon coating on the needle; the melting and maximum operating temperatures of Teflon are 335ºC and 260ºC, respectively.

The delay time provided by the existing timing controller was between 0 and 50ms. To provide delays close to zero, a delay circuit with higher resolution near zero was needed. A new triggering/timing controller box was built to cover low velocity collisions (drop and particle velocities below 0.5 m/s). The new control box should be connected to the old one and tested for lower velocity ranges.

Thermocouples measure the temperature of a single point. By changing the location of the thermocouples, it is possible to record the temperature of different locations; for instance, the collision point, the particle feeder area or the drop generator liquid container. However, using an IR camera is a better solution for determining the temperature of an individual drop or particle in collision.

The device built in this thesis can be developed and employed in drop-air jet impact studies. Conducting a set of performance tests on drop-air jet impact will help to determine this device' ability in new aspect of drop-air jet impact. It will also help to verify the required modifications or developments.

References

1. Fluidization-dynamics: the formulation and applications of a predictive theory for the fluidized state, L.G. Gibilaro, Butterworth-Heinemann, (2001), PP. 1-7
2. Combustion and Gasification in Fluidized Beds, P. Basu, CRC/Taylor and Francis Press, (2006), PP. 1-8
3. Observation of Small Drop Collisions, J.W. Telford and N.S.C. Thorndike, Journal of Meteorology, (1961), Vol. 18, PP.382-387
4. Drop Collision under Condition of Free Fall, R.H. Magarvey and J.W. Geldart Journal of the Atmospheric Sciences, (1962), Vol. 19, PP. 107-113
5. Coalescence and separation in binary collisions of liquid drops, N. Ashgriz and J.Y. Poo, Journal of Fluid Mechechanics, (1990), Vol. 221, PP. 183-204
6. A device for producing controlled collisions between pairs of drops, R.W. Park and E.J. Crosby, Chemical Engineering Science, (1965), Vol. 20, PP.39-45
7. The collision, coalescence, and disruption of water droplets, J.R. Adam, N.R. Lindblad and C.D. Hendricks, Journal of Applied Physics, (1968), Vol. 39, PP. 5173-5180
8. An experimental study of factors which promote coalescence of two colliding drops suspended in water-I, G.F. Scheele and D.E. Leng, Chemical Engineering Science, (1971), Vol. 26, PP. 1867-l 879
9. Collision and breakup of water drops at terminal velocity, J.D McTaggart-Cowan and R. List, Journal of the Atmospheric Sciences, (1975), Vol. 32, PP. 1401-1411
10. An experimental investigation of the influence of electric field on the collision-coalescence of water drops, S.K. Paul, A. Mary Selvam and Bh.V. Ramana Murty, Tellus, (1979), Vol. 31, PP. 279-289
11. Binary collision dynamics of fuel droplets, N. Ashgriz and P. Givi, International Journal of Heat and Fluid Flow, (1987), Vol. 8, PP. 205–210
12. Coalescence efficiencies of fuel droplets in binary collisions, N. Ashgriz and P. Givi, International Communications in Heat and Mass Transfer, (1989), Vol. 16, PP. 11-20
13. An experimental investigation on the collision behaviour of hydrocarbon droplets, Y.J. Jiang, A. Umemura And C.K. Law, Journal of Fluid Mechanics, (1992), Vol. 234, PP. 171-190

14. Regimes of coalescence and separation in droplet collision, By J. Qian and C.K. Law, Journal of Fluid Mechanics, (1997), Vol. 331, PP. 59-80
15. Experiments on droplet collisions, bounce, coalescence and disruption, M.E. Orme, Progress in Energy and Combustion Science, (1997), Vol. 23, PP. 65-79
16. Experiments on the dynamics of droplet collision in a vacuum, K.D. Willis, M.E. Orme, Experiments in Fluids, (2000) , Vol. 29, PP. 347-358
17. Binary droplet collisions in a vacuum environment: an experimental investigation of the role of viscosity, K.D. Willis and M.E. Orme, Experiments in Fluids, (2003), Vol. 34, PP. 28–41
18. Monodisperse sprays for various purposes – Their production and characteristics, G. Brenn, F. Durst, and C. Tropea, Particle and Particle Systems Characterization, (1996) , Vol. 13, PP. 179-185
19. Investigation of the stochastic collisions of drops produced by Rayleigh breakup of two laminar liquid jets, G. Brenn, St. Kalenderski and I. Ivanov, Physics of Fluids, (1997), Vol. 9, PP. 349-364
20. The formation of satellite droplets by unstable binary drop collisions, G. Brenn, D. Valkovska and K. D. Danov, Physics of Fluids, (2001), Vol. 13, PP. 2463-2477
21. Satellite droplet formation by unstable binary drop collisions, G. Brenn and V. Kolobaric, Physics of Fluids, (2006), Vol. 18, PP. 087101(1-18)
22. Diesel–diesel and diesel–ethanol drop collisions, R.-H. Chen, Applied Thermal Engineering, (2007), Vol. 27, PP. 604–610
23. Collision between immiscible drops with large surface tension difference: diesel oil and water, R.-H. Chen and C.-T. Chen, Experiments in Fluids, (2006), Vol. 41, PP.453–461
24. Collision between an ethanol drop and a water drop, T.-C. Gao, R.-H. Chen, J.-Y. Pu and T.-H. Lin, Experiments in Fluids, (2005), Vol. 38, PP. 731–738
25. Binary droplet collision at high Weber number, K.-L. Pan, P.-C. Chou and Y.-J. Tseng, Physical Review, (2009), Vol. 80, PP. 036301(1-8)
26. Collision of a droplet with a hemispherical static droplet on a solid, H. Fujimoto, T. Ogino, H. Takuda, N. Hatta, International Journal of Multiphase Flow, (2001), Vol. 27, PP. 1227-1245
27. Experimental investigation of a single droplet impact onto a sessile drop, N. Nikolopoulos, G. Strotos, K.S. Nikas, M. Gavaises, A. Theodorakakos, M.

Marengo, G.E. Cossali, Atomization and Sprays, (2010), Vol. 20(10), PP. 909–922

28. The onset of fragmentation in binary liquid drop collisions, C. Planchette, E. Lorenceau and G. Brenn, Journal of Fluid Mechechanics, (2012), Vol. 702, PP. 5-25
29. Binary collisions of drops of immiscible liquids, I.V. Roisman, C. Planchette, E. Lorenceau and G. Brenn, Journal of Fluid Mechanics, (2012), Vol. 690, PP. 512-535
30. Liquid encapsulation by binary collisions of immiscible liquid drops, C. Planchettea, E. Lorenceaua, G. Brenn, Colloids and Surfaces A: Physicochemical and Engineering Aspects, (2010), Vol. 365, PP. 89–94
31. Droplet-wall collision: Experimental studies of the deformation and breakup process, Chr. Mundo, M. Sommerfeld and C. Tropea, International Journal of Multiphase Flow, (1995), Vol. 21, PP. 151-173
32. Time evolution of liquid drop impact onto solid, dry surfaces, R. Rioboo, M. Marengo, C. Tropea, Experiments in Fluids, (2002), Vol. 33, PP. 112–124
33. Analysis of impact of droplets on horizontal surfaces, S. Sikalo, M. Marengo, C. Tropea, E.N. Ganic, Experimental Thermal and Fluid Science, (2002), Vol. 25, PP. 503-510
34. Impact of droplets onto inclined surfaces, S. Sikaloa, C. Tropea, E.N. Ganic, Journal of Colloid and Interface Science, (2005), Vol. 286, PP. 661–669
35. Understanding the drop impact phenomenon on soft PDMS substrates, S. Mangili, C. Antonini, M. Marengoa and A. Amirfazli, Soft Matter, (2012), Vol. 8, PP. 10045-10054
36. Evolution of liquid/solid contact area of a drop impinging on a solid surface, H. Fujimoto, H. Shiraishi and N. Hatta, International Journal of Heat and Mass Transfer, (2000), Vol. 43, PP. 1673-1677
37. Entrapment of air at 45º oblique collision of a water drop with a smooth solid surface at room temperature, H. Fujimoto and H. Takuda, International Journal of Heat and Mass Transfer, (2004), Vol. 47, PP. 3301–3305
38. Interaction phenomena of two water droplets successively impacting onto a solid surface, H. Fujimotoa, A.Y. Tongb and H. Takuda, International Journal of Thermal Sciences, (2008), Vol. 47, PP. 229–236

39. The role of dynamic surface tension and elasticity on the dynamics of drop impact, R. Crooks, J. Cooper-White and D.V. Boger, Chemical Engineering Science, (2001), Vol. 56, PP. 5575–5592
40. Dynamics of water spreading on a glass surface, D.C.D. Rouxa and J. Cooper-White, Journal of Colloid and Interface Science, (2004), Vol. 277, PP. 424–436
41. Experimental study on fuel drop impacts onto rigid surfaces: Morphological comparisons, disintegration limits and secondary atomization, A.S. Moita, A.L. Moreira, Proceedings of the Combustion Institute, (2007), Vol. 31, Vol. 2175–2183
42. Drop impact process on a hydrophobic grooved surface, R. Kannan, D. Sivakuma, Colloids and Surfaces A: Physicochemical Engineering Aspects, (2008), Vol. 317, PP. 694–704
43. Impact of Drops on Non-wetting Biomimetic Surfaces, A. Merlen, P. Brunet, Journal of Bionic Engineering, (2009), Vol. 6, PP. 330–334
44. Coalescence of two droplets impacting a solid surface, R. Li, N. Ashgriz, S. Chandra, J.R. Andrews and S. Drappel, Experiments in Fluids, (2010), Vol. 48, PP. 1025–1035
45. Regimes of droplet train impact on a moving surface in an additive manufacturing process, S. Fathi, P. Dickens and F. Fouchal, Journal of Materials Processing Technology, (2010), Vol. 210, PP. 550–559
46. Droplet–surface impact at high pressures, P.M. Dupuy, N. Kleinohl, M. Fernandino, H.A. Jakobsen and H.F. Svendsen, Chemical Engineering Science, (2010), Vol. 65, PP. 5320–5343
47. Breakup of a droplet at high velocity impacting a solid surface, K-L. Pan, K-C. Tseng and C-H. Wang, Experiments in Fluids, (2010), Vol. 48, PP. 143–156
48. Impact force of low velocity liquid droplets measured using piezoelectric PVDF film, A. Sahaya Grinspan and R. Gnanamoorthy, Colloids and Surfaces A: Physicochemical Engineering Aspects, (2010), Vol. 356, PP.162–168
49. Impact patterns and temporal evolutions of water drops impinging on a rotating disc, J-Y Li, X-F Yuan, Q Han, and G Xi, Proceedings of the Institution of Mechanical Engineers C: Journal of Mechanical Engineering Science, (2011), Vol. 226, PP. 956-967

50. Observation of the spreading and receding behavior of a shear-thinning liquid drop impacting on dry solid surfaces, S-M An, S-Y Lee, Experimental Thermal and Fluid Science, (2012), Vol. 37, PP. 37–45
51. Experimental study of drop impacts and spreading on epicarps: Effect of fluid properties, R. Andrade, O. Skurtys and F. Osorio, Journal of Food Engineering, (2012), Vol. 109, PP. 430–437
52. Thermohydrodynamic Study of a Drop Impact against a Heated Surface, V.G. Labeish, Experimental Thermal and Fluid Science, (1994) Vol. 8, PP. 181-194
53. Mapping of impact and heat transfer regimes of water drops impinging on a polished surface, J.D. Bernardin, C.J. Stebbins And I. Mudawar, International Journal of Heat Mass Transfer, (1997), Vol. 40, PP. 247-267
54. An experimental study of high Weber number impact of methoxy-nonafluorobutane $C_4F_9OCH_3$ (HFE-7100) and n-heptane droplets on a heated solid surface, S.L. Manzello and J.C. Yang, International Journal of Heat and Mass Transfer, (2002), Vol. 45, PP. 3961–3971
55. Experiment on the dynamics of a compound drop impinging on a hot surface, S.-L. Chiu and T.-H. Lin, Physics Of Fluids, (2005), Vol. 17, PP. 122103(1-9)
56. On the collision behaviors of a diesel drop impinging on a hot surface, R.-H. Chen, S.-L. Chiu and T.-H. Lin, Experimental Thermal and Fluid Science, (2007), Vol. 32, PP. 587–595
57. Collision of a liquid drop on the edge region of a plate heated, above the Leidenfrost temperature, R.-H. Chen and Y.-L. Huang, Experiments in Fluids, (2009), Vol. 47, PP. 223–237
58. Secondary atomization produced by single drop vertical impacts onto heated surfaces, G.E. Cossali, M. Marengo and M. Santini, Experimental Thermal and Fluid Science, (2005), Vol. 29, PP. 937–946
59. Drop impacts onto cold and heated rigid surfaces: Morphological comparisons, disintegration limits and secondary atomization, A.S. Moita and A.L.N. Moreira, International Journal of Heat and Fluid Flow, (2007), Vol. 28, PP. 735–752
60. Thermally induced secondary drop atomization by single drop impact onto heated surfaces, G.E. Cossali, M. Marengo and M. Santini, International Journal of Heat and Fluid Flow, (2008), Vol. 29, PP. 167–177

61. An experimental study of bouncing Leidenfrost drops: Comparison between Newtonian and viscoelastic liquids, V. Bertola, International Journal of Heat and Mass Transfer, (2009), Vol. 52, PP. 1786–1793
62. Dynamics and temperature of droplets impacting onto a heated wall, G. Castanet, T. Lienart and F. Lemoine, International Journal of Heat and Mass Transfer, (2009), Vol. 52, PP. 670–679
63. Heat transfer during drop impact onto wetted heated smooth and structured substrates: experimental and theoretical study, T. Gambaryan-Roisman, M. Budakli, I.V. Roisman and P. Stephan, Proceedings of 14th International Heat Transfer Conference, (2010), 22769(1-8)
64. Boiling heat transfer during single nanofluid drop impacts onto a hot wall, T. Okawa, K. Nagano and T. Hirano, Experimental Thermal and Fluid Science, (2012), Vol. 36, PP. 78–85
65. High-speed camera investigation of the impingement of single water droplets on oxidized high temperature surfaces, E.R. Negeed, S. Hidaka, M. Kohno, Y. Takata, International Journal of Thermal Sciences, (2013), Vol. 63, PP. 1-14
66. Collision outcome of a water drop on the surface of a deep diesel fuel pool, R.-H. Chen and C.-M. Lai, Proceedings of the Institution of Mechanical Engineers C: Journal of Mechanical Engineering Science, (2011), Vol. 225, PP. 1638-1648
67. The transitional regime between coalescing and splashing drops, M. Rein, Journal of Fluid Mechanics, (1996), Vol. 306, PP. 145-165
68. The entrainment of bubbles by drop impacts, H.C. Pumphrey and P.A. Elmore, Journal of Fluid Mechanics, (1990), Vol. 220, PP. 539-567
69. Short communication On the interaction of a liquid droplet with a pool of hot cooking oil, S.L. Manzello, J.C. Yang and T.G. Cleary, Fire Safety Journal,(2003), Vol. 38, PP. 651–659
70. Droplets splashing upon films of the same fluid of various depths, R.L. Vander Wal, G.M. Berger and S.D. Mozes, Experiments in Fluids, (2006) Vol.40, PP. 33–52
71. The impact and deformation of a viscoelastic drop at the air–liquid interface, S. Pregent, S. Adams, M.F. Butler, T.A. Waigh, Journal of Colloid and Interface Science, (2009), Vol. 331, PP. 163–173

72. Crater evolution after the impact of a drop onto a semi-infinite liquid target, A. Bisighini, G.E. Cossali, C. Tropea and I.V. Roisman, Physical Review, (2010), Vol. 82, 036319(1-11)
73. High-speed visualization of interface phenomena: single and double drop impacts onto a deep liquid layer, A. Bisighini and G.E. Cossali, Journal of Visual Experiments, (2011), Vol. 14, PP. 103–110
74. Normal droplet impact on horizontal moving films: an investigation of impact behaviour and regimes, S.K. Alghoul, C.N. Eastwick and D.B. Hann, Experiments in Fluids, (2011), Vol. 50, PP. 1305–1316
75. Transition between coalescence and bouncing of droplets on a deep liquid pool, H. Zhao, A. Brunsvold and S.T. Munkejord, International Journal of Multiphase Flow, (2011), Vol. 37, PP. 1109–1119
76. Micro-bubble morphologies following drop impacts onto a pool surface, S.T. Thoroddsen, M.J. Thoraval, K. Takehara and T.G. Etoh, Journal of Fluid Mechanics, (2012), Vol. 708, PP. 469-479
77. Interactions between drops and particles in simple shear, P.G. Smith and T.G.M. Van De Ven, Colloids and Surfaces, (1985), Vol. 15, PP. 211-231
78. Experimental investigation of sub-millimetre droplet impingement onto spherical surfaces, Y. Hardalupas, A.M.K.P. Taylor and J.H. Wilkins, International Journal of Heat and Fluid Flow, (1999), Vol. 20, PP. 477-485
79. Experimental investigation of the impact of water droplets on cylindrical objects, L.S. Hung and S.C. Yao, International Journal of Multiphase Flow, (1999), Vol. 25, PP. 1545-1559
80. Droplet–particle collision mechanics with film-boiling evaporation, Y. Ge and L.-S. Fan, Journal of Fluid Mechanics, (2007), Vol. 573, PP. 311–337
81. Impact of drops of surfactant solutions on small targets, A. Rozhkov, B. Prunet-Foch and M. Vignes-Adler, Proceeding of Royal Society A, (2010), Vol. 466, PP. 2897–2916
82. Splash control of drop impacts with geometric targets, G. Juarez, T. Gastopoulos, Y. Zhang, M.L. Siegel and P.E. Arratia, Physical Review, (2012), Vol. 85, PP. 026319 (1-6)
83. Particle-drop Impact in Midair, A. Amirfazli, S. Strzebin, O. Peise, D. Chevrollier, American Physical Sosiety, 64th Annual Meeting Division of Fluid Dynamics, Baltimore, USA, Nov. 20-22, 2011

84. The impact of drops on liquid surfaces and the underwater noise of rain, A. Prosperetti and H.N. Oguz, Annul Review of Fluid Mechanics, (1993), Vol. 25, PP. 577-602
85. The House of Quality, John R. Hauser and Don Clausing, Harvard Business Review, (1988), PP. 1-2
86. MIT open courseware, Nuclear System Design Project, Quality Function Deployment (QFD) and House of Quality, by Dr. Michael Short, Fall 2011
87. QFDonline, (http://www.qfdonline.com) Tutorials and Templates
88. Railgun experiments at the University of Texas Center for Electromechanics, R.J. Hayes, Nuclear Instruments and Methods in Physics Research, (1991), Vol.56/57, PP. 1176-1179
89. A Study of Electrothermal-Launcher Efficiencies and Gas Dynamics, D. Motes, J. Ellzey, S. Levinson, J. Parker, F. Stefani and D. Wetz, IEEE Transactions On Magnetics, (2009), Vol. 45, PP. 568-573
90. J. Webster (ed.), Wiley Encyclopedia of Electrical and Electronics Engineering. Copyright # 1999 John Wiley and Sons, Inc. PP.40-47
91. Symbols acquired from FESTO Didactic standard pneumatic symbols
92. Esco Products, Handbook of Standard and Custom Optical Components
93. Density and surface tension of dioctylphthalate, silicone oil and their solutions, E. Ricci, R. Sangiorgi and A. Passerone, Surface and Coatings Technology, (1986), Vol. 28, PP. 215-223
94. Shin-Etsu Silicone - Silicone Fluid KF-96 Technical Data, Shin-Etsu Chemical Co., Ltd.
95. ZPlus ™ Tech Brief #13, June 2008
96. Lubrication Oil (Engine, Gasoline) Copyright Environment Canada, Emergencies Science and Technology Division
97. TEMPCO Electric Heater Corporation - Engineering Data, Heat Requirement Calculations
98. By the author in The "Photonic Techniques in Fluid Dynamic" course offered by Dr. Nobes - University of Alberta (2011)
99. The 6 DOF clamps are designed and fabricated by Bernie Faulkner at mechanical shop, University of Alberta.

Appendices

Appendix A - Analysis and Calculation Data

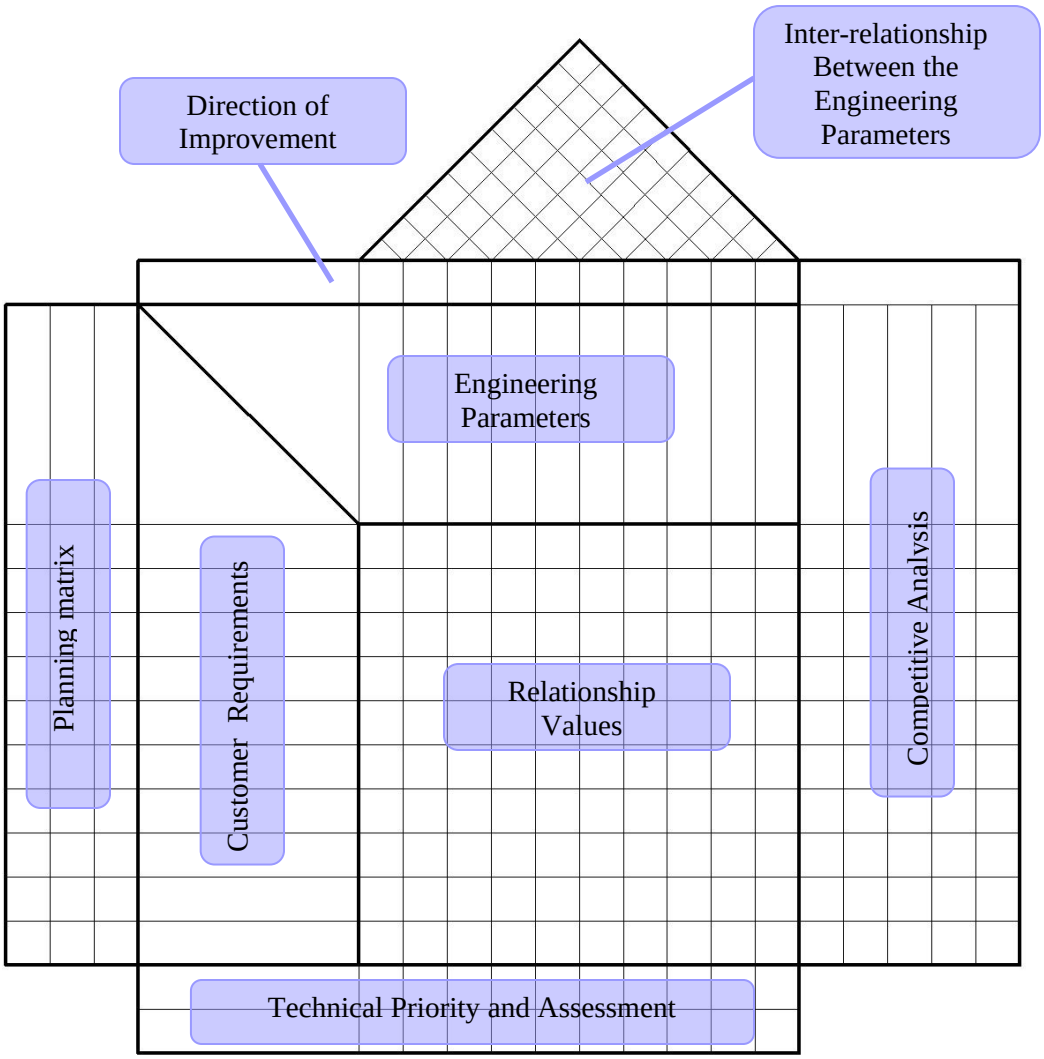

Figure A-1 Conventional House of Quality matrix (adapted and modified from [87])

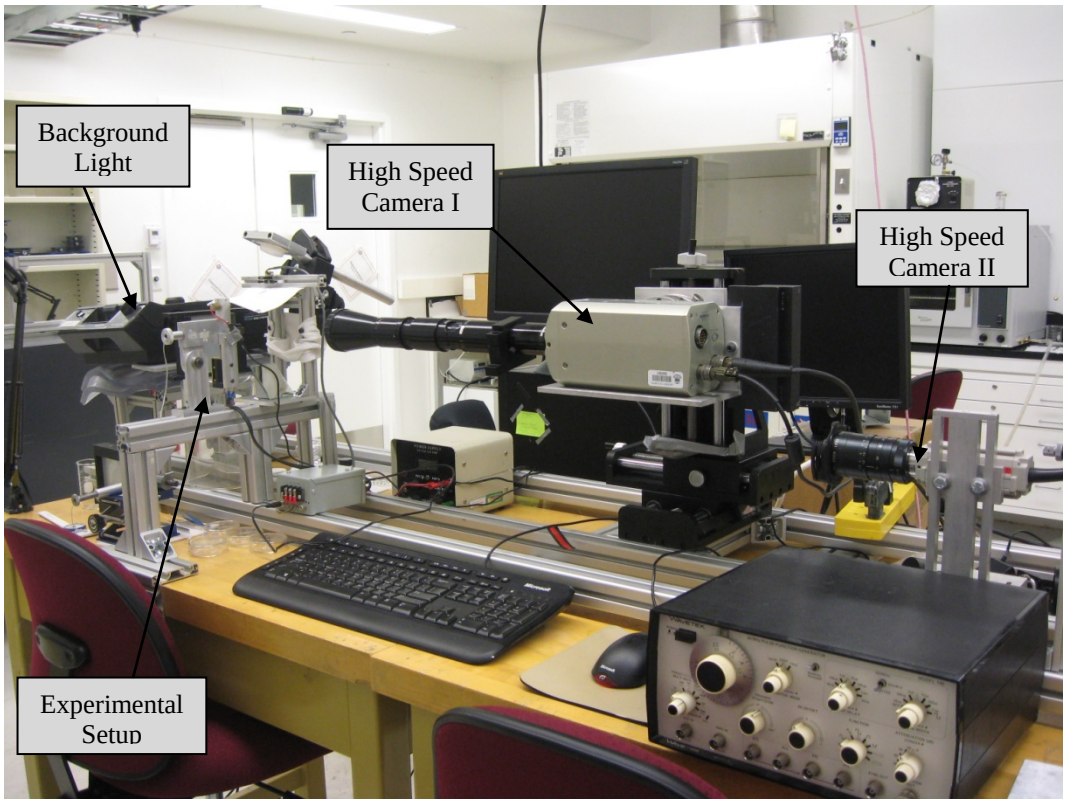

Figure A-2 The setup used for particle-drop collision in room temperature

Table A-1 Particle-drop collision; Acrylic-Water at 20°C

No.	Pre-tension (mm)	Number of Tests	Particle Velocity (m/s)	Particle Size (mm)	Drop Velocity (m/s)	Drop Size (mm)	Relative Velocity (m/s)	Weber Number
1	42	28	0.79	1.59	1.25	2.03	1.48	61.47
2	40	3	1.13	1.59	1.22	2.04	1.66	76.79
3	38	11	1.36	1.59	1.24	2.06	1.84	95.84
4	36	3	1.85	1.59	1.23	1.99	2.22	134.1
5	21-26	14	2.89	1.59	1.25	2.01	3.17	280.17
6	20	15	3.6	1.59	1.24	2.01	3.94	431.8
7	16	28	4.39	1.59	1.24	2.04	4.59	599.86
8	12	1	5.99	1.59	1.22	2.06	6.12	1059.5
Drop Average Velocity and Size:					1.24	2.03		

Table A-2 Particle-Drop collision; Nylon-Water at 20°C

No.	Pre-tension (mm)	Number of Tests	Particle Velocity (m/s)	Particle Size (mm)	Drop Velocity (m/s)	Drop Size (mm)	Relative Velocity (m/s)	Weber Number
1	42	21	0.73	1.59	1.24	2.03	1.45	60.15
2	40	6	1.15	1.59	1.22	2.02	1.68	78.12
3	38	25	1.48	1.59	1.31	2.16	1.93	105.05
4	36	2	1.46	1.59	1.24	2.02	1.92	102.2
5	21-26	26	3.05	1.59	1.21	2.02	3.17	282.06
6	20	10	3.53	1.59	1.22	2.01	3.74	388.04
7	16	17	4.45	1.59	1.24	2.04	4.76	637.54
8	12	5	6.02	1.59	1.24	2.04	6.16	1082.37
Drop Average Velocity and Size:					1.24	2.04		

Table A-3 Particle-Drop collision; Teflon-Water at 20°C

No.	Pre-tension (mm)	Number of Tests	Particle Velocity (m/s)	Particle Size (mm)	Drop Velocity (m/s)	Drop Size (mm)	Relative Velocity (m/s)	Weber Number
1	42	18	0.72	1.59	1.27	2.08	1.45	59.44
2	40	9	1.12	1.59	1.22	2.06	1.65	77.44
3	38	24	1.45	1.59	1.32	1.9	1.91	103.44
4	36	3	1.79	1.59	1.24	2.03	2.15	129.34
5	21-26	8	2.58	1.59	1.22	2.04	2.77	217.02
6	20	8	4.16	1.59	1.25	2.03	4.18	495.1
7	16	11	4.93	1.59	1.25	2.06	5.04	726.25
8	12	5	6.31	1.59	1.22	2.03	6.49	1198.66
Drop Average Velocity and Size:					1.25	2.03		

Table A-4 Velocities corresponding to the Weber numbers 60 and 1200 for silicone oil and motor oil at 200°C comparing with water at 20°C - 2mm drop

We (From Section 4.1.2)	Drop Diameter (m)	Kinematic Surface Tension (defined in section 2.2) σ (m^3/s^2)	Relative Velocity (m/s) (Calculated using Eq. 2-5)
Water @ 20°C			
60	0.002	7.3×10^{-5}	1.48
1200	0.002	7.3×10^{-5}	6.62
Motor oil - EETD 86 (used) @ 200°C			
60	0.002	3.0×10^{-5}	0.95
1200	0.002	3.0×10^{-5}	4.27
kf-96-100 @ 200°C			
60	0.002	1.4×10^{-5}	0.64
1200	0.002	1.4×10^{-5}	2.87

Table A-5 Velocities corresponding to the Weber numbers 60 and 1200 for silicone oil and motor oil at 200°C comparing with water at 20°C - 0.5mm drop

We (From Section 4.1.2)	Drop Diameter (m)	Kinematic Surface Tension (defined in section 2.2) σ (m^3/s^2)	Relative Velocity (m/s) (Calculated using Eq. 2-5)
Water @ 20°C			
60	0.0005	7.3×10^{-5}	2.96
1200	0.0005	7.3×10^{-5}	13.23
Motor oil - EETD 86 (used) @ 200°C			
60	0.0005	3.0×10^{-5}	1.91
1200	0.0005	3.0×10^{-5}	8.53
kf-96-100 @ 200°C			
60	0.0005	1.4×10^{-5}	1.28
1200	0.0005	1.4×10^{-5}	5.73

Table A-6 Velocities corresponding to the Reynolds numbers 2900 and 13000 for silicone oil and motor oil at 200°C comparing with water at 20°C - 2mm drop

Re (From Section 4.1.2)	Drop Diameter (m)	ν (m^2/s)	Relative Velocity (m/s) (Calculated using Eq. 2-4)
Water @ 20°C			
2900	0.002	1.0×10^{-6}	1.46
13000	0.002	1.0×10^{-6}	6.53
Motor oil - EETD 86 (used) @ 200°C			
2900	0.002	2.0×10^{-6}	2.90
13000	0.002	2.0×10^{-6}	13.00
kf-96-100 @ 200°C			
2900	0.002	1.1×10^{-5}	16.53
13000	0.002	1.1×10^{-5}	74.10
kf-96-1000 @ 200°C			
2900	0.002	1.0×10^{-4}	150.80
13000	0.002	1.0×10^{-4}	676.00

Table A-7 Velocities corresponding to the Reynolds numbers 2900 and 13000 for silicone oil and motor oil at 200°C comparing with water at 20°C - 2mm drop

Re (From Section 4.1.2)	Drop Diameter (m)	ν (m^2/s)	Relative Velocity (m/s) (Calculated using Eq. 2-4)
Water @ 20°C			
2900	0.0005	1.0×10^{-6}	5.82
13000	0.0005	1.0×10^{-6}	26.10
Motor oil - EETD 86 (used) @ 200°C			
2900	0.0005	2.0×10^{-6}	11.60
13000	0.0005	2.0×10^{-6}	52.00
kf-96-100 @ 200°C			
2900	0.0005	1.1×10^{-5}	66.12
13000	0.0005	1.1×10^{-5}	296.40
kf-96-1000 @ 200°C			
2900	0.0005	1.0×10^{-4}	603.20
13000	0.0005	1.0×10^{-4}	2704.00

Table A-8 Verification of the collision model

V_p : particle velocity; V_d : drop velocity; EMV: experimental measured velocity; PIC: perfectly inelastic collision; CMC: constant momentum collision

Velocity Range	Particle Material	Before Collision		After Collision			Error	
		EMV	EMV	EMV	PIC Model	CMC Model	EMV/ PIC	EMV/ CMC
		Vp (m/s)	Vd (m/s)	Vp (m/s)	Vp (m/s)	Vp (m/s)	Vp (%)	Vp (%)
Low Velocities	Acrylic	0.71	1.26	0.28	0.26	0.71	8.36	60.47
	Acrylic	0.77	1.28	0.30	0.28	0.77	7.88	60.68
	Acrylic	0.77	1.29	0.29	0.28	0.77	4.20	62.18
	Nylon	0.82	1.22	0.29	0.29	0.82	0.36	64.50
	Nylon	0.77	1.22	0.30	0.27	0.77	8.13	61.22
	Teflon	0.60	1.29	0.32	0.31	0.60	5.13	45.79
	Average	0.74	1.26	0.30	0.28	0.74	5.68	59.14
	Stdev	0.08	0.03	0.01	0.02	0.08	3.12	6.70
High Velocities	Acrylic	4.72	1.23	3.65	1.71	4.72	53.13	22.72
	Acrylic	4.55	1.22	3.58	1.65	4.55	53.94	21.35
	Acrylic	4.61	1.18	3.53	1.67	4.61	52.75	23.33
	Nylon	4.36	1.21	3.47	1.55	4.36	55.22	20.43
	Nylon	4.40	1.20	3.56	1.57	4.40	55.93	19.14
	Nylon	4.60	1.27	3.80	1.64	4.60	56.84	17.43
	Teflon	5.04	1.26	4.59	2.59	5.04	43.50	8.98
	Teflon	3.82	1.21	3.29	1.96	3.82	40.32	13.82
	Average	4.51	1.22	3.68	1.79	4.51	51.45	18.40
	Stdev	0.35	0.03	0.39	0.35	0.35	6.11	4.89

Table A-9 Velocity calculation based on perfectly inelastic collision model in low velocities - head-on collisions

m_d : drop mass; v_d : drop velocity; m_p : particle mass; v_p : particle velocity; α : particle velocity angle with horizon; V : bonding particle-velocity parcel velocity after collision; θ : bonding particle-velocity parcel velocity angle with horizon after collision; V_{Rltv} : relative velocity

Collision Angle	Drop Size	Particle Size	Drop (Before Collision)		Particle (Before Collision)			After Collision			
			m_d (mg)	v_d (m/s)	m_p (mg)	v_p (m/s)	α (D)	m_d+v_d (mg)	θ (D)	V (m/s)	V_{Rltv} (m/s)
Head-on	2 mm	2 mm	3.45	0.6	10.5	0.0	90	13.9	-90	0.00	0.6
			3.45	0.5	10.5	0.1	90	13.9	-90	0.08	0.6
			3.45	0.4	10.5	0.2	90	13.9	90	0.03	0.6
			3.45	0.3	10.5	0.3	90	13.9	90	0.23	0.6
			3.45	0.2	10.5	0.4	90	13.9	90	0.30	0.6
		0.5 mm	3.45	0.6	0.16	0.0	90	3.6	-90	0.00	0.6
			3.45	0.5	0.16	0.1	90	3.6	-90	0.00	0.6
			3.45	0.4	0.16	0.2	90	3.6	-90	0.01	0.6
			3.45	0.3	0.16	0.3	90	3.6	-90	0.01	0.6
			3.45	0.2	0.16	0.4	90	3.6	-90	0.02	0.6
	0.5 mm	2 mm	0.054	1.2	10.5	0.0	90	10.5	-90	0.00	1.2
			0.054	1.0	10.5	0.2	90	10.5	90	0.20	1.2
			0.054	0.8	10.5	0.4	90	10.5	90	0.40	1.2
			0.054	0.6	10.5	0.6	90	10.5	90	0.60	1.2
			0.054	0.4	10.5	0.8	90	10.5	90	0.80	1.2
		0.5 mm	0.054	1.2	0.16	0.0	90	0.21	-90	0.00	1.2
			0.054	1.0	0.16	0.2	90	0.21	-90	0.15	1.2
			0.054	0.8	0.16	0.4	90	0.21	90	0.07	1.2
			0.054	0.6	0.16	0.6	90	0.21	90	0.45	1.2
			0.054	0.4	0.16	0.8	90	0.21	90	0.60	1.2

Table A-10 Velocity calculation based on perfectly inelastic collision model in low velocities - oblique collisions

m_d : drop mass; v_d : drop velocity; m_p : particle mass; v_p : particle velocity; α : particle velocity angle with horizon; V : bonding particle-velocity parcel velocity after collision; θ : bonding particle-velocity parcel velocity angle with horizon after collision; V_{Rltv} : relative velocity

Collision Angle	Drop Size	Particle Size	Drop (Before Collision)		Particle (Before Collision)			After Collision			
			m_d (mg)	v_d (m/s)	m_p (mg)	v_p (m/s)	α (D)	m_d+v_d (mg)	θ (D)	V (m/s)	V_{Rltv} (m/s)
Oblique	2 mm	2 mm	3.45	0.6	10.5	0.0	45	13.9	-90	0.12	0.6
			3.45	0.5	10.5	0.1	45	13.9	-38	0.09	0.6
			3.45	0.4	10.5	0.3	45	13.9	14	0.14	0.6
			3.45	0.3	10.5	0.4	45	13.9	31	0.22	0.6
			3.45	0.2	10.5	0.4	45	13.9	38	0.30	0.6
		0.5 mm	3.45	0.6	0.16	0.0	45	3.6	-90	0.03	0.6
			3.45	0.5	0.16	0.1	45	3.6	-89	0.47	0.6
			3.45	0.4	0.16	0.3	45	3.6	-89	0.37	0.6
			3.45	0.3	0.16	0.4	45	3.6	-88	0.28	0.6
			3.45	0.2	0.16	0.4	45	3.6	-85	0.18	0.6
	0.5 mm	2 mm	0.054	1.2	10.5	0.0	45	10.5	-90	0.01	1.2
			0.054	1.0	10.5	0.3	45	10.5	44	0.26	1.2
			0.054	0.8	10.5	0.5	45	10.5	45	0.48	1.2
			0.054	0.6	10.5	0.7	45	10.5	45	0.69	1.2
			0.054	0.4	10.5	0.9	45	10.5	45	0.87	1.2
		0.5 mm	0.054	1.2	0.16	0.0	45	0.21	-90	0.53	1.2
			0.054	1.0	0.16	0.3	45	0.21	-38	0.18	1.2
			0.054	0.8	0.16	0.5	45	0.21	13	0.27	1.2
			0.054	0.6	0.16	0.7	45	0.21	31	0.43	1.2
			0.054	0.4	0.16	0.9	45	0.21	38	0.60	1.2

Table A-11 Velocity calculation based on perfectly inelastic collision model in low velocities - right-angled collisions

m_d : drop mass; v_d : drop velocity; m_p : particle mass; v_p : particle velocity; α : particle velocity angle with horizon; V : bonding particle-velocity parcel velocity after collision; θ : bonding particle-velocity parcel velocity angle with horizon after collision; V_{Rltv} : relative velocity

Collision Angle	Drop Size	Particle Size	Drop (Before Collision)		Particle (Before Collision)			After Collision			
			m_d (mg)	v_d (m/s)	m_p (mg)	v_p (m/s)	α (D)	m_d+v_d (mg)	θ (D)	V (m/s)	V_{Rltv} (m/s)
Right-angled	2 mm	2 mm	3.45	0.6	10.5	0.0	0	13.9	-90	0.16	0.6
			3.45	0.5	10.5	0.3	0	13.9	-26	0.28	0.6
			3.45	0.4	10.5	0.5	0	13.9	-16	0.35	0.6
			3.45	0.4	10.5	0.5	0	13.9	-13	0.38	0.6
			3.45	0.2	10.5	0.6	0	13.9	-7	0.43	0.6
		0.5 mm	3.45	0.6	0.16	0.0	0	3.6	-90	0.05	0.6
			3.45	0.5	0.16	0.3	0	3.6	-88	0.48	0.6
			3.45	0.4	0.16	0.5	0	3.6	-87	0.38	0.6
			3.45	0.4	0.16	0.5	0	3.6	-86	0.33	0.6
			3.45	0.2	0.16	0.6	0	3.6	-82	0.19	0.6
	0.5 mm	2 mm	0.054	1.2	10.5	0.0	0	10.5	-90	0.01	1.2
			0.054	1.0	10.5	0.7	0	10.5	0	0.67	1.2
			0.054	0.8	10.5	0.9	0	10.5	0	0.90	1.2
			0.054	0.6	10.5	1.0	0	10.5	0	1.03	1.2
			0.054	0.4	10.5	1.1	0	10.5	0	1.12	1.2
		0.5 mm	0.054	1.2	0.16	0.0	0	0.21	-90	0.75	1.2
			0.054	1.0	0.16	0.7	0	0.21	-26	0.56	1.2
			0.054	0.8	0.16	0.9	0	0.21	-16	0.70	1.2
			0.054	0.6	0.16	1.0	0	0.21	-11	0.80	1.2
			0.054	0.4	0.16	1.1	0	0.21	-7	0.86	1.2

Table A-12 Velocity calculation based on CMC model in high velocities

V_D: drop velocity; V_P: particle velocity; h: distance between collision point to drop generator tip
V_{Rltv} : relative velocity

Collision Type	V_D [m/s]	V_P [m/s]	h [mm]	V_{Rltv} [m/s]		V_D [m/s]	V_P [m/s]	h [mm]	V_{Rltv} [m/s]
Head-on (β=180°)	2mm Drop Size					0.5mm Drop Size			
	0.0	5.0	0	5.0		0.0	9.0	0	9.0
	1.0	4.0	51	5.0		1.0	8.0	51	9.0
	1.5	3.5	115	5.0		1.5	7.5	115	9.0
	2.0	3.0	204	5.0		3.0	6.0	459	9.0
	3.0	2.0	459	5.0		5.0	4.0	1275	9.0
	4.0	1.0	816	5.0		7.0	2.0	2498	9.0
	5.0	0.0	1275	5.0		9.0	0.0	4129	9.0
Oblique (β=135°)	2mm Drop Size					0.5mm Drop Size			
	0.0	5.0	0	5.0		0.0	9.0	0	9.0
	1.0	4.2	51	5.0		1.0	8.3	51	9.0
	1.5	3.8	115	5.0		1.5	7.9	115	9.0
	2.0	3.4	204	5.0		3.0	6.6	459	9.0
	3.0	2.4	459	5.0		5.0	4.7	1275	9.0
	4.0	1.3	816	5.0		7.0	2.6	2498	9.0
	5.0	0.0	1275	5.0		9.0	0.0	4129	9.0
Right-angled (β=90°)	2mm Drop Size					0.5mm Drop Size			
	0.0	5.0	0	5.0		0.0	9.0	0	9.0
	1.0	4.9	51	5.0		1.0	8.9	51	9.0
	1.5	4.8	115	5.0		1.5	8.9	115	9.0
	2.0	4.6	204	5.0		3.0	8.5	459	9.0
	3.0	4.0	459	5.0		5.0	7.5	1275	9.0
	4.0	3.0	816	5.0		7.0	5.6	2498	9.0
	5.0	0.0	1275	5.0		9.0	0.8	4129	9.0

Table A-13 Particle trajectory diagram and velocity calculation-horizontal projectile
t: time, $V_{initial}$: initial velocity, α: velocity angle with respect to the horizon, Vx_i: horizontal component of the initial velocity, Vy_i: vertical component of the initial velocity, g: acceleration of gravity, x: horizontal distance to the initial position, y: vertical distance to initial position, Vy: vertical component of the velocity, V_{total}: total velocity

t [s]	$V_{initial}$ [m/s]	α [D]	Vx_i [m/s]	Vy_i [m/s]	g [m/s2]	x [mm]	y [mm]	Vy [m/s]	V_{total} [m/s]
0.00	0.45	0	0.45	0	-9.80	0	0.00	0	0.45
0.01	0.45	0	0.45	0	-9.80	4.5	-0.49	-0.10	0.46
0.02	0.45	0	0.45	0	-9.80	9.0	-1.96	-0.20	0.49
0.03	0.45	0	0.45	0	-9.80	13.5	-4.41	-0.29	0.54
0.04	0.45	0	0.45	0	-9.80	18.0	-7.84	-0.39	0.60
0.05	0.45	0	0.45	0	-9.80	22.5	-12.25	-0.49	0.67
0.06	0.45	0	0.45	0	-9.80	27.0	-17.64	-0.59	0.74
0.07	0.45	0	0.45	0	-9.80	31.5	-24.01	-0.69	0.82
0.08	0.45	0	0.45	0	-9.80	36.0	-31.36	-0.78	0.90
0.09	0.45	0	0.45	0	-9.80	40.5	-39.69	-0.88	0.99
0.10	0.45	0	0.45	0	-9.80	45.0	-49.00	-0.98	1.08

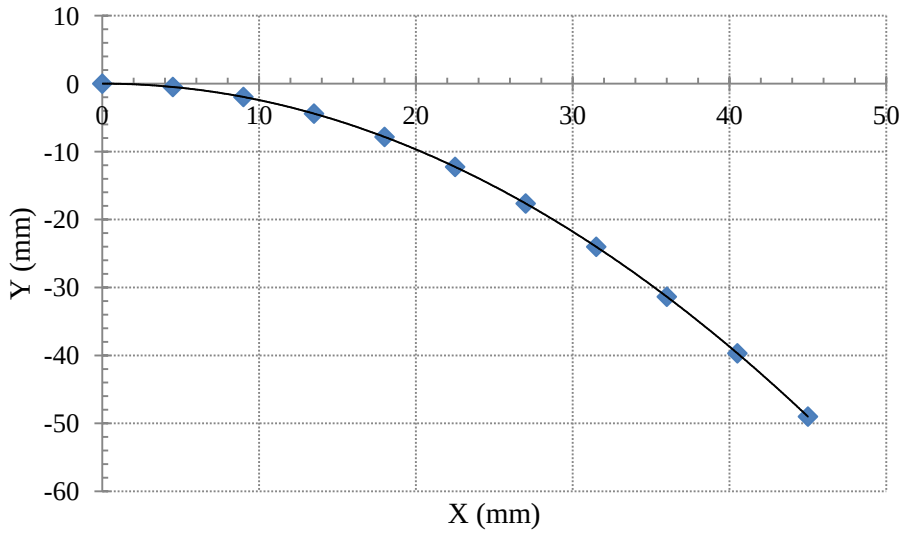

Table A-14 Particle trajectory diagram and velocity calculation-oblique/ vertical projectile
t: time, $V_{initial}$: initial velocity, α: velocity angle with respect to the horizon, Vx_i: horizontal component of the initial velocity, Vy_i: vertical component of the initial velocity, g: acceleration of gravity, x: horizontal distance to the initial position, y: vertical distance to initial position, Vy: vertical component of the velocity, V_{total}: total velocity

t [s]	$V_{initial}$ [m/s]	α [D]	Vx_i [m/s]	Vy_i [m/s]	g [m/s2]	x [mm]	y [mm]	Vy [m/s]	V_{total} [m/s]
0.00	0.30	45	0.21	0.21	-9.80	0.00	0.00	0.21	0.30
0.01	0.30	45	0.21	0.21	-9.80	2.12	1.63	0.11	0.24
0.02	0.30	45	0.21	0.21	-9.80	4.24	2.28	0.02	0.21
0.03	0.30	45	0.21	0.21	-9.80	6.36	1.95	-0.08	0.23
0.04	0.30	45	0.21	0.21	-9.80	8.49	0.65	-0.18	0.28
0.05	0.30	45	0.21	0.21	-9.80	10.61	-1.64	-0.28	0.35
0.06	0.30	45	0.21	0.21	-9.80	12.73	-4.91	-0.38	0.43
0.07	0.30	45	0.21	0.21	-9.80	14.85	-9.16	-0.47	0.52
0.08	0.30	45	0.21	0.21	-9.80	16.97	-14.39	-0.57	0.61
0.09	0.30	45	0.21	0.21	-9.80	19.09	-20.60	-0.67	0.70
0.10	0.30	45	0.21	0.21	-9.80	21.21	-27.79	-0.77	0.80

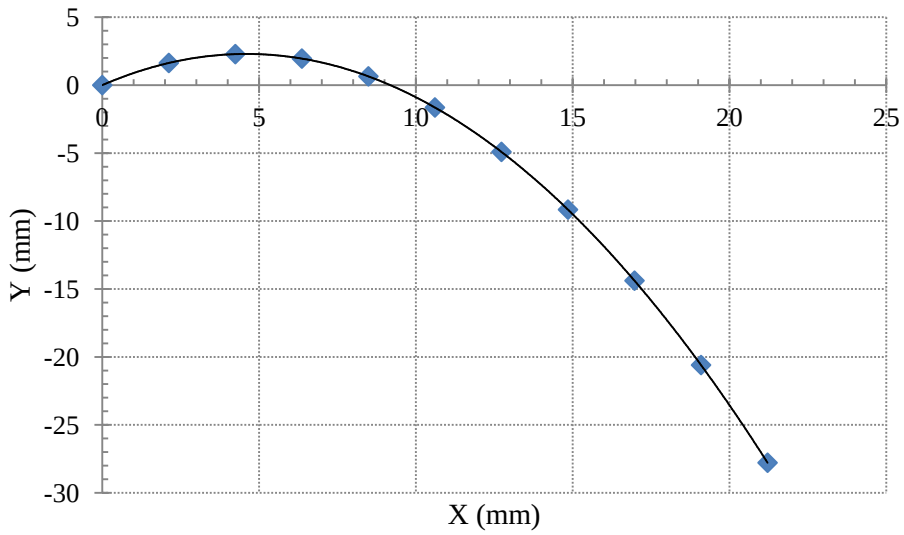

Table A-15 Drop trajectory diagram and velocity calculation-free fall
t: time, Vx_i: horizontal component of the initial velocity, Vy_i: vertical component of the initial velocity, g: acceleration of gravity, x: horizontal distance to the initial position, y: vertical distance to initial position, Vy: vertical component of the velocity

t [s]	Vx_i [m/s]	Vy_i [m/s]	g [m/s2]	x [mm]	y [mm]	Vy [m/s]
0	0	0	-9.8	0	0.00	0.00
0.01	0	0	-9.8	0	-0.49	-0.10
0.02	0	0	-9.8	0	-1.96	-0.20
0.03	0	0	-9.8	0	-4.41	-0.29
0.04	0	0	-9.8	0	-7.84	-0.39
0.05	0	0	-9.8	0	-12.25	-0.49
0.06	0	0	-9.8	0	-17.64	-0.59
0.07	0	0	-9.8	0	-24.01	-0.69
0.08	0	0	-9.8	0	-31.36	-0.78
0.09	0	0	-9.8	0	-39.69	-0.88
0.1	0	0	-9.8	0	-49.00	-0.98
0.11	0	0	-9.8	0	-59.29	-1.08
0.12	0	0	-9.8	0	-70.56	-1.18
0.13	0	0	-9.8	0	-82.81	-1.27
0.14	0	0	-9.8	0	-96.04	-1.37
0.15	0	0	-9.8	0	-110.25	-1.47

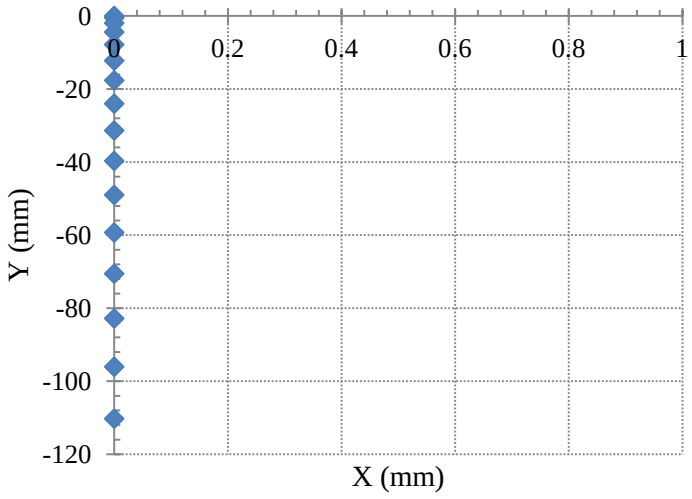

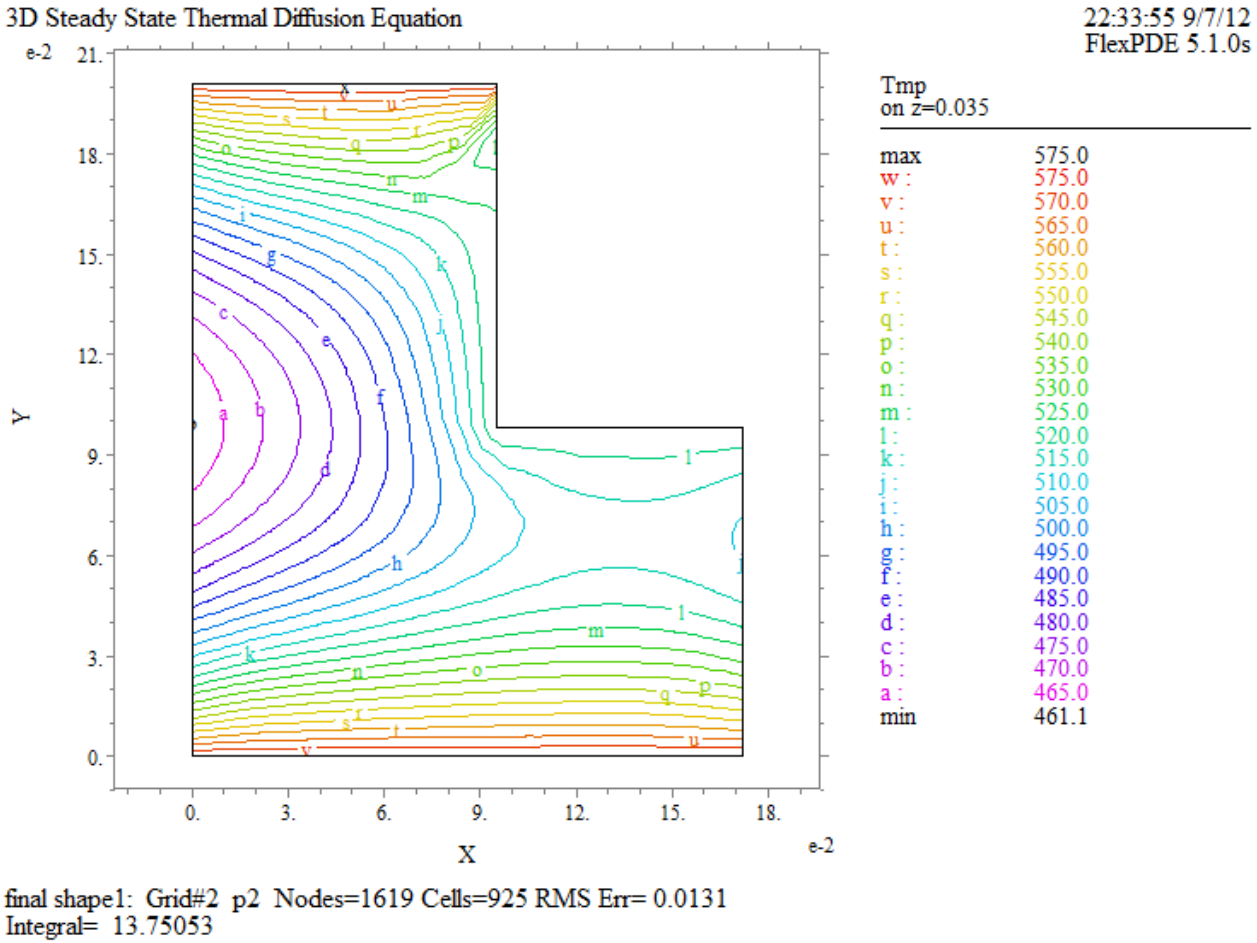

Figure A-3 Temperature gradient inside the cell on xy plane at z=0.035

.

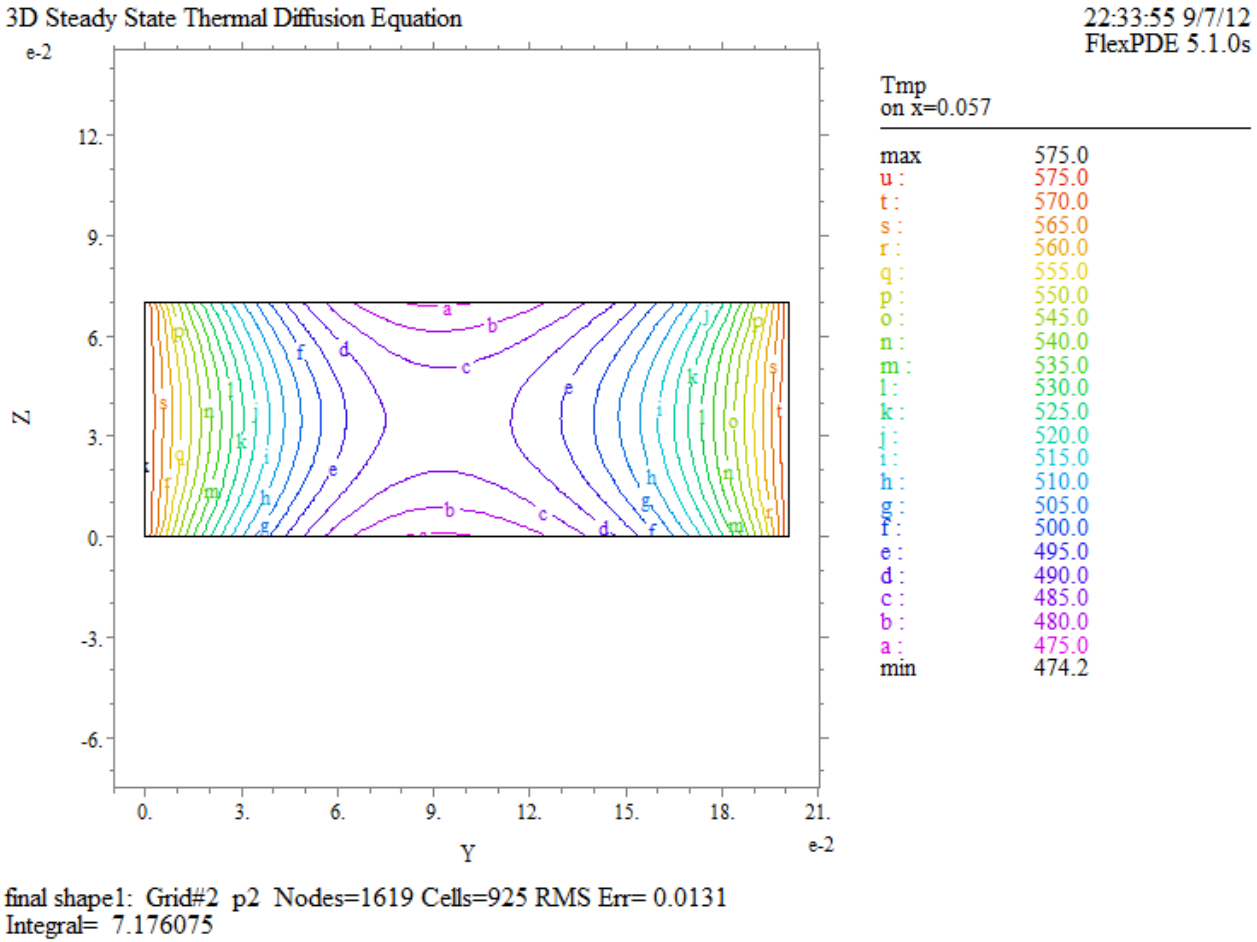

Figure A-4 Temperature gradient inside the cell on zy plane at x=0.057

.

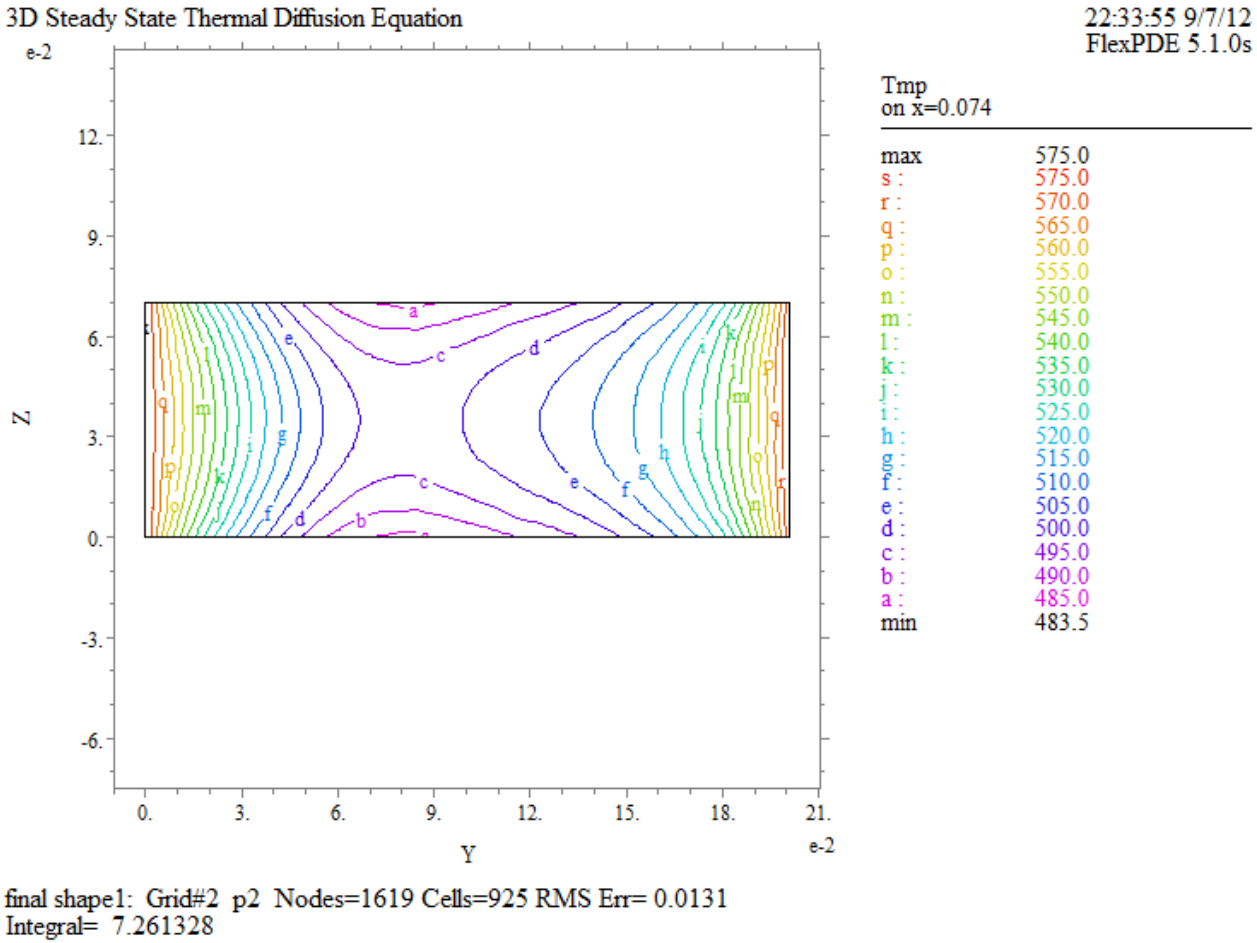

Figure A-5 Temperature gradient inside the cell on zy plane at x=0.074

.

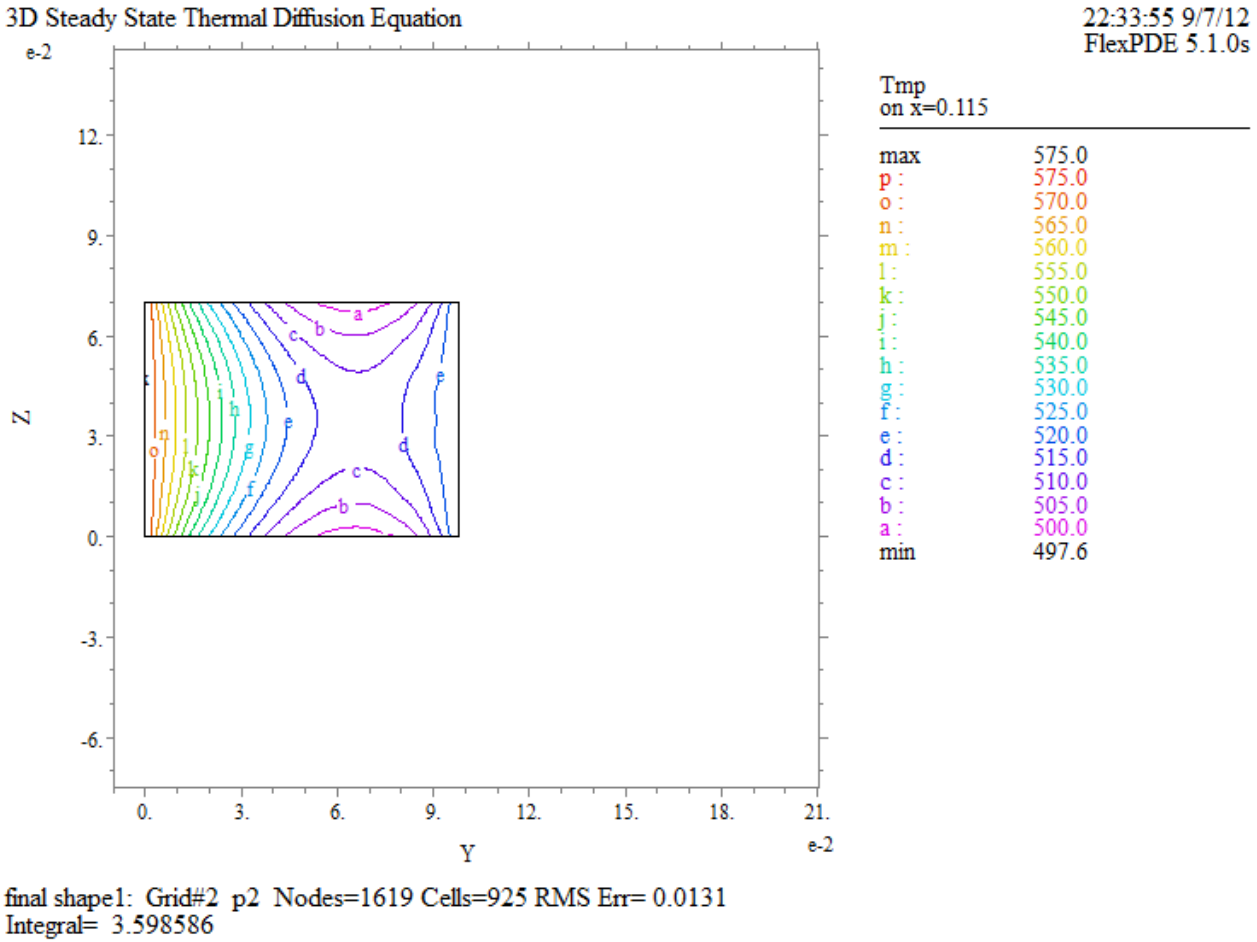

Figure A-6 Temperature gradient inside the cell on zy plane at x=0.115

.

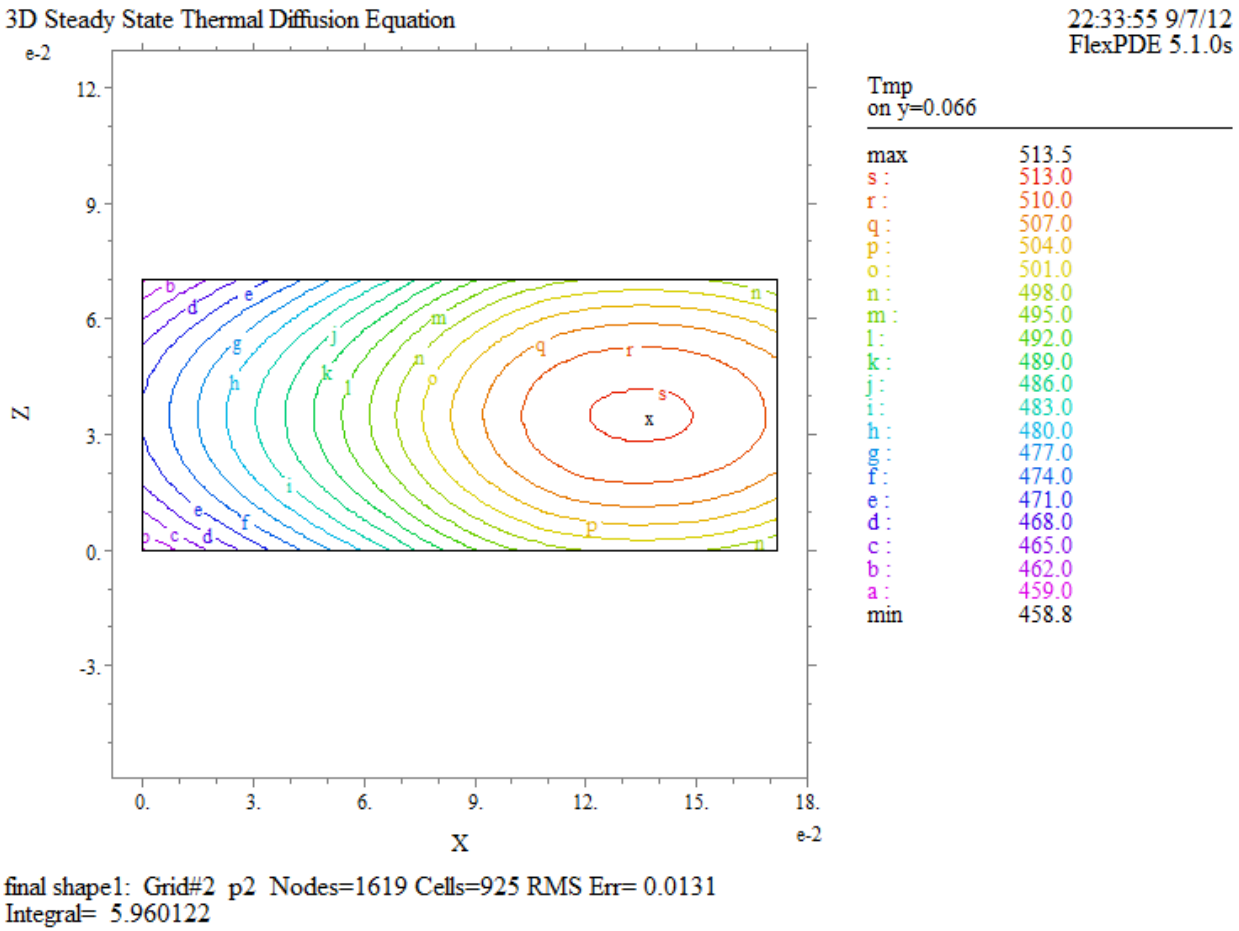

Figure A-7 Temperature gradient inside the cell on xz plane at y=0.066

.

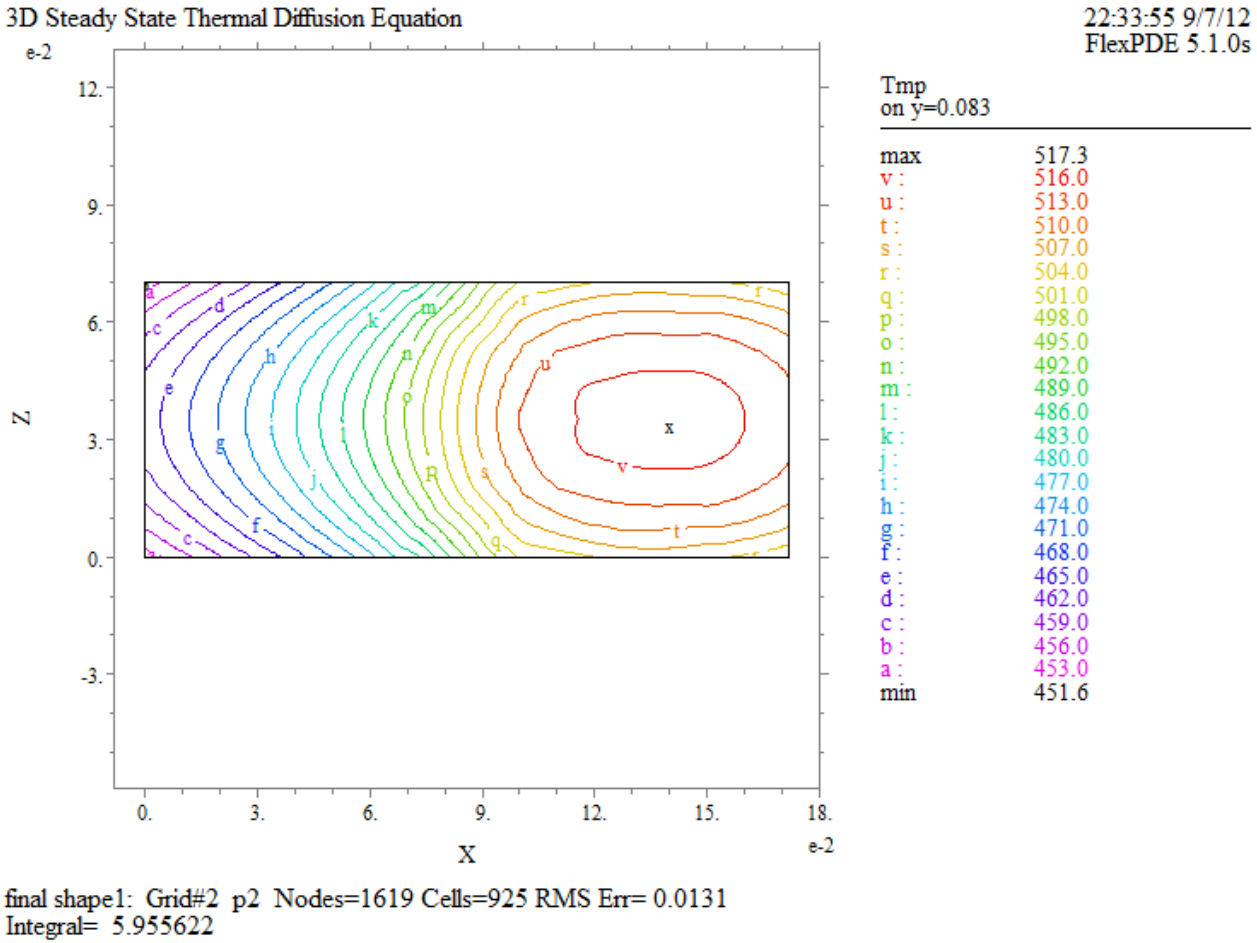

Figure A-8 Temperature gradient inside the cell on xz plane at y=0.083

.

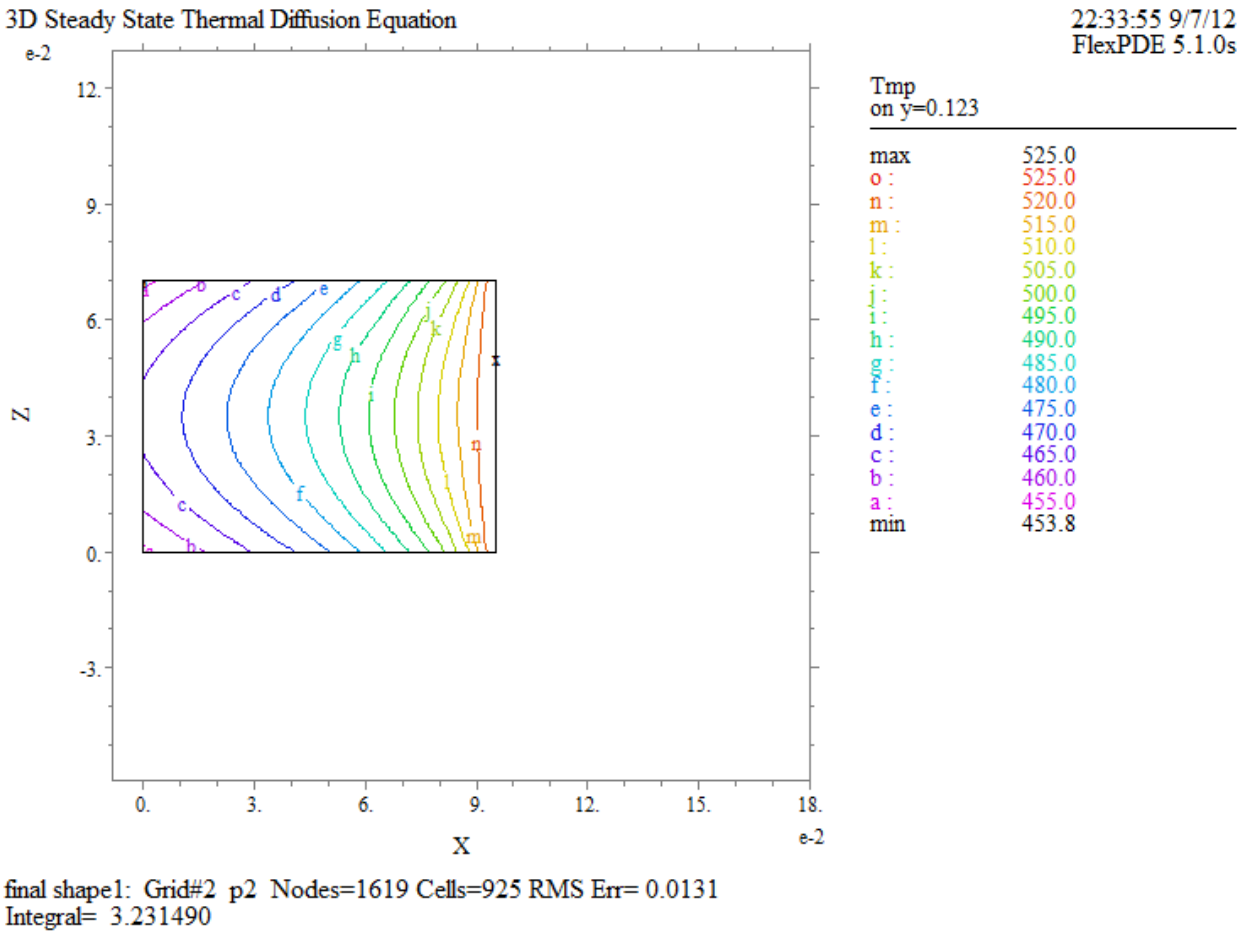

Figure A-9 Temperature gradient inside the cell on xz plane at y=0.123

FlexPDE Code and assumptions:

```
TITLE '3D Steady State Thermal Diffusion Equation'

COORDINATES cartesian3

VARIABLES
Tmp             { Inside Temperature }

DEFINITIONS
k1=4.25  { k1=k(glass)*A1/Thk}
{k(glass)=1.26[W/mK], A1=0.027[m^2] & Thk=0.008[m]-Side Walls }
k2=1.1    { k2=k(glass)*A2/Thk }
{k(glass)=1.26[W/mK], A1=0.007[m^2] & Thk=0.008[m]-Back Wall }
k3=2.2    { k3=k(glass)*A3/Thk}
{k(glass)=1.26[W/mK], A1=0.014[m^2] & Thk=0.008[m]-Front Wall }
Tout=293          { Outside Temperature [K] }
T1=575            { Bottom and Top Wall Temperature [K] }
T2=525            { Launcher Area Temperature  [K] }

EQUATIONS
div(grad(Tmp)) = 0          { 3D Transient Diffusion Equation }

EXTRUSION Z=0,0.07

BOUNDARIES

SURFACE 1 NATURAL(Tmp)=-k1*(Tmp-Tout)          { Heat Flux @ Z=0 (Side Wall) }
  REGION 1
SURFACE 2 NATURAL(Tmp)=-k1*(Tmp-Tout)     { Heat Flux @ Z=0.07 (Side Wall) }
   START(0,0)
VALUE(Tmp)=T1 LINE TO (0.172,0)                          { Fix Temperature @ Top Wall }
NATURAL(Tmp)=-k2*(Tmp-Tout)  LINE TO (0.172,0.098) { Heat Flux @ Back Wall }
VALUE(Tmp)=T2  LINE TO (0.095,0.098)   { Fix Temperature @ Top Launcher Area }
VALUE(Tmp)=T2  LINE TO (0.095,0.201)   { Fix Temperature @ Side Launcher Area }
VALUE(Tmp)=T1  LINE TO (0,0.201)                  { Fix Temperature @ Bottom Wall }
NATURAL(Tmp)=-k3*(Tmp-Tout)  LINE TO CLOSE          { Heat Flux @ Front Wall }

PLOTS

contour(Tmp) on z=0.035

contour(Tmp) on x=0.057
contour(Tmp) on x=0.074
contour(Tmp) on x=0.115

contour(Tmp) on y=0.066
contour(Tmp) on y=0.083
contour(Tmp) on y=0.123

END
```

Table A-16 Spring stiffness based on the potential/kinetic energy balance

m: total plunger mass; v: plunger velocity; x: spring displacement; k: spring stiffness; F_s: spring force; F_f: friction force

m [kg]	v [m/s]	x [mm]	k [N/m]	F_s [N]	F_f [N]
0.0070	0.2	5	11.3	0.06	0.0421
0.0070	1	5	280	1.40	0.0421
0.0070	2	10	280	2.81	0.0421
0.0070	3	8	990	7.92	0.0421
0.0070	4	11	990	10.56	0.0421
0.0070	5	13	990	13.20	0.0421
0.0070	6	12	1900	21.95	0.0421
0.0070	7	11	2800	31.09	0.0421
0.0070	8	11	3700	40.84	0.0421
0.0070	9	12	3700	45.94	0.0421

Table A-17 Spring displacement and force for Gardner spring Inc.

k: spring stiffness; v: plunger velocity; m: total plunger mass; x: spring displacement; F_s: spring force; L_f: spring free length; L_s: spring solid height; L_c: spring available compression length

k [N/mm]	v[m/s]	m[kg]	x[mm]	F_s[N]	L_f [mm]	L_s[mm]	L_c[mm]	Gardner Part#
0.28	0.2	0.007	1.0	0.28	38.1	5.8	32.3	36353G
0.28	1	0.007	5.0	1.40	38.1	5.8	32.3	36353G
0.28	2	0.007	10.0	2.81	38.1	5.8	32.3	36353G
0.99	3	0.007	8.0	7.92	38.1	11.4	26.7	36371G
0.99	4	0.007	10.7	10.56	38.1	11.4	26.7	36371G
0.99	5	0.007	13.3	13.20	38.1	11.4	26.7	36371G
1.9	6	0.007	11.6	21.95	38.1	14.5	23.6	36050G
2.8	7	0.007	11.1	31.09	38.1	17.1	21	36053G
3.7	8	0.007	11.0	40.84	38.1	18.9	19.2	36056G
3.7	9	0.007	12.4	45.94	38.1	18.9	19.2	36056G

Table A-18 Heating energy requirement

m: mass of the temperature cell body; c: specific heat; ΔT: temperature rise; t: heat-up time
A: surface area; k: thermal conductivity; L: wall thickness

Part	m [lb]	c [Btu/lb°F]	ΔT [°F]	t [hr]	Watt
Aluminum Body	7.5	0.24	507	0.17	1604.8
Air	0.0045	0.24	332	0.17	0.6
Total Start-up Heat					1605.4

Part	A [m^2]	k [W/m°K]	L [m]	ΔT [°K]	Watt
Glass Windows	0.075	1.26	0.008	232	2740.5
Insulated Walls	0.03	0.65	0.0254	232	178.1
Total Operating Heat					2918.6

Table A-19 PID temperature controller settings

Operation: Configuration Mode (Part 3 of the Manual)

Section	Command	Setting Value	Comment
Set Points	SET POINT 1	350	The required temperature of the heaters
	SET POINT 2	Blank	Not Required
	OUTPUT REDIRECTION	S1o1	Set point 1 redirected to output 1
Input Type	INPUT TYPE	CA	K type thermocouple
Reading Configuration	DECIMAL POINT	FFF.F	Arbitrary
	TEMPERATURE UNIT	°C	
OUTPUT 1	SELF	dSbL	Disabled
	MINIMUM/PERCENT LOW	0	Minimum heater load (0)
	MAXIMUM/PERCENT HIGH	99	Maximum heater load (99%)
	CONTROL TYPE	PID	
	ACTION TYPE	rurS	Reverse Acting
	AUTO PID	EnbL	Enabled
	ADAPTIVE CONTROL	EnbL	Enabled
	ANTI INTEGRAL	EnbL	Enabled
	START AUTO TUNE PID	EnbL	Enabled
	CYCLE TIME	4	4 sec.
	DAMPING FACTOR	0003	Default Value

Table A-20 Heater connection configuration

Controller Tag	Connected Heaters	Feedback Thermocouple Location
Right	Bottom Heaters: CIR-20207/240 - 1500 W Side Heaters: CIR-10121/240 - 450 W	Inside of Bottom Heaters Block
Left	Top Heaters: CIR-1060/240 - 800 W Launcher Heaters: CIR-1029/240 - 500 W	Inside of Launcher Heaters Block

MATLAB Image Processing Commands:

```
% Loading the raw images
imback = imread('440-back.bmp'); % Background Image
im1 = imread('416.bmp');
im2 = imread('418.bmp');
im3 = imread('420.bmp');
im4 = imread('421.bmp');
im5 = imread('422.bmp');
im6 = imread('423.bmp');
im7 = imread('424.bmp');
im8 = imread('425.bmp');
im9 = imread('426.bmp');
im10 = imread('428.bmp');

% Eliminating the Background Image & Inversing the Image Color
im1 = sum(255 - (imback - im1), 3);
figure
imshow(im1,[])

im2 = sum(255 - (imback - im2), 3);
figure
imshow(im2,[])

im3 = sum(255 - (imback - im3), 3);
figure
imshow(im3,[])

im4 = sum(255 - (imback - im4), 3);
figure
imshow(im4,[])

im5 = sum(255 - (imback - im5), 3);
figure
```

```
imshow(im5,[])

im6 = sum(255 - (imback - im6), 3);
figure
imshow(im6,[])

im7 = sum(255 - (imback - im7), 3);
figure
imshow(im7,[])

im8 = sum(255 - (imback - im8), 3);
figure
imshow(im8,[])

im9 = sum(255 - (imback - im9), 3);
figure
imshow(im9,[])

im10 = sum(255 - (imback - im10), 3);
figure
imshow(im10,[])
```

Appendix B - Datasheets

Table B-1 Physical properties of drop fluids

(Values for motor oil is estimated from data provided in different references)

Fluid	T (°C)	ρ (kg/m^3)	γ (mN/m)	σ=γ/ρ (m^3/s^2)	μ (Ns/m^2)	ν (m^2/s)	α (slope of γ-T)
Water	20	998.21	72.80	7.29×10^{-5}	1.00×10^{-3}	1.0×10^{-6}	0.17
	50	988.00	68.00	6.88×10^{-5}	5.46×10^{-4}	5.5×10^{-7}	
	100	958.40	59.00	6.16×10^{-5}	2.82×10^{-4}	2.9×10^{-7}	
kf-96-100 [93, 94]	25	964.97	20.90	2.17×10^{-5}	9.65×10^{-2}	1.0×10^{-4}	0.06
	100	901.97	16.78	1.86×10^{-5}	2.82×10^{-2}	3.1×10^{-5}	
	200	822.98	11.28	1.37×10^{-5}	9.38×10^{-3}	1.1×10^{-5}	
kf-96-1000 [93, 94]	25	969.97	21.20	2.19×10^{-5}	9.70×10^{-1}	1.0×10^{-3}	0.06
	100	906.97	17.08	1.88×10^{-5}	2.74×10^{-1}	3.0×10^{-4}	
	200	829.98	11.58	1.39×10^{-5}	8.63×10^{-2}	1.0×10^{-4}	
Motor oil EETD 86 (used) [95, 96]	0	894.50	31.60	3.53×10^{-5}	4.52×10^{-1}	5.1×10^{-4}	0.04
	15	884.80	31.00	3.50×10^{-5}	1.75×10^{-1}	2.0×10^{-4}	
	200	765.00	23.60	3.08×10^{-5}	1.57×10^{-6}	2.0×10^{-6}	

Table B-2 Physical properties of construction materials

The values are approximate and average.

Melting point is considered as maximum operating temperature for metals.

Property (at 25°C)	Aluminum	CS	SS	GRE	Thermoplastics (PE-100)	Glass (Borosilicate)
Density [Kg/m3]	2700	7850	7850	1800	960	2230
Thermal Conductivity [W/(mK)]	250	43 (1% Carbon)	16	0.2	0.23	1.14
Thermal Expansion [μm/(mK)]	23	11	17	16	130	3.3
Maximum Operating Temperature [°C]	660	1500	1500	260	100	150

Table B-3 Cartridge heater wattage

Part No.	Sheath Length (in)	Diameter (in)	Watt	W/in	Qty.	Total Wattage
CIR-1029/240	2 1/2	1/4	250	160	2	500
CIR-10121/240	1 1/4	1/4	225	388	2	450
CIR-1060/240	6	1/4	400	93	2	800
CIR-20207/240	2	3/8	500	262	3	1500
					Total Wattage:	3250

Table B-4 Heating control system part list

Item Code	Description	Qty.	Supplier	Country
CN77343	1/16 DIN MICROMEGA® Autotune PID Temperature/Process Controllers	2	Omega	USA
SSR330DC25	Solid State Relays	2	Omega	USA
FHS-7	Heat Sink	2	Omega	USA
KMQSS-062U-6	Thermocouples	2	Omega	USA
KMQSS-062U-12	Thermocouples	2	Omega	USA
SMPW-K-MF	Miniature Thermocouple Connectors	6	Omega	USA
HH506RA	Handheld Thermometer	1	Omega	USA
FB-2	Fuse Blocks	1	Omega	USA
KAX-25	Fuse	4	Omega	USA
GG-K-24-SLE	Thermocouples Wire	100'	Omega	USA
1414PHK	Enclosure	1	Hammond Manufacturing	Canada

Appendix C - Drawings

Table C-1 List of Drawings
The following drawings are provided as built in shop based on the author's design and applying shop modification's made by **Bernie Faulkner**

No.	Title	Drawing No.	Sheet Number
1	Previous Sample Design	MS-001-01	1/1
2	Particle Launcher Parts	AD-001-01	1/1
3	Drop Generator	AD-002-01	1/1
4	Cell Assembly-Step I	AD-003-01	1/5
5	Cell Assembly-Step II	AD-003-01	2/5
6	Cell Assembly-Step III	AD-003-01	3/5
7	Cell Assembly-Step IV	AD-003-01	4/5
8	Cell Assembly-Step V	AD-003-01	5/5
9	Setup Assembly	AD-004-01	1/3
10	Setup Assembly	AD-004-01	2/3
11	Setup Assembly	AD-004-01	3/3
12	Windows-Side Window	TC-001-01	1/2
13	Windows-Front/Back Window	TC-001-01	2/2
14	Window Frames-Side Frames	TC-002-01	1/4
15	Window Frames-Side Frames -Details	TC-002-01	2/4
16	Window Frames-Front Frame	TC-002-01	3/4
17	Window Frames-Back Frame	TC-002-01	4/4
18	Cell Walls-Top Wall	TC-003-01	1/3
19	Cell Walls-Oblique Wall	TC-003-01	2/3
20	Cell Walls-Sides and Bottom Walls	TC-003-01	3/3
21	Heater Blocks-Top Block	TC-004-01	1/4
22	Heater Blocks-Side Block	TC-004-01	2/4
23	Heater Blocks-Bottom Block	TC-004-01	3/4
24	Heater Blocks-Oblique	TC-004-01	4/4
25	Particle Launcher-Launcher Casing	PL-001-01	1/7
26	Particle Launcher-Launcher Hinge	PL-001-01	2/7
27	Particle Launcher-Hinge Clamp	PL-001-01	3/7
28	Particle Launcher-Loading Tube	PL-001-01	4/7
29	Particle Launcher-Adjustment Screw	PL-001-01	5/7
30	Particle Launcher-Plunger	PL-001-01	6/7
31	Particle Launcher-Particle Barrel	PL-001-01	7/7
32	Particle Launcher-Solenoid Pin	PL-002-01	1/1
33	Syringe Connections-I	DG-001-01	1/2
34	Syringe Connections-II	DG-001-01	2/2
35	Heating Control System Electrical Circuit	EL-001-01	1/1
36	Triggering/ Timing Electrical Circuit	EL-002-01	1/1

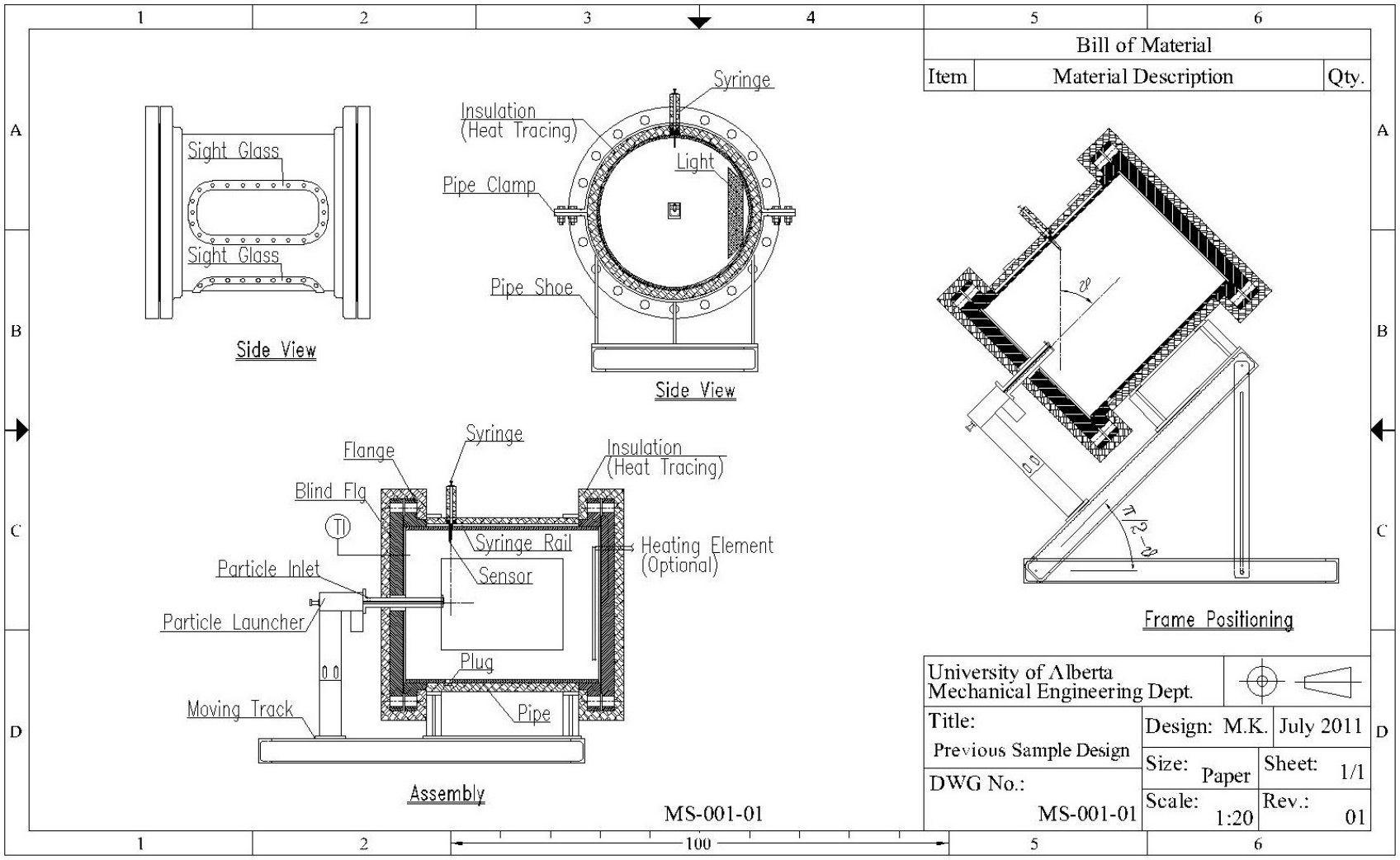
Sight Glass
Sight Glass
Side View
Syringe
Insulation
(Heat Tracing)
Light
Pipe Clamp
Pipe Shoe
Side View
Flange
Syringe
Insulation
(Heat Tracing)
Blind Flg
TI
Syringe Rail
Heating Element
(Optional)
Particle Inlet
Sensor
Particle Launcher
Plug
Moving Track
Pipe
Assembly
MS-001-01
Bill of Material
Item
Material Description
Qty.
Frame Positioning
University of Alberta
Mechanical Engineering Dept.
Title:
Previous Sample Design
Design: M.K.
July 2011
Size: Paper
Sheet: 1/1
DWG No.:
MS-001-01
Scale: 1:20
Rev.: 01
100

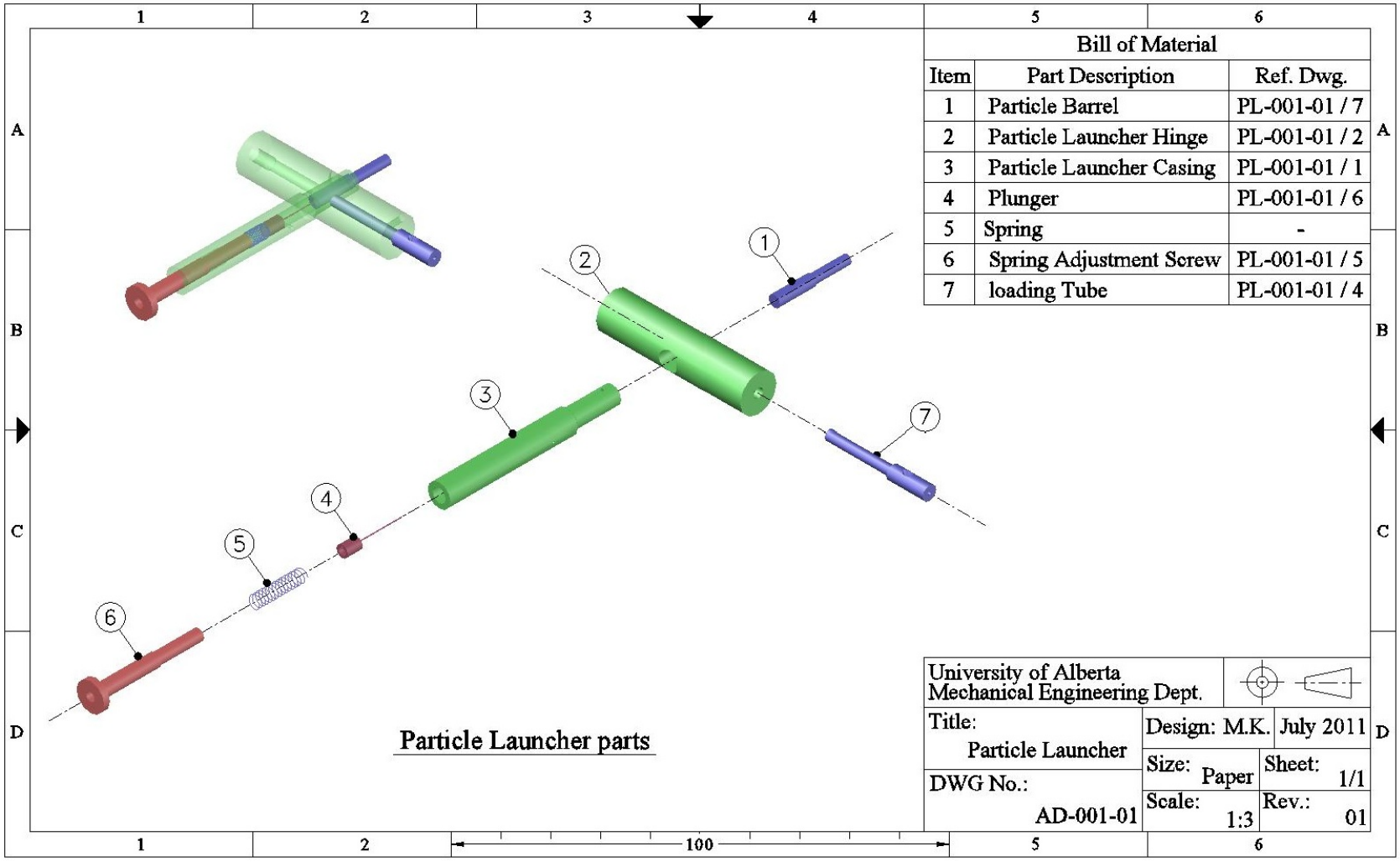

Bill of Material		
Item	Part Description	Ref. Dwg.
1	Particle Barrel	PL-001-01 / 7
2	Particle Launcher Hinge	PL-001-01 / 2
3	Particle Launcher Casing	PL-001-01 / 1
4	Plunger	PL-001-01 / 6
5	Spring	-
6	Spring Adjustment Screw	PL-001-01 / 5
7	loading Tube	PL-001-01 / 4

University of Alberta Mechanical Engineering Dept.			
Title: Particle Launcher	Design: M.K.	July 2011	
	Size: Paper	Sheet: 1/1	
DWG No.: AD-001-01	Scale: 1:3	Rev.: 01	

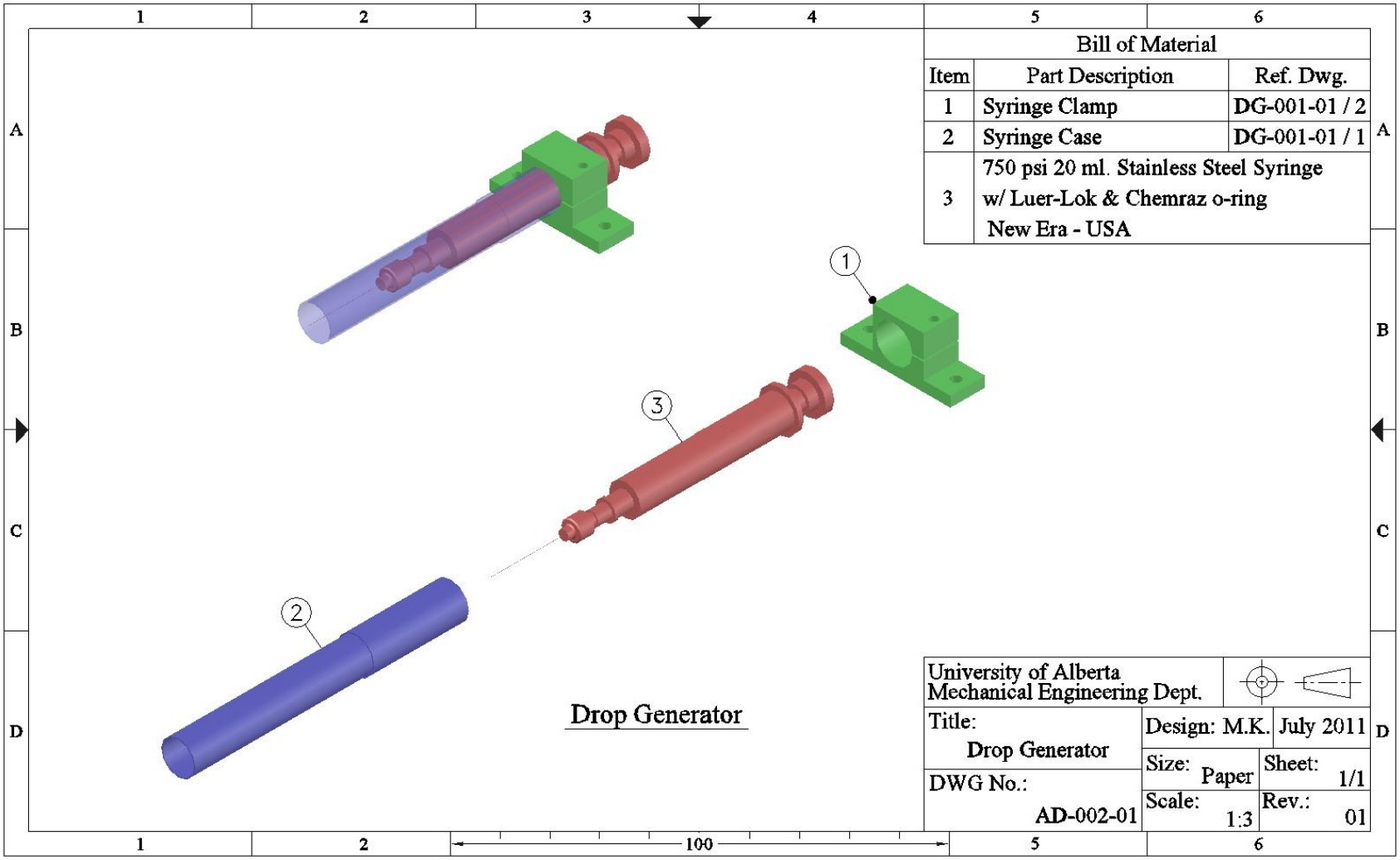
1
2
3
4
5
6
A
B
C
D
Bill of Material
Item | Part Description | Ref. Dwg.
1 | Syringe Clamp | DG-001-01 / 2
2 | Syringe Case | DG-001-01 / 1
3 | 750 psi 20 ml. Stainless Steel Syringe w/ Luer-Lok & Chemraz o-ring New Era - USA
1
2
3
Drop Generator
100
University of Alberta
Mechanical Engineering Dept.
Title:
Drop Generator
Design: M.K.
July 2011
Size:
Paper
Sheet:
1/1
DWG No.:
AD-002-01
Scale:
1:3
Rev.:
01

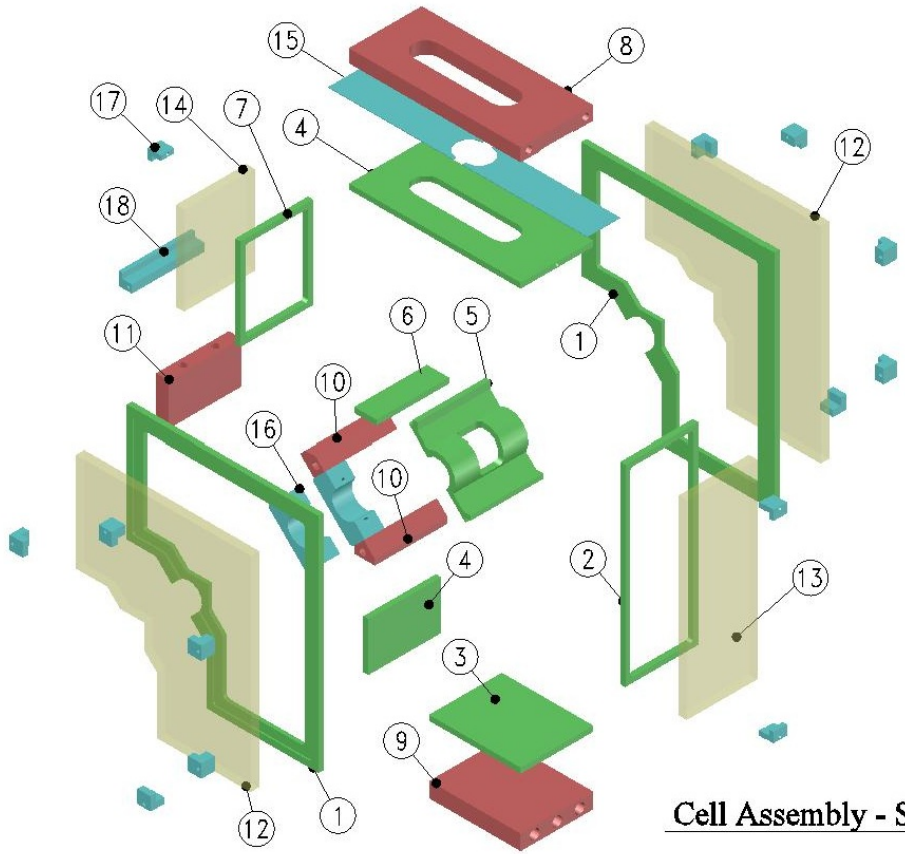

Cell Assembly - Step I

Bill of Material

Item	Part Description	Ref. Dwg.
1	Side Window Frame	TC-001-02 / 1
2	Front Wall Frame	TC-001-02 / 3
3	Bottom Wall	TC-001-03 / 3
4	Lower Side Wall	TC-001-03 / 3
5	Oblique Wall	TC-001-03 / 2
6	Upper Side Wall	TC-001-03 / 3
7	Back Wall Frame	TC-001-02 / 4
8	Top Heater Block	TC-001-04 / 1
9	Bottom Heater Block	TC-001-04 / 3
10	Oblique Heater Blocks	TC-001-04 / 4
11	Side Heater Block	TC-001-04 / 2
12	Side Window	TC-001-01 / 1
13	Front Window	TC-001-01 / 2
14	Back Window	TC-001-01 / 2
15	Top Slide Gates	DG-001-01 / 1
16	Hinge Clamp	PL-001-01 / 3
17	Glass Clamps	TC-001-02 / 2
18	Glass Clamps	TC-001-02 / 2

University of Alberta
Mechanical Engineering Dept.

Title: Cell Assembly

Design: M.K. July 2011

DWG No.: AD-003-01

Size: Paper

Sheet: 1/5

Scale: 1:5

Rev.: 01

100

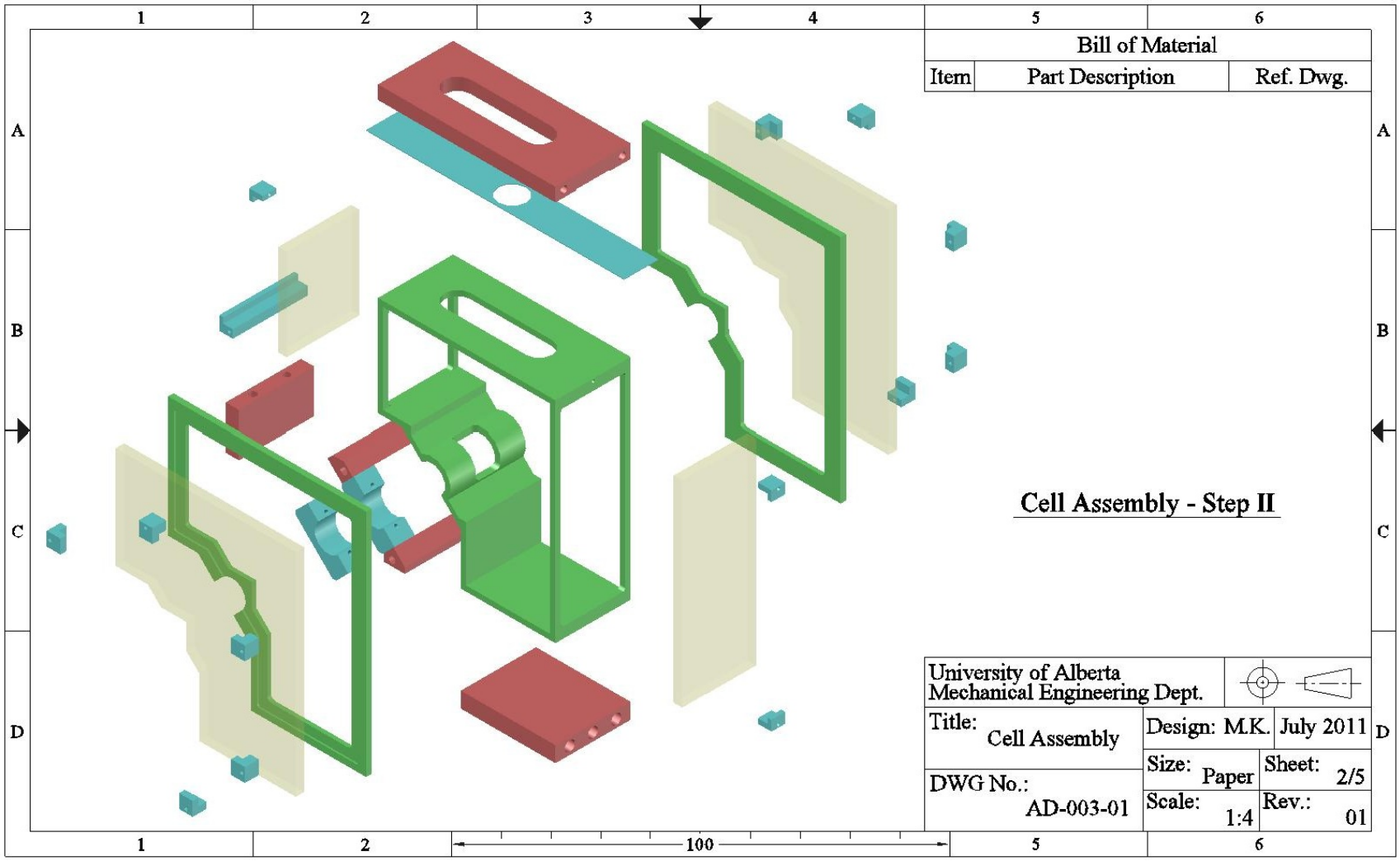
Bill of Material
Item
Part Description
Ref. Dwg.
Cell Assembly - Step II
University of Alberta
Mechanical Engineering Dept.
Title: Cell Assembly
Design: M.K.
July 2011
Size: Paper
Sheet: 2/5
DWG No.: AD-003-01
Scale: 1:4
Rev.: 01
100

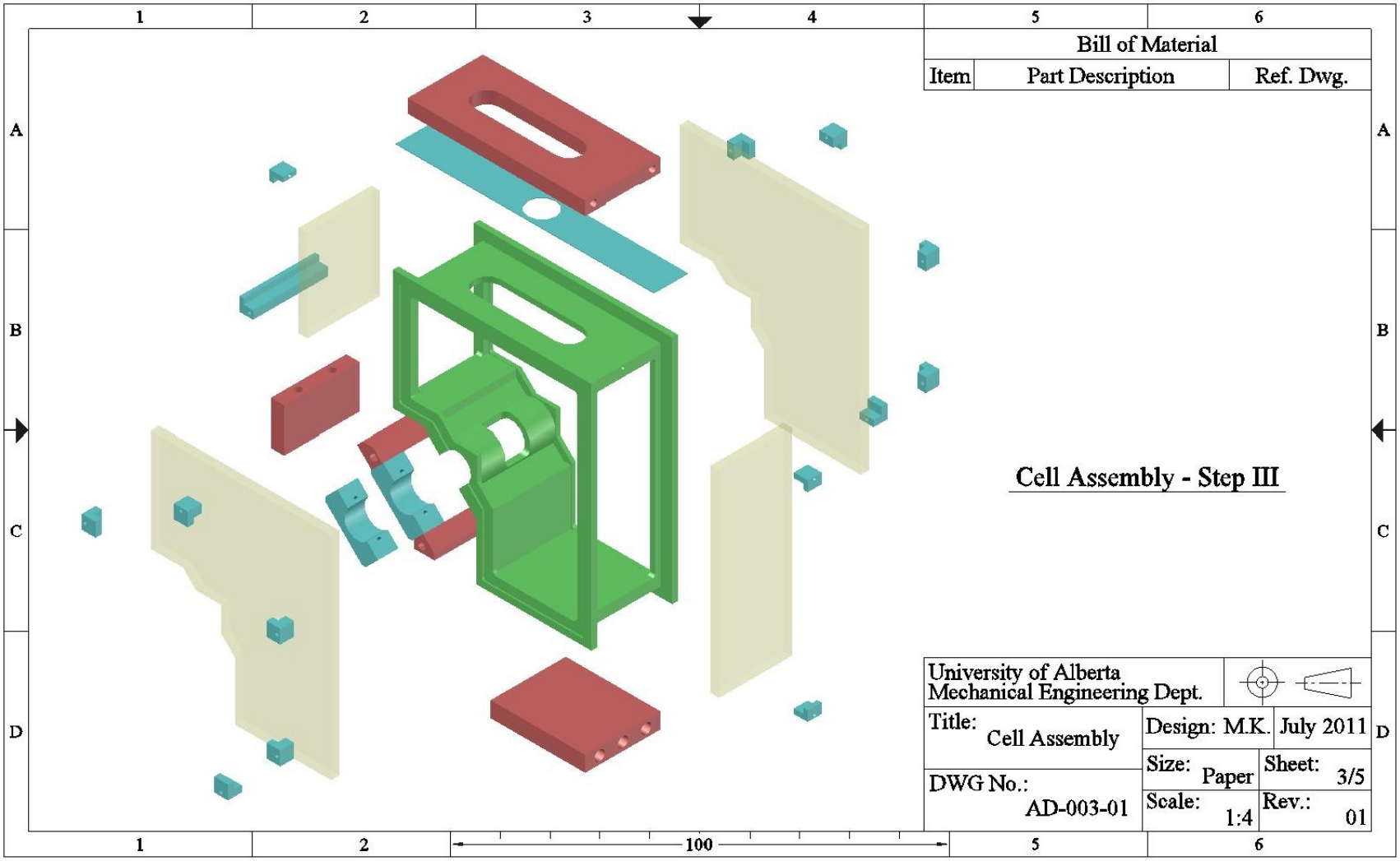
Bill of Material
Item
Part Description
Ref. Dwg.
Cell Assembly - Step III
University of Alberta
Mechanical Engineering Dept.
Title: Cell Assembly
Design: M.K.
July 2011
Size: Paper
Sheet: 3/5
DWG No.: AD-003-01
Scale: 1:4
Rev.: 01
100

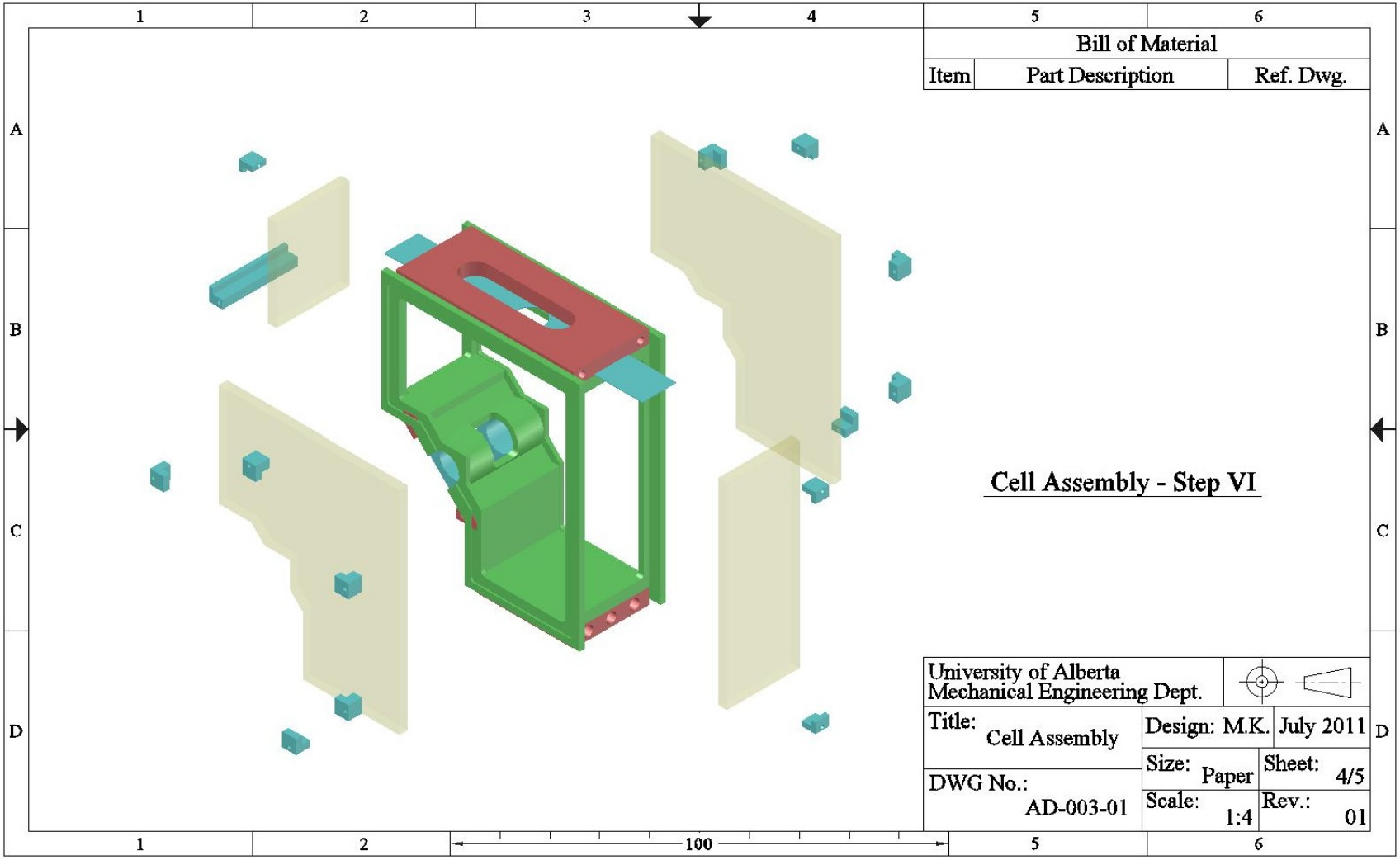
1
2
3
4
5
6
A
B
C
D
Bill of Material
Item
Part Description
Ref. Dwg.
Cell Assembly - Step VI
University of Alberta
Mechanical Engineering Dept.
Title: Cell Assembly
Design: M.K. July 2011
Size: Paper
Sheet: 4/5
DWG No.: AD-003-01
Scale: 1:4
Rev.: 01
100

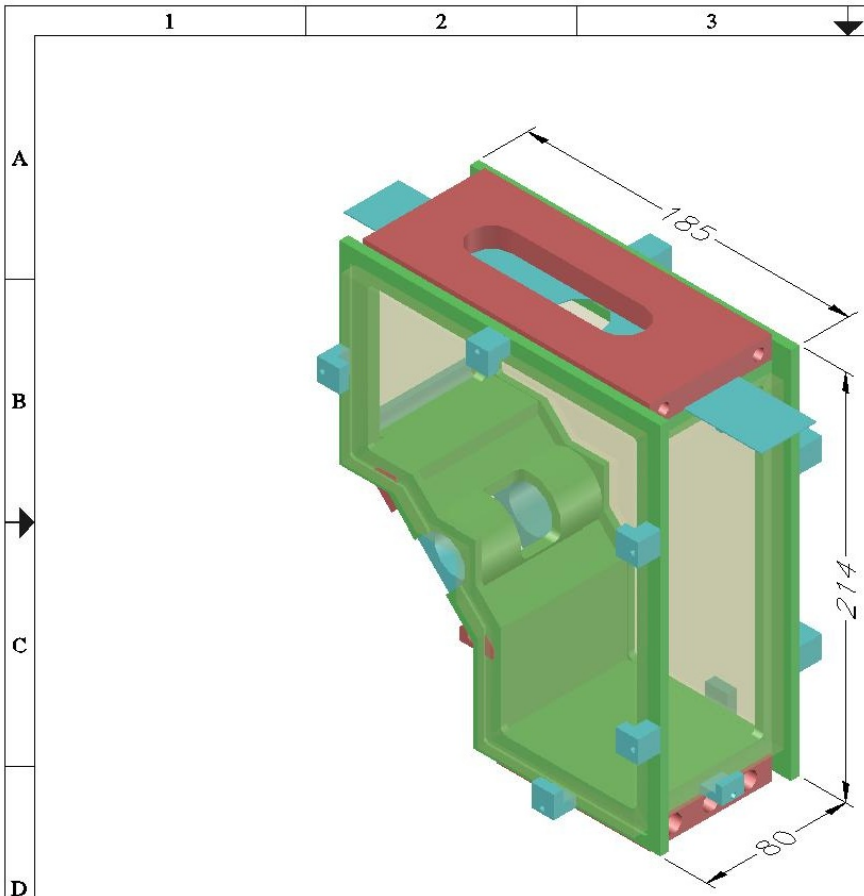

Bill of Material

Item	Part Description	Ref. Dwg.

Cell Assembly - Step V

University of Alberta Mechanical Engineering Dept.		
Title: Cell Assembly	Design: M.K.	July 2011
	Size: Paper	Sheet: 5/5
DWG No.: AD-003-01	Scale: 1:3	Rev.: 01

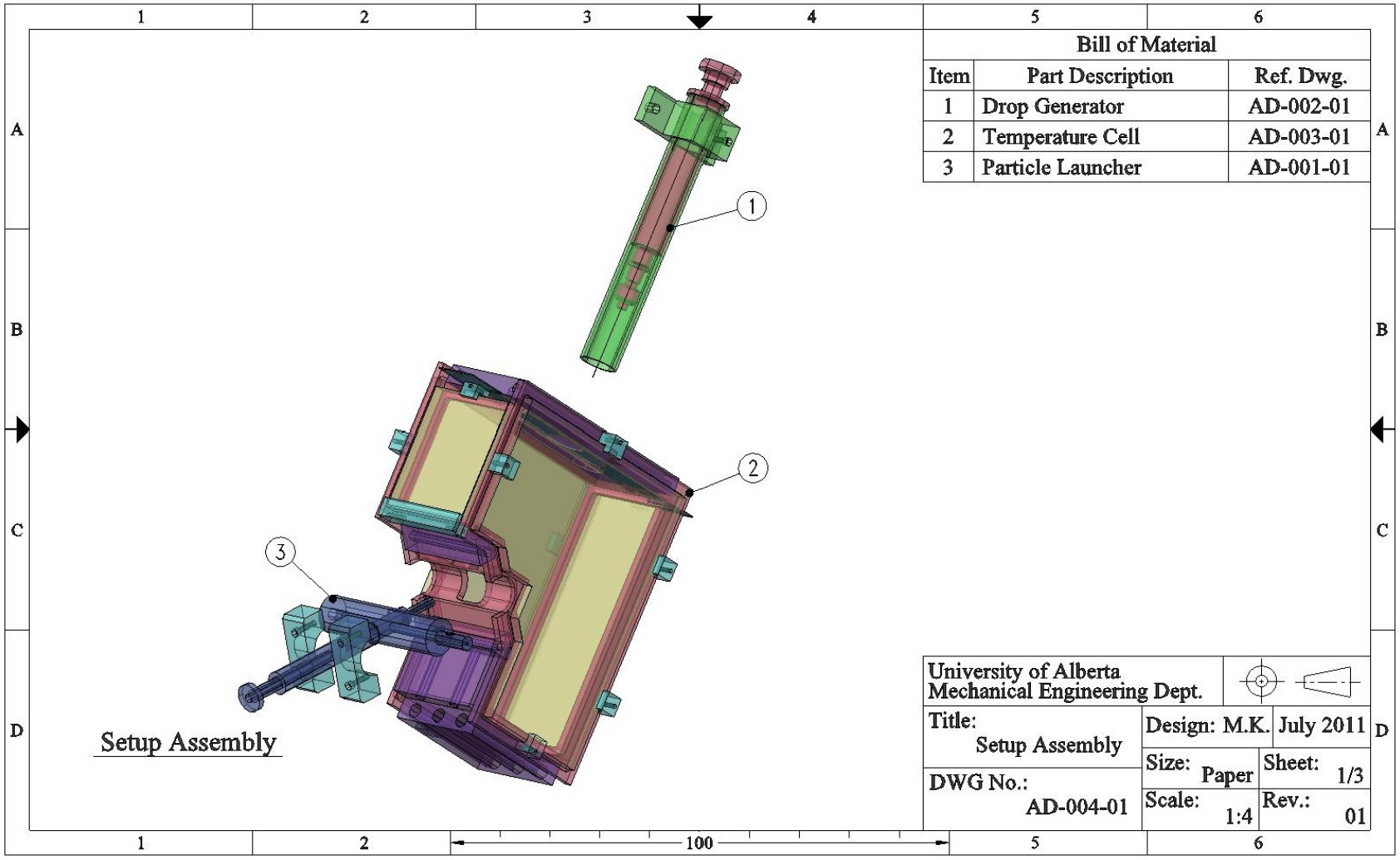
1
2
3
Setup Assembly
Bill of Material
Item | Part Description | Ref. Dwg.
1 | Drop Generator | AD-002-01
2 | Temperature Cell | AD-003-01
3 | Particle Launcher | AD-001-01
University of Alberta
Mechanical Engineering Dept.
Title: Setup Assembly
Design: M.K. July 2011
Size: Paper
Sheet: 1/3
DWG No.: AD-004-01
Scale: 1:4
Rev.: 01
100

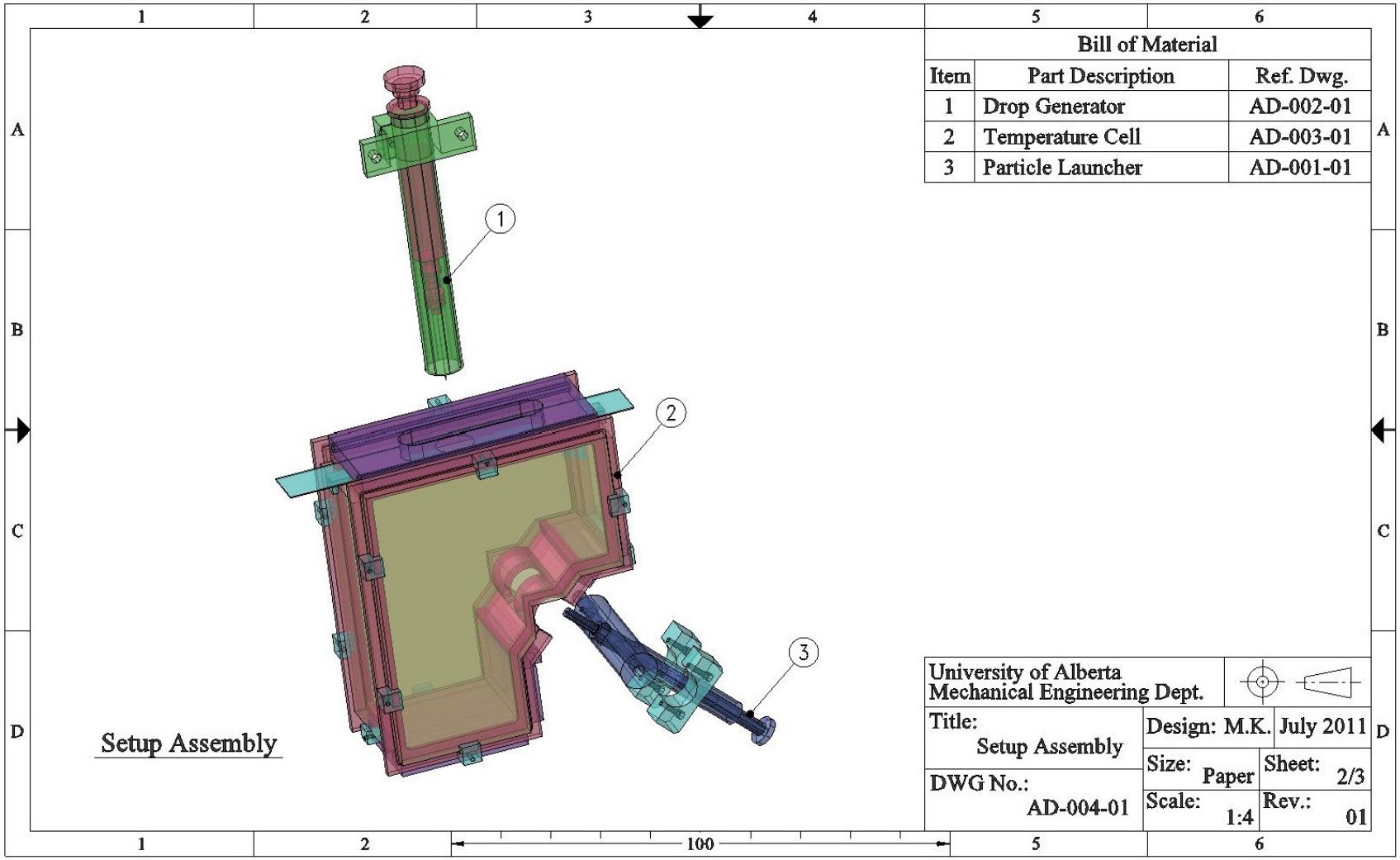

Bill of Material		
Item	Part Description	Ref. Dwg.
1	Drop Generator	AD-002-01
2	Temperature Cell	AD-003-01
3	Particle Launcher	AD-001-01

University of Alberta Mechanical Engineering Dept.		
Title: Setup Assembly	Design: M.K.	July 2011
	Size: Paper	Sheet: 2/3
DWG No.: AD-004-01	Scale: 1:4	Rev.: 01

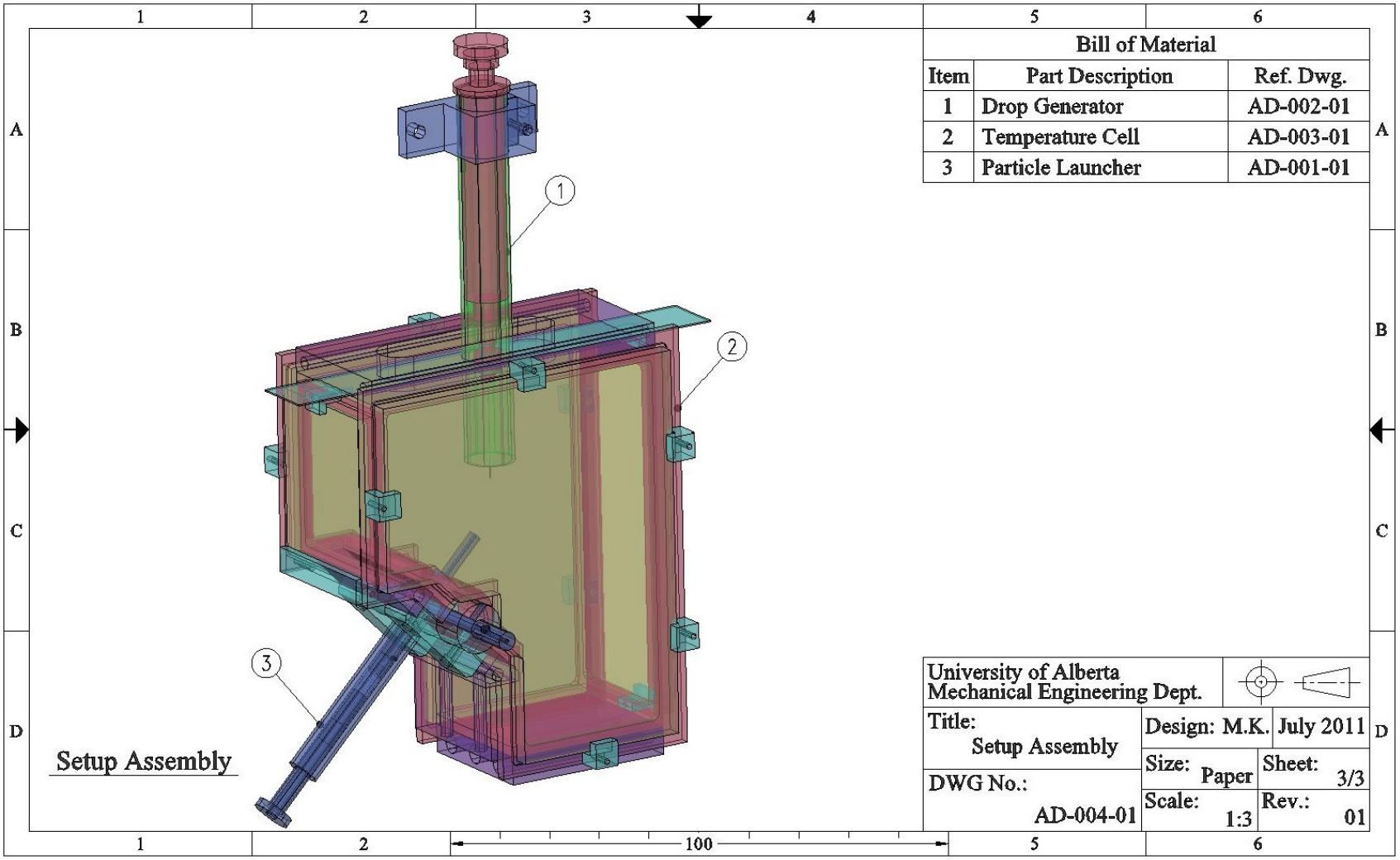
1
2
3
Setup Assembly
Bill of Material
Item | Part Description | Ref. Dwg.
1 | Drop Generator | AD-002-01
2 | Temperature Cell | AD-003-01
3 | Particle Launcher | AD-001-01
University of Alberta
Mechanical Engineering Dept.
Title: Setup Assembly
Design: M.K. July 2011
Size: Paper
Sheet: 3/3
DWG No.: AD-004-01
Scale: 1:3
Rev.: 01
100

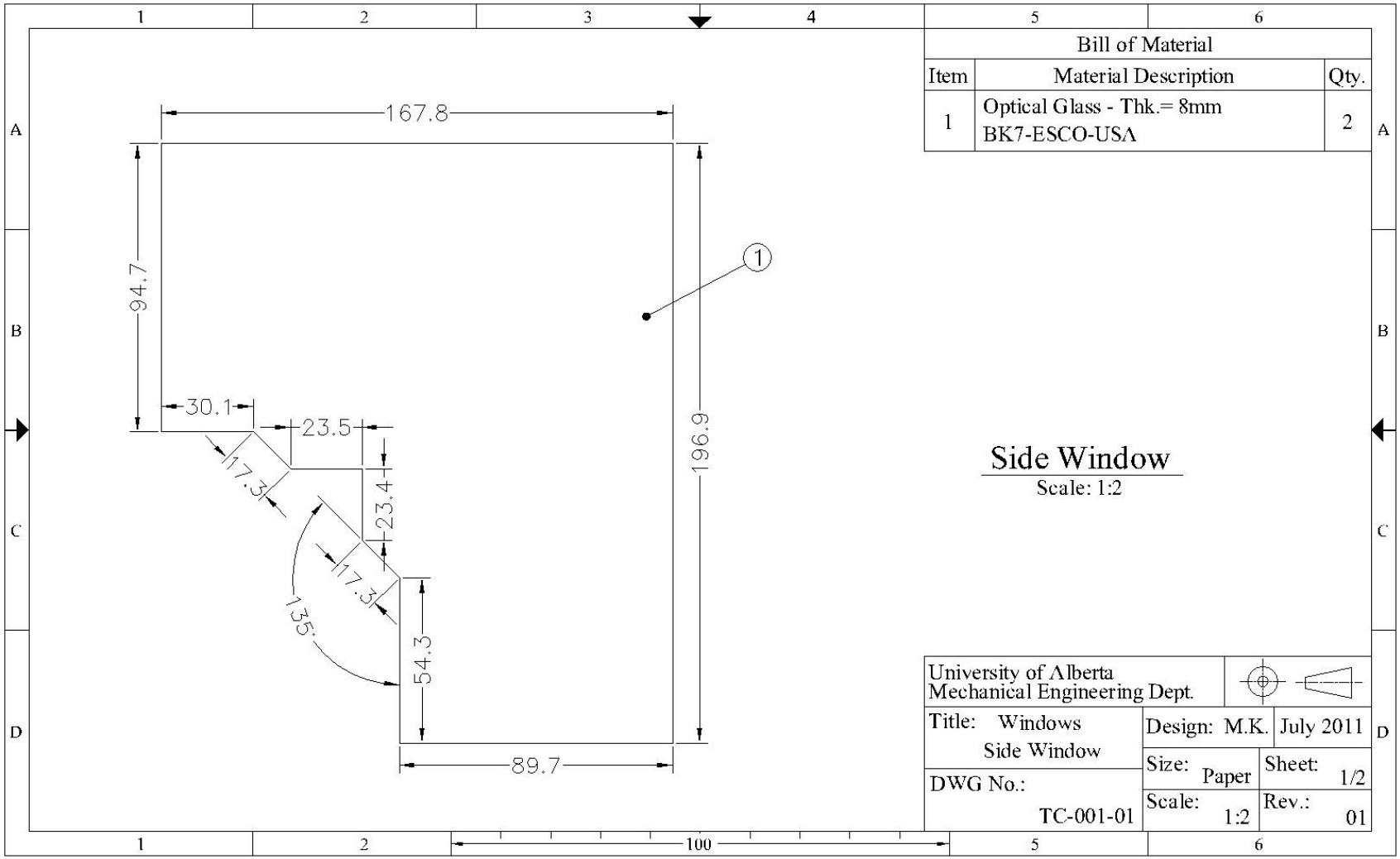
167.8
94.7
196.9
30.1
23.5
17.3
23.4
17.3
135°
54.3
89.7
1
100
Bill of Material
Item
Material Description
Qty.
1
Optical Glass - Thk.= 8mm
BK7-ESCO-USA
2
Side Window
Scale: 1:2
University of Alberta
Mechanical Engineering Dept.
Title: Windows
Side Window
Design: M.K.
July 2011
Size: Paper
Sheet: 1/2
DWG No.: TC-001-01
Scale: 1:2
Rev.: 01

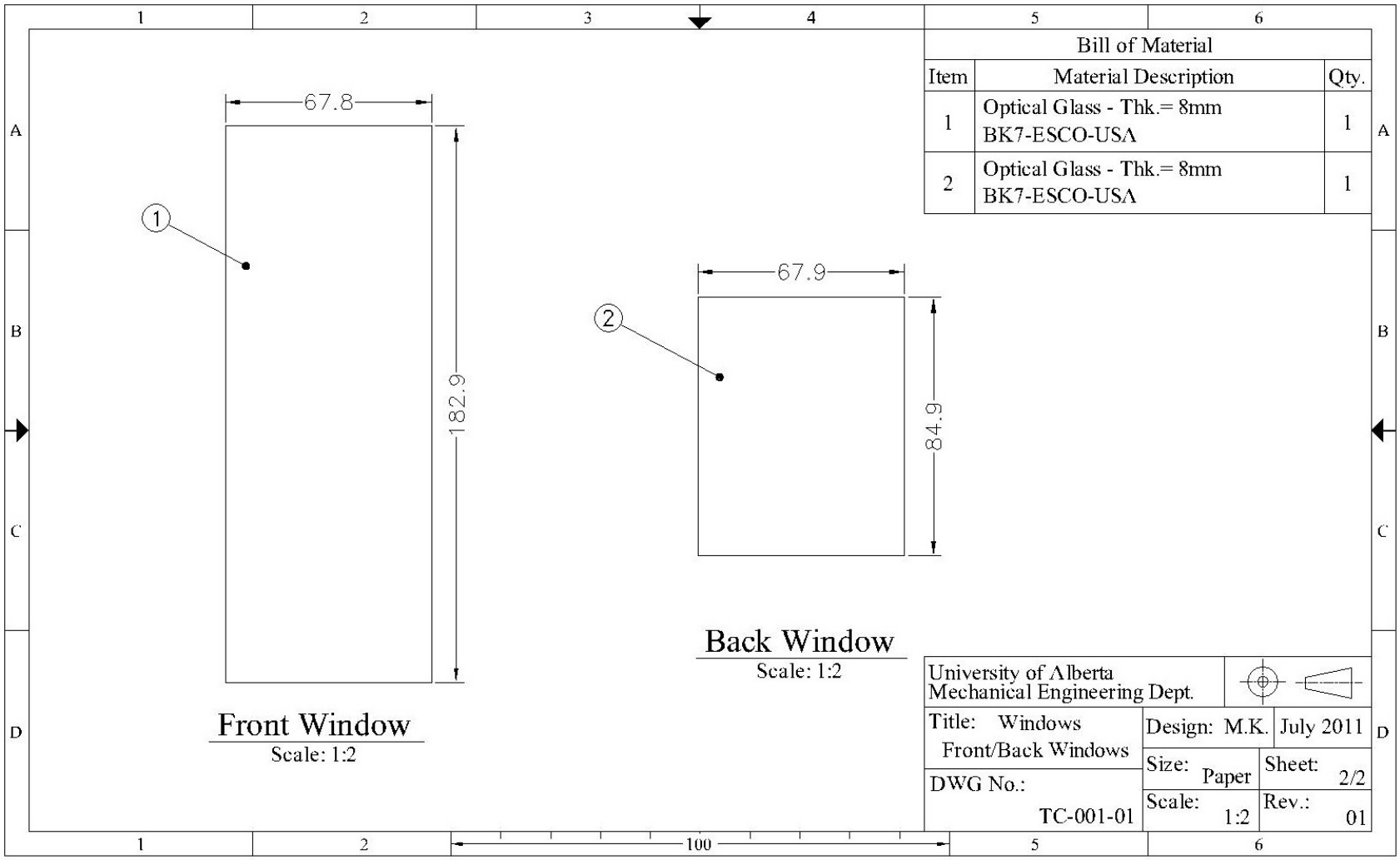
Bill of Material
Item | Material Description | Qty.
1 | Optical Glass - Thk.= 8mm BK7-ESCO-USA | 1
2 | Optical Glass - Thk.= 8mm BK7-ESCO-USA | 1
67.8
182.9
1
Front Window
Scale: 1:2
67.9
84.9
2
Back Window
Scale: 1:2
University of Alberta
Mechanical Engineering Dept.
Title: Windows
Front/Back Windows
Design: M.K.
July 2011
Size: Paper
Sheet: 2/2
DWG No.: TC-001-01
Scale: 1:2
Rev.: 01
100

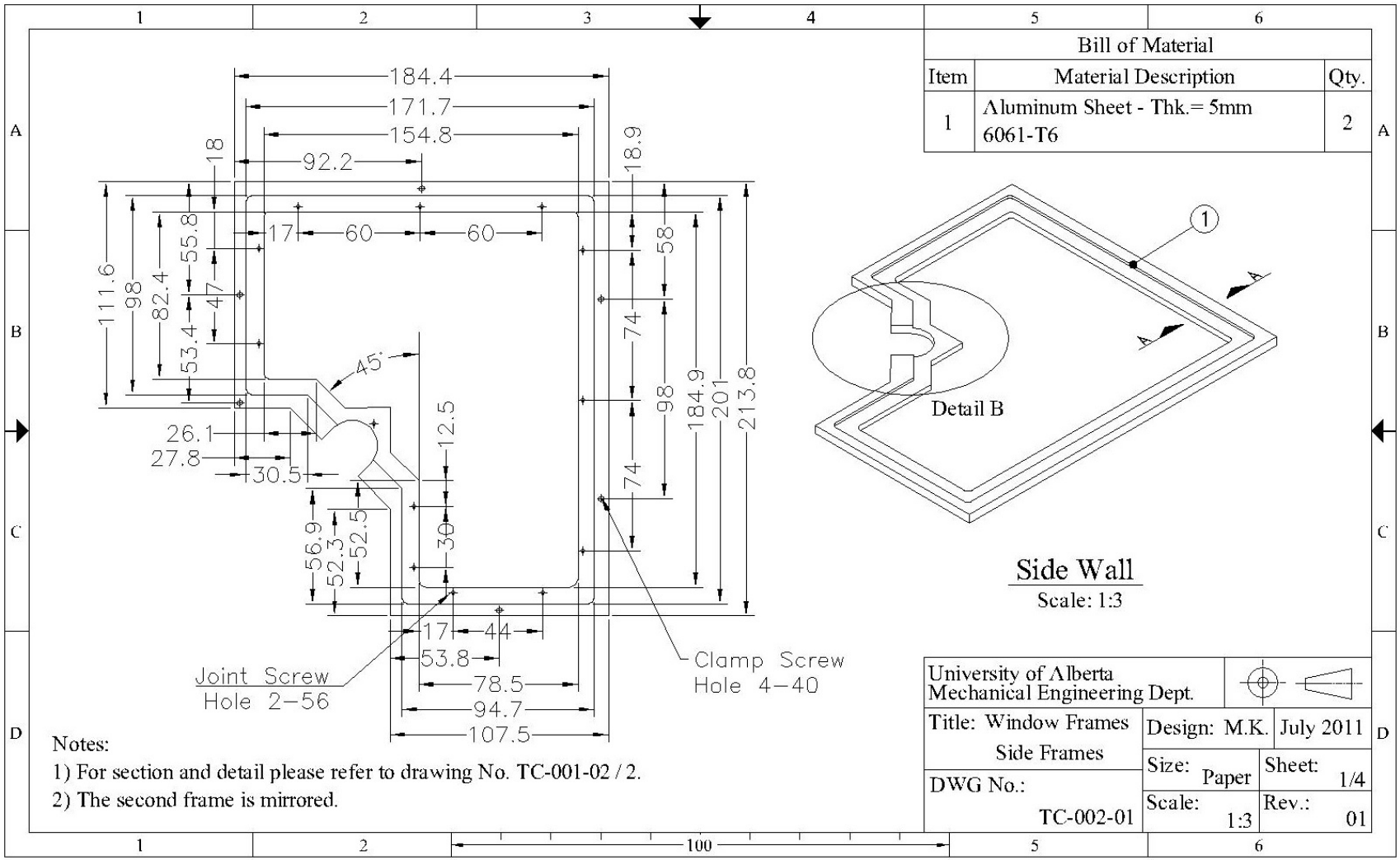
Bill of Material
Item | Material Description | Qty.
1 | Aluminum Sheet - Thk.= 5mm 6061-T6 | 2
184.4
171.7
154.8
92.2
18
18.9
17
60
60
111.6
98
82.4
55.8
47
53.4
58
74
98
184.9
201
213.8
45°
26.1
27.8
30.5
12.5
56.9
52.3
52.5
30
74
17
44
53.8
78.5
94.7
107.5
Joint Screw Hole 2–56
Clamp Screw Hole 4–40
Detail B
A
A
1
Side Wall
Scale: 1:3
Notes:
1) For section and detail please refer to drawing No. TC-001-02 / 2.
2) The second frame is mirrored.
University of Alberta
Mechanical Engineering Dept.
Title: Window Frames
Side Frames
Design: M.K.
July 2011
Size: Paper
Sheet: 1/4
DWG No.: TC-002-01
Scale: 1:3
Rev.: 01

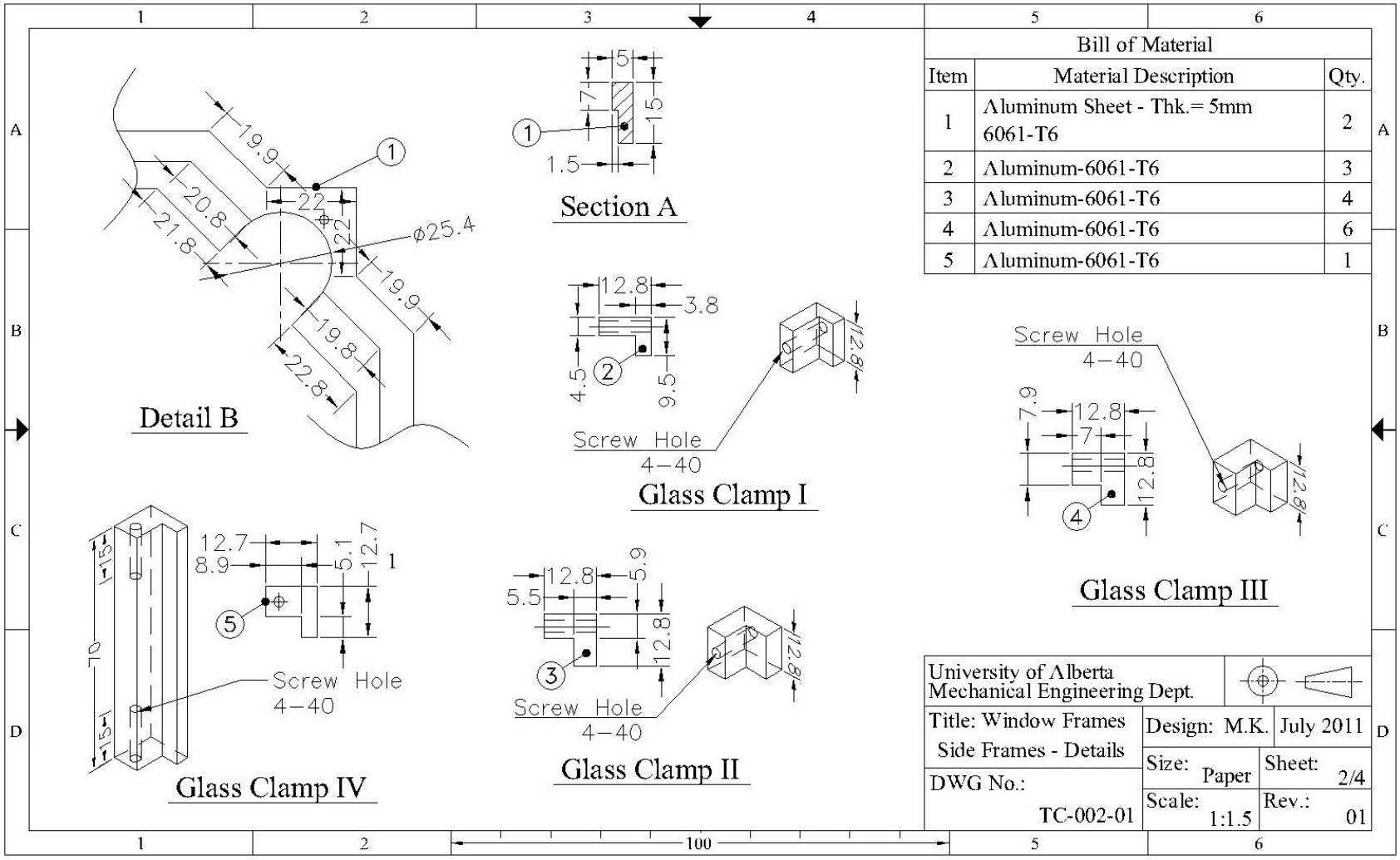
Bill of Material
Item | Material Description | Qty.
1 | Aluminum Sheet - Thk.= 5mm 6061-T6 | 2
2 | Aluminum-6061-T6 | 3
3 | Aluminum-6061-T6 | 4
4 | Aluminum-6061-T6 | 6
5 | Aluminum-6061-T6 | 1
Section A
Detail B
Glass Clamp I
Glass Clamp II
Glass Clamp III
Glass Clamp IV
Screw Hole 4−40
University of Alberta
Mechanical Engineering Dept.
Title: Window Frames Side Frames - Details
Design: M.K. July 2011
Size: Paper
Sheet: 2/4
DWG No.: TC-002-01
Scale: 1:1.5
Rev.: 01

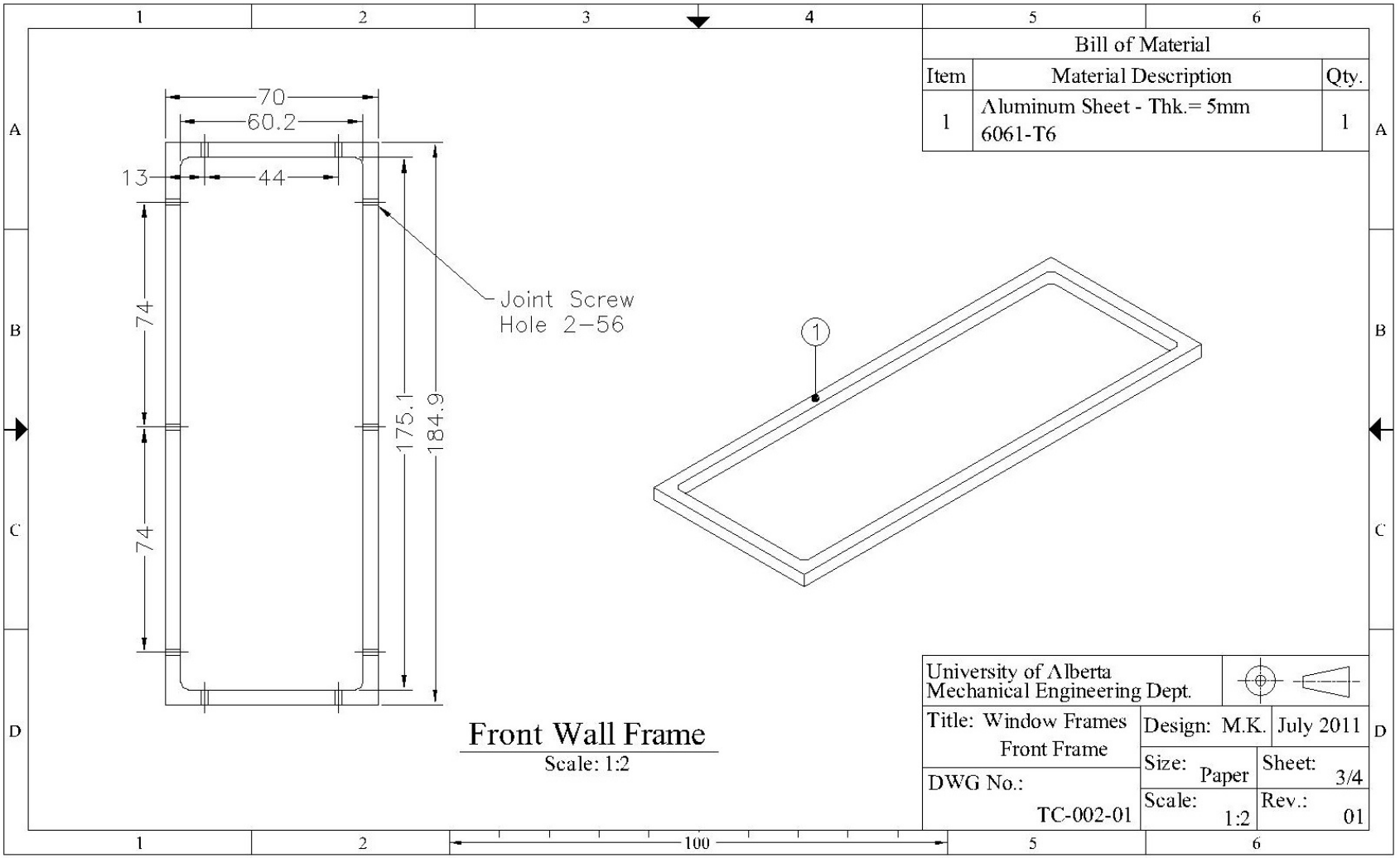
Bill of Material
Item
Material Description
Qty.
1
Aluminum Sheet - Thk.= 5mm
6061-T6
1
70
60.2
13
44
74
74
175.1
184.9
Joint Screw
Hole 2–56
1
Front Wall Frame
Scale: 1:2
University of Alberta
Mechanical Engineering Dept.
Title: Window Frames
Front Frame
Design: M.K.
July 2011
Size: Paper
Sheet: 3/4
DWG No.: TC-002-01
Scale: 1:2
Rev.: 01
100

Bill of Material		
Item	Material Description	Qty.
1	Aluminum Sheet - Thk.= 5mm 6061-T6	1

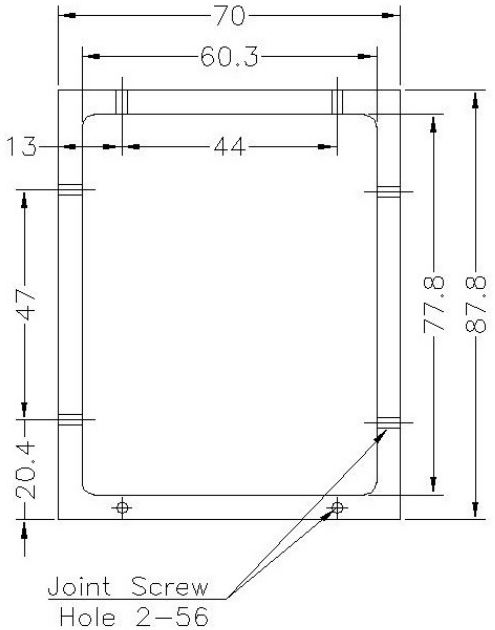

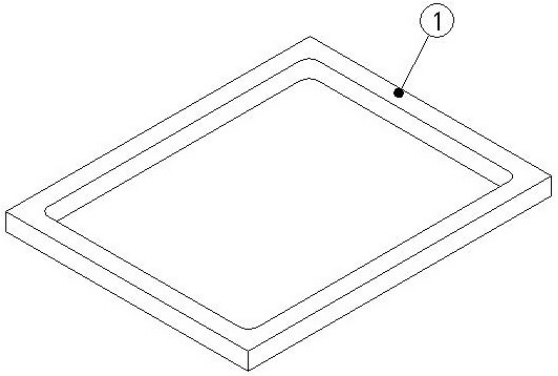

Back Wall Frame
Scale: 1:1.5

University of Alberta Mechanical Engineering Dept.			
Title: Window Frames Back Frame	Design: M.K.	July 2011	
DWG No.: TC-002-01	Size: Paper	Sheet: 4/4	
	Scale: 1:1.5	Rev.: 01	

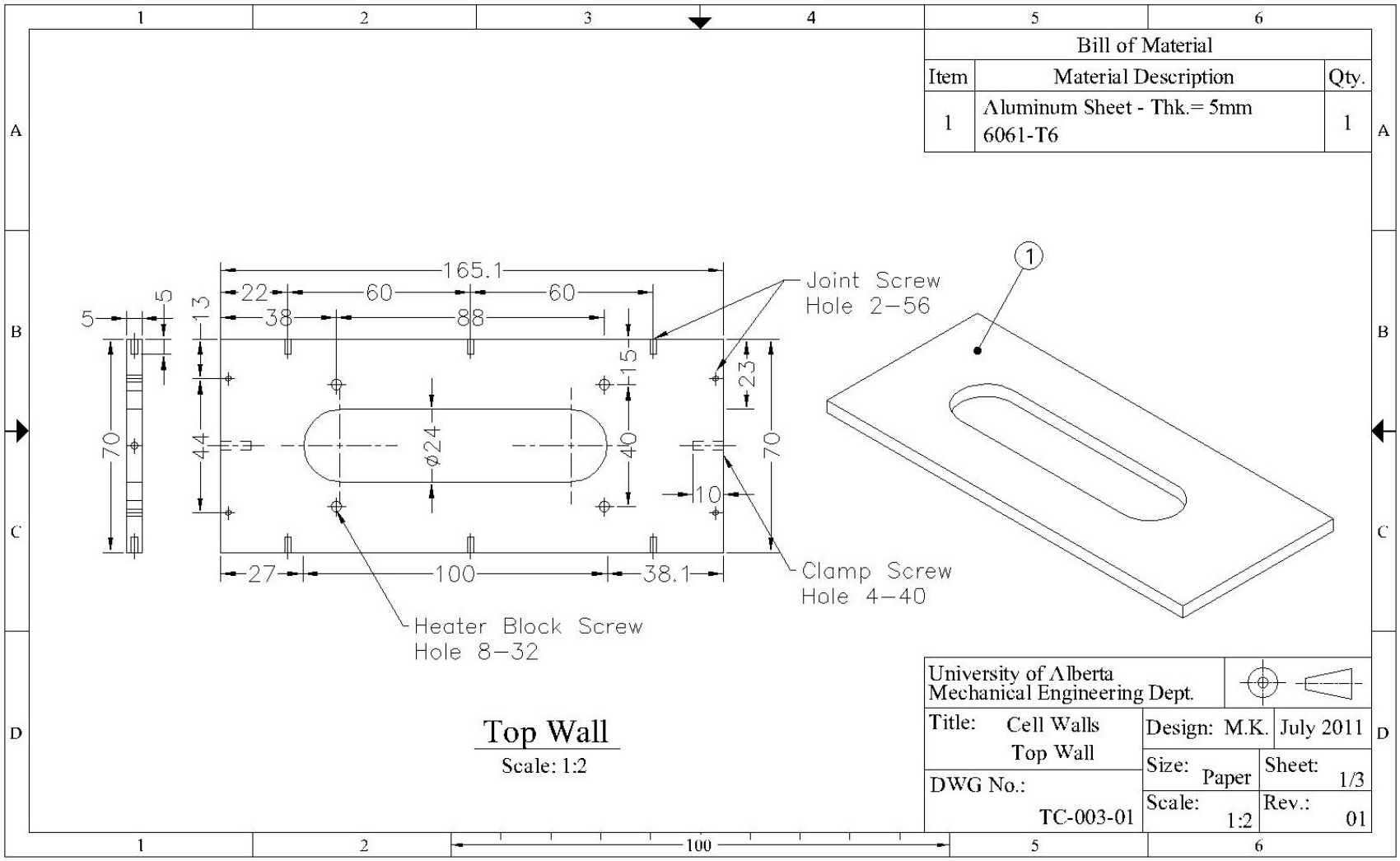
Bill of Material
Item
Material Description
Qty.
1
Aluminum Sheet - Thk.= 5mm
6061-T6
1
165.1
22
60
60
38
88
5
5
13
70
44
ø24
15
40
23
70
10
27
100
38.1
Joint Screw
Hole 2–56
Clamp Screw
Hole 4–40
Heater Block Screw
Hole 8–32
Top Wall
Scale: 1:2
University of Alberta
Mechanical Engineering Dept.
Title: Cell Walls
Top Wall
Design: M.K.
July 2011
DWG No.:
TC-003-01
Size: Paper
Sheet: 1/3
Scale: 1:2
Rev.: 01

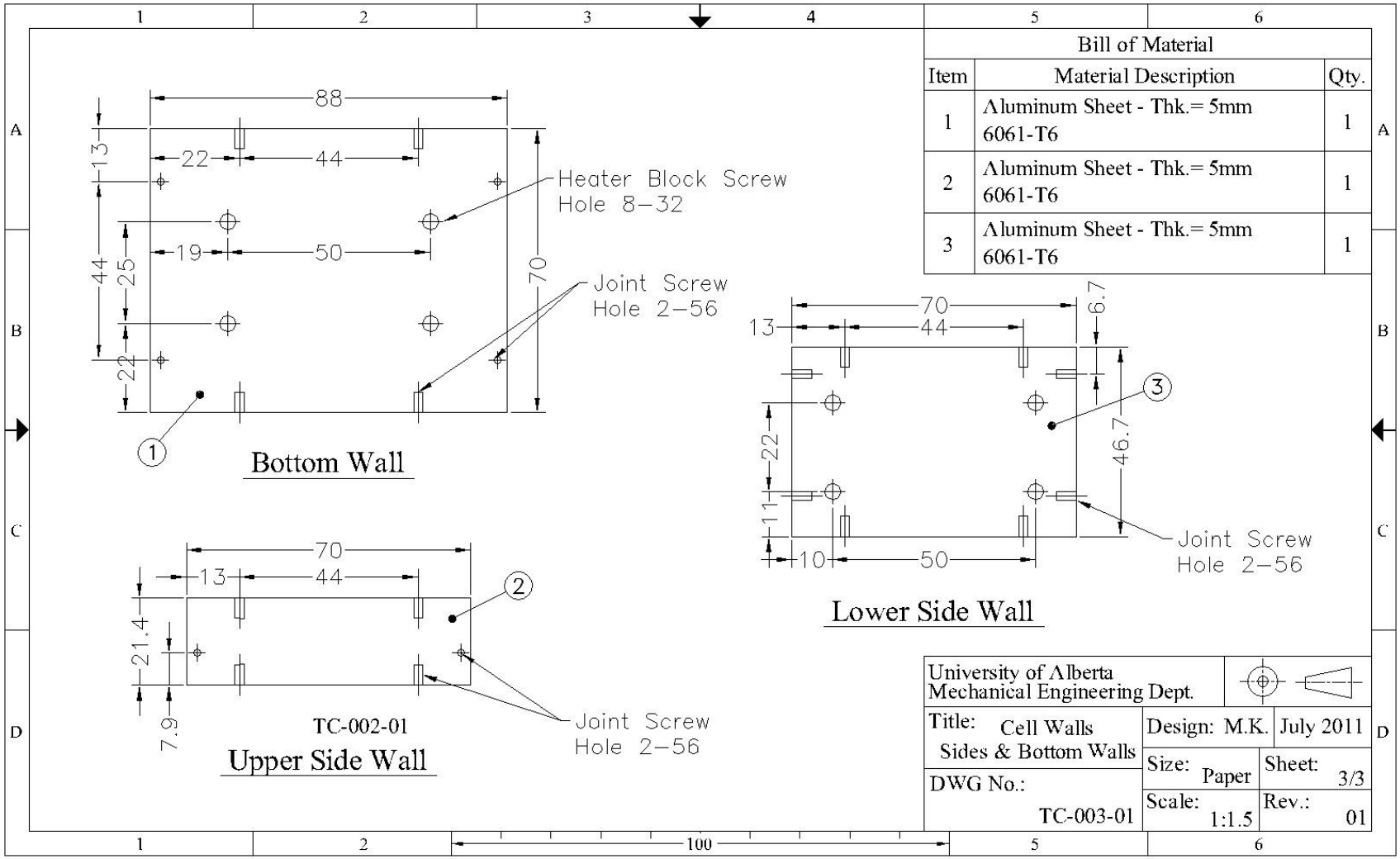
Bill of Material
Item | Material Description | Qty.
1 | Aluminum Sheet - Thk.= 5mm 6061-T6 | 1
2 | Aluminum Sheet - Thk.= 5mm 6061-T6 | 1
3 | Aluminum Sheet - Thk.= 5mm 6061-T6 | 1
88
13
22
44
19
50
44
25
22
70
Heater Block Screw Hole 8–32
Joint Screw Hole 2–56
1
Bottom Wall
70
13
44
6.7
22
11
46.7
10
50
3
Joint Screw Hole 2–56
Lower Side Wall
70
13
44
2
21.4
7.9
TC-002-01
Joint Screw Hole 2–56
Upper Side Wall
University of Alberta
Mechanical Engineering Dept.
Title: Cell Walls Sides & Bottom Walls
Design: M.K.
July 2011
Size: Paper
Sheet: 3/3
DWG No.: TC-003-01
Scale: 1:1.5
Rev.: 01
100

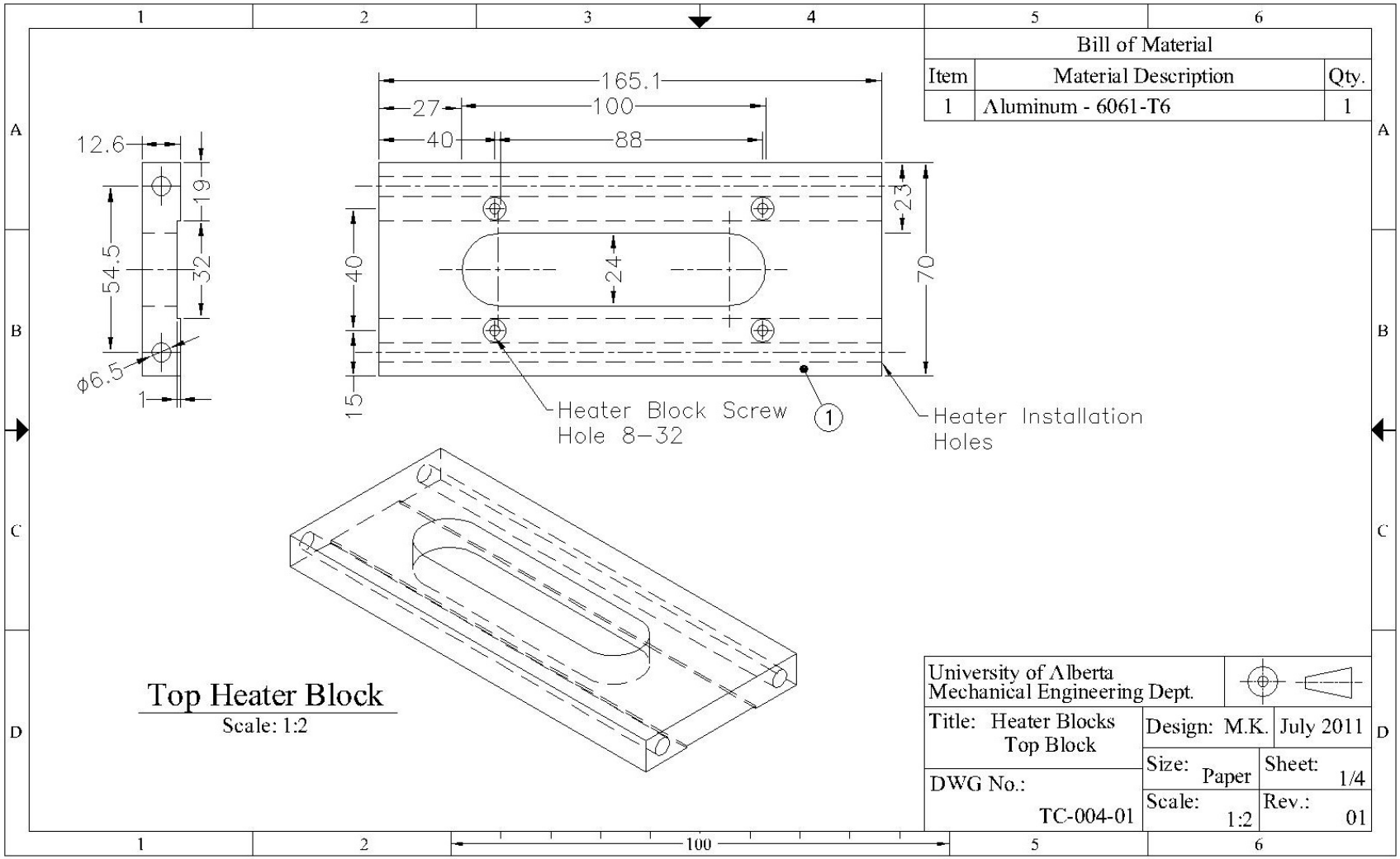
Bill of Material
Item | Material Description | Qty.
1 | Aluminum - 6061-T6 | 1
165.1
27
100
40
88
12.6
19
54.5
32
ϕ6.5
1
23
40
24
70
15
Heater Block Screw Hole 8–32
1
Heater Installation Holes
Top Heater Block
Scale: 1:2
University of Alberta
Mechanical Engineering Dept.
Title: Heater Blocks Top Block
Design: M.K. July 2011
DWG No.: TC-004-01
Size: Paper
Sheet: 1/4
Scale: 1:2
Rev.: 01

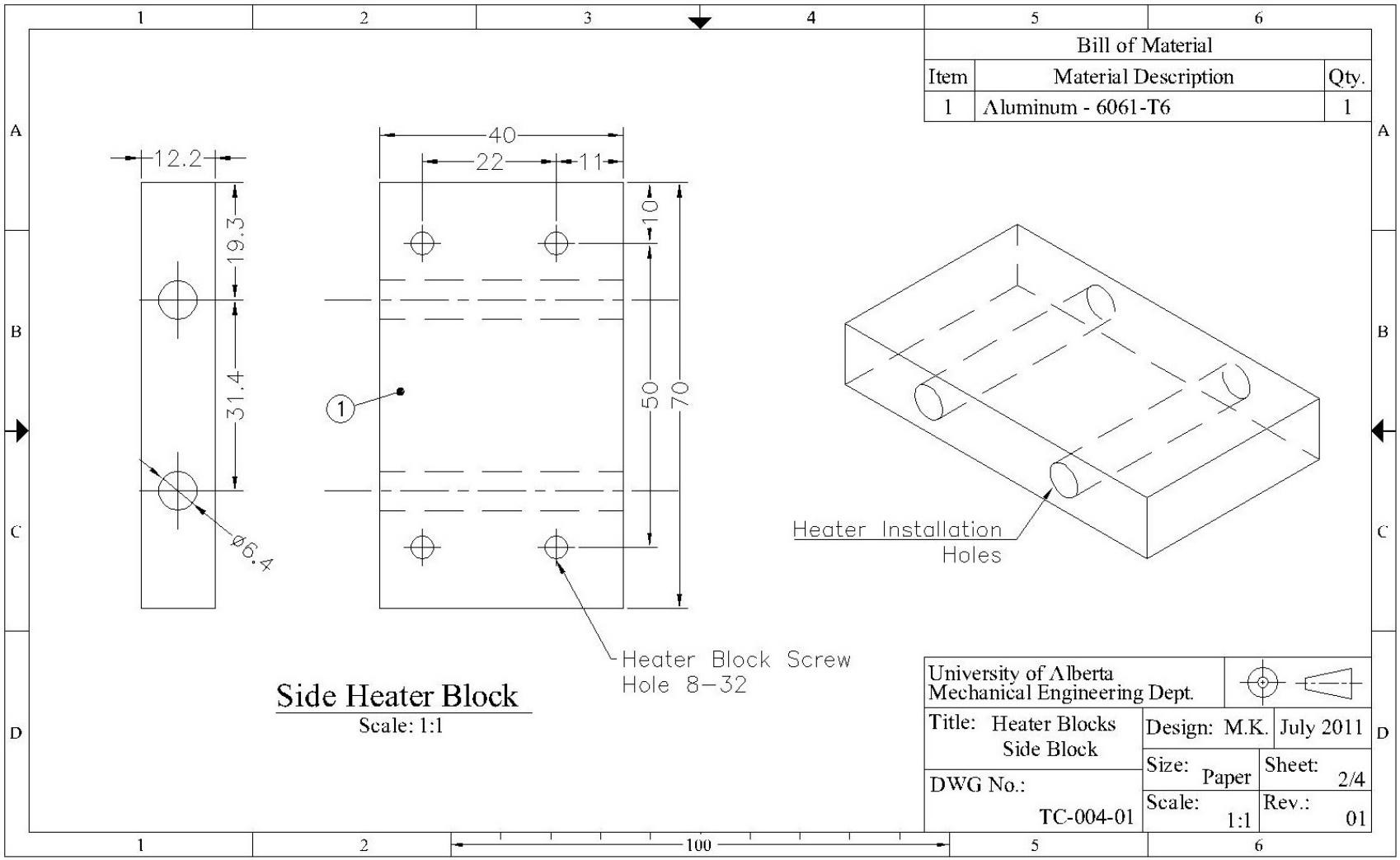
Bill of Material
Item | Material Description | Qty.
1 | Aluminum - 6061-T6 | 1
12.2
19.3
31.4
ø6.4
40
22
11
10
50
70
1
Heater Block Screw Hole 8–32
Heater Installation Holes
Side Heater Block
Scale: 1:1
University of Alberta
Mechanical Engineering Dept.
Title: Heater Blocks Side Block
Design: M.K. July 2011
DWG No.: TC-004-01
Size: Paper
Sheet: 2/4
Scale: 1:1
Rev.: 01
100

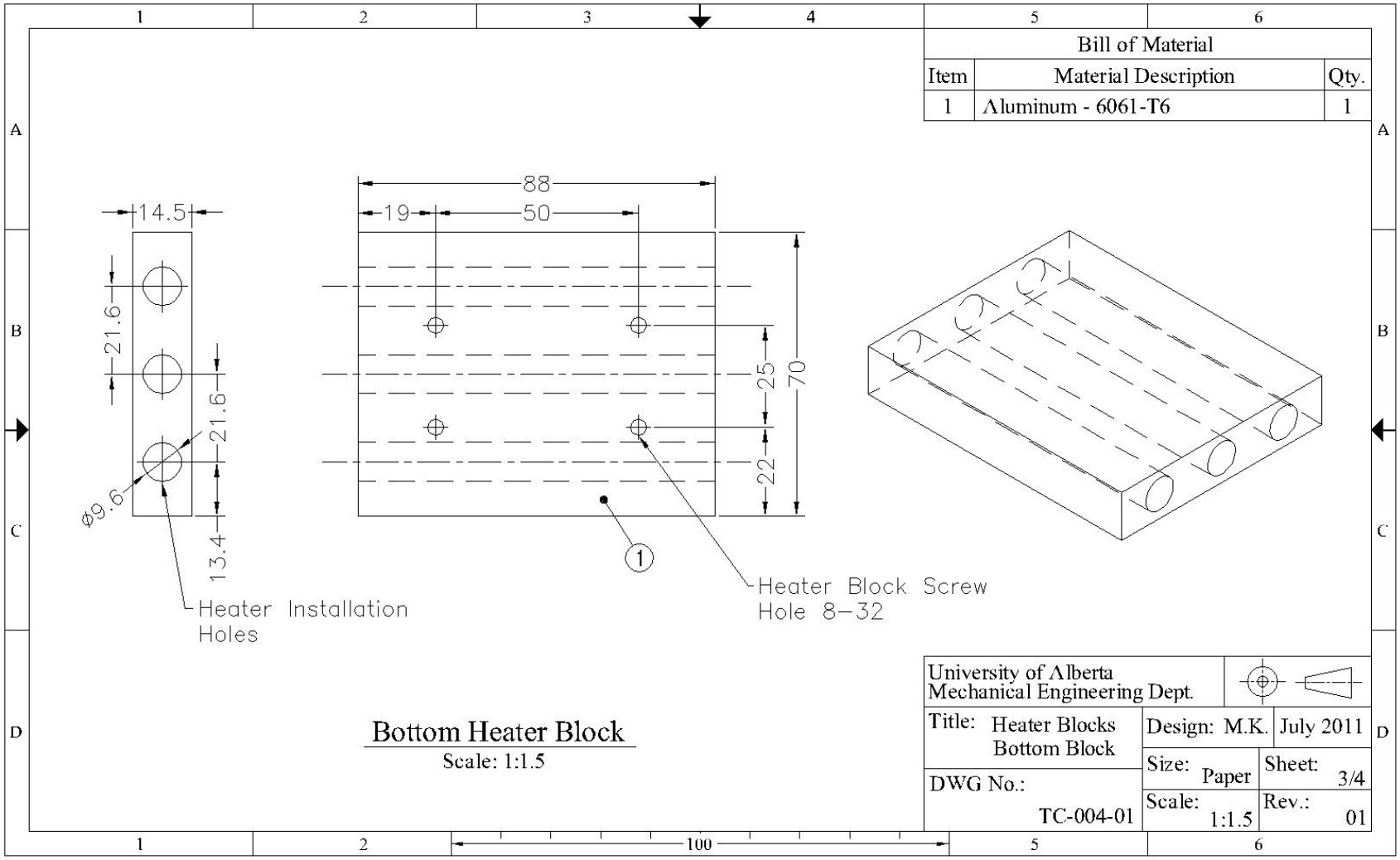
Bill of Material
Item | Material Description | Qty.
1 | Aluminum - 6061-T6 | 1
14.5
21.6
21.6
13.4
ø9.6
88
19
50
25
22
70
1
Heater Installation Holes
Heater Block Screw Hole 8–32
Bottom Heater Block
Scale: 1:1.5
University of Alberta
Mechanical Engineering Dept.
Title: Heater Blocks Bottom Block
Design: M.K.
July 2011
DWG No.: TC-004-01
Size: Paper
Sheet: 3/4
Scale: 1:1.5
Rev.: 01
100

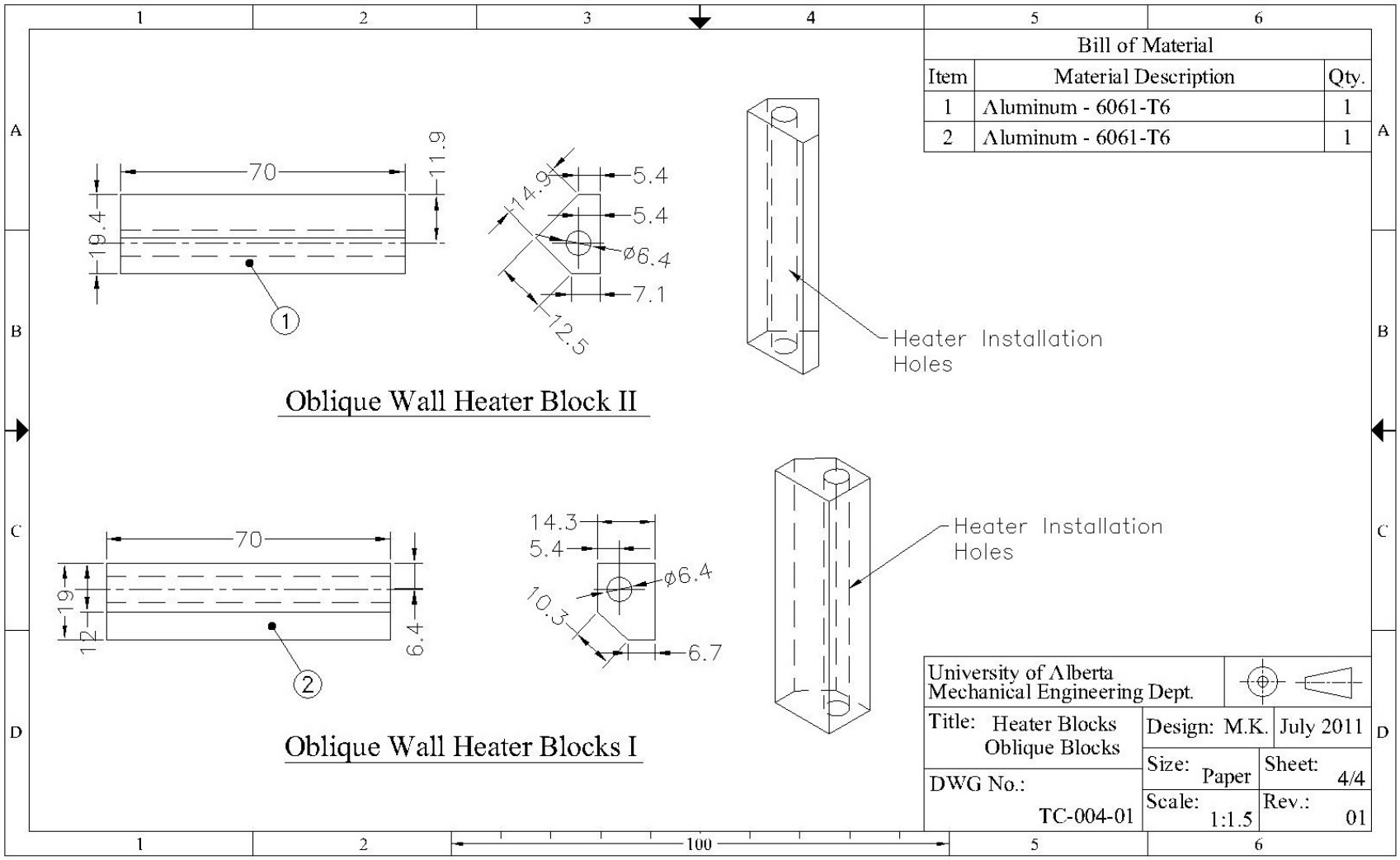
Bill of Material
Item | Material Description | Qty.
1 | Aluminum - 6061-T6 | 1
2 | Aluminum - 6061-T6 | 1
70
11.9
19.4
1
14.9
5.4
5.4
ø6.4
7.1
12.5
Heater Installation Holes
Oblique Wall Heater Block II
70
19
12
6.4
2
14.3
5.4
ø6.4
10.3
6.7
Heater Installation Holes
Oblique Wall Heater Blocks I
University of Alberta
Mechanical Engineering Dept.
Title: Heater Blocks
Oblique Blocks
Design: M.K.
July 2011
Size: Paper
Sheet: 4/4
DWG No.: TC-004-01
Scale: 1:1.5
Rev.: 01
100

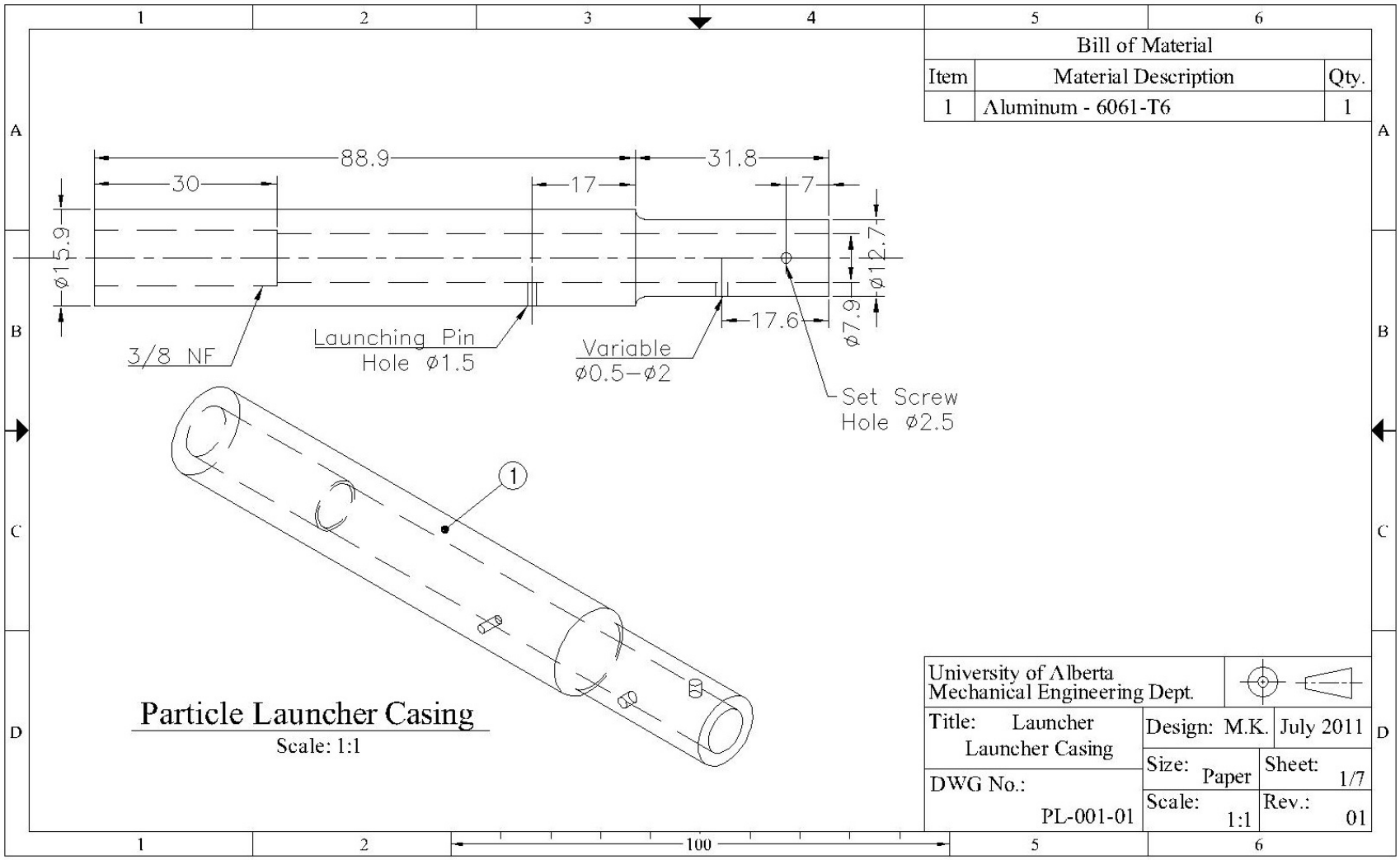
Bill of Material
Item | Material Description | Qty.
1 | Aluminum - 6061-T6 | 1
88.9
31.8
30
17
7
ø15.9
ø12.7
ø7.9
17.6
3/8 NF
Launching Pin Hole ø1.5
Variable ø0.5–ø2
Set Screw Hole ø2.5
1
Particle Launcher Casing
Scale: 1:1
University of Alberta
Mechanical Engineering Dept.
Title: Launcher
Launcher Casing
Design: M.K.
July 2011
Size: Paper
Sheet: 1/7
DWG No.: PL-001-01
Scale: 1:1
Rev.: 01
100

Bill of Material		
Item	Material Description	Qty.
1	Steel-1018	1

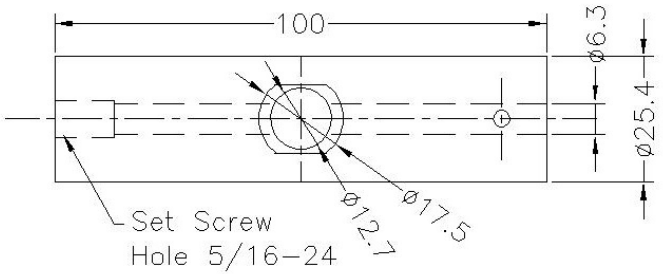

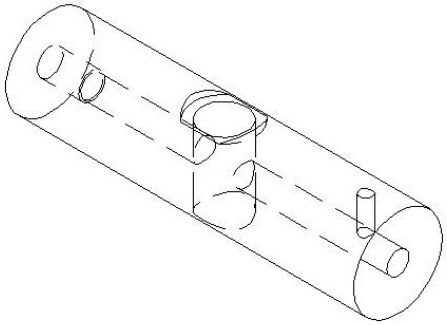

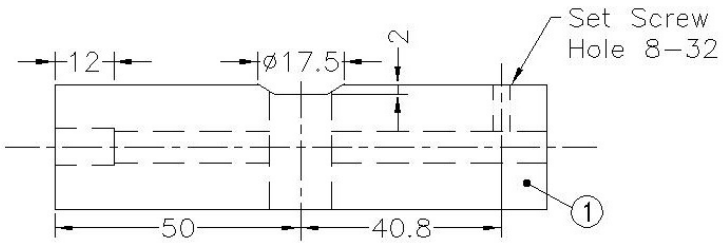

Particle Launcher Hinge

Scale: 1:1.5

University of Alberta Mechanical Engineering Dept.			
Title: Launcher Launcher Hinge		Design: M.K.	July 2011
DWG No.: PL-001-01		Size: Paper	Sheet: 2/7
		Scale: 1:1.5	Rev.: 01

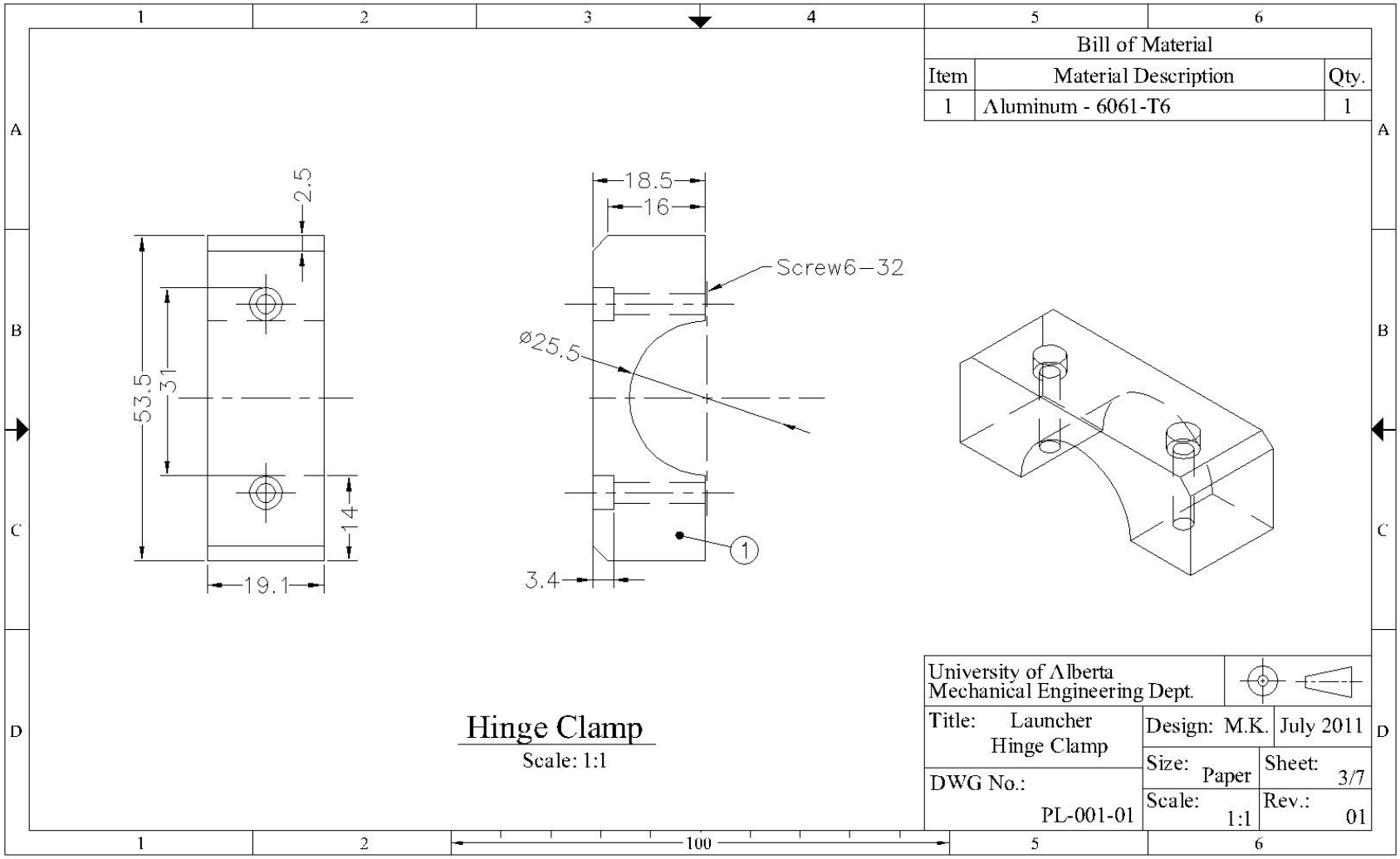
Bill of Material
Item | Material Description | Qty.
1 | Aluminum - 6061-T6 | 1
2.5
53.5
31
14
19.1
18.5
16
Screw6−32
ø25.5
1
3.4
Hinge Clamp
Scale: 1:1
University of Alberta
Mechanical Engineering Dept.
Title: Launcher Hinge Clamp
Design: M.K.
July 2011
Size: Paper
Sheet: 3/7
DWG No.: PL-001-01
Scale: 1:1
Rev.: 01
100

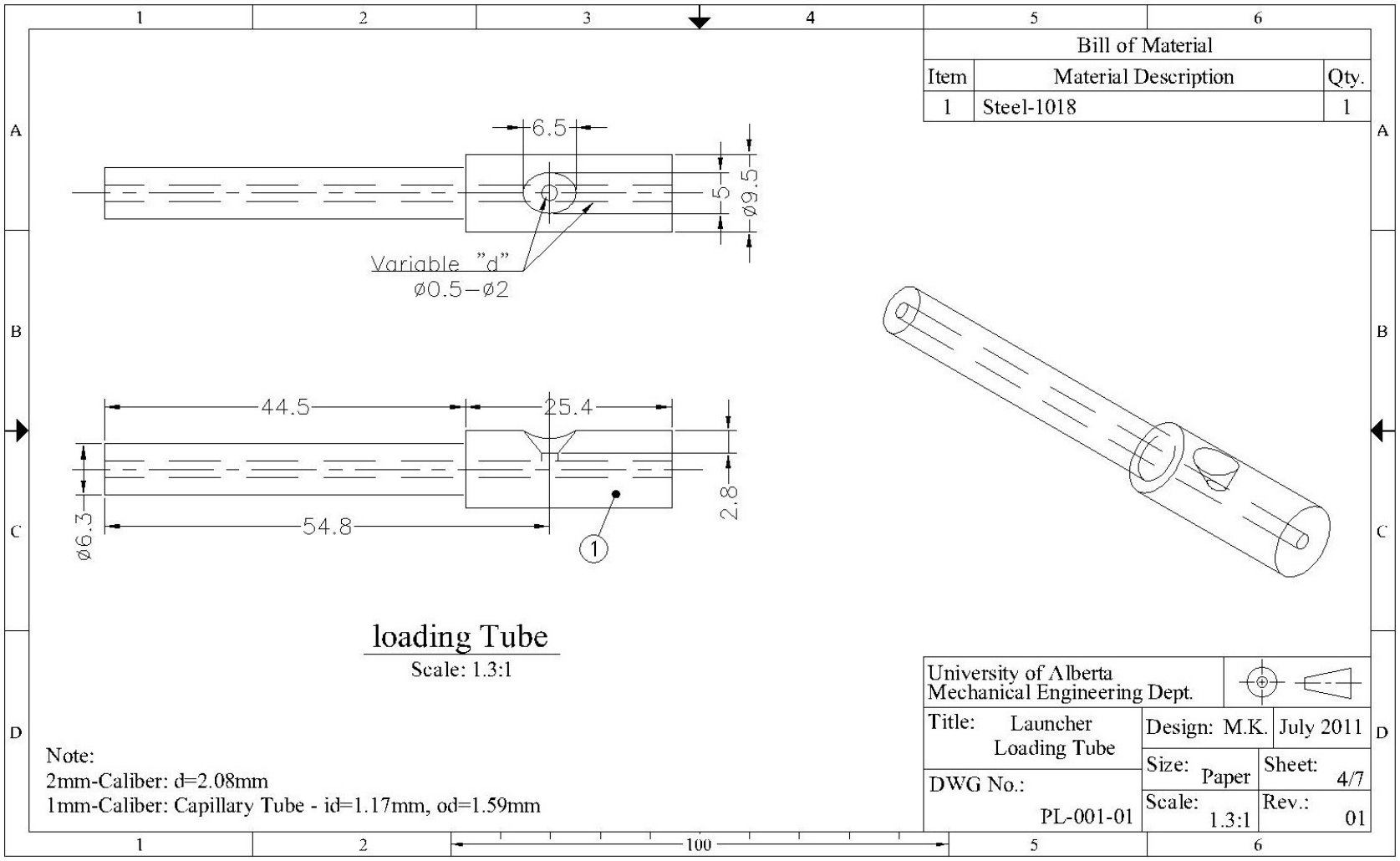
Bill of Material
Item | Material Description | Qty.
1 | Steel-1018 | 1
6.5
ø9.5
5
Variable "d"
ø0.5–ø2
44.5
25.4
2.8
ø6.3
54.8
1
loading Tube
Scale: 1.3:1
Note:
2mm-Caliber: d=2.08mm
1mm-Caliber: Capillary Tube - id=1.17mm, od=1.59mm
University of Alberta
Mechanical Engineering Dept.
Title: Launcher Loading Tube
Design: M.K.
July 2011
Size: Paper
Sheet: 4/7
DWG No.: PL-001-01
Scale: 1.3:1
Rev.: 01

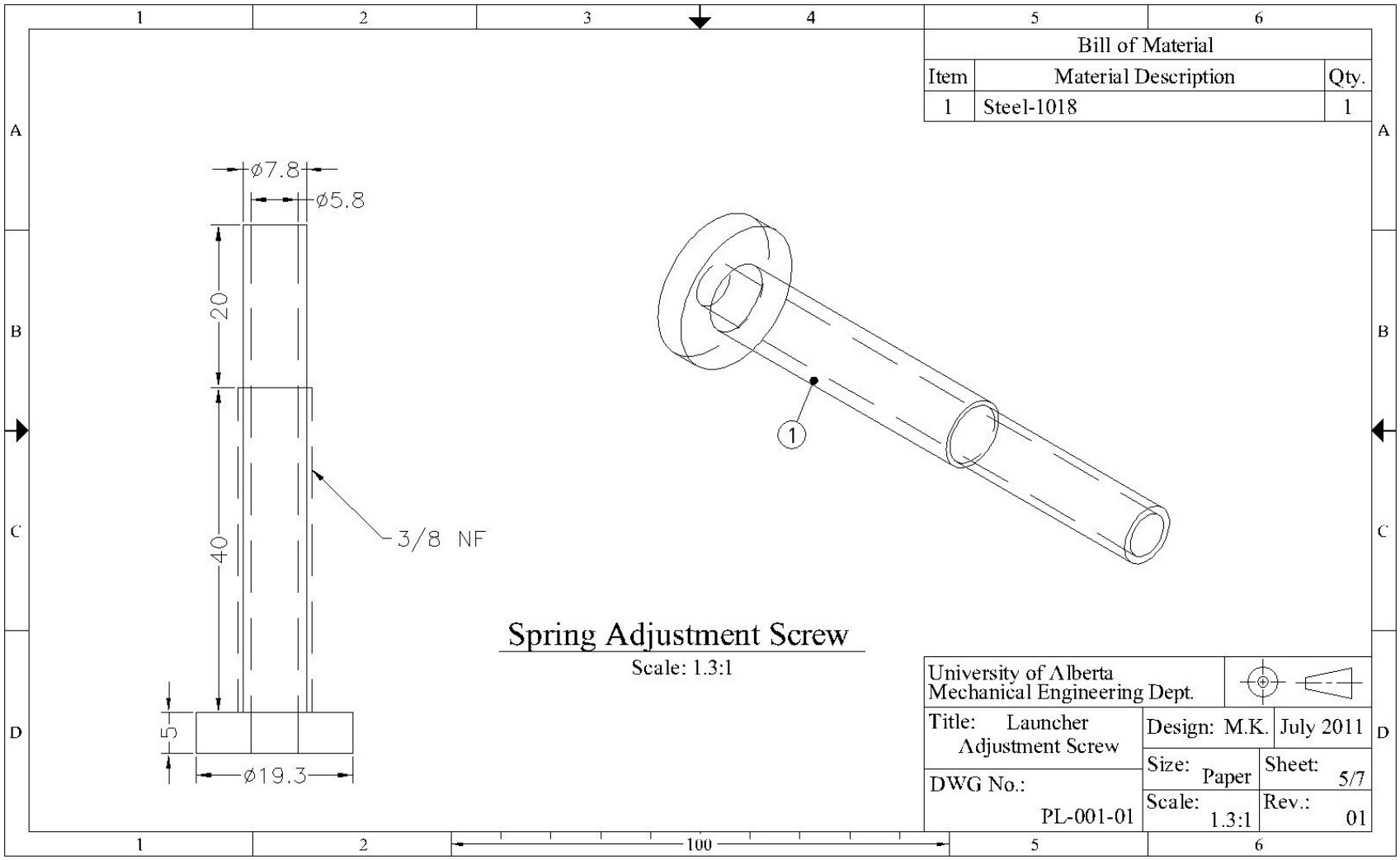
Bill of Material
Item | Material Description | Qty.
1 | Steel-1018 | 1
ø7.8
ø5.8
20
40
5
ø19.3
3/8 NF
1
Spring Adjustment Screw
Scale: 1.3:1
University of Alberta
Mechanical Engineering Dept.
Title: Launcher Adjustment Screw
Design: M.K. July 2011
Size: Paper
Sheet: 5/7
DWG No.: PL-001-01
Scale: 1.3:1
Rev.: 01
100

Bill of Material		
Item	Material Description	Qty.
1	Steel-1018	1

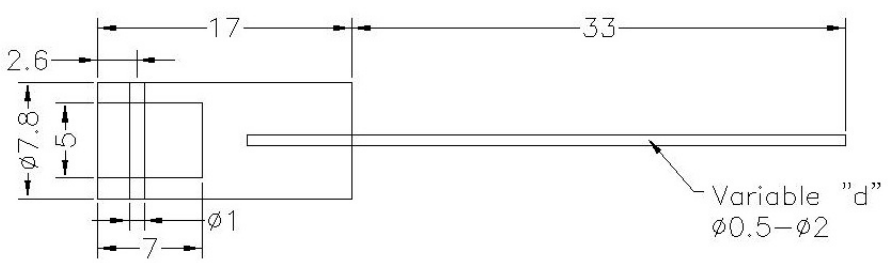

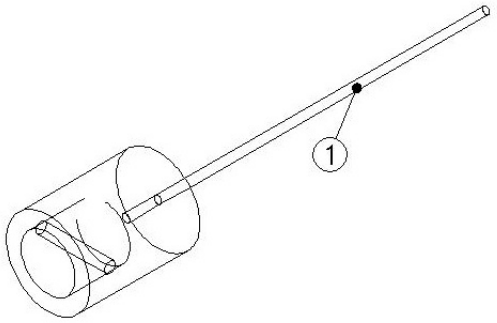

Plunger

Scale: 2:1

Note:
2mm-Caliber: d=1.5mm
1mm-Caliber: d=0.75mm

University of Alberta Mechanical Engineering Dept.			
Title: Launcher Plunger		Design: M.K.	July 2011
		Size: Paper	Sheet: 6/7
DWG No.: PL-001-01		Scale: 2:1	Rev.: 01

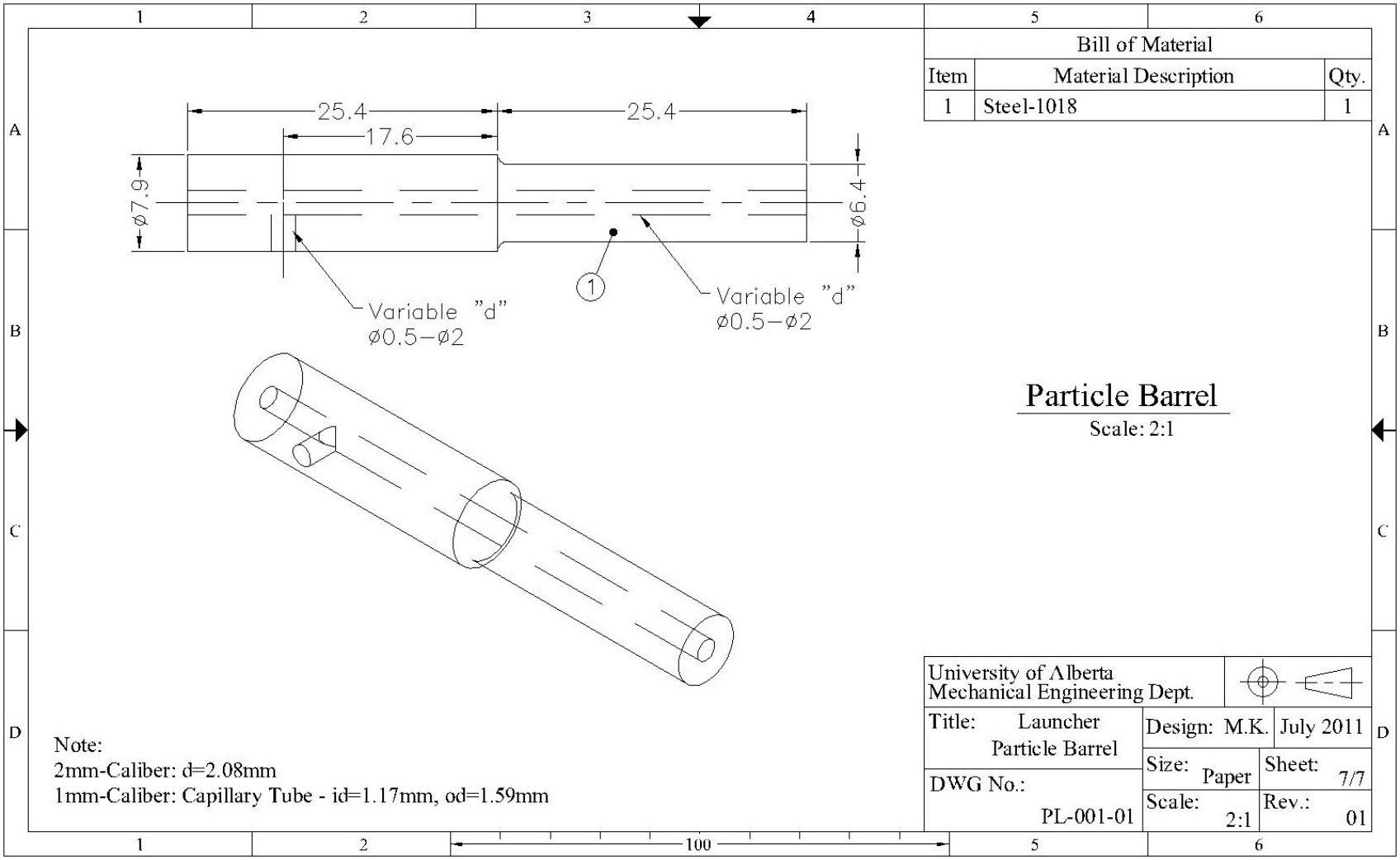
Bill of Material
Item | Material Description | Qty.
1 | Steel-1018 | 1
25.4
17.6
25.4
ø7.9
ø6.4
Variable "d"
ø0.5–ø2
1
Variable "d"
ø0.5–ø2
Particle Barrel
Scale: 2:1
Note:
2mm-Caliber: d=2.08mm
1mm-Caliber: Capillary Tube - id=1.17mm, od=1.59mm
University of Alberta
Mechanical Engineering Dept.
Title: Launcher
Particle Barrel
Design: M.K. July 2011
DWG No.: PL-001-01
Size: Paper
Sheet: 7/7
Scale: 2:1
Rev.: 01
100

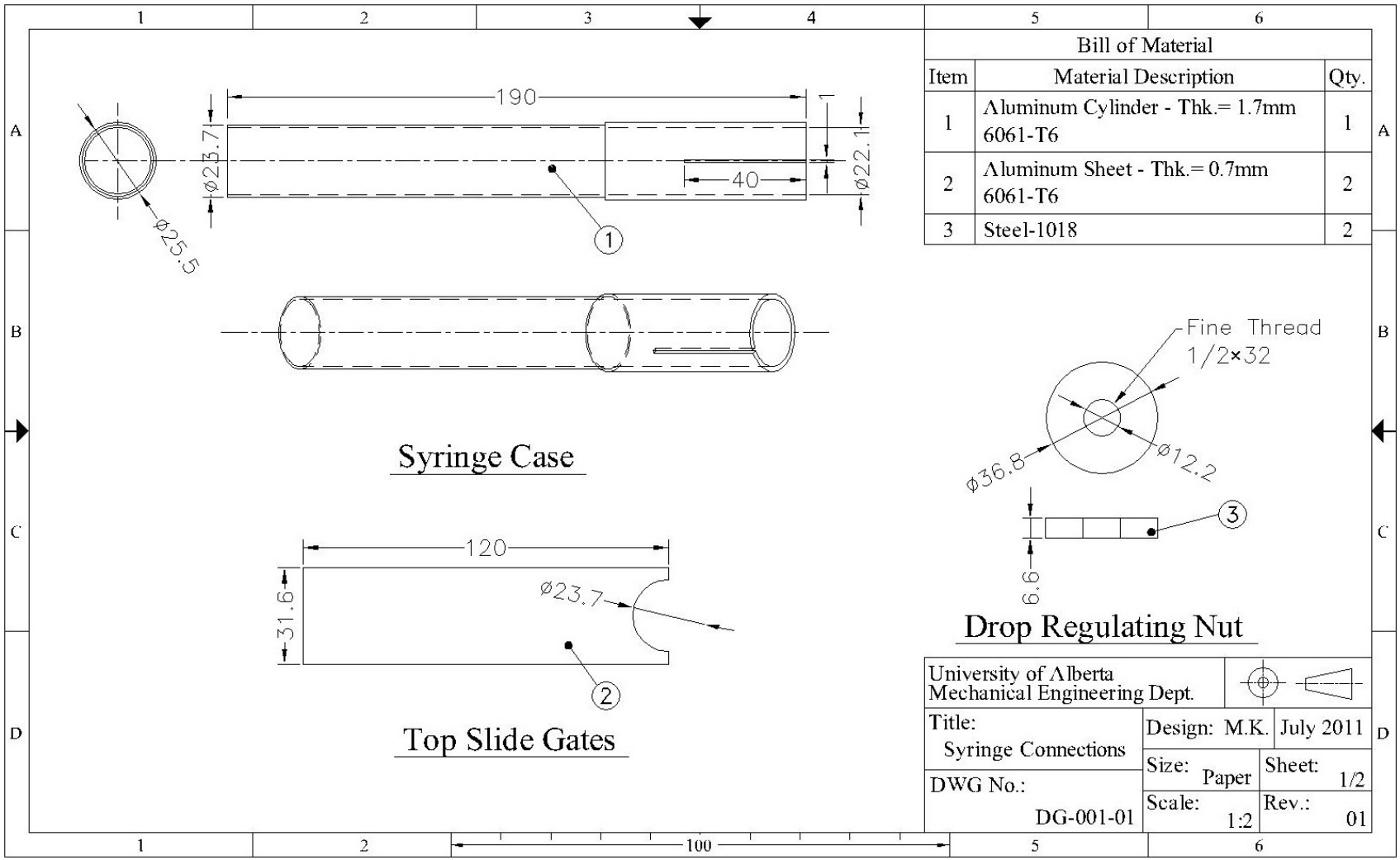

Bill of Material		
Item	Material Description	Qty.
1	Aluminum Cylinder - Thk.= 1.7mm 6061-T6	1
2	Aluminum Sheet - Thk.= 0.7mm 6061-T6	2
3	Steel-1018	2

University of Alberta Mechanical Engineering Dept.		
Title: Syringe Connections	Design: M.K.	July 2011
DWG No.: DG-001-01	Size: Paper	Sheet: 1/2
	Scale: 1:2	Rev.: 01

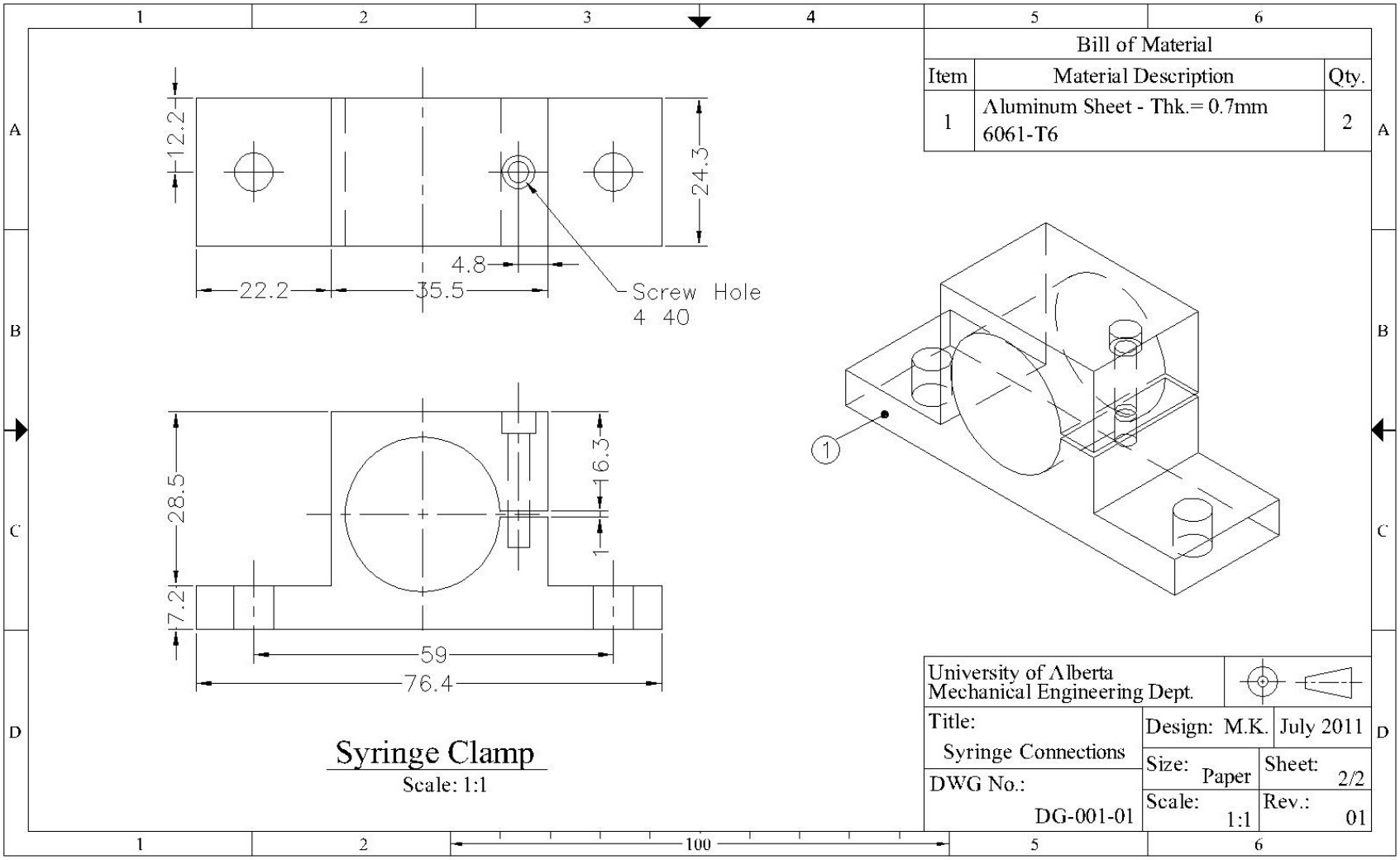
Bill of Material
Item
Material Description
Qty.
1
Aluminum Sheet - Thk.= 0.7mm
6061-T6
2
12.2
24.3
4.8
22.2
35.5
Screw Hole
4 40
28.5
16.3
1
7.2
59
76.4
1
Syringe Clamp
Scale: 1:1
University of Alberta
Mechanical Engineering Dept.
Title:
Syringe Connections
Design: M.K.
July 2011
Size:
Paper
Sheet:
2/2
DWG No.:
DG-001-01
Scale:
1:1
Rev.:
01
100

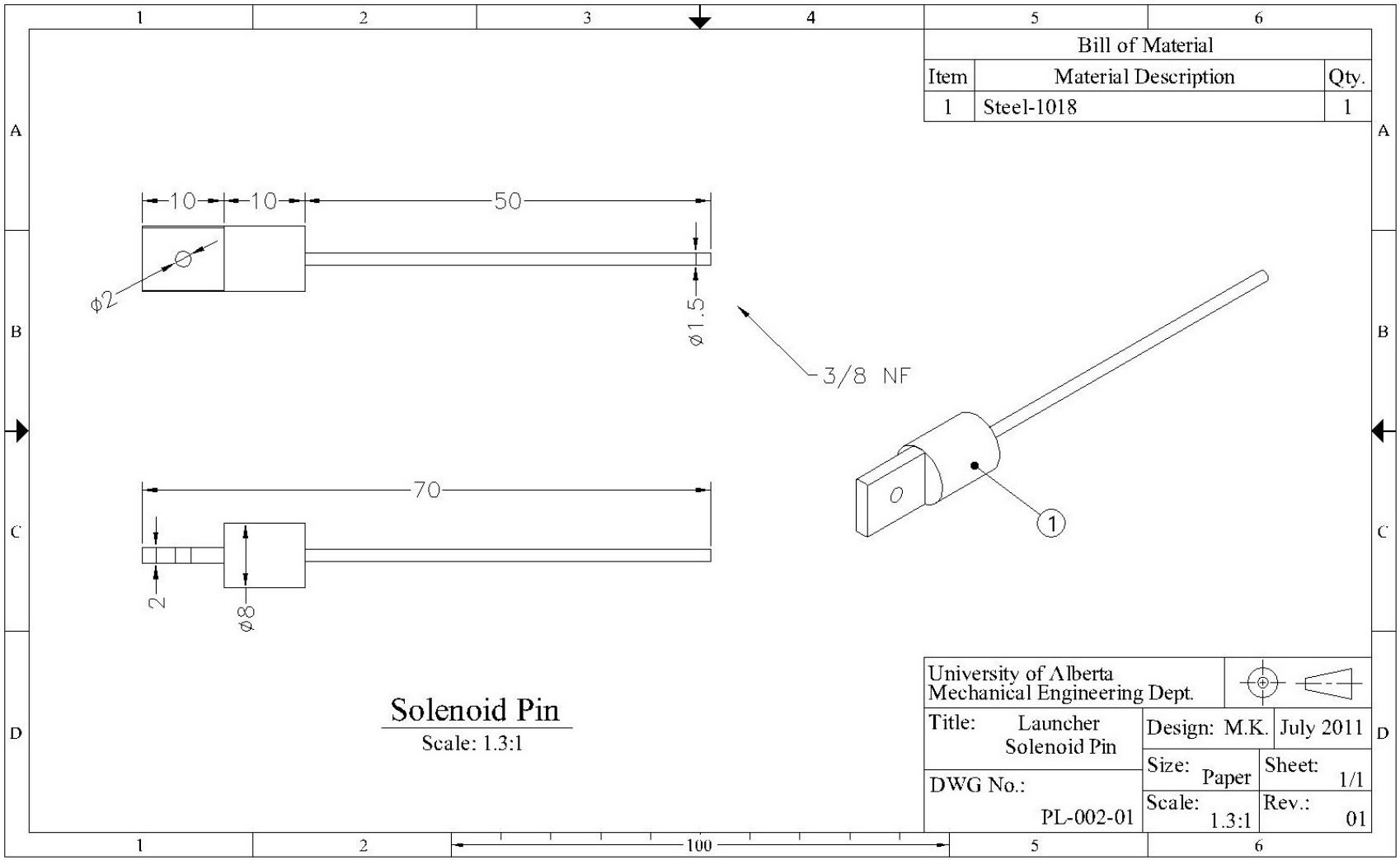
Bill of Material
Item | Material Description | Qty.
1 | Steel-1018 | 1
10
10
50
ϕ2
ϕ1.5
3/8 NF
70
2
ϕ8
1
Solenoid Pin
Scale: 1.3:1
University of Alberta
Mechanical Engineering Dept.
Title: Launcher Solenoid Pin
Design: M.K. July 2011
Size: Paper
Sheet: 1/1
DWG No.: PL-002-01
Scale: 1.3:1
Rev.: 01
100

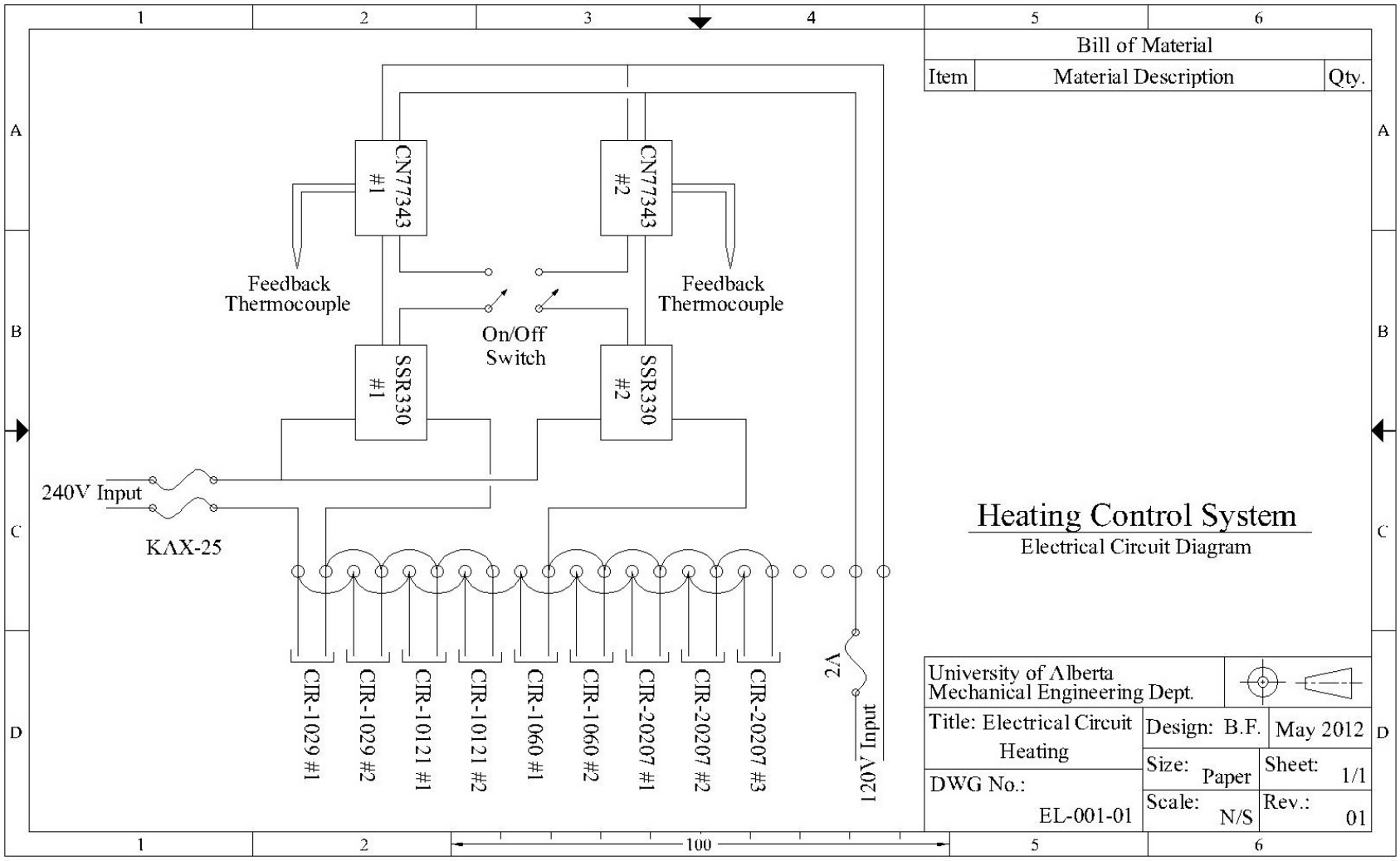
Bill of Material
Item
Material Description
Qty.
CN7343 #1
CN7343 #2
Feedback Thermocouple
Feedback Thermocouple
On/Off Switch
SSR330 #1
SSR330 #2
240V Input
KAX-25
CIR-1029 #1
CIR-1029 #2
CIR-10121 #1
CIR-10121 #2
CIR-1060 #1
CIR-1060 #2
CIR-20207 #1
CIR-20207 #2
CIR-20207 #3
2A
120V Input
Heating Control System
Electrical Circuit Diagram
University of Alberta
Mechanical Engineering Dept.
Title: Electrical Circuit Heating
Design: B.F.
May 2012
Size: Paper
Sheet: 1/1
DWG No.: EL-001-01
Scale: N/S
Rev.: 01
100

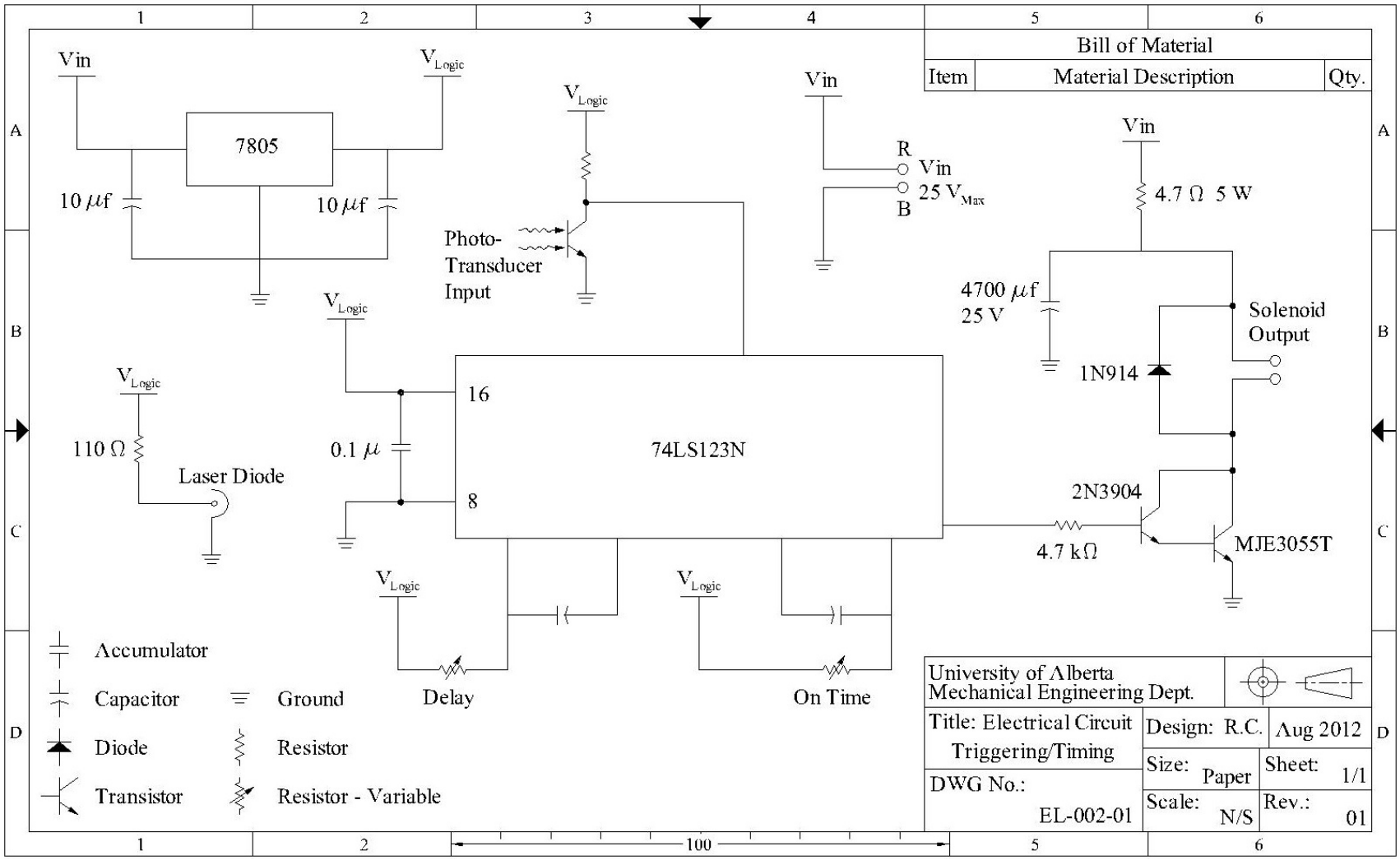
Vin
V_{Logic}
7805
10 μf
10 μf
Photo-
Transducer
Input
R
Vin
25 V_{Max}
B
4.7 Ω 5 W
4700 μf
25 V
Solenoid
Output
1N914
110 Ω
Laser Diode
0.1 μ
16
8
74LS123N
2N3904
MJE3055T
4.7 kΩ
Delay
On Time
Accumulator
Capacitor
Diode
Transistor
Ground
Resistor
Resistor - Variable
Bill of Material
Item
Material Description
Qty.
University of Alberta
Mechanical Engineering Dept.
Title: Electrical Circuit
Triggering/Timing
Design: R.C.
Aug 2012
Size: Paper
Sheet: 1/1
DWG No.:
EL-002-01
Scale: N/S
Rev.: 01
100